Generation and Characterization of COL4A1 Small Vessel Disease Mutations in a Human iPSC Model

Joseph Kroeger

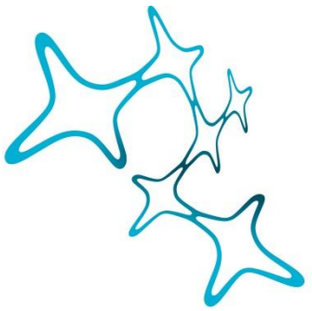

Graduate School of
Systemic Neurosciences
LMU Munich

Dissertation der Graduate School of Systemic Neurosciences
der Ludwig-Maximilians-Universität München

December 2022

Supervisor
Prof. Dr. Dominik Paquet
Institute for Stroke and Dementia Research
University Hospital, LMU Munich

First Reviewer: Prof. Dr. Dominik Paquet
Second Reviewer: Prof. Dr. Martin Dichgans
External Reviewer: Prof. Dr. Julian Grünewald

Date of Submission: 06.12.2022
Date of Defense: 11.04.2023

Table of Contents

Abbreviations ..... **v**

Abstract **1**

Chapter 1 Introduction **2**

1.1 Cerebral Small Vessel Disease 2

1.1.1 Typical imaging features of cSVD 2

1.1.2 Risk factors for cSVD 2

1.1.3 Monogenic forms of cSVD 3

1.1.4 Sporadic vs monogenic cSVD 4

1.1.5 Proposed mechanisms of cSVD 4

1.1.6 Experimental cSVD models 4

1.2 The blood-brain-barrier (BBB) 5

1.2.1 Specialized tight junctions seal cell-cell edges of BBB endothelial cells 5

1.2.2 BBB specific reduction of transcytosis and leukocyte adhesion molecules (LAMs) 6

1.2.3 Specialized transport systems of the BBB 6

1.2.3 The neurovascular unit (NVU) 7

1.2.4 The endothelial glycocalyx is the first line of defense of the BBB 9

1.2.5 The components and function of the NVU basement membrane 9

1.3 Type IV collagen 10

1.3.1 Heterotrimer formation 11

1.3.2 Posttranslational modifications 11

1.3.3 Collagen IV trafficking and secretion 11

1.4 Assembly and function of the NVU BM 12

1.4.1 Mechanical properties of the BM 12

1.4.2 Cell signaling mediated by the BM 13

1.4.3 The role of MMPs in basement membrane remodeling 14

1.5 COL4A1 and COL4A2 mutations in pathology 14

1.5.1 Proposed cSVD mechanisms of COL4A1 and COL4A2 mutations 14

1.6 *In vivo* and *in vitro* models to study monogenic collagen IV cSVD 16

1.6.1 Primary and immortalized cell lines for *in vitro* modeling 17

1.6.2 Induced pluripotent stem cells for disease modeling 17

1.6.3 *In vitro* BBB models 19

1.6.4 Functional assays to assess BBB characteristics in *in vitro* BBB models 20

1.7. The importance of genome editing and impact of CRISPR 21

1.7.1 Discovery of CRISPR in the archaea and bacteria immune system 21

1.7.2 Applications of the CRISPR/Cas9 system 22

1.7.3 Modes of CRISPR/Cas9 delivery for genome editing 23
1.7.4 DNA repair after Cas9 mediated DSB 23
1.7.6 Quality controls in iPSCs after genome editing 25
1.8 Aims of the thesis 25
Chapter 2 Materials and Methods 27
2.1 hiPSC lines 27
2.2 hiPSC maintenance 27
2.3 Design of CRISPR/Cas9 sgRNAs 27
2.4 Testing sgRNA activity in HEK293 cells 28
2.5 Design of repair template single-stranded oligodeoxynucleotides (ssODNs) 28
2.6 Electroporation of hiPSCs 29
2.7 Single cell clone generation and isolation 30
2.8 Single cell clone screening 30
2.8.1 Replica plating and cell lysis 30
2.8.2 Genotyping PCR 31
2.8.3 RFLP clone screening assay and clonal expansion 31
2.9 Quality controls of CRISPR/Cas9 edited hiPSCs 32
2.9.1 BCL2L1 assay 32
2.9.2 OnTE qgPCR assay 33
2.9.3 Off-target analysis 33
2.9.4 LOH analysis 34
2.9.5 DNA Fingerprinting 34
2.9.6 Molecular karyotyping 35
2.9.7 Pluripotency analysis 35
2.10 Endothelial cell differentiation and culturing 35
2.11 Pericyte differentiation and culturing 36
2.12 Smooth muscle cell differentiation and culturing 37
2.13 Immunofluorescence stainings 37
2.14 Gene expression analysis by qPCR 38
2.15 TEER measurements with cellZscope 39
2.16 Generation of 3D-cultures 40
2.16.1 Perfusion of 3D-cultures 41
2.17 List of primers 41
Chapter 3 Results 44
3.1 COL4A1 KO genome editing in hiPSCs 44
3.1.1 Generation of the COL4A1 KO in hiPSCs 45
3.1.2 COL4A1^{G755R} genome editing in hiPSCs 49

3.1.3 Design of COL4A1 3'-UTR (c.*35C>A) KI 51
3.2 COL4A1 KO characterization 56
3.2.1 Functional analysis of barrier formed by COL4A1 KO ECs 58
3.2.2 Effect of 3'-UTR (c.35*C>A) mutation on collagen IV expression 59
3.2.3 COL4A1^{G755R} KI exhibits normal COL4A1 expression 60
3.2.4 Collagen IV expression pattern of COL4A1^{G755R} KI ECs in 3D cultures 61
3.2.5 Perfusion of 3D cultures 61
3.3 Chapter summary 62
Chapter 4 Discussion 64
4.1 CRISPR/Cas9 is a versatile genome editing tool 64
4.1.1 RNP delivery of Cas9/sgRNA complex efficiently edits hiPSCs 64
4.1.2 HDR enhancing compounds reduced Indel formation but did not increase HDR rates 64
4.1.3 Asymmetric repair template design had a small locus dependent effect on HDR 65
4.1.4 Single cell KI clones could not be generated without Indels in the absence of blocking mutations 66
4.1.5 Blocking mutations substantially increase HDR 66
4.1.6 HiFi Cas9 (R691A) mitigated off-target detection in the top 10 predicted *in silico* off-target regions 67
4.1.7 Genome editing human iPSCs selects for a triplication of BCL2L1 on chromosome 20 68
4.1.8 OnTEs were nearly absent across all editing experiments 68
4.1.9 Karyotyping via a SNP microarray confirms origin of single cell clones and suggests COL4A1 heterozygous KO lines could be derived from the same clone 69
4.1.10 Pluripotency stainings performed for COL4A1 KOs reveal no evident loss of pluripotency 69
4.2 Characterization of Collagen IV expression in the COL4A1 mutants 70
4.2.1 COL4A1 and COL4A2 mRNA seem to fluctuate in hiPSC-EC cultures 71
4.2.2 Silent mutations incorporated in the COL4A1^{G755R} KI do not impact COL4A1 expression 72
4.2.3 COL4A1^{G755R} KI endothelial cells readily secrete collagen IV in 3D 72
4.2.4 Unexpected TEER measurement from KO: potential compensating mechanism or clonal effect? 73
4.3 Strengths and limitations of the monogenic COL4A1 cSVD human iPSC model 74
4.3.1 The 3D microfluidic *in vitro* system in this work provides easy visualization and complete cellular control 74
4.3.2 Comparison of animal models to a human cellular system 74
4.3.3 Advantages and drawbacks of the 3D NVU model 75
4.3.4 Application of flow to the 3D NVU model 76
4.4 Outlook and future perspectives 76
4.4.1 Determination of a conclusive effect of COL4A1 mutations on TEER 77
4.4.2 Complete characterization of TJs expression and organization 78

4.4.3 Quantification of ER stress and intracellular accumulation of collagen IV 78
4.4.4 RNA-seq and proteomics study of COL4A1 mutants 79
4.4.5 Characterize the COL4A1 mutants in 3D microfluidic cultures 79
4.5 Conclusion 80
5. References 81
6. Acknowledgements x
7. Curriculum Vitae xi
8. List of publications xii
9. Eidesstattliche Erklärung/Affidavit xiii
10. Declaration of author contributions xiv

Abbreviations

+CTRL	Positive Control
-CTRL	Negative Control
2D	Two-Dimensional
3D	Three-Dimensional
3'-UTR	Three Prime Untranslated Region
4-PBA	4-Phenylbutyric Acid
AA	Ascorbic Acid
ABC	ATP-Binding Cassette
ADA2	Adenosine Deaminase 2
AJ	Adherens Junction
ALK5	TGFβ Type I Receptor Kinase
Ang-1	Angiopoietin 1
APEL2	Albumin Polyvinylalcohol Essential Lipids 2
APOE	Apolipoprotein E
APP	Amyloid Precursor Protein
AQP4	Aquaporin-4
ASL-fMRI	Arterial Spin Labeling-Functional Magnetic Resonance Imaging
ATF6	Activating Transcription Factor 6
ATP	Adenosine Triphosphate
BBB	Blood-Brain-Barrier
BCL2L1	Bcl-2-Like Protein 1
Bcl-Xl	B-cell Lymphoma-Extra Large
bFGF	Basic Fibroblast Growth Factor
BiP	Binding Immunoglobulin Protein
BIR	Break-Induced Replication
BM	Basement Membrane
BMEC	Brain Microvascular Endethelial Cells
bp	Base Pair
BSA	Bovine Serum Albumin
C. Elegans	Caenorhabditis Elegans
CAA	Cerebral Amyloid Angiopathy
CADASIL	Cerebral Autosomal Dominant Arteriopathy with Subcortical Infarcts and Leukoencephalopathy
CARASAL	Cathepsin A-Related Arteriopathy with Strokes and Leukoencephalopathy
CARASIL	Cerebral Autosomal Recessive Arteriopathy with Subcortical Infarcts and Leukoencephalopathy
Cas9	CRISPR Associated Protein 9
Cav-1	Caveolin 1
CD13	Aminopeptidase N
CFD	Cutting Frequency Determination
CHOP	C/EBP Homologous Protein
Chr	Chromosome
Cld-5	Claudin-5
CMT	Carrier Mediated Transport
c-Myc	Cellular Myelocytomatosis
CNS	Central Nervous System

CNTF	Ciliary Neurotrophic Factor
CNV	Copy Number Variation
COL4A1-6	Collagen Type IV Alpha Chain 1-6
COPII	Coat Protein Complex II
CORRECT	Consecutive Re-guide or Re-Cas Steps to Erase CRISPR/Cas-Blocked Targets
Cp	Crossing Point
CRISPR	Clustered Regularly Interspaced Short Palindromic Repeats
crRNA	CRISPR RNA
CSF	Cerebral Spinal Fluid
cSVD	Cerebral Small Vessel Disease
Ct	Cycle Threshold
CTSA	Cathepsin-A
Da	Daltons
DAPI	4',6-Diamidino-2-Phenylindole
DIV	Dynamic *In Vitro*
DMEM	Dulbecco's Modified Eagle Medium
DMEM/F-12	Dulbecco's Modified Eagle Medium/Nutrient Mixture F-12
DMSO	Dimethyl Sulfoxide
DNA	Deoxyribonucleic Acid
Dnajb1	DnaJ Heat Shock Protein Family (Hsp40) Member B1
DNA-PKcs	DNA-Dependent Protein Kinase, Catalytic Subunit
DSB	Double Strand Break
DSM	Double Silent Mutation
E6	Essential 6
E8F	Essential 8 Flex
EC	Endothelial Cell
ECM	Extracellular Matrix
ECM2	Endothelial Cell Growth Medium 2
EDTA	Ethylenediaminetetraacetic Acid
EGF	Epidermal Growth Factor
eIF2α	Eukaryotic Initiation Factor 2
EM	Electron Microscopy
EMC7	ER Membrane Protein Complex Subunit 7
EP_4	Prostaglandin E2 Receptor 4
ER	Endoplasmic Reticulum
ESAM	Endothelial Selective Adhesion Molecule
ESC	Embryonic Stem Cell
ETV2	Erythroblast Transformation Specific Variant Transcription Factor 2
FAK	Focal Adhesion Kinase
FBS	Fetal Bovine Serum
FGF	Fibroblast Growth Factor
FN1	Fibronectin 1
FOXC1	Forkhead Box C1
FOXF2	Forkhead Box F2
g	Gravitational Acceleration
GAG	Glycosaminoglycans
gDNA	Genomic DNA

GDNF	Glial-Derived Neurotrophic Factor
GFAP	Glial Fibrillary Acidic Protein
GFP	Green Fluorescent Protein
GLUT-1	Glucose Transporter 1
GOM	Granular Osmiophilic Material
GSK-3	Glykogensynthase-Kinase 3
GTP	Guanosine Triphosphate
GWAS	Genome Wide Association Studies
HANAC	Hereditary Angiopathy, Nephropathy, Aneurysms, and Muscle Cramps
HDR	Homology Directed Repair
HiFi Cas9	High-Fidelity Cas9
hiPSCs	Human Induced Pluripotent Stem Cells
HR	Homologous Recombination
HSP47	Heat Shock Protein 47
HSPG	Heparin Sulfate Proteoglycan
HTRA1	High-Temperature Requirement A Serine Peptidase 1
Hz	Hertz
ICAM1	Intercellular Adhesion Molecule 1
ICE	Inference of CRISPR Edits
ICH	Intracranial Hemorrhage
IL-1β	Interleukin-1 Beta
Indel	Insertions and/or Deletions
iPSCs	Induced Pluripotent Stem Cells
ITGB1	Integrin Subunit Beta 1
JAMs	Junctional Adhesion Molecules
Kb	Kilobase
kDa	Kilodalton
KI	Knock-In
Klf4	Krüppel-Like Factor 4
KO	Knock-Out
LAM	Leukocyte Adhesion Molecule
LAMC1	Laminin Subunit Gamma 1
LH1-3	Lysyl Hydroxylase 1-3
LIF	Leukemia Inhibitory Factor
LOH	Loss of Heterozygosity
MACS	Magnetic Activated Cell Sorting
MAPK	Mitogen-Activated Protein Kinase
Mfsd2a	Major Facilitator Superfamily Domain-Containing Protein 2
MIM	Mesoderm Induction Medium
miR-29	microRNA-29
MIT	Massachusetts Institute of Technology
MMEJ	Microhomology-Mediated End Joining
MMP	Matrix Metalloproteinase
MRI	Magnetic Resonance Imaging
mRNA	Messenger RNA
MYH11	Myosin Heavy Chain 11
NADPH	Nicotinamide Adenine Dinucleotide Phosphate

NC1	Non-Collagenous Domain 1
NFIA	Nuclear Factor I A
NG2	Neural/Glial Antigen 2
NHEJ	Non-Homologous End Joining
NMD	Nonsense-Mediated Decay
NOTCH3	Neurogenic Locus Notch Homolog Protein 3
NVU	Neurovascular Unit
Oct-4	Octamer-Binding Transcription Factor 4
OnTEs	On-Target Effects
P-gp	P-Glycoprotein
P3H2	Prolyl 3-Hydroxylase 2
P4H	Proline-4-Hydroxylase
PADMAL	Pontine Autosomal Dominant Microangiopathy with Leukoencephalopathy
PAM	Protospacer Adjacent Motif
PBS	Phosphate-Buffered Saline
PCR	Polymerase Chain Reaction
PDAI3	Protein Disulfide Isomerase Family A Member 3
PDGF-BB	Platelet-Derived Growth Factor B
PDGFRβ	Platelet-Derived Growth Factor Receptor Beta
PDZ	PSD95, Dlg1, and ZO-1
PE	Pericyte
PECAM-1	Platelet Endothelial Cell Adhesion Molecule (CD31)
PFA	Paraformaldehyde
PGE_2	Prostaglandin E2 (Dinoprostone)
PITX2	Paired Like Homeodomain 2
PTC	Premature Termination Codon
QC	Quality Control
qgPCR	Quantitative Genotyping PCR
qPCR	Quantitative PCR
RA	Retinoic Acid
RFLP	Restriction Fragment Length Polymorphism
RI	Rock Inhibitor
RPL22	Ribosomal Protein L22
RMT	Receptor Mediated Transport
RNA	Ribonucleic Acid
RNA-seq	RNA-Sequencing
RNP	Ribonucleoprotein
ROS	Reactive Oxygen Species
rpm	Rotations Per Minute
rv	Reverse
S100β	S100 Calcium-Binding Protein Beta
SDSA	Synthesis-Dependent Strand Annealing
SF	Stem Flex
sgRNA	Single Guide RNA
SHH	Sonic Hedgehog
SLC2A1	Solute Carrier Family 2 Member 1
SMAD	Small Mothers Against Decapentaplegic

SMC	Smooth Muscle Cell
SMC2	Smooth Muscle Cell Growth Medium 2
SMMHC	Smooth Muscle Myosin Heavy Chain
SNP	Single Nucleotide Polymorphism
Sox2	SRY (Sex Determining Region Y)-Box 2
Sox9	SRY (Sex Determining Region Y)-Box 9
SSA	Single-Strand Annealing
SSEA4	Stage-Specific Embryonic Antigen-4
SSeCKs	Src-Supressed C-Kinase Substrate
ssODN	Single-Stranded Oligodeoxynucleotides
STRIVE	Standards for Reporting Vascular changes on nEuroimaging
TALEN	Transcription Activator-Like Effector Nuclease
TALEs	Transcription Activator-Like Effectors
TANGO1	Transport and Golgi Organization Protein 1
TEER	Transendothelial Eletrical Resistance
TERT	Telomerase Reverse Transcriptase
TGFß	Transforming Growth Factor Beta
TGFβR2	Transforming Growth Factor, Beta Receptor 2
TIDE	Tracking of Indels by Decomposition
TIMP	Tissue Inhibitor of Metalloproteinase
TJ	Tight Junction
Tra-160	T Cell Receptor Alpha Locus 1-60
TREX1	3’ Repair Exonuclease I
tTJ	Tricellular Tight Junction
UPR	Unfolded Protein Response
VE-cadherin	Vascular Endothelial Cadherin (CD144)
VEGF	Vascular Endothelial Growth Factor
VEGFR2	Vascular Endothelial Growth Factor Receptor 2
VNTR	Variable Number of Tandem Repeats
vSMC	Vascular Smooth Muscle Cell
VTN	Vitronectin
WB	Western Blot
WMH	White Matter Hyperintensity
WNT	Wingless (pathway)
WT	Wild Type
XRCC4	X-Ray Repair Cross-Complementing Protein 4
ZFN	Zinc Finger Nuclease
ZFP	Zinc Finger Protein
ZO-1-3	Zonula Occludens-1-3
α-GAL	Alpha-Galactosidase
α-SMA	Alpha-Smooth Muscle Actin

Abstract

Cerebral small vessel disease (cSVD) is responsible for 1 out of every 4 strokes and contributes to half of the cases of dementia. Despite its burden to society, there are currently no treatments available. Genetics are a major risk factor with variants linked to an increased risk of sporadic cSVD and monogenic cSVD with varying penetrance. There is a substantial overlap of imaging features between sporadic and monogenic cases of cSVD and variants in the same genes have been associated with both types of cSVD. However, disease mechanisms of both sporadic and monogenic cSVD remain to be elucidated. Data from patients and mouse models indicate that reduced cerebral blood flow and dysfunction of the blood-brain barrier (BBB) as well as the neurovascular unit (NVU) seem to be implicated with cSVD progression.

Investigation of cSVD has been hindered by the inability to visualize the affected small arterioles and capillaries in patients. As a result, animal models of monogenic cSVD have yielded several insights in cSVD research. While visualization of small vessels is possible in animal models, drugs developed using these systems can have limited translatability. Recently, patient-derived human induced pluripotent stem cells (hiPSCs) have been used to model CADASIL, a form of monogenic cSVD caused by NOTCH3 mutations. Moreover, significant advancements have been made towards 3D *in vitro* NVU modeling using hiPSCs. A major advantage of hiPSC models is their applicability to examine the human and cell-specific mechanisms responsible for the disease and serve as a reliable drug-screening platform.

Several mutations linked to both sporadic and monogenic cSVD have been identified in COL4A1 (collagen IV type α1) and COL4A2 (collagen IV type α2). These two proteins combine to form a collagen IV heterotrimer that is the main constituent of the basement membrane (BM) providing necessary scaffolding and conferring structural stability to the NVU. The mechanisms by which mutations in these genes cause cSVD remains unknown.

In this thesis, 3 monogenic cSVD mutations in COL4A1 (COL4A1 KO, (c.*35C>A), and COL4A1^{G755R}) that differentially impact the protein were inserted into wild-type hiPSCs using CRISPR/Cas9 genome editing, resulting in 3 isogenic lines. Two of the mutations affect the expression of COL4A1 in opposite directions. The 3rd mutation is a missense mutation predicted to impact folding of the heterotrimer. Edited cell lines were rigorously quality controlled to confirm the genome remained unaffected by deleterious side effects of genome editing. COL4A1 KO was confirmed by qPCR and immunofluorescence in endothelial cells (ECs). Unexpectedly, the TEER of KO ECs was increased in one clone coinciding with increased integrin β1 and junction proteins measured by qPCR. However, the increased TEER was not reproduced by two other KO clones. The (c.*35C>A) mutant expressed significantly higher levels of COL4A1 mRNA in pericytes but not in other NVU (neurovascular unit) cell types suggesting pericytes may have a relevant contribution to PADMAL, the subtype of cSVD caused by this mutation. Lastly, ECs from the COL4A1^{G755R} mutant were observed to secrete collagen IV when cultured as 3D vessel-like tubes indicating that heterotrimer formation occurs in this mutant.

Taken together, this work has established a platform to study COL4A1 monogenic cSVD in an *in vitro* human NVU model in both 2D and 3D. The CRISPR/Cas9 genome editing and quality control workflow was used to generate multiple cell lines for each mutation. The expression of COL4A1 was characterized in each mutant to establish the validity of these cell lines as a disease model for monogenic cSVD. Further experiments are needed to determine reproducibility of observed phenotypes as well as the suitability of the system to investigate underlying disease mechanisms.

Chapter 1 Introduction

1.1 Cerebral Small Vessel Disease

Cerebral small vessel disease (cSVD) is an umbrella term used to classify a wide range of pathologies affecting the small arteries, arterioles, capillaries, and venules of the brain. Roughly one out of four ischemic strokes and nearly all hemorrhagic strokes are caused by cSVD (Wardlaw et al., 2019). In addition to directly impacting the brain's small vasculature, cSVD is a contributor to about half of the cases of dementia (Shi & Wardlaw, 2016; Wardlaw et al., 2019). Manifestations of cSVD are commonly discovered through incidental MRI findings (Chojdak-Łukasiewicz et al., 2021). There are several predictive risk factors for cSVD, with age being the largest. Cerebral microbleeds affect over one third of people in their 80s and by age 90 nearly every individual will display MRI white matter hyperintensities (Chojdak-Łukasiewicz et al., 2021). With an aging population there is a substantial burden on society causing a strong medical need to further investigate causes and potential clinical treatments for cSVD.

1.1.1 Typical imaging features of cSVD

Patients diagnosed with cSVD exhibit various imaging irregularities that were standardized by the publication of the STRIVE (Standards for Reporting Vascular changes on nEuroimaging) protocol in 2013 (Wardlaw et al., 2013). The defined radiological phenotypes comprise recent subcortical infarcts near a penetrating arteriole, white matter hyperintensities, lacunas of presumed vascular origin, widened perivascular space, cerebral microbleeds, and brain atrophy not related to prior stroke or head injury. White matter hyperintensities are characterized by hyperintense signal on T2 weighted images that differs from CSF signal. Lacunas are round or ovoid fluid-filled cavities with signal similar to CSF. Widened perivascular spaces are fluid-filled spaces following the course of penetrating vessels. Lastly, cerebral microbleeds are characterized by a 2-5mm diameter void of signal (Chojdak-Łukasiewicz et al., 2021; Wardlaw et al., 2019). **(Figure 1.1)**

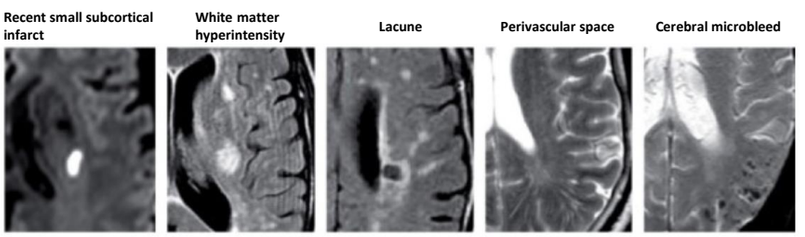

Figure 1.1 Examples of clinical cSVD features defined by STRIVE. Adapted with permission from (Wardlaw et al., 2013). © 2013 Elsevier Ltd. All rights reserved.

Most cSVD events are subclinical and it is estimated that about 10 brain changes occur for every symptomatic stroke (E. Smith et al., 2017). Although silent, these cSVD MRI features confer an increased risk of future stroke and dementia (Pasi & Cordonnier, 2020). In fact, presence of individual features correlates with an increased risk of both ischemic and hemorrhagic stroke, depression, dementia, and mortality and a combination of multiple features further strengthens the association (Rensma et al., 2018).

1.1.2 Risk factors for cSVD

Since it is well established that cSVD is a predicative risk factor of stroke, dementia, and overall mortality, it is important to identify risk factors for cSVD itself. Age is the largest yet unmodifiable risk factor. Hypertension and salt intake increase the incidence of white matter hyperintensities (Heye et al., 2016) and are considered very strong yet modifiable risk factors for cSVD. Lowering blood pressure reduces stroke and cognitive decline (Benavente et al., 2013). Controlling this and other modifiable risk factors such as smoking, obesity, and dyslipidemia can help prevent or lessen the burden of cSVD (Qian Li et al., 2018). Nevertheless, family history studies suggest that sporadic cSVD is highly heritable.

Moreover, types of monogenic cSVD disease are expected to help bridge the gap between genetics and clinical cSVD by enabling generation of powerful genetic models to investigate the cellular and molecular changes in the disease (Choi, 2015).

1.1.3 Monogenic forms of cSVD

In addition to an association between family history and incidence of cSVD, there are several types of inherited monogenic cSVD that are responsible for around 5% of all strokes (Choi, 2015). Caused by mutations in NOTCH3, CADASIL is the most prevalent form of monogenic cSVD and very closely mirrors the progression and pathology of sporadic cSVD (di Donato et al., 2017). Rare variants in COL4A1, COL4A2, HTRA1, TREX1, FOXF2, FOXC1, APP, ADA2, α-GAL, and CTSA have also been identified as causes of monogenic cSVD (Choi, 2015; Joutel & Faraci, 2014; Rannikmäe et al., 2020; Rost et al., 2016).

CADASIL stands for cerebral autosomal dominant arteriopathy with subcortical infarcts and leukoencephalopathy. Patients display a variety of symptoms ranging from psychiatric disorders, migraines, subcortical ischemic events, and cognitive impairment (di Donato et al., 2017). CADASIL pathology is hallmarked by deposition of granular osmiophilic material (GOM) on small vessels and vascular smooth muscle cell degeneration (Mizuno et al., 2020). Accumulation of fibrous ECM (extracellular matrix) proteins in the tunica media is also frequently observed. Several NOTCH3 mutations have been reported in CADASIL patients, most of which affect one of the 34 cysteine residues in the epidermal growth factor-like repeat (EGFr) (Papakonstantinou et al., 2019). Mutations that affect one of the first 6 residues are markedly more severe causing onset of stroke an average 12 years before mutations affecting residues 7-34 (Rutten et al., 2019). Other cysteine-sparring missense mutations in NOTCH3 have been identified. Only a subset of these mutations cause GOM (Muiño et al., 2017).

CARASIL (cerebral autosomal recessive arteriopathy with subcortical infarcts and leukoencephalopathy) is the recessive form of CADASIL. Differing from CADASIL, mutations in high-temperature requirement A serine peptidase 1 (HTRA1) are responsible for CARASIL. These patients have homozygous mutations that impair or abolish the protease activity. HTRA1 normally suppresses TGFβ (transforming growth factor beta) signaling and without this inhibition, rampant TGFβ signaling is thought to lead to the manifestation of CARASIL (Hara et al., 2009).

Caused by mutations in CTSA, the gene encoding cathepsin-A, CARASAL (cathepsin A-related arteriopathy with strokes and leukoencephalopathy) is a very rare monogenic cSVD. One of the functions of cathepsin-A is to degrade endothelin-I and there is some evidence also linking endothelin-I to CARASAL (Bugiani et al., 2016).

Patients found to have mutations in FOXC1 display all of the typical cSVD MRI features and suffer from frequent ischemic episodes. FOXC1 is highly expressed in pericytes which are crucial for maintenance of the blood-brain-barrier (BBB) (Choi, 2015). Moreover, GWAS studies have implicated single nucleotide polymorphisms that influence FOXC1 transcript levels in cSVD (French et al., 2014). A paralogue to FOXC1, the transcription factor FOXF2 has also been linked to cSVD stroke in a GWAS study (Chauhan et al., 2016). FOXF2 -/- mice exhibit a leaky BBB (Reyahi et al., 2015). It is believed that PITX2, an interaction partner of FOXC1 and independent risk locus for atrial fibrillation and cardioembolic stroke, may be involved in a shared mechanism for FOXC1 and FOXF2 cSVD (Choi, 2015). However, this link remains to be fully elucidated.

Frame shift mutations in the C-terminus of TREX1 (3' repair exonuclease I) have been associated with vascular retinopathy and cerebral leukodystrophy (Rice et al., 2015). Patients typically exhibit punctate white matter lesions and suffer from neurological deficits, migraine, cognitive impairment, psychiatric disturbances, and sometimes seizures (Stam et al., 2016). Fabry disease is an X-linked lysosomal storage disorder triggered by mutations in α-GAL that block activity of the enzyme α-galactosidase A. Without activity of this enzyme, glycosphingolipids accumulate across multiple tissues (Rosenberg & Pascual, 2020). White matter hyperintensities are frequently present in Fabry's disease patients (Rost

et al., 2016) and incidence of stroke is much higher than in the average population, with ischemic strokes occurring more frequently than hemorrhagic strokes (Sims et al., 2009). Patients with a loss of function mutation in ADA2 (adenosine deaminase 2) suffer from early-onset lacunar strokes and systemic vasculopathy (Zhou et al., 2014). Variants in mitochondrial DNA have also been implicated in a monogenic form of cSVD termed MELAS (mitochondrial encephalomyopathy with lactic acidosis and stroke-like episodes) (Dunn et al., 2022). A distinct type of cSVD called cerebral amyloid angiopathy or CAA is categorized by the deposition of beta-amyloid fibrils around cerebral vessels leading to typical manifestations of cSVD such as cerebral microbleeds and white matter hyperintensities (Viswanathan & Greenberg, 2011). CAA can occur sporadically, but mutations in APP, such as E22Q, have been causally linked to the disease (Kamp et al., 2014).

Type IV collagen is a component of the extracellular matrix in most tissues in the human body. COL4A1 and COL4A2 form one of the three possible type IV collagen heterotrimers and several mutations causing multi-system disorders have been identified (Meuwissen et al., 2015). Most pathogenic COL4A1 and COL4A2 mutations affect glycine residues in the collagenous domain and inhibit correct heterotrimer formation (Jeanne & Gould, 2017; Kuo et al., 2012). However, there have been documented haploinsufficiency mutations (Lemmens et al., 2013) as well as 3'-UTR mutations affecting collagen IV expression levels (Qing Li et al., 2022; Mönkäre et al., 2021; Sakai et al., 2020; Saskin et al., 2018; Siitonen et al., 2017; Verdura et al., 2016; Y. Zhao et al., 2019).

1.1.4 Sporadic vs monogenic cSVD

While there seem to be subtle differences that can be teased out between different monogenic forms of cSVD (Giau et al., 2019; Whittaker et al., 2022), there is a significant overlap of imaging pathology and clinical symptoms between monogenic and sporadic cSVD (Marini et al., 2020). Mounting evidence suggests that common variants in monogenic cSVD genes such as COL4A2, HTRA1, and NOTCH3 are also associated with sporadic cSVD (Rannikmäe et al., 2020; Whittaker et al., 2022). However, the exact mechanisms of both sporadic and monogenic cSVD are incompletely understood (Choi, 2015; Giau et al., 2019; Tan et al., 2017).

1.1.5 Proposed mechanisms of cSVD

Reduced cerebral blood flow or ability for arterioles and capillaries to dilate in response to increased neural activity otherwise known as neurovascular coupling, is thought to contribute to cSVD (Wardlaw et al., 2019). For example, CADASIL patients exhibit lower neurovascular coupling in response to similar neural activity patterns detected by ASL-fMRI (Huneau et al., 2018). Studies have linked reactive oxygen species (ROS) to cerebral vascular dysfunction (de Silva & Miller, 2016), and there has been interest in targeting the activity of NADPH oxidases as a treatment for vascular disease (Drummond et al., 2011).

Breakdown of the blood-brain-barrier (BBB) and dysfunction of the neurovascular unit (NVU) have been implicated in the progression of cSVD pathology (Joutel & Faraci, 2014; Wardlaw, 2010; Wardlaw et al., 2019). Contrast enhanced MRI has demonstrated that cSVD patients exhibit higher BBB permeability even in otherwise normal white matter regions (Topakian et al., 2010). Moreover, increased BBB permeability was also observed in patients with lacunar stroke compared to patients with cortical stroke (Wardlaw et al., 2008).

1.1.6 Experimental cSVD models

MRI techniques allowing researchers to quantify BBB permeability in cSVD patients are constantly being improved, (Thrippleton et al., 2019) but direct visualization of the small arterioles and capillaries (50-400 µm in diameter) is not currently feasible (Chojdak-Łukasiewicz et al., 2021). Consequently, post-mortem studies have been invaluable to elucidate disease pathology (Müller et al., 2017). However, these end stage studies do not provide insights into the progression of the disease and there is a need for alternative model systems to study the progression of cSVD. Monogenic cSVD animal

models can help elucidate disease mechanisms that may be convergent between sporadic and monogenic cSVD (Joutel & Faraci, 2014). Recently, patient-derived iPSCs have been used to model hereditary cSVD (Y. Yamamoto et al., 2020) and significant advancements have been made in the development of BBB models using human iPSCs (Delsing et al., 2020; Workman & Svendsen, 2020).

1.2 The blood-brain-barrier (BBB)

The blood-brain-barrier (BBB) was first described at the beginning of the 20th century. While investigating potential chemotherapeutic agents, Ehrlich discovered that dyes failed to stain the brain despite diffusing into nearly every other tissue (Ehrlich, 1906). Lewandowski continued Ehrlich's experiments and demonstrated that Prussian blue reagents did not cross from the blood into the brain and formulated the first concept of the BBB he termed Bluthirnschranke (Lewandowski, 1900). Our understanding of the BBB has greatly evolved over the last century. The microvasculature of the CNS (central nervous system) is composed of highly specialized nonfenestrated continuous vessels designed to precisely regulate the influx and efflux of molecules in the brain (Daneman & Prat, 2015). Brain microvascular endothelial cells that compose this microvasculature have specialized cell-cell junctions, exhibit low rates of transcytosis, and have unique transport systems. All of which contribute to a highly selective BBB (Daneman & Prat, 2015).

1.2.1 Specialized tight junctions seal cell-cell edges of BBB endothelial cells

Brain microvascular endothelial cells (BMECs) express adherens junction proteins (Campbell et al., 2017) and an enrichment of tight junction proteins (Wallez & Huber, 2008) that interact with the actin cytoskeleton and mediate cell-cell adhesion by effectively sealing the gaps between adjacent endothelial cells. This prevents unwarranted paracellular transport into the brain and even restricts the diffusion of small ions such as Na+ and Cl- (Abbott et al., 2006). There are several characterized tight junction proteins including claudins, occludin, tricellulin, zonula occludens protein-1,2, and 3, and junctional adhesion molecules (JAMs)(Abbott et al., 2006; Furuse, 2010).

Occludin, an approximately 65 kDa protein comprised of 4 transmembrane domains and 2 extracellular loops, was the first integral membrane tight junction protein reported (Furuse et al., 1993). Its carboxy terminal cytoplasmic region has been demonstrated to bind to zonula occludens proteins 1, 2, and 3 (Furuse, 2010). Similar to occludin, expression of claudins 3, 5, and 12 are found in the BBB endothelium and these tight junction proteins have 4 transmembrane domains and 2 extracellular loops (Abbott et al., 2006). Claudin tight junctions, and especially claudin-5, are integral for normal tight junction function evidenced by a claudin-5 knockout mouse model that has a reported BBB leakage limited to small molecules less than 800 daltons (Nitta et al., 2003). Typical tight junctions between two adjacent cells close the cell-cell junction like a molecular zipper but inevitably there will be regions in which 3 cell membranes come into contact. In these regions, the protein tricellulin is enriched and tricellular tight junctions (tTJs) are formed (Furuse, 2010). Tricellulin contains a carboxy terminus with sequence similarity to occludin and it also been binds to zonula occludens 1 (Riazuddin et al., 2006). At tTJs, tricellulin orients perpendicular to zonula occludens 1 and forms a pillar at these tricellular contacts sealing the remaining gaps (Higashi & Miller, 2017). Zonula occludens-1,2, and 3 (ZO-1, ZO-2, and ZO-3) lie just below the plasma membrane and contain PDZ domains that interact with tight junction integral membrane proteins such as claudins, JAMs, occludin, and tricellulin anchoring them to the actin cytoskeleton (Furuse, 2010). One study found that depletion of both ZO-1 and ZO-2 in mouse epithelial cells disrupted normal tight junction formation but reintroduction of exogenous ZO-1 or ZO-2 but not ZO-3 rescued the phenotype (Umeda et al., 2006). Junctional adhesion molecules (JAM-A, JAM-B, and JAM-C) and endothelial selective adhesion molecule (ESAM) are immunoglobulin superfamily membrane proteins present at brain endothelial cell tight junctions and

also bind with ZO-1 through their PDZ binding domain (Stamatovic et al., 2016). **Figure 1.2** illustrates the organization of TJs in BMECs.

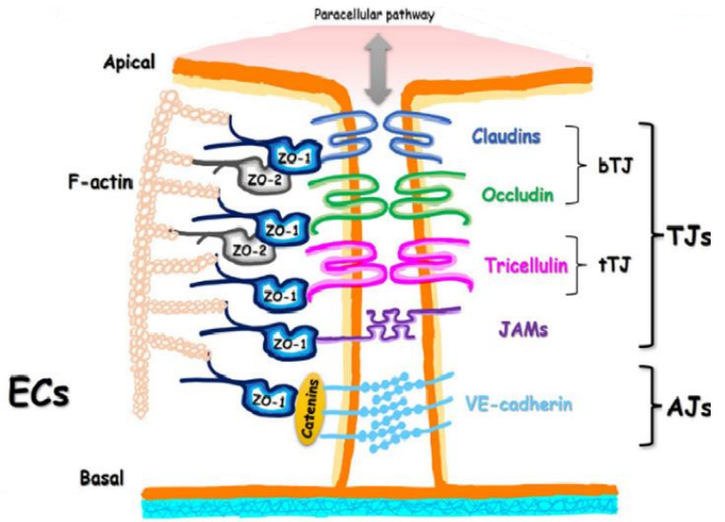

Figure 1.2 Overview of tight and adherens junctions in brain capillaries. Tight junctions and adherens junctions block paracellular transport of most molecules. Claudins and occludin are the integral membrane TJ proteins at bicellular tight junctions (bTJ). Tricellulin seals the gaps where 3 cells meet to form a tricellular tight junction (tTJ). Zonula occludens proteins anchor the integral membrane junction proteins to the actin cytoskeleton. Adapted with permission from (Brunner et al., 2021). © 2021 Elsevier B.V.

1.2.2 BBB specific reduction of transcytosis and leukocyte adhesion molecules (LAMs)

Unlike the endothelium in most organs, BMECs allow extremely low levels of passive diffusion and exhibit reduced expression of leukocyte adhesion molecules (LAMs) such as ICAM1 (intracellular adhesion molecule 1) preventing an excessive number of immune cells from entering the brain (Siegenthaler et al., 2013). Caveolae and clathrin mediated transcytosis represent the known types of transcytosis in the BBB endothelium (Ayloo & Gu, 2019). However, caveolae-mediated transcytosis is severely reduced in BMECs achieved by expression of Mfsd2a that efficiently reduces the number of caveolin-I vesicles (Andreone et al., 2017; Ben-Zvi et al., 2014). Clathrin mediated transcytosis is required for some receptor mediated transport (RMT) such as the transferrin and insulin receptors (Villaseñor et al., 2019).

1.2.3 Specialized transport systems of the BBB

The BBB is highly impermeable to passive transport and alternative transport routes are necessary in order to supply the brain with nutrients and molecules necessary for its function (Daneman & Prat, 2015; Sweeney et al., 2019). Carrier mediated transport (CMT), receptor mediated transport (RMT), active efflux, and ion transport represent the transport systems utilized by the BBB to precisely control molecular transfer between the circulating blood and the brain (Sweeney et al., 2019). CMT employs proteins that permit highly specific transport of molecules such as glucose, amino acids, and nucleosides (Curley & Cady, 2018). Responsible for transport of glucose into the brain, GLUT-1, encoded by SLC2A1, is one of the most characterized CMT transporters (Sweeney et al., 2019). Concentration of glucose is higher in the blood than the CNS and this gradient drives glucose into the brain through GLUT-1 carrier proteins (Mann et al., 2003). Most circulating proteins such as albumin, fibrinogen, thrombin, and growth factors are prevented from entering the CNS. Conversely, other molecules such as iron, insulin, and leptin are actively trafficked into the brain via RMT through transferrin receptors (TfR), insulin receptors (IR), and leptin receptors respectively (A. Jones & Shusta, 2007; Sweeney et al., 2019). Other RMT proteins regulate the efflux of specific proteins out of the brain. For example, LRP1 (LDL receptor related protein 1) typically localizes on the abluminal side of the BBB, binds amyloid beta, and mediates its clearance from the brain (Zhao et al., 2015). ABC efflux transporters utilize ATP hydrolysis to actively drive molecular transport, are highly expressed in BMECs,

and are critical for clearing the brain of toxins, drugs, and xenobiotics (Qosa et al., 2015). ABC efflux proteins are capable of transporting drugs with diverse structure and varying size ranging from morphine (285 Da) to cyclosporine-A (1200 Da) (Qosa et al., 2015). Several ion pumps reside on the BBB endothelium and are responsible for maintaining proper CNS function by controlling concentration gradients, regulating pH, and mediating vasodilation (Sweeney et al., 2019; Zlokovic, 2008).

1.2.3 The neurovascular unit (NVU)

Many defining characteristics of BMECs are induced by other brain cell types (Sweeney et al., 2019). In 2001, at the first Stroke Progress review group, the term neurovascular unit (NVU) was coined to describe the entire structure composed of several cell types with a specialized basement membrane (BM) that is responsible for the formation and maintenance of a healthy BBB (Iadecola, 2017). **Figure 1.3** shows the structure of the NVU.

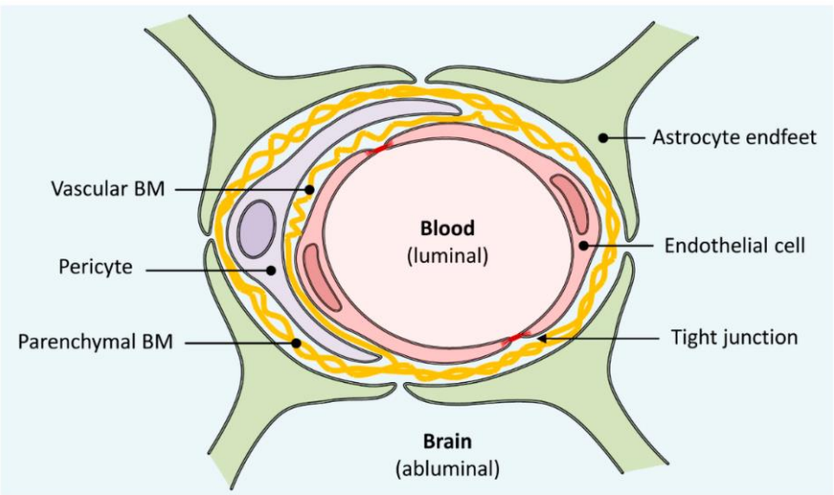

Figure 1.3 The Neurovascular Unit (NVU). Endothelial cells form a lumen that separates blood from the brain. The BM encases the endothelial cells providing support. Pericytes are embedded in the BM and tightly attach to endothelial cells. Finally, astrocytes extend endfeet to contact the BM of the NVU. Adapted with permission from (Neumaier et al., 2021).

1.2.3.1 Astrocytes

Astrocytes are the most abundant cell type in the brain performing several functions ranging from maintaining ion homeostasis, regulating the pH, recycling neurotransmitters, CNS repair after injury, relaying signals from neurons to vessels, and maintaining the BBB (Blanchette & Daneman, 2015; Kadry et al., 2020). At the BBB, Astrocytes extend polarized processes towards the vessels and contact the BM (Profaci et al., 2020). These endfeet ensheathing the microvasculature express a high density of orthogonal array of particles (OAPs) containing the astroglial water channel aquaporin-4 (AQP4) and the Kir4.1 potassium channel (Abbott et al., 2006). AQP4 channels facilitate the influx of CSF through the brain parenchyma, aid in the clearance of solutes from the interstitial fluid, and have even been shown to clear amyloid β from the brain (Iliff et al., 2012).

Astrocytes have been demonstrated to mediate cerebral blood flow changes in capillaries through a signaling cascade that begins with ATP being released from firing neurons triggering an influx of Ca2+ in the astrocytes eventually leading to the downstream release of the vasodilator PGE_2 onto pericytes inducing vasodilation via the EP_4 receptor (Mishra et al., 2016).

Co-culturing astrocytes with endothelial cells *in vitro* enhances barrier properties of endothelial cells (Dehouck et al., 1990). Many factors secreted by astrocytes act directly on endothelial cells including transforming growth factor β (TGFβ), glial-derived neurotrophic factor (GDNF), retinoid acid (RA), basic fibroblast growth factor (bFGF), angiopoietin 1 (Ang-1), sonic hedgehog (SHH), src-supressed C-kinase

substrate (SSeCKS), and apolipoprotein (APOE) (Abbott et al., 2006; Blanchette & Daneman, 2015; Daneman & Prat, 2015).

Astrocytic secreted SHH increases expression of tight junctions and decreases LAM intercellular adhesion molecule-1 (ICAM1) (Alvarez et al., 2011). SSeCKs expressing astrocytes exhibit increased Ang-1 expression and reduced vascular endothelial growth factor (VEGF) both of which result in a decreased endothelial cell permeability (Lee et al., 2003). GDNF, was first described as an astrocyte secreted neuroprotective factor (Henderson et al., 1994; Lin et al., 1993) but can also induce tighter barrier formation in porcine brain endothelial cells (Igarashi et al., 1999). RA is implicated as a regulator of numerous pathways including Wnt, Hh, and FGF suggesting that it could be an upstream regulator controlling several pathways important for normal BBB function (Daneman & Prat, 2015; Halilagic et al., 2007; Paschaki et al., 2012). APOE has three known isoforms (APOE 2, 3, and 4) (Mahley et al., 2009), and studies suggest that APOE4 but not 2 or 3 impair normal BBB function (Bell et al., 2012; Jackson et al., 2021). Astrocytes produce and deposit brain-specific laminin into the NVU BM. Specifically these isoforms maintain normal NVU pericyte physiology and inhibit their differentiation into contractile pericytes (Yao et al., 2014).

1.2.3.2 Mural cells

Mural cells are centrally located within the NVU and directly contact the endothelial cells of the brain vasculature (Iadecola, 2017). Cerebral arteries and penetrating arterioles are wrapped by vascular smooth muscle cells (vSMCs) that provide support by stiffening the vessels and contract or relax to control the rate of blood flow in response to neural activity (Hill et al., 2015; Profaci et al., 2020; Smyth et al., 2018). As cerebral microvessels become smaller, pericytes gradually replace vSMCs to form peg and socket connections with BMECs in capillaries, pre-capillary arterioles, and post-capillary venules (Iadecola, 2017; Sweeney et al., 2016). Transitional pericytes, termed ensheathing pericytes, have been reported between cerebral arterioles and capillaries and display the typical “bump on a log” pericyte morphology but express vSMC markers α-SMA (alpha smooth muscle actin) and SMMHC (smooth muscle myosin heavy chain) along with pericyte markers NG2, desmin, and CD13 (Grant et al., 2019; Ratelade et al., 2020; Smyth et al., 2018).

Pericytes are found throughout the vasculature but are most common in the CNS where they cover approximately 30% of the abluminal surface (Armulik et al., 2011). Embedded in the same basement membrane, they make connections with BMECS through N-cadherin and connexins (Kadry et al., 2020). Similar to astrocytes, pericytes perform several functions that include regulating BBB permeability, angiogenesis, entrance of immune cells into the brain, control of cerebral blood flow, and CNS clearance (Sweeney et al., 2016).

Angiogenic endothelial cells recruit pericytes to the vessel wall by secreting platelet-derived growth factor B (PDGF-BB) into the extracellular matrix (Andrae et al., 2008; Armulik et al., 2011). PDGF-BB binds to the PDGFRβ (platelet-derived growth factor receptor beta) expressed on pericyte lumens beginning signaling cascades that promote pericyte migration, proliferation, and survival (Sweeney et al., 2016; Winkler et al., 2011). PDGF-BB/ PDGFRβ signaling is required for normal pericyte recruitment and deleting the retention motif of PDGF-BB is sufficient to severely inhibit pericyte recruitment to microvessels in mice (Lindblom et al., 2003).

A pericyte deficient PDGFR -/- mouse model was reported to exhibit increased BBB permeability to biotin (0.5kDa) attributed to an increase of transcytosis (Daneman & Prat, 2015). Moreover, TJ protein expression was not altered but fewer properly sealed TJs were observed (Daneman & Prat, 2015). Pericyte deficient mice exhibit a redistribution of AQP4 away from astrocyte endfeet suggesting a role in astrocyte polarization (Armulik et al., 2011). Additionally, pericytes deposit basement membrane proteins fibronectin, nidogen, and laminin aiding the maturation of newly formed vessels (Stratman et al., 2009). Recently, it was demonstrated that pericyte-secreted vitronectin interacts with the α5

integrin receptor on endothelial cells to inhibit transcytosis and maintain BBB integrity (Ayloo et al., 2022).

There is bidirectional TGFβ signaling between BMECs and pericytes as they both secrete TGFβ and express the TGFβR2 (transforming growth factor, beta receptor 2) (Winkler et al., 2011). Endothelial secreted TGFβ activates the ALK5 Smad2/3 pathway in pericytes preventing proliferation, enhancing contractile protein expression, and promoting secretion of extracellular matrix proteins (Sieczkiewicz & Herman, 2003; van Geest et al., 2010). In BMECs, TGFβ signaling works in convergence with NOTCH signaling to upregulate the expression of N-cadherin securing pericyte-endothelial attachment (F. Li et al., 2011; Winkler et al., 2011). Inhibition of endothelial cell-pericyte TGFβ signaling increases BBB permeability and disrupts organization of ZO-1 and occludin TJs (Dohgu et al., 2005; Walshe et al., 2009). Recently, studies have begun to elucidate the role of pericytes in neurovascular coupling. Pericytes express receptors for the vasoactive compounds catecholamines, endothelin-1, vasopressin, and angiotensin II, and a subset of pericytes express contractile proteins (Hamilton, 2010). Moreover, Hall et al. (2014) found that pericyte covered capillaries in mice dilated in response to whisker stimulation before arterioles and accounted for 80% of the blood flow increase in the capillary bed.

1.2.4 The endothelial glycocalyx is the first line of defense of the BBB

Located on the luminal side of the BBB, the endothelial glycocalyx is a negatively charged matrix coating composed of proteoglycans, glycosaminoglycans (GAGs), and associated plasma proteins (Iba & Levy, 2019). Proteoglycans are the core proteins of the glycocalyx anchored to endothelial cells through transmembrane connections (Reed et al., 2019). One or more GAGs, such as heparan sulfate (HS), chondroitin sulfate (CS), keratan sulfate (KS), and hyaluronic acid (HA), are then covalently attached to the proteoglycans (F. Zhao et al., 2021). Considered a vasculoprotective lining for vessels, the endothelial glycocalyx has a dynamically changing thickness (Reitsma et al., 2007) that more densely covers the brain capillaries than lung and heart capillaries (Ando et al., 2018). In a rat model, when the glycocalyx was destroyed with hyaluronidase there was a more permeable BBB (Zhu et al., 2018). The endothelial glycocalyx is the first line of defense of the BBB blocking leukocytes, erythrocytes, platelets, and other blood-borne molecules from colliding with the endothelium wall (F. Zhao et al., 2021). Taken together, the endothelial glycocalyx regulates BBB permeability and is an essential component of the NVU (Haeren et al., 2018).

1.2.5 The components and function of the NVU basement membrane

The BM is a specialized extracellular matrix located centrally within the NVU on the abluminal side of endothelial cells and surrounding pericytes (Xu et al., 2019). A distinction can be made between the endothelial basement membrane separating BMECs and pericytes and the parenchymal basement membrane covering the opposite side of pericytes (Yao, 2019). The NVU BM has a thickness of approximately 50-100 nm and is a highly organized mesh primarily consisting of collagen IV, laminin, nidogen, heparin sulfate proteoglycans (HSPGS), and fibronectin (Reed et al., 2019; Yurchenco, 2011). Many functions are attributed to the NVU BM including providing structural support and stability of the cerebral microvessels, serving as a growth factor reservoir, and mediating matrix-cell signaling through interactions with integrins and dystroglycans (Baeten & Akassoglou, 2011; S. Kim et al., 2011; Yurchenco, 2011).

1.2.5.1 Laminin

Laminins are large 400-900 KDa heterotrimeric T-shaped proteins composed of an α, β, and γ chain that are essential to the assembly of the basement membrane (Reed et al., 2019; Yao, 2017). Each laminin subunit contains various globular domains, rod-like repeats, and coiled-coil domains (Yao, 2017, 2019). There are 5 α, 4 β, and 3 γ chains that combine at their coiled-coil domains to form several different laminin isoforms (Aumailley et al., 2005; Yao, 2017). Laminin isoforms are differentially expressed by each NVU cell type (Reed et al., 2019). Endothelial cells and pericytes produce laminin isoforms 411 (α4β1γ1) and 511 (α5β1γ1) (Gautam et al., 2016; Sixt et al., 2001) while astrocytes

produce laminin 211 (α2β1γ1) and 111 (α1β1γ1) (Jucker et al., 1996; Sixt et al., 2001) effectively generating a differential distribution of laminin between the parenchymal and endothelial BMs (Yao, 2019). Laminin is a critical component of the basement membrane required for BBB maintenance and removal of astrocytic laminin causes breakdown of the BBB and intracranial hemorrhaging in mice (Menezes et al., 2014; Yao et al., 2014). Conversely, mice deficient for pericyte-derived laminin only show BBB defects late in life (Yao, 2019). Moreover, laminins 411 and 511 derived by endothelial cells are able to compensate for each other in single KO mouse models (Kang & Yao, 2020).

1.2.5.2 Nidogen

There are two identified nidogen isoforms (nidogen-1 and nidogen-2) that are large glycoproteins containing 3 globular domains (Reed et al., 2019). They are produced by endothelial cells, mural cells, and to a lesser extent by astrocytes (Vanlandewijck et al., 2018). In the BM, nidogens bind to collagen IV and laminins bridging them together to confer additional stability (Yurchenco, 2011). While ablation of both nidogen-1 and -2 in mice results in perinatal lethality (Bader et al., 2005), single KO of nidogen 1 causes thinning of the BM (Dong et al., 2002) and a nidogen 2 KO has no overt phenotype (Schymeinsky et al., 2002) suggesting a mutual compensating mechanism. Moreover, nidogen-1 is important for astrocyte attachment *in vitro* (Grimpe et al., 1999).

1.2.5.3 Perlecan

Heparan sulfate proteoglycan 2 (HSPG2), also known as perlecan, is a large (>200 nm) HSPG in the BM generated by endothelial cells and pericytes (Farach-Carson et al., 2014; M. Thomsen et al., 2017). Like nidogens, perlecan crosslinks the laminin and collagen IV networks (Behrens et al., 2012). Perlecan has an additional function in mediating matrix-cell signaling as it is known to bind VEGF, FGF, TGFβ, and hedgehog (Farach-Carson & Carson, 2007; Whitelock et al., 2008).

1.2.5.4 Agrin

Agrin is another large HSPG found in the NVU BM (Barber & Lieth, 1997; Reed et al., 2019) that is synthesized by neurons, glia, and vascular cells (Kang & Yao, 2020). The accumulation of agrin around the cerebral microvasculature coincides with the formation of the BBB and agrin stabilizes VE-cadherin and ZO-1 junctions in mouse brain ECs (Barber & Lieth, 1997; Kröger & Schröder, 2002; Steiner et al., 2014). A conditional endothelial agrin KO displayed lower levels of AQP4 coinciding with elevated amyloid beta in the brain (Rauch et al., 2011).

1.3 Type IV collagen

Type IV collagen, a helical protein composed of three collagen IV α chains, is the most abundant protein in the NVU BM (Xu et al., 2019; Yao, 2019). Collagen IV α chains are large peptides 400 nm in length with an N-terminal 7S domain, triple helix domain composed of collagenous Gly-X-Y repeats with 21-26 non-collagenous interruptions, and a C-terminal NC1 (non-collagenous) domain (Chioran et al., 2017; Khoshnoodi et al., 2008). To date, there have been six α chains identified (COL4A1-6) with each exhibiting variable expression throughout the body (Hudson et al., 1993). These genes are arranged in 3 pairs with COL4A1 and COL4A2 on chromosome 13, COL4A3 and COL4A4 on chromosome 2, and COL4A5 and COL4A6 on chromosome X, all of which have bidirectional promoters to regulate transcription (Khoshnoodi et al., 2008; Sado et al., 1998). These chains can combine to form 3 different type IV collagen heterotrimers α1α1α2, α3α4α5, and α5α5α6 (Khoshnoodi et al., 2008; Sado et al., 1998). COL4A1 and COL4A2 are the only ubiquitously expressed alpha chains and constitute the predominant isoform of type IV collagen in the NVU BM (Sado et al., 1998; Xu et al., 2019). Type IV collagen is synthesized in the brain by endothelial cells, mural cells, and astrocytes (Vanlandewijck et al., 2018) and provides essential structure to the BM as a molecular scaffolding for other ECM molecules and mediates cell-matrix signaling through integrin binding (Fidler et al., 2017; Reed et al., 2019).

1.3.1 Heterotrimer formation

During translation of an α chain, proline residues within the Gly-X-Y repeats undergo an enzymatic cis-trans isomerization catalyzed by peptidyl-prolyl isomerase (PPI) (J. Davis et al., 1989). This isomerization generates a slight turn in the triple helix domain allowing it to form a more stable triple helix (Chioran et al., 2017). Heterotrimer formation occurs intracellularly and is initiated by interactions between NC1 domains (Boutaud et al., 2000). Protein disulfide isomerase catalyze disulfide bonds between respective NC1 domains solidifying their connection allowing the triple helix domains to begin twisting around each other to form the triple helix in a zipper-like fashion (Chioran et al., 2017; R. Wilson et al., 1998). Through hydrophobic interactions, the small nonpolar glycine residues within the Gly-X-Y motifs are guided towards the center of the forming triple helix (Chioran et al., 2017). The non-collagenous interruptions of the Gly-X-Y motifs confer flexibility to the triple helix and serve as binding sites for integrins (Chioran et al., 2017; Khoshnoodi et al., 2008). A type IV collagen heterotrimer is illustrated in **Figure 1.4**.

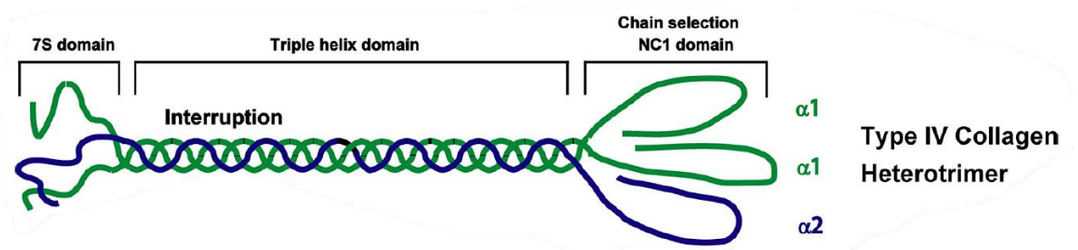

Figure 1.4 Collagen IV heterotrimer α1α1α2. Interactions between the NC1 domains of two α1 and one α2 chains initiate heterotrimer formation. Subsequently, a triple helix is coiled beginning from the NC1 domains and ending before the 7S domains. Adapted with permission from (Xiao et al., 2015). © 2015 American Society for Biochemistry and Molecular Biology.

1.3.2 Posttranslational modifications

Collagen IV heterotrimers are subjected to several post-translational modifications before being secreted to the extracellular space (Myllyharju, 2005). Prolines are hydroxylated by proline-4-hydroxylase (P4H) and prolyl 3-hydroxylase 2 (P3H2) (Holster et al., 2007; Pokidysheva et al., 2014). Hydroxylation of prolines within the Gly-X-Y motifs was demonstrated to increase the thermal stability of the protomer (Erdmann & Wennemers, 2010; Yu et al., 2011). While approximately 80% of proline hydroxylation is attributed to P4H (Holster et al., 2007), P3H2 hydroxylation importantly blocks the interaction between embryonic collagen IV and the maternal platelet-specific glycoprotein VI (GPVI) preventing platelet aggregation and thrombosis (Pokidysheva et al., 2014). Moreover, P3H2 hydroxylation facilitates collagen IV interactions with nidogen -1 and -2 (Montgomery et al., 2018). Lysine residues in the Y position of Gly-X-Y motifs are hydroxylated by the lysyl hydroxylases 1, 2, and 3 (LH1-3) and glycosylated through LH3 activity (Sipilä et al., 2007; Valtavaara et al., 1998). Lysyl hydroxylation is required for extracellular cross-linking of the collagen IV network (Saito & Marumo, 2010). Only LH3 has galactosyltransferase and glucosyltransferase activity (Sipilä et al., 2007) and is required for normal collagen IV synthesis and secretion (Rautavuoma et al., 2004; Saito & Marumo, 2010). Additionally, glycosylation has been shown to influence the strength of collagen IV binding to integrins (Stawikowski et al., 2014).

1.3.3 Collagen IV trafficking and secretion

Inside the ER, the collagen specific chaperone heat shock protein 47 (HSP47) recognizes Gly-X-Arg-Gly motifs and binds to and stabilizes collagen IV protomers (Chioran et al., 2017; Koide et al., 2002). A salt bridge between the arginine in a Pro-Arg-Gly triplet and the highly conserved Asp385 of HSP47 form the connection between the protomer and the HSP47 (Widmera et al., 2012). HSP47 remains bound until it reaches the cis-Golgi apparatus where it dissociates because its binding affinity is reduced at the lower pH (Chioran et al., 2017; Oecal et al., 2016). Following dissociation, HSP47 is recycled back to the ER by its canonical RDEL retrieval signal (Ragg, 2007).

The enormous size of collagen IV heterotrimers (400 nm) necessitates specialized coat protein complex II (COPII) vesicles to transport the protein (Chioran et al., 2017). The size of classical COPII vesicles is between 60 and 90nm (Chioran et al., 2017), but TANGO1 (transport and Golgi organization protein 1) forms a ring structure in COPII vesicles delaying their budding from the ER increasing their size before binding to HSP47 and mediating collagen IV loading into the vesicle (Ishikawa et al., 2016; Raote et al., 2017). Removal of TANGO1 in both mice and Drosophila melanogaster severely inhibit the secretion of collagen and other large molecules resulting in activation of the unfolded protein response (UPR) and ER stress (M. Liu et al., 2017; D. Wilson et al., 2011). After reaching the Golgi complex, collagen IV heterotrimers are secreted (Chioran et al., 2017).

1.4 Assembly and function of the NVU BM

Assembly of the NVU BM begins with secreted laminin heterotrimers that self-assemble at their N-terminal domains in a calcium dependent manner to form an organized lattice structure that is subsequently anchored to the cell surface through interactions between the laminin long arms and integrin and dystroglycan cellular receptors (Hohenester & Yurchenco, 2013; Jayadev & Sherwood, 2017; LeBleu et al., 2007).

Collagen IV heterotrimers, like laminin, are formed intracellularly and then secreted (Khoshnoodi et al., 2008). Driven by the higher chloride ion concentration in the extracellular space, the Arg76-Asp78 salt bridge is disrupted allowing the dimerization of two NC1 domains (Brown et al., 2017; Cummings et al., 2016). Following initial NC1 oligomerization, peroxidasin forms sulfilimine cross links further stabilizing the newly formed dimer (Bhave et al., 2012; Vanacore et al., 2009). Tetramers are spontaneously formed by four N-terminal 7S regions containing overlaps stabilized through disulfide and non-disulfide crosslinking (Brown et al., 2017; Duncan et al., 1983). Lateral associations are also formed within the collagen IV lattice (Yurchenco & Ruben, 1987). Illustrated in **Figure 1.5**, the collagen IV mesh network is deposited on the previously formed laminin lattice and secured through interactions with perlecan, agrin, and nidogen linking the two networks together to form a structurally sound and mature basement membrane (Behrens et al., 2012; Hohenester & Yurchenco, 2013; Joutel et al., 2016).

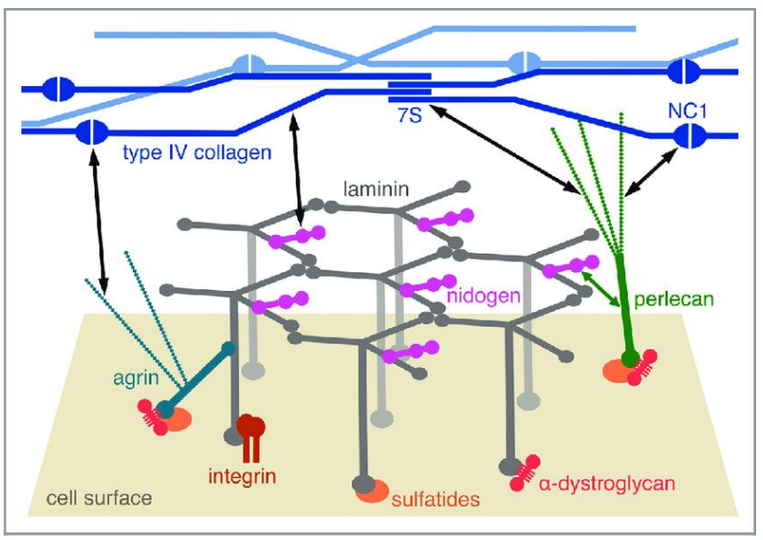

Figure 1.5 Structure and formation of the NVU BM. Initially laminin forms an organized lattice structure and is anchored to the cell surface through integrins and dystroglycans. Collagen IV heterotrimers associate via their NC1 domains and 7S domains to form a chicken-wire mesh that is deposited on top of the laminin grid. Other ECM molecules such as nidogens, perlecan, and agrin further strengthen the association between the collagen and laminin networks. Adapted with permission from Hohenester & Yurchenco, 2013). Copyright © 2012 Landes Bioscience.

1.4.1 Mechanical properties of the BM

Inferring from its structure, the most obvious BBB basement membrane function is to provide structural support for cerebral microvessels of the NVU (Khalilgharibi & Mao, 2021). The mechanical attributes of the basement membrane, however, are not limited to imparting physical support but also contribute to cell growth and differentiation (Janmey et al., 2013). For example, merely changing the rigidity of the substrate, mesenchymal stem cells (MSCs) can be directed into any one of the 3 germ

layers *in vitro* (Engler et al., 2007). Furthermore, matrix stiffness directly impacts capillary angiogenesis through transcriptional regulation of VEGFR2 (vascular endothelial growth factor receptor 2) (Mammoto et al., 2009).

Integrins, located on the cell surface and linked with cytoskeletal elements, bind to ECM molecules such as laminin and collagen IV and can respond to external forces such as blood flow but also passively detect the BM stiffness by transferring forces directly to the cytoskeleton (Kechagia et al., 2019). Moreover, changes in matrix stiffness are associated with diseases such as cancer, fibrosis, atherosclerosis (Janmey et al., 2013), and cSVD (Lemmens et al., 2013).

1.4.2 Cell signaling mediated by the BM

Dystroglycans are one of the two main types of receptors mediating cell-cell and cell-matrix interactions and adhesion (Baeten & Akassoglou, 2011). They are composed of an alpha and beta subunit translated from the same gene before being cleaved (Moore & Winder, 2010). Neurons, astrocytes, and endothelial cells express dystroglycans (Moore & Winder, 2010; Zaccaria et al., 2001). A high affinity for laminin allows dystroglycans to guide AQP4 localization in astrocytes (Tham et al., 2016).

Integrins are the other major adhesion protein and receptor facilitating cell-cell and cell-matrix interactions (Baeten & Akassoglou, 2011). In vertebrates there are 18 alpha and 8 beta integrin subunits that combine to form 24 known heterodimer combinations (Barczyk et al., 2010). The integrin heterodimer contains an extracellular domain that binds to ligands, a transmembrane domain, and an intracellular cytoplasmic tail that connects with the cytoskeleton and facilitates intracellular signaling (Edwards & Bix, 2019). Integrins can exist in multiple states (e.g. on, at rest, and off) that are represented by conformational changes that differentially expose the binding domain (Edwards & Bix, 2019). Integrins possess the capability of inside-out and outside-in signaling that can integrate and respond to both mechanical and chemical cues (S. Kim et al., 2011). Inside-out integrin signaling is initiated through the binding of talin, a protein connected to the actin cytoskeleton, and sometimes also kindlin, to distinct locations on the cytoplasmic tail of the beta subunit (Moser et al., 2008). These binding events produce extracellular conformational changes exposing the ligand binding epitope (Kechagia et al., 2019). Additionally, the intracellular signaling causes integrins to co-localize and form focal adhesion complexes (Kechagia et al., 2019).

ECM ligand binding to cell-surface integrins has profound effects on cell signaling including cell proliferation, apoptosis, migration, and differentiation (Baeten & Akassoglou, 2011). Outside-in signaling events are highly specific to the ligand/integrin pair and can involve several different signaling pathways including focal adhesion kinase (FAK), Ras/ERK (MAPK), and small GTPases (Miranti & Brugge, 2002). There is an abundance of crosstalk between integrins and other cellular receptors (Miranti & Brugge, 2002). For example, VEGF, EGF, and PDGF receptors can all be transactivated by integrins (Baeten & Akassoglou, 2011; Moro et al., 1998; Sundberg & Rubin, 1996; J. Wang et al., 2001). Integrins have also been demonstrated to activate latent forms of growth factors such TGFβ (Annes et al., 2003).

There is increasing evidence that integrins substantially influence cell-cell junctions. Activation of αvβ3 integrin with fibronectin has reportedly disrupted VE-cadherin adherens junctions (J. Wang & Milner, 2006). Conversely, β1 integrin signaling was shown to be essential for normal VE-cadherin localization and microvessel stability (H. Yamamoto et al., 2015). Moreover, TIMP1 (tissue inhibitor of metalloproteinase-1) was recently demonstrated to form a ternary complex with CD63 and integrin β1 essential for maintaining barrier properties (Tang et al., 2020). This complex activates integrin β1 to trigger downstream FAK signaling that stabilizes actin and cell-cell junctions (Tang et al., 2020). Inhibiting this pathway depleted expression of tight junction proteins claudin-5, occludin, and ZO-1 and reorganized VE-cadherin away from cell junctions (Tang et al., 2020). Similar studies have blocked

integrin β1 signaling in brain endothelial cells *in vitro* on collagen IV and laminin substrates observing a reduction and reorganization of TJs (Izawa et al., 2018; Osada et al., 2011).

1.4.3 The role of MMPs in basement membrane remodeling

The basement membrane is a dynamic structure that can be remodeled throughout life (Bonnans et al., 2014). Every BM protein can be degraded by one of the 23 identified matrix metalloproteinases (MMPs) (Bonnans et al., 2014; P. Lu et al., 2011). Following ischemic stroke, MMPs are reported to increase and correlate with aggravated neuronal injury (Heo et al., 1999). There are 4 tissue inhibitors of MMPs (TIMP1-4) that primarily regulate MMP activity through inhibition and are crucial to maintaining the balance between ECM production and degradation (Ries, 2014).

1.5 COL4A1 and COL4A2 mutations in pathology

Since the collagen IV heterotrimer α1α1α2 is ubiquitously expressed, several diseases and disorders are caused by mutations affecting COL4A1 or COL4A2. These include ocular disorders, brain diseases, kidney glomerular disorders, myopathy, and in rare cases Raynaud's syndrome and arrhythmia (Gatseva et al., 2019; Rannikmäe et al., 2020). The location and nature of COL4A1 and 2 mutations are variable and largely determine disease type and progression (Gatseva et al., 2019). Approximately 80% of COL4A1 and COL4A2 mutations affect glycine residues within the Gly-X-Y motif (Gatseva et al., 2019). HANAC syndrome (Hereditary Angiopathy, Nephropathy, Aneurysms, and Muscle Cramps) is associated with glycine missense mutations within the CB3[IV] region of the collagen IV triple helix domain and is associated with retinal tortuosity, kidney defects, muscle cramps, Raynaud's, and sometimes cSVD (Plaisier et al., 2007, 2010). The CB3[IV] region contains the binding sites for several integrins (α1β1, α2β1, and α3β1) and disruption of collagen IV-integrin binding may contribute to the progression of HANAC syndrome (Khoshnoodi et al., 2008; Plaisier et al., 2010). Other mutations such as nonsense frameshift mutations (Lemmens et al., 2013) as well as several 3'-UTR mutations have also been identified (Qing Li et al., 2022; Mönkäre et al., 2022; Sakai et al., 2020; Saskin et al., 2018; Siitonen et al., 2017; Verdura et al., 2016; Y. Zhao et al., 2019). The frameshift mutations described in Lemmens et al. (2013) cause haploinsufficiency of COL4A1 in patients and result in highly penetrant cSVD with porencephaly, ICH, microbleeds, and WMH. Mutations in the 3'-UTR disrupt binding of miR-29 and prevent the downregulation of COL4A1 (Verdura et al., 2016). Consequently, patients with COL4A1 3'-UTR mutations exhibit higher expression of COL4A1 and develop a subtype of cSVD called PADMAL (pontine autosomal dominant microangiopathy with leukoencephalopathy) (Verdura et al., 2016).

1.5.1 Proposed cSVD mechanisms of COL4A1 and COL4A2 mutations

The exact mechanisms causing monogenic COL4A1 and COL4A2 cSVD are incompletely understood, but there are several proposed non-mutually exclusive mechanisms (Kuo et al., 2012). One of these is an intracellular accumulation of misfolded protomers (Jeanne et al., 2015; Jeanne & Gould, 2017; Murray et al., 2014). Murray et al. (2014) used the chemical chaperone 4-PBA to reduce the amount of intracellular collagen accumulation in cSVD patient cells harboring the COL4A2^{G702D} mutation. ER-stress and apoptosis were reduced when intracellular accumulation was attenuated (Murray et al., 2014). Moreover, a study investigating mutations in the C. elegans orthologues to COL4A1 and COL4A2, EMB-9 and TET-2 respectively, suggested that the severity of phenotype was correlated with the amount of intracellular accumulation (Gupta et al., 1997). A genotype-phenotype study investigating several COL4A1 and COL4A2 mutations in mice and patients revealed that the most frequent mutations, glycine substitutions in the triple helix domain, have a position dependent effect on the cerebral phenotype (Jeanne & Gould, 2017). **Figure 1.6** shows the position, relative amount of intracellular accumulation, and the frequency of ICH in mice harboring different mutations. Glycine mutations within the triple helix domain closer to the NC1 domain resulted in more intracellular accumulation and ICH compared to mutations closer the 7S domain (Jeanne & Gould, 2017). Only the in-frame COL4A1$^{\Delta ex41}$ mutation, an exon skipping mutation, fluctuated from the correlation.

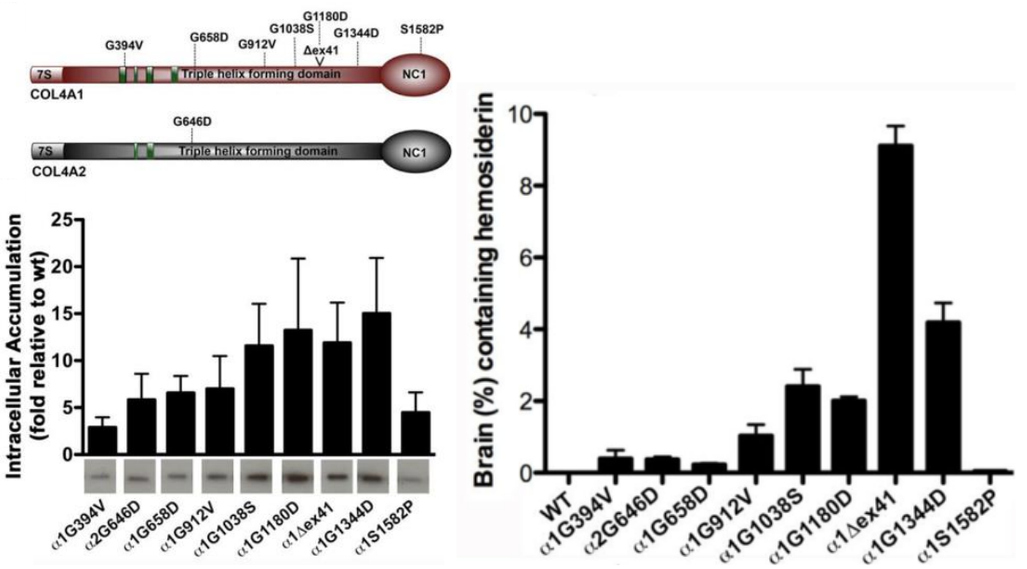

Figure 1.6 Mutation position dependent effect on intracellular accumulation and correlation to ICH. (Left) Intracellular accumulation correlates with mutation position within the triple helix domain. **(Right)** Increased intracellular accumulation corresponds to more widespread ICH. Adapted with permission from (Jeanne & Gould, 2017). Copyright © 2022 Elsevier B.V.

Interestingly, this correlation was only predictive for cerebral phenotypes as the COL4A1^{G394V} mutation caused the most severe myopathy (Jeanne & Gould, 2017).

In the same study, Jeanne and Gould (2017) also investigated patients with mutations in COL4A1 and COl4A2 revealing corroborating results that more severe cerebral phenotypes are associated with more C-terminally positioned glycine mutations within the triple helix domain. Moreover, this correlation was also restricted to cerebral phenotypes as mutations in exons 24, 25, and 31 caused more severe aneurysms, nephropathy, myopathy, and a diagnosis of HANAC syndrome (Jeanne & Gould, 2017).

Deficiency of deposited collagen IV heterotrimers or an incorporation of mutant heterotrimers are other proposed cSVD disease mechanisms (Gatseva et al., 2019; Kuo et al., 2012). Patients with haploinsufficiency mutations exhibit a remarkable 100-fold thickening of skin capillary BM indicating an alternative disease mechanism to intracellular accumulation and ER stress (Lemmens et al., 2013). However, in mice, COL4A1 and COL4A2 are dispensable for normal BM deposition but are required to provide stability allowing the BM to resist mechanical stress (Pöschl et al., 2004).

Incorporation of mutant heterotrimers causing a dominant negative effect could account for disease phenotypes. Patients with heterozygous glycine mutations in COL4A1, assuming random combination, would generate 25% WT heterotrimers, 50% single mutant heterotrimers, and 25% double mutant heterotrimers. **(Figure 1.7)** Patients with heterozygous COL4A2 mutations would generate equal amounts of normal and mutant heterotrimers. It is unclear, and likely mutation dependent which heterotrimer combinations are secreted. Incorporation of single or double mutant heterotrimers could both cause a dominant negative effect by disrupting the normal suprastructure of the BM (Kuo et al., 2012; Mao et al., 2015).

Recently, Ratelade et al. reported a hypermuscularized region between the arterioles and capillaries in the COL4A1^{G498V} mouse mutant. This hypermuscularization increased contractility and blood pressure upstream suggesting a novel mechanism for COL4A1 mutation related ICH (Ratelade et al., 2020). Interestingly, a genetic reduction of Notch3 attenuated the phenotype (Ratelade et al., 2020).

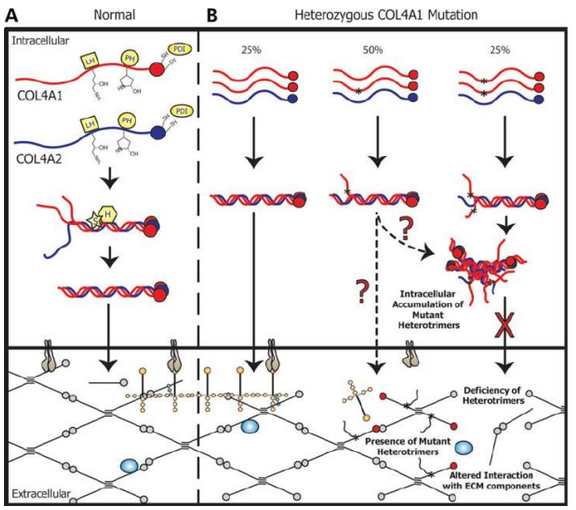

Figure 1.7 Proposed mechanisms of collagen IV related cSVD. (A) Illustrates normal collagen IV secretion and deposition. (B) Represents the diseased state. The stars on the protomers indicate mutations and the predicted distribution of mutant heterotrimers as well as proposed disease mechanisms are shown. Adapted with permission from (Kuo et al., 2012). Copyright © 2012 Oxford University Press.

1.6 *In vivo* and *in vitro* models to study monogenic collagen IV cSVD

Collagen IV and its orthologues have been demonstrated to be essential to BM stability and function in many model organisms including mice, drosophila, zebrafish, and C. elegans (Borchiellini et al., 1996; Fidler et al., 2014; Gupta et al., 1997; Pöschl et al., 2004). Insights from drosophila melanogaster helped determine that TANGO1 associates with ER exit sites forming a ring-like structure in COPII vesicles (M. Liu et al., 2017) and notch signaling is required for collagen type IV secretion (Gross et al., 2021). Several mutations in the C. elegans orthologues to COL4A1 and COL4A2 helped reveal that glycine substitutions were generally more severe than null mutations (Gupta et al., 1997). Additionally, mouse models have yielded several insights into collagen IV cSVD (Jeanne et al., 2015; Jeanne & Gould, 2017; Kuo et al., 2012; Pöschl et al., 2004; Ratelade et al., 2020). COL4A1$^{\Delta ex41}$ mice exhibit subcortical ICH, arteriolar tortuosity, and porencephaly. All of which are clinical features in human patients with COL4A1 mutations (Gould et al., 2005, 2006). Mutant pups suffer cerebral hemorrhaging during birth that is prevented through surgical delivery suggesting caesarian sections be performed for human patients with collagen IV mutations (Gould et al., 2006). Furthermore, the COL4A1^{G498V} mouse model closely mimics the human HANAC syndrome exhibiting retinal tortuosity defects, albuminuria and hematuria in newborns, glomerular cysts, and muscular defects (Chen et al., 2016; Guiraud et al., 2017; Trouillet et al., 2017). Ratelade et al. (2018) demonstrated the retinal arterial lesion load and retinal SMC degeneration strongly correlates with incidence of subcortical macrohemorrhages proposing that retinal screening could be a viable tool to diagnose ICH risk in human patients.

Individual mouse models can recapitulate some aspects of COL4A1/2 monogenic cSVD and are helpful tools to elucidate disease mechanisms. However, genetic background is a major contributor to disease progression (Kuo et al., 2012). Interestingly, the COL4A1$^{\Delta ex41}$ resulted in retinal arterial tortuosity in a C57B6 background but not CASTB6 (Gould et al., 2006). Furthermore, the COL4A1$^{\Delta ex41}$ mutation expressed in a B6 and B6129F1 background but not a CASTB6 background resulted in severe ICH (Jeanne et al., 2015). Ocular anterior segment dysgenesis (ASD) caused by the COL4A1$^{\Delta ex41}$mutation in C57B6 mice was not present when crossed into a 129 or CAST background and it was discovered that a region on chromosome 1 was a genetic modifier responsible for this observation (Gould et al., 2007). Given that the COL4A1$^{\Delta ex41}$ mutation, a significant deletion more severe than glycine substitutions, causes severe phenotypes in a B6 background but not in other backgrounds, it is doubtful that a single mouse model in a single genetic background will recapitulate the complex mechanisms of human monogenic COL4A1/2 cSVD (Hainsworth & Markus, 2008). Therefore, other experimental models such as human *in vitro* models are necessary tools providing insights available models cannot offer.

1.6.1 Primary and immortalized cell lines for *in vitro* modeling

Regardless of the design of an in vitro BBB model, the cell types must be selected. Primary cells have been used in BBB models with primary rat cells (ECs, astrocytes, and pericytes) (Nakagawa et al., 2009), mouse cells (ECs and astrocytes) (Coisne et al., 2005), bovine cells (ECs, glia, and pericytes) (Vandenhaute et al., 2011), porcine cells (ECs, astrocytes, and pericytes) (L. Thomsen et al., 2015), and human BMECs (Bernas et al., 2010).

However, primary cells can be hard to isolate and are not always readily available creating a need for other cell types in *in vitro* BBB models (Helms et al., 2015). Immortalized cell lines are a potential substitute as multiple mouse and human endothelial immortalized cell lines have been investigated within *in vitro* BBB models (Burek et al., 2012; Omidi et al., 2003; Prudhomme et al., 1996; Sano et al., 2010; Stins et al., 2001). The murine immortalized brain endothelial cell line, b.End3, does not form a tight barrier and is deemed unsuitable for BBB permeability studies (Omidi et al., 2003). A comparative analysis of the four immortalized human brain endothelial cells lines hCMEC/D3, hBMEC, TY10, and BB19 determined that the hBMEC line formed the most impermeable barrier and showed the highest tight junction expression (Eigenmann et al., 2013). However, co-culture systems do no further induce BBB properties with this line (Eigenmann et al., 2013). The hCMEC/D3 line is the most widely used and characterized line (Helms et al., 2015). It has provided valuable insights in drug uptake, active transport, and inflammatory response studies but lacks consistent TJs and barrier properties (Weksler et al., 2013).

1.6.2 Induced pluripotent stem cells for disease modeling

The discovery of mouse induced pluripotent stem cells (iPSCs) (Takahashi & Yamanaka, 2006) and subsequently human iPSCs (Takahashi et al., 2007) provide an alluring alternative for renewable and inherently customizable BBB models. These cells have the capacity to differentiate into cells from all 3 of the germ layers (Takahashi & Yamanaka, 2006). Reprogramming cells is merely dependent on expression of the Yamanaka factors (Oct-4, Sox2, c-Myc, and Klf4) and can be accomplished with both integrative and non-integrative viral methods, RNA delivery, and protein delivery (Ban et al., 2011; González et al., 2011; Haridhasapavalan et al., 2020).

Human iPSCs (hiPSCs) are nearly indistinguishable from embryonic stem cells (ESCs) yet they circumvent ethical issues connected to ESCs. HiPSCs can self-renew indefinitely providing an unlimited cellular source (C. Liu et al., 2018). Moreover, patient specific hiPSCs can be generated to directly study disease mechanisms in disease relevant cell types (C. Liu et al., 2018). Studies with patient-specific iPSCs have recapitulated animal model phenotypes for several diseases (Sterneckert et al., 2014). Furthermore, CRISPR/Cas9 can generate disease causing mutations or correct mutations in patient iPSCs (Hockemeyer & Jaenisch, 2016). Additionally, hiPSCs overcome human-animal differences and provide a route for more translatable drug screening (Rowe & Daley, 2019). Despite their exciting potential, there are a few drawbacks to hiPSC disease modeling. Intrinsic to every *in vitro* disease model, is the absence of a full organism making it difficult to mimic complicated disease pathology (Pen & Jensen, 2017). With the advent of organoids and 3D culturing systems, researchers are attempting to overcome this pitfall (Campisi et al., 2018; C. Liu et al., 2018; Rowe & Daley, 2019). Concerns about the genomic stability, epigenetic memory, and difficult iPSC maintenance remain concerns for hiPSC disease modeling but thorough quality controls can address most of these problems (Tapia & Schöler, 2016).

1.6.2.1 Differentiation of brain endothelial cells

Successful differentiation of brain-like endothelial cells is critical for *in vitro* BBB modeling. The four most commonly used methods for differentiating ECs are co-culturing with stromal cells or neural cell types, embryoid body formation, 2D monoculture, and transdifferentiation through expression of transcription factors such as ETV2 (Williams & Wu, 2019). The first brain endothelial differentiation

was published by Lippmann et al. in 2012, where endothelial cells and neural cells were simultaneously differentiated in a 2D monolayer followed by a purification of the endothelial cell population through a matrix selection (Lippmann et al., 2012). Addition of retinoic acid increased TJ expression and TEER in ECs generated from this protocol that was further enhanced by co-culture with astrocytes and pericytes (Lippmann et al., 2014). Several alternative brain EC protocols have been subsequently published. The use of E6, a derivative of E8 iPSC maintenance media lacking growth factors that maintain pluripotency, allowed bypassing the iPSC expansion phase and substantially shortened the Lippmann protocol from 13 to 8 days (Hollmann et al., 2017). Differentiation under hypoxic conditions (5% O_2) markedly increased the expression of VE-cadherin, PECAM-1, Glut-1, P-gp, and VEGF-A (Park et al., 2019). Moreover, a fully defined, serum free protocol was recently established that limits batch to batch variability produced by undefined media components (Neal et al., 2019). Activation of WNT signaling with CHIR99021, a small molecule inhibitor of glycogen synthase kinase-3 (GSK-3), during EC differentiation has been illustrated to rapidly induce BBB properties in differentiated cells (Gastfriend et al., 2021; Lian et al., 2014; Qian et al., 2017). A key advancement in iPSC-EC differentiation was the application of CD31+ MACS sorting to purify endothelial cell populations (Gastfriend et al., 2021; Praça et al., 2019). The differentiation of arterial and venous subtypes of endothelial cells was another significant development (Rosa et al., 2019).

Despite the considerable advancements made in generation of brain ECs, there have been reports that cells produced by these protocols express common epithelial genes such as claudin-7 and other TJs (Delsing et al., 2018; Vatine et al., 2019). Based on transcriptomic data, T. Lu et al. (2021) claims that cells generated by the Lippmann protocol have been misidentified as brain ECs and more closely resemble epithelial cells. The EC differentiation used in our lab differs substantially from the Lippmann protocol. In our unpublished protocol, hiPSCs are first induced towards mesoderm with a fully defined but proprietary induction medium (possibly containing CHIR99021) and then through the addition of VEGF and forskolin are pushed towards an EC fate. Instead of a matrix selection, the cells are MACS sorted for endothelial-specific marker CD144. However, iPSC-derived ECs display a more mature BBB phenotype in 3D cultures systems especially when co-cultured with other brain cell types (Campisi et al., 2018; Vatine et al., 2019). Brain-like EC differentiations will continue to improve but the physical context of differentiated ECs is arguably as important for inducing and maintaining BBB properties.

1.6.2.2 Differentiation of mural cells

There is a spectrum of cells that transition from classical vSMC to pericytes along the arterioles to the capillaries (Ratelade et al., 2020). Pericyte specific markers have not been identified requiring simultaneous expression of several markers such as NG2, CD13, and PDGFRβ to classify pericytes (Jeske et al., 2020; Ratelade et al., 2020). Moreover, forebrain pericytes are thought to arise from a neural crest lineage while midbrain, brainstem, and spinal cord pericytes are derived from mesoderm (Etchevers et al., 2001; Korn et al., 2002; Reyahi et al., 2015). However, the precise lineage of brain pericytes is still debated. Several pericyte differentiation protocols from iPSCs begin with an induction towards mesoderm followed by subculturing cells negative for CD31 in pericyte selective conditions (Dar et al., 2012; Kusuma et al., 2013; Orlova et al., 2014). An alternative mesoderm directed protocol first generates mesenchymoangioblasts that are further directed to SMCs (calponin high, MYH11 high, NG2 low), arterial pericytes (NG2 high, SMA high, MYH11 absent), and capillary pericytes (NG2 high, SMA low, MYH11 absent) depending on the cocktail of factors added to the media (Kumar et al., 2017). Differentiation protocols deriving pericytes from neural crest have also been described (Faal et al., 2019; Jeske et al., 2020; Stebbins et al., 2019). Following generation of a neural crest stem cells and activation of Wnt signaling with CHIR99021, serum directs the cells towards a pericyte cell fate that can induce BBB characteristics in human iPSC-BMECs (Faal et al., 2019).

The other mural type found in the brain, vSMCs (vascular smooth muscle cells), are predominantly derived from mesoderm but also to a certain extent from neural crest (Stephenson et al., 2020) and there are published vSMC protocols from each lineage (Stephenson et al., 2020). Patsch et al. (2015) described a mesoderm induction protocol capable of producing both ECs and vSMCs. The progenitor

cells were pushed towards a vSMC fate with PDGF-BB and activin A. The vSMCs from this protocol were shown to be very similar to their primary counterparts through transcriptomic and metabolomic analysis (Patsch et al., 2015). Cheung et al. (2014) described a protocol to induce the differentiation of vSMCs from neural ectoderm, lateral plate mesoderm, and paraxial mesoderm. Cells derived from each lineage where indistinguishable by expression of calponin and MYH11 but demonstrated slight differences in response to IL-1β and TIMP and MMP activation (Cheung et al., 2012, 2014).

1.6.2.3 Differentiation of astrocytes

Human astrocytes have a long developmental process that continues after birth (Robertson, 2014) making it difficult to generate iPSC-derived astrocytes in a timely manner (Delsing et al., 2020). Successfully differentiated astrocytes typically are shown to express GFAP, CD44, S100β, and vimentin and can perform astrocyte specific tasks such as glutamate uptake (Delsing et al., 2020). Inducible factors NFIA and Sox9 have been used to decrease the differentiation time of astrocytes, but this labor-intensive process still requires at least one month (X. Li et al., 2018). Other differentiation protocols generate neural precursor cells and transform them into astrocytes by culturing them with EGF (epidermal growth factor) and FGF (fibroblast growth factor) (Krencik et al., 2011). Some differentiation protocols rely on the use of serum to induce an astrocytic fate from a pool of neural precursor cells (Y. Li et al., 2015; TCW et al., 2017; Yan et al., 2013). Altering the seeding density and substrate resulted in classical star-shaped astrocytes and an upregulation of astrocyte markers from the TCW protocol (Voulgaris et al., 2022). However, serum induces major transcriptomic changes in hiPSC-derived astrocytes that reflects an inflammatory response and activated cell phenotype (Perriot et al., 2018). Perriot et al. (2018) published a serum-free protocol using LIF (Leukemia inhibitory factor) to direct NPCs to glial precursors and CNTF (ciliary neurotrophic factor) to generate mature astrocytes. Importantly, all subtypes of astrocytes can extend their endfeet to the NVU (Tabata, 2015) meaning that hiPSC-astrocytes likely have the capacity to serve a functional role in an *in vitro* BBB model (Delsing et al., 2020).

1.6.3 *In vitro* BBB models

The simplest *in vitro* BBB model is the transwell system where a porous semipermeable membrane separates the simulated luminal and abluminal side of the BBB (Naik & Cucullo, 2012). Both compartments are filled with media and the porous membrane allows diffusion of most molecules but not cells between compartments (Naik & Cucullo, 2012). ECs are typically seeded on top of the porous membrane and astrocytes and/or mural cells are seeded on the bottom of the well (non-contact) or on the reverse side of the porous membrane (contact) (Wolff et al., 2015). Transwell systems are ideal for kinetic transport studies and permeability assays because of the fixed media volumes in each compartment (Sivandzade & Cucullo, 2018). However, the 2D configuration is non-physiological and lacks complexity (Sivandzade & Cucullo, 2018).

1.6.3.2 Organoids

Organoids are self-organized cell aggregates that overcome the two-dimensional limitation of transwell systems (Pacitti et al., 2019). BBB spheroids have been generated by combining primary ECs, pericytes, and astrocytes resulting in a layered organoid with astrocytes in the middle, followed by the pericytes, and finally the endothelial cells on the outside (Urich et al., 2013). These spheroids express AJs, TJs, active efflux pumps, and can perform receptor mediated transport of angio-pep2 demonstrating their usefulness for drug screening (Bergmann et al., 2018; Cho et al., 2017). However, these organoids develop a necrotic core due to a lack of oxygen and nutrients at the center, lack the physiological relevance of blood flow, and are not consistently reproducible (Bhalerao et al., 2020; Pacitti et al., 2019).

1.6.3.3 The DIV (dynamic *in vitro*) BBB model

In the DIV BBB model, ECs are grown inside of hollowed out porous polypropylene fibers and other desired cell types such as astrocytes and mural cells are grown on the outer surface of these fibers (Naik & Cucullo, 2012). These artificial capillaries can be subjected to an adjustable flow (Naik & Cucullo, 2012). Stanness et al. (1996) used this system to co-culture primary bovine ECs with rat astrocytes showing that flow prolongs cell survival. Inflammatory response, drug transport, and TEER measurements can be made with this system (Cucullo et al., 2008; Naik & Cucullo, 2012; Stanness et al., 1996). Nevertheless, a large number of cells are needed, the system is not designed for high throughput, visualization of cells is impossible, and specialized technical skills are required (Naik & Cucullo, 2012).

1.6.3.4 3D cell embedded ECM BBB models

An alternative BBB model can be generated by suspending cells in an ECM scaffold that self-polymerizes providing quasi physiological cues and chemical gradients necessary for cell-cell communication (Naik & Cucullo, 2012). However, it has been demonstrated that matrix stiffness directly impacts cell differentiation (Engler et al., 2007) and endothelial cell angiogenesis (Mammoto et al., 2009). Consequently, the absence of even a minor ECM component could significantly alter the physiology and architecture of the cells (Naik & Cucullo, 2012). Without a complete understanding of the brain ECM it is exceedingly difficult to use this BBB model in translatable research (Bhalerao et al., 2020).

1.6.3.5 Microfluidic systems adapted to BBB modeling

The recent intersection of microfluidic devices and BBB *in vitro* models has given researchers a unique opportunity. Microfluidic devices are typically made from polydimethylsiloxane (PDSM) and the dimensions can be tailored to create physiological dimensions (Sivandzade & Cucullo, 2018). Most microfluidic devices can be attached to a pump and subjected to flow (Delsing et al., 2020). Several *in vitro* BBB models using microfluidic devices have been recently published (Campisi et al., 2018; DeStefano et al., 2017; Jamieson et al., 2019; Linville et al., 2019; Park et al., 2019; Vatine et al., 2019). The Searson group observed that monoculture hBMECs resisted orientating in the direction of flow compared to human umbilical vein endothelial cells in a microfluidic setup (Ye et al., 2014). They speculated this is a characteristic of brain capillary ECs and subsequently showed the same phenotype in iPSC-derived ECs (DeStefano et al., 2017). In another study, Campisi et al. (2018) embedded ECs in a gel inside a microfluidic device and the ECs self-organized into tubes that decreased in size when pericytes and/or astrocytes were added. The application of microfluidic chips to BBB *in vitro* modeling provides several benefits but has some disadvantages. Brain capillaries have a diameter of approximately 5 µm (Popel & Johnson, 2005) which is difficult to mimic *in vitro*. There are also documented gene expression differences between regions along the vascular tree further complicating whether arteries, capillaries, or veins are modeled in a specific microfluidic device (A. Yang et al., 2022). Moreover, microfluidic devices are frequently not compatible with TEER measurements (Sivandzade & Cucullo, 2018). Furthermore, unique designs complicate comparing across studies and fabrication of microfluidic devices requires specialized knowledge (Delsing et al., 2020; Sivandzade & Cucullo, 2018).

1.6.4 Functional assays to assess BBB characteristics in *in vitro* BBB models

The resistance across an EC layer is called TEER (transendothelial electrical resistance) and is a good indicator of barrier strength (Srinivasan et al., 2015). TEER measurements provide real-time information about the cell barrier (Naik & Cucullo, 2012; Sivandzade & Cucullo, 2018). One of the most common methods to measure TEER is with chopstick electrodes where one electrode is manually placed in the upper compartment and the other in the lower compartment before applying a 12.5 Hz alternating current. The resistance is then calculated by Ohm's law (Srinivasan et al., 2015). This method yields inconsistent results dependent on electrode position and systematically overestimates TEER (Srinivasan et al., 2015; Vigh et al., 2021). Impedance spectroscopy is a more accurate alternative

TEER measurement that applies a sweeping range of alternating currents through the cell layer and measures the amplitude and phase shift of the resulting current (Benson et al., 2013). The impedance spectrum is calculated from these values and contains the resistance and capacitance of the cell layer (Benson et al., 2013). Nanoanalytics has developed the cellZscope for performing TEER measurements with impedance spectroscopy. Its design ensures the electrodes are always in the same position for each measurement.

Permeability assays provide complementary data to TEER measurements by measuring the uptake and diffusion of small molecules such as sodium fluorescein or dextran across the endothelial barrier (Naik & Cucullo, 2012; Neuhaus et al., 2006; Sivandzade & Cucullo, 2018). There is limited human *in vivo* data concerning the permeability of the human BBB (Workman & Svendsen, 2020), but values obtained from permeability assays are comparable to *in vivo* data measured in rat microvessels (Delsing et al., 2020; Yuan et al., 2009). It is common to perform qPCR and western blot in addition to TEER and permeability assays to investigate correlations between the assays and barrier related proteins such as ZO-1, Cld-5, Occludin, and Cav-1 (Sivandzade & Cucullo, 2018).

1.7. The importance of genome editing and impact of CRISPR

Genome editing technology is crucial to investigating disease-causing mutations but also extremely valuable for basic biological scientific research. Prior to the dawn of CRISPR/Cas9 genome editing, zinc finger nucleases (ZFN), transcription activator–like effector nucleases (TALENs), and to some extent meganucleases were utilized for targeted genomic editing (Riordan et al., 2015). ZFNs were the first widely available genome editing tool developed by linking zinc finger proteins (ZFP) recognizing specific 3-4bp DNA sequences to the cleavage domain of the nonspecific endonuclease FokI (Y. Kim et al., 1996). DNA cleavage by FokI occurs when the bound ZFP binds the recognized DNA sequence (Y. Kim et al., 1996; Santiago et al., 2008; Urnov et al., 2005). Novel DNA binding domains called transcription activator–like effectors (TALEs) recognizing individual bases were discovered in plant pathogens (Christian et al., 2010), and like ZFPs, TALEs were coupled to the cleavage domain of FokI generating TALENs that can target any DNA sequence (Christian et al., 2010). Meganucleases recognize long DNA sequences over 12 bp and have been used to generate DNA double strand breaks (DSBs) (Rouet et al., 1994) but their use even before CRISPR/Cas9 was not widespread (Paques & Duchateau, 2007).

These genome editing systems could generate targeted DNA DSBs. However, they must be specifically tailored for each target, requiring in most cases the engineering of a novel protein (Riordan et al., 2015). CRISPR/Cas9 revolutionized genome editing by having the capability to target nearly any DNA sequence with the same protein by solely interchanging bases on the guide RNA (Riordan et al., 2015). This widely accessible method has become the gold-standard for genome editing.

1.7.1 Discovery of CRISPR in the archaea and bacteria immune system

Francisco Mojica discovered clustered, regularly, interspaced, palindromic repeats (CRISPR) in the archaea *Haloferax mediterranei* in 1992 (Mojica & Rodriguez-Valera, 2016). Similar repeat palindromic sequences were subsequently identified in other archaea and several species of bacteria (Mojica et al., 2000). The first CRISPR associated proteins (Cas) were discovered a couple of years later adjacent to CRISPR loci (Jansen et al., 2002). Mojica and his team provided the first evidence suggesting that CRISPR could confer adaptive immunity against foreign invaders (Mojica et al., 2005). Based on computational analysis, it was hypothesized that CRISPR and its associated proteins function as a defense mechanism against invading phages (Makarova et al., 2006; Mojica et al., 2005). In 2007, it was discovered that bacteria integrated new spacer sequences into their CRISPR regions following a viral challenge derived from the invader (Barrangou et al., 2007). CRISPR RNAs (crRNAs) are transcribed, cleaved, and then complexed with Cas proteins guiding the complex towards invading phages (Brouns et al., 2008).

There are III CRISPR/Cas systems within archaea and bacteria. Type I and II systems rely on protospacer adjacent motifs (PAMs) near the target sequence that prevent Cas proteins from recognizing and

cutting their own CRISPR RNA (Shah et al., 2013). Type I and III systems rely on several Cas proteins to process crRNAs and generate anti-viral defense (Hatoum-Aslan et al., 2011; Nam et al., 2012). Conversely, type II systems only require a single Cas protein and crRNA to target DNA sequences allowing them to be easily engineered and adapted as a genome editing tool (Doudna & Charpentier, 2014).

1.7.2 Applications of the CRISPR/Cas9 system

The type II CRISPR/Cas9 system in *Streptococcus pyogenes* only requires a trans-activating crRNA (tracrRNA) and crRNA duplex to direct Cas9 to a target (Deltcheva et al., 2011; Jinek et al., 2012). Furthermore, a single engineered RNA chimera (sgRNA) can be generated to fulfill the role of a crRNA (Jinek et al., 2012). In addition to complementary base pairing of the sgRNA, there must be a contiguous PAM sequence present (NGG for Cas9) (Jinek et al., 2012). Cas9 contains an HNH cleavage domain that cleaves the sequence complementary to the sgRNA and an RuvC cleavage domain responsible for cleaving the opposite strand (Jinek et al., 2012; Riordan et al., 2015). The structure of the Cas9/sgRNA complex is shown in **Figure 1.8**. Mutations that inactivate one of the cleavage domains create a Cas9 nickase that generates only single strand DNA breaks and inactivating both cleavage domains produces a dead cas9 (dCas9) that is essentially a DNA binding protein (Doudna & Charpentier, 2014; Gasiunas et al., 2012; Jinek et al., 2012).

Designing a new sgRNA following Watson-Crick base pairing rules, can effectively target any 20bp DNA

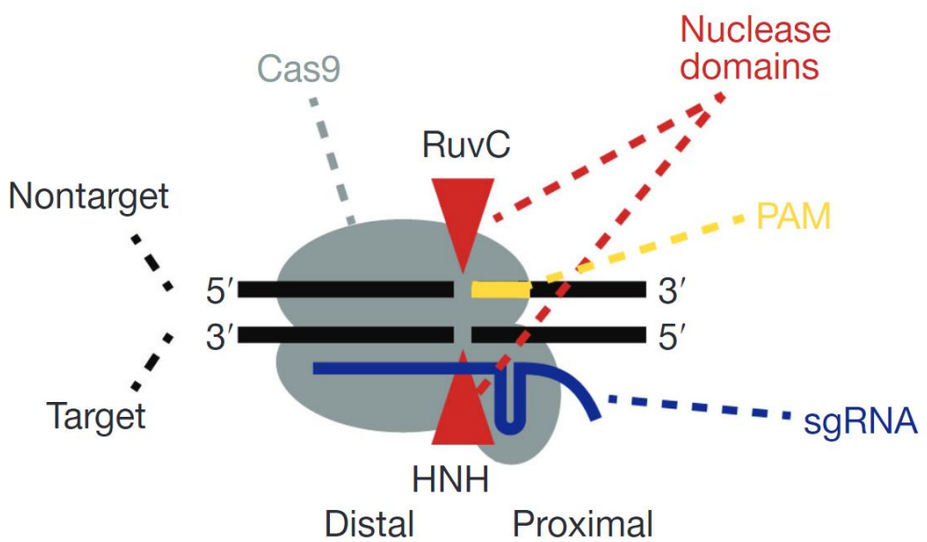

Figure 1.8 Structure and function of the Cas9 sgRNA Complex. The Cas9/sgRNA complex can peel back double stranded DNA to patrol for sequences complementary to the sgRNA. Once the sgRNA binds to a complementary sequence in the presence of a PAM, the nuclease domains, HNH and RuvC, become active and each nick one strand of DNA to generate a DSB. Adapted with permission from (Richardson et al., 2016). © 2016 Nature America, Inc. All rights reserved.

sequence adjacent to a PAM (Doudna & Charpentier, 2014). With this versatility CRISPR/Cas9 has become a widely used tool for generating gene KOs (knock-outs) and KIs (knock-ins) across several species both *in vivo* and *in vitro* (Hsu et al., 2014). Mismatches between DNA and the sgRNA, especially in the PAM distal region, can occasionally be tolerated and unintended off-target editing can occur (Hsu et al., 2013). Aiming to reduce off-target activity, several Cas9 variants have been reported to increase on-target specificity (Pickar-Oliver & Gersbach, 2019). The R691A Cas9 variant (HiFi Cas9) increases specificity without sacrificing on-target efficacy when delivered as a ribonucleoprotein (RNP) complex (Vakulskas et al., 2018). Moreover, alternative Cas proteins have been discovered and engineered with different PAM requirements awarding researchers flexibility to target more regions of the genome (J. Hu et al., 2018; Kleinstiver et al., 2015). Furthermore, inactivated Cas proteins can

be linked to gene repressors (Yeo et al., 2018), activators (Gilbert et al., 2013), and base editing enzymes (Komor et al., 2016).

1.7.3 Modes of CRISPR/Cas9 delivery for genome editing

There are 3 primary approaches to deliver Cas9 and an sgRNA to a cell: DNA, mRNA, and protein (Yip, 2020). A plasmid containing instructions for Cas9 and sgRNA expression can be delivered into cells or an organism of choice (Yip, 2020). This is inexpensive and feasible for most molecular biology labs. However, plasmid delivery results in sustained expression of Cas9 increasing the likelihood of off-target effects (Wu et al., 2014), and toxicity commonly results from exogenous DNA vectors (Xue & Greene, 2021). Delivery of CRISPR machinery via mRNA causes faster, more transient expression (Yip, 2020) attenuating the risk of off-target editing (Wu et al., 2014). RNP (ribonucleoprotein) delivery of Cas9/sgRNA complexes causes the most immediate and transient editing, further reducing off-target effects (Yip, 2020).

1.7.4 DNA repair after Cas9 mediated DSB

Cas9 generates a targeted DNA DSB with blunt ends that activates DNA repair mechanisms (Pickar-Oliver & Gersbach, 2019). The primary DNA repair mechanisms are non-homologous end joining (NHEJ), microhomology-mediated end joining (MMEJ), and homology directed repair (HDR) (Yeh et al., 2019).

NHEJ is considered the default pathway occurring in every cell cycle and cell type (Pickar-Oliver & Gersbach, 2019; Riordan et al., 2015), and begins when the Ku70/Ku80 complex binds to the broken DNA ends serving as the scaffolding for DNA-PKcs, XRCC4, DNA ligase IV, and XLF (A. Davis et al., 2014; Spagnolo et al., 2006). This error-prone mechanism will frequently generate Indels (insertions and/or deletions) that can disrupt gene expression by causing a frameshift that introduces a premature termination codon (Pickar-Oliver & Gersbach, 2019).

MMEJ repair plays an important role comparable to NHEJ (Shen et al., 2018). As the name indicates, MMEJ occurs when there is a micro-homology between the 2 sides of the DSB (Yeh et al., 2019). There is some evidence that MMEJ can be used to generate certain KI mutations without a donor template (Allen et al., 2019; Shen et al., 2018). However, this is sequence dependent and a majority of mutations cannot be generated through undirected MMEJ.

Specific KI gene editing experiments exploit the HDR pathway (Pickar-Oliver & Gersbach, 2019). Several HDR pathways have been described (canonical HR, synthesis-dependent strand annealing, break-induced replication, and single-strand annealing) (Yeh et al., 2019). Single-strand annealing (SSA) is very similar to MMEJ but requires larger regions of homology of over 200bp in mammalian cells (Liskay et al., 1987). Unlike SSA, both break-induced replication (BIR) and synthesis-dependent strand annealing (SDSA) are rad-51 dependent processes (Yeh et al., 2019). In SDSA, a D-loop forms when the unbroken double stranded DNA opens. This is followed by the broken strand annealing to the exposed homologous region of the unbroken DNA strand in a process called strand invasion (McVey et al., 2016). Next, polymerase δ synthesizes DNA from the repair template and the newly synthesized DNA then shares homology and can bind with the other strand of the DSB (Yeh et al., 2019). BIR occurs as a last resort to repair the DSB when the second DSB cannot be located (Yeh et al., 2019) and is characterized by error prone polymerases that synthesize the missing DNA sequence from the break to the chromosome end (Verma & Greenberg, 2016). NHEJ and HDR DNA repair pathways after CRISPR/Cas9 editing are illustrated in **Figure 1.9**.

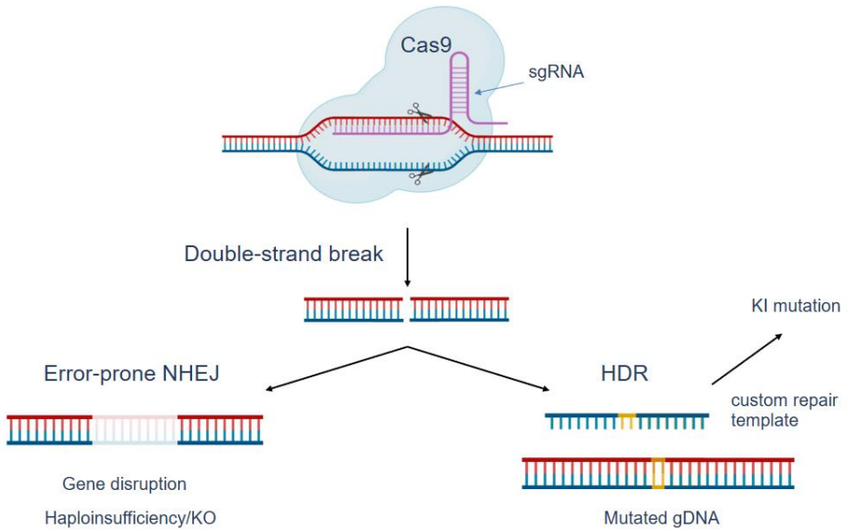

Figure 1.9 Leveraging DNA repair pathways for genome editing. Following a DSB, DNA repair mechanisms will desperately try to repair the damage. NHEJ does not require a repair template. This pathway is error-prone and frequently results in frameshift Indels that can introduce a premature stop codon into the reading frame and disrupt gene expression. Alternatively, HDR can repair the DSB. Providing a custom repair template with the desired mutation can trick the cell into incorporating a precisely designed mutation into the DNA. Created with BioRender.com

1.7.5 Improving HDR efficiency

The HDR pathway is less commonly recruited compared to NHEJ and MMEJ making HDR KI generation exceedingly inefficient in some cases (Pickar-Oliver & Gersbach, 2019). Methods to increase rates of HDR have been extensively investigated (Aird et al., 2018; Z. Hu et al., 2018; Riesenberg et al., 2019; Riesenberg & Maricic, 2018; Skarnes et al., 2019). Delivery of a repair template tethered to a Cas9 sgRNA complex increases the rate of HDR rates either by proximity of the repair template to the DSB or through increased nuclear localization (Aird et al., 2018). The ligase inhibitor SCR7 inhibits other DNA repair pathways to favor HDR (Z. Hu et al., 2018). Although, SCR7 does not consistently improve rates of HDR (Skarnes et al., 2019), and it is debated whether SCR7 inhibits NHEJ specific ligase IV or the MMEJ ligases I and III (Greco et al., 2016). Inhibitors of DNA-PKcs such as M3814 and NU7026 block DNA-PKcs kinase activity preventing NHEJ (Riesenberg et al., 2019; Riesenberg & Maricic, 2018). A commercially available small molecule with an undisclosed structure and mechanism called “Alt-R HDR Enhancer” increased HDR rates in hiPSCs (Skarnes et al., 2019). In this study, HDR was further increased by cold-shocking following transfection and utilizing asymmetrically designed repair templates (Skarnes et al., 2019).

Many studies have focused on optimizing repair template design to increase HDR (Liang et al., 2017; Richardson et al., 2016; Skarnes et al., 2019; Y. Wang et al., 2018). Cas9 releases the 3’ end of the non-target strand (the strand containing the PAM) before the opposite strand inclining Richardson et al. (2016) to design repair ssODNs asymmetrically matching the target sequence and complementary to the strand that is released first. Richardson and colleagues designed repair ssODNs with longer homology arms on the PAM proximal side than the PAM distal side matching the target strand sequence and demonstrated this rational design produced higher HDR editing rates (Richardson et al., 2016). Y. Wang et al. (2018) reported asymmetric repair ssODNs matching the target strand with longer overhangs on the PAM-distal side but not the PAM-proximal side resulted in higher HDR rates. These inconsistent reports indicate that the effect of repair template design on HDR editing may be locus dependent.

The design of the sgRNAs can considerably impact the HDR editing outcome. The location of the sgRNA relative to the mutation largely determines the percentage of homozygous, heterozygous, and wild type editing outcomes (Paquet et al., 2016). Since many disease-causing mutations are heterozygous in patients, Paquet et al. (2016) demonstrated there is an optimal window approximately 10bp from the cut-site that heterozygous mutations can be efficiently incorporated with homozygous incorporation being favored closer to the cut site and wild type outcomes at more distant locations. Furthermore, mutations that do not block the sgRNA or PAM are frequently incorporated with

extremely low rates of HDR (Paquet et al., 2016). Due to PAM constraints, it is not always feasible to design an sgRNA that is blocked from re-cutting by a disease mutation. Silent protein coding mutations can be implemented in coding regions to effectively block sgRNAs, but in non-coding regions this is not possible. However, a two-step editing strategy called CORRECT can be executed (Kwart et al., 2017). The first step of CORRECT incorporates both the intended KI mutation and a designed blocking mutation either modifying the PAM or the sgRNA binding sequence. In the 2nd step, either a different Cas enzyme or sgRNA that recognizes the new sequence is used. The KI mutation is preserved but the initial blocking mutation is removed now blocking cutting activity of Cas/sgRNA in the 2nd step (Kwart et al., 2017; Paquet et al., 2016).

1.7.6 Quality controls in iPSCs after genome editing

Although versatile, CRISPR/Cas9 can cause unwanted effects. Editing at off-target locations with a similar sequence to the target sequence has been reported (Hsu et al., 2013; Zhang et al., 2015). Whole genome sequencing can be performed after editing as an unbiased detection method for off-target effects but it is relatively expensive (Veres et al., 2014). Because Cas9 nuclease activity is sgRNA and PAM dependent, off-target sites can be predicted *in silico* with computer algorithms and regions with high probability of off-target editing can be sequenced in edited cell lines or organisms (Heigwer et al., 2014; Ran et al., 2013; Singh et al., 2015).

Previously undetected on-target effects (OnTEs) have recently been reported by our lab and others (Simkin et al., 2022; Weisheit et al., 2020, 2021). Single cell human iPSC clones edited with apparent homozygous mutations were frequently shown to be hemizygous (Weisheit et al., 2020). Single allele insertions, deletions, and complex rearrangements were detected that initially escaped detection through standard genotyping PCRs and Sanger sequencing (Weisheit et al., 2020). We developed a quantitative genotyping PCR (qgPCR) that adds a fluorescent probe to the genotyping PCR to quantify the number of alleles around the edited locus to ensure all alleles remain intact (Weisheit et al., 2021). Furthermore, we found that Cas9 induced regions of LOH that affected less than 6Kb and up to entire chromosome arms (Weisheit et al., 2020). Genotyping nearby heterozygous SNPs on both sides of the cut site after editing can exclude LOH (Weisheit et al., 2021). Genome wide SNP analysis with SNP microarrays can be used to detect large copy number variations, chromosomal aberrations, and LOH when nearby heterozygous SNPs cannot be identified (Weisheit et al., 2020, 2021).

1.8 Aims of the thesis

Several COL4A1 and COL4A2 mutations have been identified to cause monogenic cSVD. Animal models, especially mouse models, have yielded valuable information regarding collagen IV related cSVD progression. However, such animal models do not fully recapitulate human biology. With the recent discovery of hiPSCs, there are novel opportunities to derive human models of cSVD. The advent of CRISPR/Cas9 genome editing technology has made it feasible to generate disease causing mutations in hiPSCs or alternatively to correct disease mutations directly in patient derived cells. A hiPSC model of collagen IV cSVD recapitulating human disease biology on a cellular level could provide new insights into human disease formation and may also provide a platform to study cell type specific contributions to the disease. While the mechanisms of how COL4A1 and COL4A2 mutations cause cSVD are incompletely understood, current hypotheses postulate non-mutually exclusive contributions that include intracellular accumulation from improperly folded heterotrimers causing ER stress, insufficient collagen IV deposition in the BM causing instability or impaired matrix-cell signaling, and/or integration of mutant heterotrimers in the BM thereby altering physiological functions of the BM.

The goal of this thesis is to generate and characterize human cSVD models caused by monogenic COL4A1 mutations, following 3 major aims:

First, using CRISPR/Cas9 genome editing at the Col4A1 locus, I aimed to generate a set of isogenic COL4A1 mutant hiPSC lines. These included homozygous and heterozygous KO lines carrying a haploinsufficiency frameshift mutation (ClinVar: VCV000161440.4) generated via NHEJ, and lines with

a COL4A1^{G755R} missense mutation (ClinVar: VCV000161974.16) as well as the 3'-UTR (c.*35C>A) miR-29 binding site mutation (ClinVar: VCV000689432.1) generated using HDR. Each line was generated from the same hiPSC WT line so they will share the same isogenic control.

Second, I aimed to perform necessary CRISPR/Cas9 editing quality controls on all four generated cell lines, to exclude deleterious side effects of CRISPR/Cas9 genome editing. I excluded OnTEs and a common type of trisomy by quantifying the number of alleles by qgPCR at the edited loci and a common triplicated region in hiPSCs on chromosome 20. Nearby SNP genotyping ruled out LOH and sequencing predicted off-target regions excluded the most likely off-target effects. DNA fingerprinting ensured the correct WT line was edited, and finally molecular karyotyping determined there are no large chromosomal aberrations present in the edited lines.

Third, I aimed to differentiate these iPSCs into the cell types of the NVU and characterize collagen IV expression, expecting that COL4A1 is reduced in the frameshift mutations, similar to WT levels in the COL4A1^{G755R} mutant, and elevated in the (c.*35C>A) mutant. Finally, using 2D transwell and 3D microfluidic *in vitro* models of the BBB, I investigated potential phenotypes of cSVD such as barrier permeability and collagen IV secretion.

Chapter 2 Materials and Methods

2.1 hiPSC lines

hiPSC experiments were performed according to all of the relevant guidelines and regulations. Female WT hiPSC line A18944 was purchased from Thermo Fisher (#A18945) and used to generate single cell clones with COLA1 KO, COL4A1^{G755R}, and COL4A1 (c.*35C>A) mutations.

2.2 hiPSC maintenance

hiPSCs were maintained with essential 8 flex medium (E8F, Thermo Fisher #A2858501) on 6-well plates (Corning #353046) coated with vitronectin (VTN, Thermo Fisher #A14700). VTN was diluted 1:100 with in Dulbecco's phosphate buffered saline without Calcium/Magnesium (PBS, Sigma-Aldrich #D8537) before 1 ml of VTN solution was added to each well. The coating solution was left for at least 1 hour at room temperature. The cells were grown as colonies at 37 °C and 5% CO_2 and split twice per week. To split hiPSCs, cells were washed with 1ml PBS before incubating them in PBS with 0.5 mM UltraPure EDTA (Thermo Fisher #15575020). The PBS/EDTA was aspirated and the cells were washed off of the plate with 3 ml of DMEM/F-12 (Thermo Fisher #11320074). Using a Pasteur pipette (Carl Roth, #EA66.1), the cell solution was triturated to break up large clumps and then the cells were transferred to a new VTN-coated plate in E8F medium.

Freezing hiPSCs was performed by detaching the cells with PBS/EDTA as described above before washing them off with cold freezing media composed of 45% E8F, 45% fetal bovine serum (FBS, Thermo Fisher #10500064), 10% DMSO (Sigma-Aldrich #D2650) with 10 µM rock inhibitor Y27632 (RI, Selleckchem #S1049). Cell suspensions were briefly triturated as described above and transferred to cryovials (Carl Roth #X549.1) and stored at -80 °C. After 24 hours, the cryovials were placed in a liquid nitrogen tank at -140 °C. To thaw hiPSCs, the cryovials were rapidly warmed in a 37 °C water bath until just thawed. The cell suspension was transferred to a 15 ml conical tube (VWR #525-0061) with 9 ml of room temperature DMEM/F-12, and the solution was centrifuged at 1000 rpm (162 g) for 4 minutes. The supernatant was aspirated and the cells were resuspended as colonies (not as single cells) in 2 ml E8F containing 10 µM RI and plated onto 6-well plates coated with VTN.

2.3 Design of CRISPR/Cas9 sgRNAs

All sgRNAs were designed using the online CRISPOR tool (http://crispor.tefor-net/) (Concordet & Haeussler, 2018). The sgRNAs that were tested in HEK293 cells were cloned into the MLM3636 plasmid (a gift from K. Joung, Addgene 43860). Guides selected for hiPSC editing were ordered from or IDT as an Alt-R™ CRISPR-Cas9 sgRNA or Synthego as a CRISPRevolution sgRNA EZ Kit. See **Table 2.1** for sgRNA sequences.

Locus	Name	Location in COL4A1	Sequence (5'-3')	RNP manufacturer
COL4A1 KO	5 rv	Exon 29	CCAGGTCGCCCGGGATTTAA	NA
COL4A1 KO	15 rv	Exon 28	ATTGGATTTCCAGGGCCCCC	IDT
COL4A1 KO	23 rv	Exon 29	ATGGGGCCACCGGGGACTCC	NA
COL4A1 KO	25 fw	Exon 29	CCATTAAATCCCGGGCGACC	NA
COL4A1 KO	40 rv	Exon 29	ACGGCTTACCTGGAGACATG	NA
COL4A1 KO	115 fw	Exon 28	GGGAAAGCCTCGGTCTCCTG	NA
COL4A1^{G755R}	45 rv	Exon 30	CGGCATTCCTGGCACACCCG	Synthego
(c.*35C>A)	57 rv	Exon 52	ACTCAGCTAATGTCACAACA	Synthego
(c.*35C>A)	4 rv	Exon 52	CTGACTCAGCTAATGTCACA	Synthego

Table 2.1 Location and sequence of sgRNAs

2.4 Testing sgRNA activity in HEK293 cells

The cutting efficiency of each COL4A1 KO sgRNA was tested by transfecting HEK293 cells with the MLM3636 plasmid cloned with one of the sgRNAs and pCas9_GFP (a gift from K. Musunuru, Addgene #44719). Transfections were performed by adding 2.4 µl X-tremeGENE™ 9 DNA Transfection Reagent (Sigma-Aldrich #6365779001) to 100 µl DMEM (Thermo Fisher #31966021) and incubating for 5 minutes at room temperature. Separately, 0.8 µg Cas9 plasmid and 0.4 µg sgRNA plasmid were mixed and 100 µl of the X-tremeGENE™ 9/DMEM mixture was added and incubated for 20 minutes at room temperature. Subsequently, 100 µl of this solution was added dropwise and distributed evenly across a 12-well (Corning #3513) of HEK293 cells. After approximately 24 hours, the cells were visually analyzed for GFP expression to ensure the transfection was successful. Two days after transfection, the HEK293 cells were pelleted and the gDNA was extracted with a NucleoSpin Tissue Kit (Macherey-Nagel #740952.250). Genotyping PCRs were performed using OL2092/OL2093 for sgRNAs in exon 28 and OL2094/OL2095 for sgRNAs in exon 29. These were Sanger sequenced and the cutting efficiency was estimated by TIDE (https://tide.nki.nl/) (Brinkman et al., 2014).

2.5 Design of repair template single-stranded oligodeoxynucleotides (ssODNs)

Repair templates were designed manually. The standard design for the ssODNs was 50 bp around the cut site or intended mutation and containing the sequence of the PAM strand so that it does not contain the complementary sequence of the sgRNA to prevent unwanted binding. Several asymmetric and non-PAM strand ssODNs were also designed and all used ssODNs are show in **Table 2.2**. ssODNs were ordered as Ultramers from IDT.

ssODN	Sequence (5'-3')
COL4A1^{G755R} Symmetric	TCTACCGGGACTCAAAGGTTTGCCAGGTCTTCC**CGGCATTCCTGGCACAC** **CCA**GGGAGAAGGGGAGCATTGGGGTACCAGGCGTTCCTGGAGAACATGGA
COL4A1^{G755R} Asymmetric	AACGCCTGGTACCCCAATGCTCCCCTTCTCCC**TGGGTGTGCCAGGAATGC** **CG**GGAAGACCTGGCAAACCTTTGAGTCCCGGTAGACCAACTCCAGGCTCT
COL4A1^{G755R} DSM	AACGCCTGGTACCCCAATGCTCCCCTTCTCTC**TAGGTGTGCCAGGAATGC** **CG**GGAAGACCTGGCAAACCTTTGAGTCCCGGTAGACCAACTCCAGGCTCT
(c.*35C>A) Symmetric	ATGAGAAGAACATAATGAAGCCTG**ACTCAGCTAATGTCACAACA**TGGTGA TACTTCTTCTTCTTTTTGTTAACAGCAACGAACCCTAGAAATATATCCTG
(c.*35C>A) Asymmetric	TTCGTTGCTGTTAACAAAAAGAAGAAGAAGTATCACCA**TGTTGTGACATT** **AGCTGAGT**CAGGCTTCATTATGTTCTTCTCATACAGACTTGGCAGCGGCT
(c.*35C>A) 1st step CORRECT	AGTCTGTATGAGAAGAACATAATGAAGCCTG**ACTCAGCTAATGTCACAGG** **G**TGGTGATACTTCTTCTTCTTTTTGTTAACAGCAACGAACCCTAGAAATA

Table 2.2 Sequences of ssODNs. PAM sequences are underlined, location but not necessarily sequence of sgRNAs are shown in bold, red indicates the intended mutation, and blue indicates blocking mutations.

2.6 Electroporation of hiPSCs

Two days before electroporation, a 6-well plate was coated with Geltrex (Thermo Fisher #A1413302) diluted 1:150 in DMEM/F12 at 37 °C for at least 1 hour. HiPSCs were detached using Accutase (Thermo Fisher #A1110501) for 5 minutes at 37 °C. The enzymatic detachment was stopped with DMEM/F-12 and the cells were triturated into single cells. The cell suspension was collected and the cells were mixed 1:1 with trypan blue (Sigma-Aldrich #T8154) to stain dead cells and the live cells were counted with a Neubauer chamber (Wagner & Munz GmbH #7178 05). Subsequently, 250K cells were transferred to a 15 ml conical tube and centrifuged for 4 minutes at 100 rpm (162g). The supernatant was aspirated and the cells were resuspended and plated on a 6-well Geltrex-coated plate in StemFlex media (SF, Gibco # A3349301) with 10 µM RI.

The electroporation was performed either with a BTX Gemini X2 electroporation system (BTX #45-2006) or a Lonza 4D nucleofector system composed of a 4D nucleofector core unit (Lonza #AAF-1003B) and a 4D nucleofector X-unit (Lonza #AAF-1003X). The protocols for each respective system are similar but have key differences. The procedure for electroporating with the Lonza 4D nucleofector system is described below and **Table 2.3** details where the electroporation using the BTX Gemini X2 differs. The hiPSCs were detached with Accutase for 5 minutes and the cell suspension is collected as described earlier in this section. The cells were counted and 200k cells were set aside. Meanwhile, 30 pmol of Cas9 (Alt-R® S.p. Cas9 Nuclease V3, IDT #1081058 or Alt-R® S.p. HiFi Cas9 Nuclease V3, IDT #1081060) and 60 pmol of sgRNA were added together and mixed by slowly pipetting 2 to 3 times strictly avoiding air bubbles. The Cas9/sgRNA complex was incubated 10 to 20 minutes at room temperature. The hiPSCs set aside were then centrifuged at 162g for 4 minutes and resuspended in P3 Primary cell solution (Lonza #PBP3-00675) composed of 16.4 µl of the nucleofector solution and 3.6 µl of the P3 supplement. The cell suspension was pipetted onto the Cas9/sgRNA complex mixture after incubation. If an ssODN was used, 120 pmol was added on top. The mixture was pipetted up and down to mix and 20 µl was added to the cuvette (Lonza #V4XP-3032) and it was placed in the Lonza 4D nucleofector X-unit. The program CA137 was applied to the cells and then 100 µl of SF and 1X RevitaCell (Thermo Fisher #A2644501) was added on top of the cells and they recovered for 10 minutes at room

temperature in the cuvette before being plated into a Geltrex-coated 12-well plate with SF and 1X RevitaCell. The following day, the media was changed to provide fresh SF with 1X RevitaCell.

Parameter	Lonza 4D nucleofector	BTX Gemini X2 electroporation system
Cells electroporated	200k	400k
Resuspension volume	20 µl	40 µl
Buffer	P3 Primary cell solution (Lonza #PBP3-00675)	BTXpress™ High Performance Electroporation Solution (VWR #732-1285)
Electroporation volume	20 µl	40 µl
Cuvette	16-well Nucleocuvette™ Strip (Lonza #V4XP-3032)	1mm cuvette (Fisher Scientific #15437270)
Safety dome	NA	BTX #45-2021
Cas9 amount	30 pmol	60 pmol
sgRNA amount	60 pmol	120 pmol
ssODN amount	120 pmol	240 pmol
Recovery time	10 minutes before plated	Directly plated after electroporation
Electroporation parameters	CA137	Two 20 ms pulses of 95V or 110V

Table 2.3 Differences between Lonza 4D nucleofector and BTX Gemini X2 electroporation system protocols

2.7 Single cell clone generation and isolation

Approximately 3 to 4 days after electroporation, the hiPSCs were dissociated from the 12-well plate with Accutase for 10 minutes to ensure complete single cell generation. The cells were triturated to form single cells and collected. After counting the cells, they were plated onto Geltrex-coated 10 cm plates (Thermo Fisher #150350) at a density between 500-2k cells/plate in SF with 1X RevitaCell. The plated single cells grew into colonies after roughly 7 to 8 days. At which point, the colonies were mechanically isolated and transferred to a well of a 96-well plate (Corning # 5380522) coated with Geltrex in SF with 10 µM RI.

2.8 Single cell clone screening

2.8.1 Replica plating and cell lysis

In order to collect gDNA for clone screening while keeping the clones in culture, a replica split was performed. For each 96-well plate of clones, a new 96-well plate was coated with Geltrex. The clones were incubated with 40 µl of Accutase at 37 °C for 10 minutes that was stopped with the addition of 100 µl SF with 10 µM RI. The cells were washed off of the plate and approximately 20-30 µl of the cell suspension from each well was transferred to the newly Geltrex-coated 96-well plate in 100 µl SF with 10 µM RI at the same position. Subsequently, the rest of the cell material was centrifuged in the original 96-well plate at 4000 rpm (2500 g) for 12 minutes. These cell pellets were lysed by adding 25 µl of lysis buffer **(Table 2.4)** on each pellet and placing the plate on a rotational shaker at 150 rpm for at least 10 minutes at room temperature. After incubation, the cells pellets were washed from the plate and transferred to a 96-well PCR plate (Brand #781374) and incubated at 55 °C for 4 hours followed by 95 °C for 10 minutes to inactivate the proteinase K.

Lysis Buffer	Volume for 1 plate (µl)
Proteinase K (NEB #P8107S)	41.25
Ultrapure H_2O (Thermo Fisher #10977035)	2431
Jumpstart Buffer 10X	275

Table 2.4 Lysis buffer composition

Jumpstart Buffer 10X	Volume (ml)
1M Tris pH8.3 (Carl Roth #0188.3)	3
1M KCl (AppliChem #A3582)	15
1M $MgCl_2$ (Carl Roth # KK36.1)	0.45
0.1% Gelatin (Sigma-Aldrich #ES006B)	3
MilliQ H_2O	8.55
Total	30

Table 2.5 Jumpstart 10X buffer composition

2.8.2 Genotyping PCR

Following cell lysis, a genotyping PCR was performed to amplify the edited region. For each mutation, there was a different genotyping PCR with the primer combinations for each listed in **Table 2.6**. The genotyping PCR was performed by combining 10 µl of the genotyping PCR master mix (**Table 2.7**) to 2.5 µl of cell lysate and running the genotyping PCR program (**Table 2.8**).

Locus		Primer name
COL4A1 KO	Forward primer	OL2092
	Reverse primer	OL2093
COL4A1^{G755R}	Forward primer	OL2096
	Reverse primer	OL2097
(C.*35C>A)	Forward primer	OL2421
	Reverse primer	OL2422

Table 2.6 Genotyping PCR primer combinations

Genotyping PCR master mix	For 1 plate (µl)
OneTaq® Quick-Load® 2X Master Mix (NEB #M0482L)	687.5
Ultrapure H_2O (Thermo Fisher #10977035)	407
Forward primer (100 µM)	2.75
Reverse primer (100 µM)	2.75

Table 2.7 Genotyping PCR master mix composition

Step	Temperature (°C)	Time (minutes:seconds)	Cycles
Initial Denaturation	95	02:00	1
Denaturation	95	00:30	35
Annealing	59	00:30	
Extension	68	00:30	
Final Extension	68	02:00	1
Hold	10	∞	1

Table 2.8 Genotyping PCR program

2.8.3 RFLP clone screening assay and clonal expansion

To identify edited clones, the genotyping PCR product of each clone was digested with a restriction enzyme to screen for either a loss or a gain of a restriction site indicative of successful editing. The RFLP assay was performed by mixing 5 µl of the RFLP master mix (**Table 2.9**) with 5 µl of the genotyping PCR master mix followed by incubation at the temperature given in **Table 2.10**. The cleavage products were separated by electrophoresis on a 2% agarose (Serva, #11406.02) gel and examined. The PCR products of edited clones identified in the RFLP assay were Sanger sequenced at GATC/Eurofins or Microsynth Seqlab GmbH.

RFLP master mix	For 1 plate (µl)
CutSmart buffer (NEB #B7204S) – (PasI Buffer 10X Thermo Fisher #B27 was used for PasI)	110
Restriction Enzyme (Table 2.10)	13.75
Ultrapure H_2O (Thermo Fisher #10977035)	426.25

Table 2.9 RFLP master mix composition

Locus	Mutation screened	Enzyme	Incubation	Gain/Loss	Unedited (bp)	Heterozygous (bp)	Homozygous (bp)
COL4A1 KO	**Indels**	ApaI (NEB #R0114S)	12 hours, 25 °C	Loss	263/62	325/263/62	325
COL4A1^{G755R}	**COL4A1^{G755R} KI**	PasI (Thermo Fisher #ER1861)	3 hours, 55 °C	Gain	155/144	155/144/92/63	92/63
(c.*35C>A)	**(c.*35C>A) KI**	HphI (NEB #R0158S)	3 hours, 37 °C	Gain	351	351/191/160	191/160
(c.*35C>A)	**ACA>GGG CORRECT 2nd step KI**	NlaIII (NEB #R0125S)	3 hours, 37 °C	Gain	351	351/196/155	196/155

Table 2.10 Design parameters of RFLP assays

Edited clones with a confirmed genotype from Sanger sequencing were expanded from a 96-well plate to a 12-well plate and finally to a 6-well. Briefly, clones were washed with PBS in the 96-well plate and then incubated with 40 µl PBS/EDTA (0.5mM) for 5 minutes at room temperature. Without aspirating the PBS/EDTA, the cells were washed off with E8F with 10 µM RI and transferred to a 12-well VTN-coated plate in E8F medium with 10 µM RI. Once the cells became nearly confluent in the 12-well well, they were split according to the maintenance protocol (**Section 2.2**) into a 6-well VTN-coated plate. If there was a substantial amount of spontaneous differentiation present in the 12-well well, the incubation with PBS/EDTA was shortened. Once transferred to a 6-well plate, if spontaneous differentiation persisted, it could be manually removed with a pipette tip under the microscope. Finally, the cells were frozen according to **Section 2.2**. During freezing, around 20% of the cell suspension from a nearly confluent 6-well was collected, pelleted by centrifugation at 162g for 4 minutes, the supernatant was removed, and the pellet was stored at -20 °C for gDNA extraction.

2.9 Quality controls of CRISPR/Cas9 edited hiPSCs

Before beginning any of the quality control assays, the gDNA was extracted from the cell pellets of the clones to be tested using the NucleoSpin Tissue Kit according to manufacturer's instructions. After measuring the concentration of the extracted gDNA with a spectrophotometer, the QC assays were performed.

2.9.1 BCL2L1 assay

One of the most common deleterious outcomes from genome editing and single cell clone generation observed was a triplication of the BCL2L1 locus that confers a growth advantage to the hiPSCs. To determine whether this has occurred in an edited clone, a qgPCR is performed to quantify the number of BCL2L1 alleles present in the gDNA. The composition of each qgPCR reaction is given in **Table 2.11**.

qgPCR master mix	Volume (µl)
2x PrimeTime Gene Expression Master Mix (IDT #1055772)	7.5
20x human TERT TaqMan Copy Number Reference Assay (Thermo Fisher #4403316)	0.75
20x qgPCR assay	0.75
Ultrapure H_2O (Thermo Fisher #10977035)	3
gDNA (20 ng/µl)	3

Table 2.11 qgPCR reaction composition

The 20x qgPCR assay is composed of the genotyping primers (0.5 pmol/µl) and the PrimeTime Eco Probe (0.25 pmol/µl) for BCL2L1 given in **Table 2.13**. The gDNA was first diluted with Ultrapure H_2O to 50 ng/µl and the concentration was re-measured

before being diluted to 20 ng/µl and used in the qgPCR assay. The qgPCR reaction was performed using a StepOne Plus Real-Time PCR system (Thermo Fisher #4376600) with the program in **Table 2.12**. The Ct values were normalized to the human TERT that served as the internal control and the values were compared to the unedited WT and karyotyped clones as well as positive control clones that were shown to have an additional copy of BCL2L1 in previous qgPCR experiments. Duplicates were performed for each sample and averaged.

Step	Temperature (°C)	Time (minutes:seconds)	Cycles
Polymerase activation	95	05:00	1
Denaturation	95	00:15	40
Annealing/extension	60	01:00	
Hold	10	∞	1

Table 2.12 qgPCR program

2.9.2 OnTE qgPCR assay

CRISPR/Cas9 editing can cause deleterious deletions, insertions, or complex rearrangements at the on-target allele that escape standard genotyping by PCR and Sanger sequencing (Weisheit et al., 2020). To quantify the number of intact on-target alleles, a qgPCR was performed with the genotyping primers and a fluorescent probe designed according to (Weisheit et al., 2021). The same qgPCR master mix and qgPCR program with a StepOne Plus Real-Time PCR system used for the BCL2L1 assay was used for the OnTE qgPCR. Different genotyping primers and probes were used for each edited locus (**Table 2.13)**. Normalizations and quantifications were performed the same as for the BCL2L1 qgPCR.

Locus	Primers	Probe
BCL2L1	BCL2L1_F	56-FAM/TGTGGAAGA/ZEN/GAACAGGACTGAGGC/3IABkFQ
	BCL2L1_R	
COL4A1 KO	OL2092	56-FAM/AATTCCAGC/ZEN/TCACCGGGATACCAC/3IABkFQ
	OL2093	
COL4A1^{G755R}	OL2096	56-FAM/TGGCAAACC/ZEN/TTTGAGTCCCGGTAG/3IABkFQ
	OL2097	
(c.*35C>A)	OL2421	56-FAM/TTCTCATAC/ZEN/AGACTTGGCAGCGGC/3IABkFQ
	OL2422	

Table 2.13 Primer and probe combinations for qgPCR BCL2L1 and OnTE assays

2.9.3 Off-target analysis

Using the online CRISPOR tool (http://crispor.tefor.net/), the top 5 off-target regions from the CFD and the MIT database were exported for each sgRNA. Primers were designed with the online Primer3Plus tool (https://www.primer3plus.com/) to amplify the region around each off-target sequence. PCRs for each off-target were performed with the reagents in the ratios given in **Table 2.14** with 100 ng of gDNA and the PCR program in **Table 2.8**. For PCRs that did not initially amplify the correct product, the annealing temperature was adjusted until the expected product was amplified. After optimization, the off-target regions were amplified in the edited clones and Sanger sequenced. See **Table 2.15** for off-target primers for each sgRNA.

OneTaq® PCR master mix	Amount for 50 µl reaction
OneTaq® Quick-Load® 2X Master Mix (NEB #M0482L)	25 µl
Forward primer (10 µM)	1 µl
Reverse primer (10 µM)	1 µl
gDNA	100 ng
Ultrapure H_2O (Thermo Fisher #10977035)	To 50 µl

Table 2.14 OneTaq® PCR master mix composition

Off-target	COL4A1 KO sgRNA 15 rv	COL4A1^{G755R} sgRNA 45 rv	(c.*35C>A) sgRNA 57 rv	(c.*35C>A) sgRNA 4 rv
CFD 1	OL2301/OL2302	OL2921/OL2922	OL2747/OL2748	OL2824/OL2825
CFD 2	OL2303/OL2304	OL2923/OL2924	OL2749/OL2750	OL2826/OL2827
CFD 3	OL2305/OL2306	OL2925/OL2926	OL2751/OL2752	OL2840/OL2841
CFD 4	OL2307/OL2308	OL2927/OL2928	OL2753/OL2754	OL2844/OL2845
CFD 5	OL2309/OL2310	OL2929/OL2930	OL2755/OL2756	OL2832/OL2833
MIT 1	OL2311/OL2312	Same as CFD 4	OL2792/OL2793	Same as CFD 2
MIT 2	OL2313/OL2314	OL2931/OL2932	OL2759/OL2760	OL2834/OL2835
MIT 3	OL2315/OL2316	OL2933/OL2934	OL2794/OL2795	Same as CFD 3
MIT 4	OL2317/OL2318	OL2935/OL2936	OL2796/OL2797	OL2836/OL2837
MIT 5	OL2319/OL2320	OL2937/OL2938	OL2765/OL2766	OL2838/OL2839

Table 2.15 Primer combinations used to amplify off-target regions

2.9.4 LOH analysis

We recently reported that CRISPR/Cas9 editing can result in regions of LOH on either side of the sgRNA cut site (Weisheit et al., 2020). To verify this has not occurred in edited cell lines, SNP genotyping was employed to ensure nearby heterozygous SNPs have maintained their zygosity according to Weisheit et al. (2021). In the unedited WT line, SNPs rs12864958 and rs617478 were identified to be heterozygous. The region around these SNPs was amplified with OL2378/OL2379 for rs12864958 and OL2380/OL2381 for rs617478 and subsequently Sanger sequenced in edited clones. See **Table 2.16** for the distance from the edit to each SNP.

	rs12864958	rs617478
COL4A1 KO	-53 Kb	34 Kb
COL4A1^{G755R}	-49 Kb	38 Kb
(c.*35C>A)	-20 Kb	67 Kb

Table 2.16 Distance of SNPs from each mutation

2.9.5 DNA Fingerprinting

To verify single cell clones were generated from the correct cell line, the VNTR (variable number tandem repeat) D1S80 was amplified by PCR. To this end, primers OL1240/OL1241 were used to make 20 µl of OneTaq® PCR master mix according the ratios of **Table 2.14** and the PCR was performed with the parameters from **Table 2.8** adjusted to a 70°C annealing temperature and 60 second extension time. The PCR product bands were separated by electrophoresis using a 2% agarose gel and the size and band patterns were examined and compared to the unedited cell line.

2.9.6 Molecular karyotyping

Freshly extracted gDNA was diluted to 60 ng/µl using the buffer provided in the NucleoSpin Tissue Kit and sent to Life&Brain GmbH (only COL4A1 KO clone P2H5) or HelmholtzZentrum München for karyotyping analysis with a SNP microarray.

2.9.7 Pluripotency analysis

COL4A1 KO hiPSC clones were analyzed by immunofluorescence for the expression of the pluripotency markers Tra-160, SSEA4, Nanog, and Oct-4. First, coverslips (VWR # 630-2190) were acid-etched by incubating them overnight in 30% HCl (Carl Roth # X896.2) on a rotational shaker. The coverslips were washed 3 times with ddH_2O and stored in 100% ethanol (VWR # 20.821.310). After acid-etching, hiPSCs were split with EDTA in small colonies according the **Section 2.2** and plated on the acid-etched cover slips coated with VTN in E8F medium. One to two days later while the hiPSCs were still colonies, the cells were fixed for 10 minutes at room temperature with 4% PFA (Morphisto #1.176.201.000). Cells were then stained for the pluripotency markers Tra-160, SSEA4, Nanog, and Oct-4 according to **Section 2.13**.

2.10 Endothelial cell differentiation and culturing

This differentiation protocol was developed in collaboration with Tom Webb, University of Leicester, UK. The day before beginning the differentiation, hiPSCs were detached with Accutase and plated as single cells in SF with 10 µM RI on a Geltrex-coated 6-well plate according to the split preceding the electroporation in **Section 2.6** but at a density of 350k cells per 6-well. The next day, as close to 24 hours as possible, the media was changed to 3 ml/well of mesoderm induction media (MIM, StemCell #05220). On Day 2, the medium was again exchanged for 3 ml/well of fresh MIM. On Days 3 and 4, the cells were fed with 3 ml/well of Albumin Polyvinylalcohol Essential Lipids 2 media (APEL2, StemCell #05270) supplemented with 200 ng/µl $VEGF_{165}$ (Peprotech # 100-20) and 2 µM forskolin (Peprotech #6652995).

The cells were MACS (magnetic-activated cell sorting) sorted for CD144 (VE-cadherin) on day 5. Before beginning, MACS buffer was prepared and stored at 4 °C (**Table 2.17**) and 6-well plates were coated with collagen IV from human placenta (Sigma-Aldrich #C-5533). To this end, collagen IV was first dissolved in H_2O to make a stock solution of 600 µg/ml and then diluted 1:40 in PBS for coating. 1 ml of collagen IV coating solution was applied to each 6-well well and incubated at 37 °C for at least 1 hour. To begin the MACS, cells were washed with PBS and then incubated with Accutase for 10 minutes at 37 °C. Endothelial cell growth medium 2 (ECM2, Promocell #C-22011) was added on top to stop the Accutase and the cells were washed off and triturated to generate single cells. The cells were collected in a 15 ml conical tube and centrifuged at 162g for 4 minutes. After centrifugation, the supernatant was aspirated and the cell pellet was resuspended in 80 µl of ECM2 before adding 20 µl of magnetic CD144 MicroBeads (Miltenyi #130-097-857) and mixing. The cell suspension was then incubated for 15 minutes at 4 °C. Meanwhile, an LS column (Miltenyi #130-042-401) was secured to a MACS® MultiStand (Miltenyi #130-042-303) and washed with 3 ml of MACS buffer. After incubation, 1 ml of MACS buffer was added to the cell suspension before it was centrifuged at 162g for 4 minutes. The supernatant was removed and the cell pellet was resuspended in 1 ml of MACS buffer and it was subsequently loaded onto the LS column. The LS column was washed 3 times with 3 ml of MACS buffer

before removing the column from the MACS® MultiStand and placing it over a 15 ml conical tube. At which point, 5 ml of MACS buffer was applied to the column and the plunger was used to forcefully flush the solution through the column to remove the cells. The number of cells were counted as in **Section 2.6** and the cell suspension was centrifuged for 4 minutes at 162g. Following aspiration of the supernatant, the cells were resuspended in ECM2 with $VEGF_{165}$ (50 ng/µl) and plated on collagen IV at a density of 350k cells per 6-well well.

MACS buffer	Amount for 1 sample
PBS without calcium or magnesium (Sigma-Aldrich #D8537)	21.67 ml
BSA (Bovine serum albumin) fraction V (7.5%) (Thermo Fisher #15260037)	3.33 ml
UltraPure EDTA (Thermo Fisher #15575020)	100 µl

Table 2.17 Composition of MACS buffer

To split endothelial cells, the cells were washed with PBS and then incubated with Trypsin/EDTA (0.05%, Thermo Fisher #25300054) for 2 to 3 minutes at room temperature until just before the cells detach from the plate. The incubation time depends on the cell line and density of the endothelial cells. The Trypsin/EDTA was then aspirated and the cells were washed off with ECM2 with $VEGF_{165}$ (50 ng/µl) and plated in a 6-well well with either collagen IV, fibronectin, or gelatin coating in ECM2 medium with $VEGF_{165}$ (50 ng/µl). For each coating, the protein was diluted to the concentration in **Table 2.18** and 1 ml of coating solution was added per 6-well well and incubated at 37 °C for at least one hour. Endothelial cells were fed ECM2 with $VEGF_{165}$ (50 ng/µl) 1-2 times per week as needed. If ascorbic acid was added, L-ascorbic-acid-2-phosphate (Sigma-Aldrich #A8960) was dissolved in H_2O to 50 mg/ml and then added 1:1000 to the media with a final concentration of 50 µg/ml. To freeze endothelial cells, they were detached with Trypsin/EDTA as described above and then washed off with ECM freeze medium (90% ECM2, 10% DMSO) and transferred to cryovials that were stored at -80° C for 24 hours and subsequently at -140 °C. Thawing endothelial cells was performed as described in **Section 2.2** but the cells were resuspended in ECM2 with $VEGF_{165}$ (50 ng/µl) and plated onto a collagen IV-coated 6-well well.

Coating	Stock solution	Coating solution
Collagen IV (Sigma-Aldrich #C-5533)	600 µg/ml in H_2O	15 µg/ml in PBS
Fibronectin (Sigma #F4759)	1 mg/ml	10 µg/ml in PBS
Gelatin (Millipore #ES-006-B)	0.1 % H_2O	0.1% in H_2O

Table 2.18 Concentrations of different coatings used for endothelial cell cultures

2.11 Pericyte differentiation and culturing

The pericyte differentiation is based on the protocol published by Orlova et al. (2014). It exactly follows the endothelial cell protocol for the first 5 days up to the MACS sorting. However, the CD144 (-) fraction was collected and counted. The cells were centrifuged for 4 minutes at 162g and plated on gelatin-coated 6-wells (coated according to **Table 2.18**) in ECM2 medium at a density of 200k cells/well. The cells were grown for 3-4 days until they became 80-90% confluent and then split by washing with PBS before applying 1 ml of TryplE (Thermo Fisher #12604013) and incubating at room temperature for 2 minutes. The TryplE was aspirated and the cells were washed off with DMEM, high glucose, pyruvate (Thermo Fisher #41966052) containing 10% fetal bovine serum (FBS, Thermo Fisher #10500064), 2

ng/mL of TGFß3 (Peprotech #100-36E), and 4 ng/mL of PDGF-BB (Peprotech #100-14B). The cells were transferred at a ratio of 1:1 to a gelatin-coated 6-well with DMEM, high glucose, pyruvate with 10% FBS, 2 ng/mL of TGFß3, and 4 ng/mL of PDGF-BB. After 3 days, the medium was changed to DMEM, high glucose, pyruvate with 10% FBS. Pericytes were fed fresh DMEM, high glucose, pyruvate with 10% FBS 1-2 times per week as needed. Splitting pericytes was performed the same as described above but at the desired ratio and without the addition of TGFß3 and PDGF-BB. Pericytes were frozen by splitting them as described but washing them off in pericyte freezing media (DMEM, high glucose, pyruvate with 10% FBS and 10% DMSO) and storing them at -80° C for 24 hours and subsequently at -140 °C. Thawing pericytes was performed as described in **Section 2.2** but the cells were resuspended in DMEM, high glucose, pyruvate with 10% FBS and plated onto a gelatin-coated 6-well well. However, survival after a freeze-thaw cycle was typically poor.

2.12 Smooth muscle cell differentiation and culturing

The smooth muscle cell differentiation was developed in collaboration with Tom Webb, University of Leicester, UK. The hiPSCs were split on Geltrex at a density of 350k/well exactly the same as in the endothelial cell differentiation. On the first 3 days, the media was changed to 3 ml of MIM per 6-well. On days 5 and 7, the media is changed with 3 ml of APEL2 supplemented with 50 ng/µl $VEGF_{165}$ and 25 ng/µl BMP4 (Peprotech #AF 120-05ET). The cells were split at 1:6 ratio on day 8. To this effect, the cells were washed with PBS and then incubated with Trypsin/EDTA for 3-4 minutes until the cells begin to detach. The Trypsin/EDTA was aspirated and the cells were washed off with smooth muscle cell growth medium 2 (SMC2, Promocell #C-22062) containing 10 ng/mL PDGF-BB (Peprotech #100-14B) and 2 ng/mL TGFß1 (Peprotech #AF-100-21C). The cells were transferred in the same media into 6-well collagen IV-coated plate. The cells were cultured at least until day 14 before being used for experiments and fed 1-2 times per week with SMC2 medium containing 10 ng/mL PDGF-BB and 2 ng/mL TGFß1. Maintenance splitting of smooth muscles cells was performed exactly the same as the split on day 8 but at the desired ratio. To freeze smooth muscle cells, they were first detached with Trypsin/EDTA as described above and then washed off with smooth muscle cell freeze medium (SMC2 with 10% DMSO) and stored at -80° C for 24 hours and subsequently at -140 °C. Thawing smooth muscle cells was performed as described in **Section 2.2** but the cells were resuspended in SMC2 with PDGF-BB (10 ng/mL) and TGFß1 (2 ng/mL) and plated onto collagen IV-coated 6-well wells.

2.13 Immunofluorescence stainings

Endothelial cells were split with Trypsin/EDTA (**Section 2.10**) onto acid-etched (**Section 2.9.7**) and fibronectin coated coverslips in ECM2 medium supplemented with 50 ng/µl $VEGF_{165}$. The cells were grown until they became confluent at which point they were washed with PBS and fixed with 4% PFA for 10 minutes at room temperature. For pluripotency stainings, cells were prepared and fixed according to **Section 2.9.7**. Following fixation, cells were then washed 3 times for 5 minutes in PBS at room temperature and incubated in blocking solution containing 3% donkey serum (Jackson ImmunoResearch #017-000-121), 0.1% Triton-X-100 (Thermo Fisher #85111), and 0.02% NaN_3 (Sigma-Aldrich #S2889) for at least 1 hour at room temperature.. Next, cells were incubated overnight at 4 °C in primary antibodies (**Table 2.19**) diluted in blocking solution. To remove excess antibody, cells were washed 3 times for 5 minutes with PBS. Subsequently, cells were incubated with secondary antibodies diluted in blocking solution (**Table 2.20)** and 4',6-diamidino-2-phenylindole (DAPI, Thermo Fisher

#D1306) diluted 1:50,000 in blocking solution for 2 hours in the dark. Excess antibody was removed again by washing 3 times for 5 minutes with PBS and the coverslips were mounted onto glass slides (Thermo Fisher #J1800AMNZ) in Fluoromount-G (Thermo Fisher #00-4958-02). Endothelial cell immunofluorescence stainings were imaged with a Zeiss LSM 880 confocal microscope using Airyscan and a 40X objective on Zen block software and hiPSCs pluripotency stainings were imaged with a fluorescence microscope (Zeiss Axio Observer Z.1). All 2D images were processed using Fiji (Schindelin et al., 2012).

To stain 3D cultures, the cells were rinsed with 120 µl of PBS applied to the media ports. All solutions were applied like a normal feed in **Section 2.16**. Cultures were then fixed with 4% PFA for 15 minutes at room temperature. Excess PFA was washed away with PBS and the cultures were permeabalized with 0.1% Triton-X-100 in H_2O for 5 minutes at room temperature. Cultures were blocked with 2% BSA blocking buffer in PBS for 30 minutes at room temperature and incubated with primary antibodies diluted in 2% BSA blocking buffer overnight at 4 °C. PBS was used to wash the cultures twice for 10 minutes at room temperature followed by incubation with secondary antibodies (except for DAPI) diluted in 2% BSA blocking buffer overnight at 4 °C in the dark. Two washes for 10 minutes with PBS were then performed followed by incubation with DAPI (1:1000) in 2% BSA blocking buffer for 15 minutes at room temperature in the dark. Excess DAPI was removed with two 10 minute washes with PBS and the cultures were imaged with the 10X and 40X objectives of a Zeiss LSM 880 confocal microscope using Zen block software. Image analysis was done with Zen blue edition software.

Primary antibody	Species	Manufacturer	Reference #	Dilution 2D	Dilution 3D
NANOG	Rabbit	Cell Signaling	4903	1:500	NA
OCT-4	Rabbit	Stemgent	S090023	1:500	NA
SSEA4	Mouse	Abcam	ab16287	1:500	NA
TRA-160	Mouse	Millipore	MAB4360_2016625	1:500	NA
ZO-1	Mouse	Thermo Fisher	33-9100	1:150	NA
Type IV collagen	Goat	Southern Biotech	1340-01	1:500	1:200
COL4A1	Rat	Chondrex	7070	NA	1:60
COL4A2	Rat	Chondrex	7071	1:100	NA
CD31	Rabbit	Abcam	ab32457	NA	1:200

Table 2.19 Primary antibodies

Secondary antibody	Species	Manufacturer	Reference #	Dilution 2D	Dilution 3D
Anti-mouse Alexa Fluor Plus 488	Donkey	Thermo Fisher	A32766	1:500	1:500
Anti-rabbit Alexa Fluor 647	Goat	Thermo Fisher	A27040	1:500	NA
Anti-goat Cy3	Donkey	Jackson Laboratories	705-165-147	1:500	1:500
Anti-rat Alexa Fluor 647	Goat	Thermo Fisher	A21247	1:500	1:250

Table 2.20 Secondary antibodies

2.14 Gene expression analysis by qPCR

For qPCR experiments analyzing mRNA transcript levels, RNA was first extracted using a NucleoSpin RNA/Protein Kit (Macherey-Nagel #740993) according to the manufacturer's instructions. RNA was then measured using a spectrophotometer and stored at -80 °C or directly used for cDNA synthesis. For cDNA synthesis, a High-Capacity cDNA Reverse Transcription Kit (Thermo Fisher #4368814) without RNAase inhibitor was used according to manufacturer's instructions. Different amounts of cDNA were synthesized for each experiment depending on amount of available RNA (**Table 2.21**). With the exception of experiment #1 (6 ng/µl) the cDNA for every experiment was diluted to 1 ng/µl for qPCR. The qPCR reactions were prepared according to **Table 2.22** in a LightCycler 480 Multiwell Plate 384 (Roche #04729749001). The qPCR was performed in Roche LightCycler 480 according to the program

in **Table 2.23**. The melting curves were examined to ensure a single product was amplified for each primer combination and the Cp values for each reaction were then exported. Triplicates for each condition were performed and the resulting Cp values were averaged before 2^{-Cp} was calculated. This value was normalized to the housekeeping gene.

#	Experiment	Primers used	cDNA
1	COL4A1 and COL4A2 in KO ECs (**Figure 3.26**)	COL4A1 B: OL2806/OL2808; COL4A1 E: OL2810/OL2811 ; COL4A2 G: OL2816/OL2817 ; RPL22:	250 ng
2	qPCR panel of KO ECs on gelatin (**Figure 3.31**)	ITGB1: OL3031/OL3032; TIMP1: OL3035/OL3036; FN1: OL3039/OL3040; LAMC1: OL3043/OL3044; HSPG2: OL3047/OL3048; Cldn-5: OL3055/OL3056; ZO-1: OL3057/OL3058; Occludin: OL3059/OL3060; VE-Cadherin: OL3061/OL3062; CD31:OL3063/OL3064; EMC7: OL3065/OL3066	200 ng
3	qPCR TJs and AJs in KO ECs on fibronectin (**Figure 3.31**)	Cldn-5: OL3055/OL3056; ZO-1: OL3057/OL3058; Occludin: OL3059/OL3060; VE-Cadherin: OL3061/OL3062; CD31:OL3063/OL3064; EMC7: OL3065/OL3066	100 ng
4	COL4A1 and COL4A2 expression of (c.*35C>A) KI in neurovascualr cell types (**Figure 3.33**)	COL4A1 E: OL2810/OL2811 ; COL4A2 G: OL2816/OL2817; EMC7: OL3065/OL3066	85 ng
5	Comparison of collagen IV in hiPSC-derived neurovascular cell types (**Figure 3.34**)	COL4A1 E: OL2810/OL2811 ; COL4A2 G: OL2816/OL2817; EMC7: OL3065/OL3066	85 ng
6	COL4A1 and COL4A2 in WT and COL4A1^{G755R} DSM KI clone C3 (**Figure 3.35**)	COL4A1 E: OL2810/OL2811 ; COL4A2 G: OL2816/OL2817; EMC7: OL3065/OL3066	200 ng

Table 2.21 Primers used and cDNA synthesized by experiment

qPCR master mix	1 reaction (µl)
QuantiNova SYBR Green PCR Master Mix (Qiagen #208054)	6
Forward primer (10µM)	0.24
Reverse primer (10µM)	0.24
Ultrapure H_2O (Thermo Fisher #10977035)	3.52
cDNA	2

Table 2.22 qPCR master mix composition

Step	Temperature (°C)	Time (sec)	Cycles	Analysis mode
Denaturation	95	10 min	1	None
Amplification	95	30	40	Quantification
	60	1 min		Acquisition mode: single at 60°C
Melting curve	95	10	1	Melting curve
	60	10		
	95	Continuous (5 acquisitions/°C)		
Cooling	40	Forever	1	None

Table 2.23 LightCycler 480 qPCR program

2.15 TEER measurements with cellZscope

Cell culture transwells for a 24-well plate (Corning #353095) were coated with either gelatin or fibronectin as described in **Section 2.10**. In the bottom pot, 800 µl of ECM2 was added, the coated transwell was placed in the pot, and 400 µl of ECM2 was added on top of the transwell. The CellZscope was placed in the incubator and the reference program was run overnight to determine reference values for that transwell/coating/medium combination (if not previously performed). After a reference values were determined, endothelial cells were split with Trypsin/EDTA, collected in a 15 ml conical tube and counted as previously described. In the bottom pot of the CellZscope from Nanoanalytics, 800 µl of fresh medium (ECM2 with 50 ng/µl $VEGF_{165}$) was added. The coating solution was removed from the transwell and it was placed in the pot. Then, 20k endothelial cells were diluted to 400 µl in ECM2 with 50 ng/µl $VEGF_{165}$ and added to the top of the transwell. The CellZscope was placed in the

incubator and the measurement was started with the appropriate reference values. On the next day, the media was changed to ECM2 without $VEGF_{165}$.

2.16 Generation of 3D-cultures

This protocol was adapted from Campisi et al. (2018). Fibrinogen from bovine plasma (Sigma-Aldrich #F8630) was dissolved in PBS without calcium and magnesium (Sigma-Aldrich #D8537) at a concentration of 6 mg/ml, incubated at 37 °C for one hour and filtered with a 0.2 µm pore filter (Integra #156608) before being stored at -20 °C. Thrombin (Sigma-Aldrich #T7326) was dissolved in 0.1% BSA in H_2O at a concentration of 100 U/ml and stored at -20°C.

On day 1, fibrinogen (6 mg/ml) and thrombin (100 U/ml) solution was thawed on ice. Then, 250 µl of ECM2 medium was mixed with 22.5 µl of thrombin solution and kept on ice to create the suspension medium. Endothelial cells were split with Trypsin/EDTA (**Section 2.10**) and collected in conical 15 ml tubes. The cells were counted as previously described and 1.2M cells were centrifuged at 162g for 4 minutes. After the supernatant was aspirated, the cells were resuspended in 30 µl of suspension medium (ECM2 + thrombin) and placed back on ice. Then 10 µl of cell suspension was combined with 20 µl of suspension media (containing no cells) to make the diluted cell suspension. Next 10 µl of fibrinogen was mixed with 10 µl of diluted cell suspension and 10 µl of this fibrinogen-containing solution was quickly injected into the middle port of an AIM Biotech 3D culture chip (Tebubio #DAX-TrialKit). The injection was done quickly to avoid premature polymerization of the gel. After injection, the gel polymerized for 15 minutes at room temperature and the reservoirs in the AIM chip holder (Tebubio #Hol-2) were filled with sterile H_2O. Fibronectin (Sigma #F4759) was diluted in ECM2 to 60 µg/ml and 15 µl was injected into each media port before the cultures were incubated for 1 hour at 37 °C. After incubation, 70 µl of ECM2 with 50 ng/µl $VEGF_{165}$ was added to the left media ports and 50 µl to the right media ports. Daily feeds were performed by aspirating the media from the ports without directly applying suction to the channel followed by addition of 70 µl of medium to the left channels and 50 µl to the right channels.

On day 3, the side channels were seeded with endothelial cells. To this effect, endothelial cells were split from 2D 6-well plates with Trypsin/EDTA, collected, and counted as described above. The cells were centrifuged at 162g for 4 minutes and resuspended in ECM2 with 50 ng/µl $VEGF_{165}$ at a concentration of 1.5M cells/ml and placed on ice. The media was aspirated from the media ports and 30 µl of fresh medium was added to the left-side media ports before 10 µl of cell suspension was injected into each side channel. The cell distribution was examined under the microscope and additional cell suspension was added as needed before the chips were left at room temperature for 5 minutes for the cells to attach. Then, the media was removed from every port and 50 µl of fresh medium was applied to every media port before 10 µl of cell suspension was injected to every left-side port and the H_2O was removed from the holder. After examining the cells under the microscope to ensure enough cell suspension was added, the chips and holder were placed inside the incubator upside down for 90 minutes so that the cells would attach to the top of the channel. Following attachment, all media was aspirated and replaced with fresh medium like a normal feed described above and sterile H_2O was added to the holder. The cells were then placed back in the incubator. On day 4, seeding of the side channels was repeated if cell coverage was not complete. Otherwise, only a normal feed was performed. From day 5 onward, the daily feeds were done with ECM2 without $VEGF_{165}$ supplementation.

2.16.1 Perfusion of 3D-cultures

3D microfluidic cultures were generated and seeded as described above with the exception that the gel ports were sealed with adhesive tape after polymerization. The day before perfusion, a yellow perfusion set (Ibidi #10965) was filled to the 2 ml mark in each syringe with ECM2 with 1:100 Penicillin-streptomycin (Thermo Fisher #15140-122) and placed in the pump system (Ibidi #10902). The media was circulated overnight to remove air bubbles and equilibrate the media to the incubator. The next day (day 5) Luer lock adapters (Sigma-Aldrich #LUC01) were filled with medium and carefully fitted into the media ports to apply as little direct pressure to the culture as possible. Diagonal media ports were then capped with a male Luer lock cap. The other diagonal media ports were connected to the yellow perfusion set. Using the PumpControl software, the media was perfused with a pressure of 2 mbar for the first day and 3 mbar on the following days.

2.17 List of primers

Primer ID	Name	Sequence
BCL2L1_F	BCL2L1 CNV assay F Set 1	GGTGGTTGACTTTCTCTCCTAC
BCL2L1_R	BCL2L1 CNV assay R Set 1	TCTCCGATTCAGTCCCTTCT
OL1240	D1S80-F_IW	GAAACTGGCCTCCAAACACTGCCCGCCG
OL1241	D1S80-R_IW	GTCTTGTTGGAGATGCACGTGCCCCTTGC
OL2092	Col4A1_Ex28_fw1	AGTCACAGGTGGACCAAAGG
OL2093	Col4A1_Ex28_rv1	CAAAGGGTGAACCAGGAAAA
OL2094	Col4A1_Ex29_fw1	AGAAGGGTCATGGAGGGAAT
OL2095	Col4A1_Ex29_rv1	GGCATCTCTGGGCAAGACTA
OL2096	Col4A1_Ex30_fw1	GGCCTCTAAGATTTGCATCG
OL2097	Col4A1_Ex30_rv1	TCTGTGCTTTGGGGATTTTC
OL2277	RPL22_Frw	CACGAAGGAGGAGTGACTGG
OL2278	RPL22_Rev	TGTGGCACACCACTGACATT
OL2301	Col4A1_gRNA15rv_CFD_OT1_F1_JAK	CAGTGAATGGGGTCAGGACT
OL2302	Col4A1_gRNA15rv_CFD_OT1_R1_JAK	AGGCCTGAAGTGCTCAGCTA
OL2303	Col4A1_gRNA15rv_CFD_OT2_F1_JAK	GTTATCGCCAGGAGCTGAAG
OL2304	Col4A1_gRNA15rv_CFD_OT2_R1_JAK	GGCTTAACAATCCGAAAGGA
OL2305	Col4A1_gRNA15rv_CFD_OT3_F1_JAK	TGCTCTGCCAGCAGAATAAA
OL2306	Col4A1_gRNA15rv_CFD_OT3_R1_JAK	CTCAGACTTCCAGCCTCCAG
OL2307	Col4A1_gRNA15rv_CFD_OT4_F1_JAK	AAGGGAATCAAATGGGGAGT
OL2308	Col4A1_gRNA15rv_CFD_OT4_R1_JAK	ACATAAACAGGCCCCTCCTC
OL2309	Col4A1_gRNA15rv_CFD_OT5_F1_JAK	TCCCTCCCTCCTTTTTGAGT
OL2310	Col4A1_gRNA15rv_CFD_OT5_R1_JAK	AGAAGGAGGACCCAAACCAT
OL2311	Col4A1_gRNA15rv_CFD_MIT1_F1_JAK	CCCGGAGTATTCATGGTACG
OL2312	Col4A1_gRNA15rv_CFD_MIT1_R1_JAK	TGTCAGGAATGCTTGAATGG
OL2313	Col4A1_gRNA15rv_CFD_MIT2_F1_JAK	GAATGGACCAGCCCTGACTA
OL2314	Col4A1_gRNA15rv_CFD_MIT2_R1_JAK	TGGGAGTTATCGTCGGAGTC
OL2315	Col4A1_gRNA15rv_CFD_MIT3_F1_JAK	CATGGTTAGCAAGTGCAGGA
OL2316	Col4A1_gRNA15rv_CFD_MIT3_R1_JAK	GTTGGCAGAGGACTCTGAGG
OL2317	Col4A1_gRNA15rv_CFD_MIT4_F1_JAK	CAGCTCTAGGTGGGCTTTGT
OL2318	Col4A1_gRNA15rv_CFD_MIT4_R1_JAK	GGGTCTTTTCCCCAAGTGAT
OL2319	Col4A1_gRNA15rv_CFD_MIT5_F1_JAK	TCACTCTGGGGAAACACAAA
OL2320	Col4A1_gRNA15rv_CFD_MIT5_R1_JAK	GAGTATGGGGAAATCCGACA
OL2378	rs12864958_F1_JAK	GCTTCTGCTTCTGTGGCTCT
OL2379	rs12864958_R1_JAK	TTCTTCCCTGGAGGTGAGTG
OL2380	rs617478_F1_JAK	GGAACCAGAGCAGAGCAAAC
OL2381	rs617478_R1_JAK	CCATGGATTTTTGGACCTTG
OL2421	miR-29_F1_JAK	TGCCATTTGGTATGCCACTA
OL2422	miR-29_R1_JAK	CTGTGAGATGATGGCCAATG
OL2747	miR-29_gRNA57rv_CFD_OT1_F1_JAK	CAAATGTCACCACCCTCCCA
OL2748	miR-29_gRNA57rv_CFD_OT1_R1_JAK	GTCACTCGCTCCCCAAATCT

OL2749	miR-29_gRNA57rv_CFD_OT2_F1_JAK	AATGTCACCACCGTCCCATC
OL2750	miR-29_gRNA57rv_CFD_OT2_R1_JAK	ACCCCAGCTGGTATCTCAGT
OL2751	miR-29_gRNA57rv_CFD_OT3_F1_JAK	TTCCTGGCTGTGTGACAAGG
OL2752	miR-29_gRNA57rv_CFD_OT3_R1_JAK	AGGCTGGAAGGGAACATTCG
OL2753	miR-29_gRNA57rv_CFD_OT4_F1_JAK	AGGCATTGCTAGGAACCAGG
OL2754	miR-29_gRNA57rv_CFD_OT4_R1_JAK	ACCTCTCATCATCAGCTTAGGC
OL2755	miR-29_gRNA57rv_CFD_OT5_F1_JAK	AGCCTTCAGGGGTTCCTTTT
OL2756	miR-29_gRNA57rv_CFD_OT5_R1_JAK	TGACATTGGCTTGCTCACTTG
OL2759	miR-29_gRNA57rv_MIT_OT2_F1_JAK	CAACCCCCAGACACCATCTC
OL2760	miR-29_gRNA57rv_MIT_OT2_F1_JAK	ACATTGCTGCTACCCTCACC
OL2765	miR-29_gRNA57rv_MIT_OT5_F1_JAK	CCAGAGCCCCTGATCTCTCT
OL2766	miR-29_gRNA57rv_MIT_OT5_F1_JAK	TTACGTGCACCAGACCACTC
OL2792	miR-29_gRNA57rv_MIT_OT1_F2_JAK	AGGCCAAATCCTGAGGATACA
OL2793	miR-29_gRNA57rv_MIT_OT1_R2_JAK	TGGGCAACAGAGTAAGATGGT
OL2794	miR-29_gRNA57rv_MIT_OT3_F2_JAK	GCACCCGGCCTATTATGACA
OL2795	miR-29_gRNA57rv_MIT_OT3_R2_JAK	CAGCTGTGTCCATCATCAGGT
OL2796	miR-29_gRNA57rv_MIT_OT4_F2_JAK	GCACCCGGCCTATTATGACA
OL2797	miR-29_gRNA57rv_MIT_OT4_R2_JAK	TCCCAAGAGGACATAGGTACCA
OL2806	Col4A1_qPCR_F2	GAGGAGTTGGATTCCCAGGC
OL2808	Col4A1_qPCR_R2	TGGTTCACCCTTTGGACCTG
OL2810	Col4A1_qPCR_F3	GAAGCAGGTCTTCCTGGGAC
OL2811	Col4A1_qPCR_R4	ATTCCATCACTGCCTGGCTC
OL2816	Col4A2_qPCR_F2	TTCATAGGAAGCCGGGGTGA
OL2817	Col4A2_qPCR_R2	TCACCGAAATCACCAGTCGC
OL2921	G755R_gRNA45rv_CFD_OT1_F1_JAK	TTGAGAACAGGCCCCCAGAT
OL2922	G755R_gRNA45rv_CFD_OT1_R1_JAK	ACAGCAAGCCAGTGATAAGCA
OL2923	G755R_gRNA45rv_CFD_OT2_F1_JAK	TGGGAAGGGAAATGGAGGAGA
OL2924	G755R_gRNA45rv_CFD_OT2_R1_JAK	GGTTTGTGGAAAAGGGCAGC
OL2925	G755R_gRNA45rv_CFD_OT3_F1_JAK	CCATTTCCCATCACCCGAGT
OL2926	G755R_gRNA45rv_CFD_OT3_R1_JAK	GAGACTCAGGCCACAGCATT
OL2927	G755R_gRNA45rv_CFD_OT4_F1_JAK	AAGCCCTCCTAGGTCTCCTG
OL2928	G755R_gRNA45rv_CFD_OT4_R1_JAK	GAGTGTGGAAGGAACTGGGG
OL2929	G755R_gRNA45rv_CFD_OT5_F1_JAK	CTCCAGTGAGTGACTCCAGC
OL2930	G755R_gRNA45rv_CFD_OT5_R1_JAK	AGATGTTCCACAGTGCTCCT
OL2931	G755R_gRNA45rv_MIT_OT2_F1_JAK	TGTCCTGCCCACACAGTTTT
OL2932	G755R_gRNA45rv_MIT_OT2_R1_JAK	ACGGATAGTTGGAAGCTGGC
OL2933	G755R_gRNA45rv_MIT_OT3_F1_JAK	GGTTCCTGCCTCATGCTGAT
OL2934	G755R_gRNA45rv_MIT_OT3_R1_JAK	CAGTTTGCAACTTCCGTGGG
OL2935	G755R_gRNA45rv_MIT_OT4_F1_JAK	GTCCATAGGCAGCCATGGTT
OL2936	G755R_gRNA45rv_MIT_OT4_R1_JAK	CCCTGCCTCTTCTGAGTTGG
OL2937	G755R_gRNA45rv_MIT_OT5_F1_JAK	GTCACAGCTGCAGGAGGC
OL2938	G755R_gRNA45rv_MIT_OT5_R1_JAK	GGGTTCTGGTCTCCTGGCA
OL3031	ITGB1 Comb1 Fw_JAK	TGCTCAAACAGATGAAAATAGATGT
OL3032	ITGB Comb1 Rv_JAK	GTGCACCACCCACAATTTGG
OL3035	TIMP1 comb1 fw_JAK	CTCGTCATCAGGGCCAAGTT
OL3036	TIMP1 comb1 rv_JAK	CCCTAAGGCTTGGAACCCTT
OL3039	FN comb1 fw_JAK	ATCGAGGAAACCTGCTCCAG
OL3040	FN comb1 rv_JAK	GATCCGCTCGATGTGGTCTG
OL3043	LAMC1 comb1 fw_JAK	TTGCTGTAGGTGGCAGATGT
OL3044	LAMC1 comb1 rv_JAK	TGTTTGCAATTACACACCAGCT
OL3047	HSPG2 comb1 fw_JAK	AGCATCTCAGGAGACGACCT
OL3048	HSPG2 comb1 rv_JAK	TGAGGGCTGTACTCGATGGA
OL3055	Claudin5_comb1_F_JG	GTGGTGTCACCTGAACTGGG
OL3056	Claudin5_comb1_R_JG	AGCCTCTGGCAGCTCTCAAT
OL3057	ZO1_comb1_F_JG	CCGCGGAGTTTCGGGTC
OL3058	ZO1_comb1_R_JG	TCCTCCATTGCTGTGCTCTTG
OL3059	Occludin_ Campisietal _F_JG	ACAAGCGGTTTTATCCAGAGTC
OL3060	Occludin_ Campisietal _R_JG	GTCATCCACAGGCGAAGTTAAT
OL3061	VECadh_comb2_F_JG	TGGTGGAAGCGCGAGAT
OL3062	VECadh_comb2_R_JG	AAATGTGTACTTGGTCTGGGT
OL3063	CD31_ Campisietal _F_JG	ATTGCAGTGGTTATCATCGGAGT
OL3064	CD31_ Campisietal _R_JG	CTGGTTGTTGGAGTTCAGAAGTG

OL3065	hEMC7_F	AAAGGAGGTAGTCAGGCCGT
OL3066	hEMC7_R	GTTGCTTCACACGGTTTTCCA

Table 2.24 List of all primer IDs, names, and sequences according to the Paquet database

Chapter 3 Results

Three mutations in COL4A1 that cause monogenic cSVD are investigated in this thesis. Each mutation has a distinctive impact on COL4A1. As described in the introduction, the frameshift mutation (ClinVar: VCV000161440.4) reduces COL4A1 in patient fibroblasts, the PADMAL 3'-UTR (c.*35C>A) mutation (ClinVar: VCV000689432.1) increases COL4A1 in patient fibroblasts, and the COL4A1^{G755R} KI (ClinVar: VCV000161974.16) alters the triple helix domain potentially impacting the protein structure and/or interactions (**Section 1.5**). In this chapter, the first two aims of this thesis are addressed by editing each of the three mutations into hiPSCs and performing all of the necessary quality controls on the generated cell lines. Finally, the expression of collagen IV in neurovascular cell types derived from hiPSCs carrying these mutations is investigated to address the final aim of this thesis.

3.1 COL4A1 KO genome editing in hiPSCs (ClinVar: VCV000161440.4)

To successfully generate a COL4A1 KO, the region to target with CRISPR/Cas9 must be strategically selected. Typically, a gene KO strategy employs an sgRNA to target one of the first few exons. However, COL4A1 is an enormous gene with 52 exons. Patients-derived fibroblasts from two families with COL4A1 frameshifts in the middle of COL4A1 **(Figure 3.1 A-B)** exhibit nonsense-mediated decay (NMD) of the mRNA and decreased the COL4A1 protein expression **(Figure 3.1 C)**. Since a frameshift in this

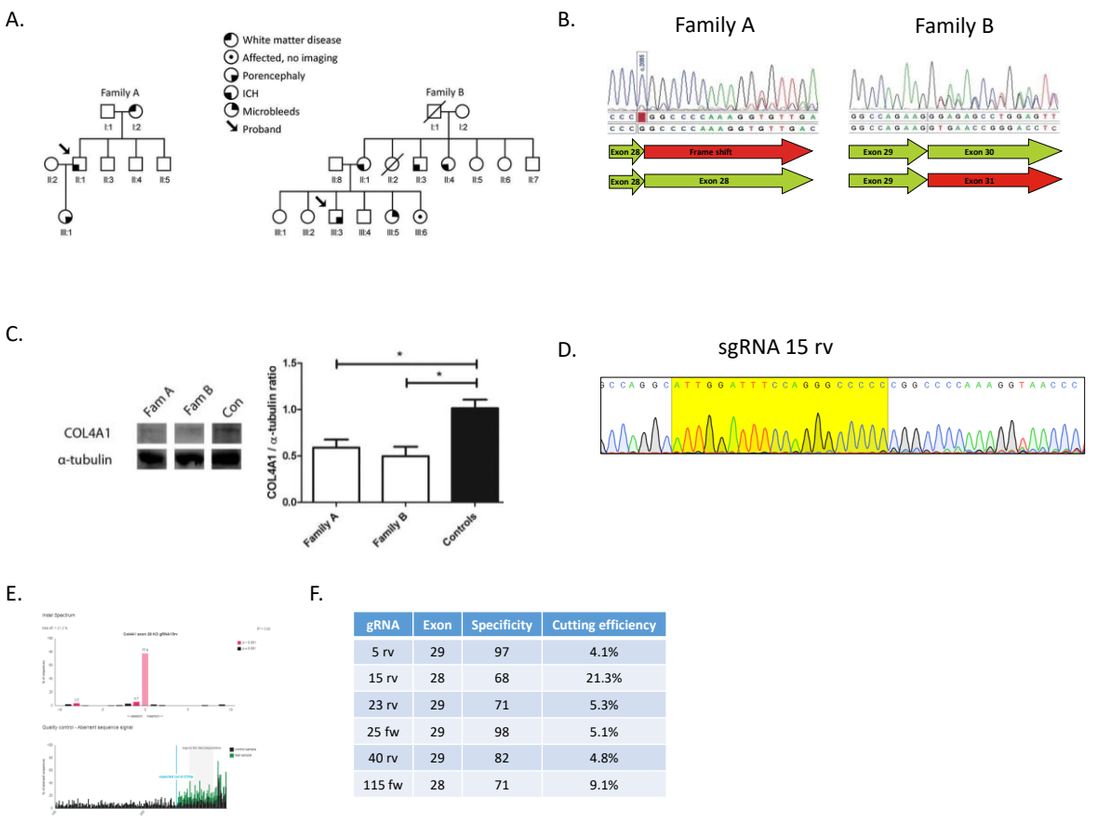

gRNA	Exon	Specificity	Cutting efficiency
5 rv	29	97	4.1%
15 rv	28	68	21.3%
23 rv	29	71	5.3%
25 fw	29	98	5.1%
40 rv	29	82	4.8%
115 fw	28	71	9.1%

Figure 3.1. COL4A1 KO sgRNA design. (A) Family pedigrees of two families with penetrant cSVD. Note that several distinct cSVD MRI features are present in both families. **(B)** Sequences of frameshift mutations present in family A and B obtained after cycloheximide treatment of patient fibroblasts to prevent mRNA nonsense-mediated decay. **(C)** Analysis of COL4A1 in patient fibroblasts. (D) Sequencing reaction from pooled HEK293 cells transfected with sgRNA 15rv. The sgRNA sequence is highlighted in yellow and double peaks can be seen downstream from the sgRNA indicative of Indels present in some cells within the pool. (E) TIDE analysis example for sgRNA 15rv. The estimated cutting activity and prediction of contribution of each Indel are shown at the top and the region of decomposition is shown at the bottom. (F) Table of tested sgRNAs with exon, specificity score, and estimated cutting efficiency determined by TIDE analysis shown. Adapted with permission from Lemmens et al., 2013. Copyright © 2012. Oxford University Press. All rights reserved.

region is sufficient to cause haploinsufficiency in patients, six sgRNAs targeting the middle of COL4A1 in exons 28 and 29 were designed and tested for cutting efficiency in HEK293 cells via plasmid delivery (**Figure 3.1 D-F**). TIDE (Tracking of Indels by Decomposition) (Brinkman et al., 2014) analysis was performed to estimate the cutting efficiency of each sgRNA **(Figure 3.1 E-F)**. The highest cutting efficiency was observed for sgRNA 15 rv. However, this guide has a lower specificity score compared to the other sgRNAs making it more prone to edit off-target regions. The specificity scores are calculated by the MIT specificity algorithm given on http://crispor.tefor.net/ with a higher number corresponding to a more specific sgRNA. In general, sgRNAs are excluded with specific scores below 70. However, because sgRNA 15 rv cuts in exon 28 exactly where a frameshift is observed in patients from family A with COL4A1 haploinsufficiency (ClinVar: VCV000161440.4) and the cutting efficiency was the highest, this sgRNA was selected for generating the KO in hiPSCs.

3.1.1 Generation of the COL4A1 KO in hiPSCs

Both plasmid and RNP delivery of Cas9 and sgRNA 15 rv for the COL4A1 KO in hiPSCs were initially tested. The editing efficiencies were analyzed by ICE (Inference of CRISPR Edits) (Conant et al., 2022) **(Figure 3.2 Top)** and resulted in similar editing efficiencies of 63% for RNP delivery and 61% for plasmid delivery. Given that the plasmid delivery system requires a 3-day puromycin selection step and results in sustained Cas9 expression that increases off-target editing potential, RNP delivery of Cas9 machinery was selected. Several-hundred single cell clones were screened from RNP delivered cells by RFLP

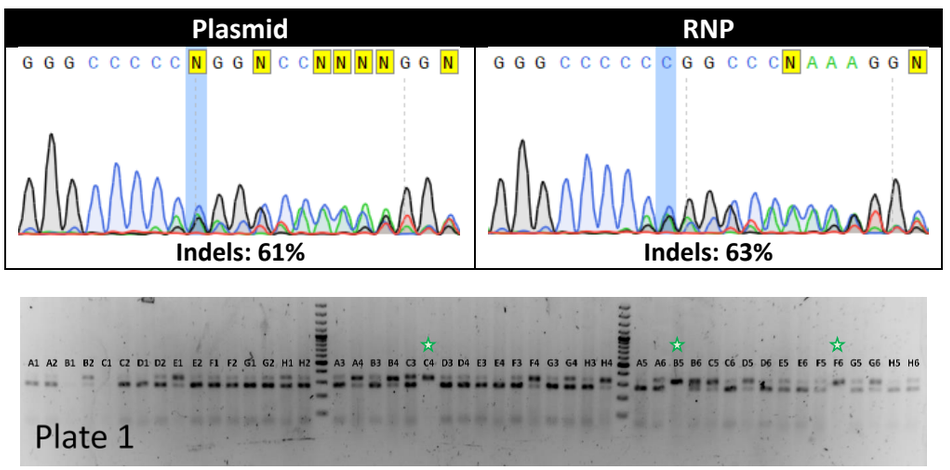

WT	Heterozygous	Homozygous
263/62 bp	325/263/62 bp	325 bp

Figure 3.2 COL4A1 KO generation in hiPSCs. (Top) Comparison of plasmid vs RNP delivery of Cas9 machinery**.** The blue highlighted base is the deleted base in Family A from **Figure 3.1. (Bottom)** Example of RFLP clone screening of clones edited with sgRNA 15 rv. The table gives the expected product length for each genotype. Green stars indicate the homozygous clones.

(Restriction Fragment Length Polymorphism) analysis **(Figure 3.2 Bottom),** and Sanger sequencing confirmed 13 clones with frameshifts on both alleles.

3.1.1.1 Quality controls allow excluding clones with deleterious side effects of CRISPR editing

The 13 KO clones were first analyzed for a BCL2L1 triplication, one of the most common side effects of single-cell cloning in iPSCs **(Figure 3.3).** There are two distinct populations: Clones with BCL2L1 copy numbers greater than 2.5 were considered to harbor a triplication at this locus and the 5 clones with BCL2L1 values slightly lower than 2 were assumed to have two copies of BCL2L1. These 5 clones were

then analyzed for off-target editing by sequencing the top 10 *in silico* predicted off-target regions for sgRNA 15 rv. Initially, an off-target was discovered in clone P1D2 **(Figure 3.4 A)**. Testing the remaining

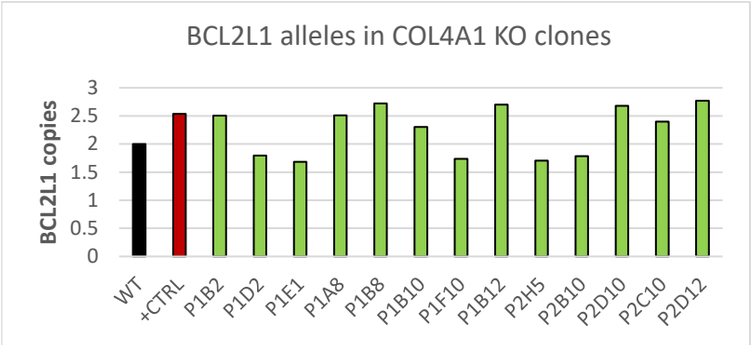

Figure 3.3 BCL2L1 assay of COL4A1 homozygous KO clones. Quantification of BCL2L1 copy numbers of 15 COL4A1 KO clones. The unedited WT (black) is set to 2 copies. The positive control (red) was an independently generated single cell clone that has given 3 BCL2L1 copies in this assay in previous experiments. The clones are shown in green. Duplicates were performed for each sample and averaged.

A.

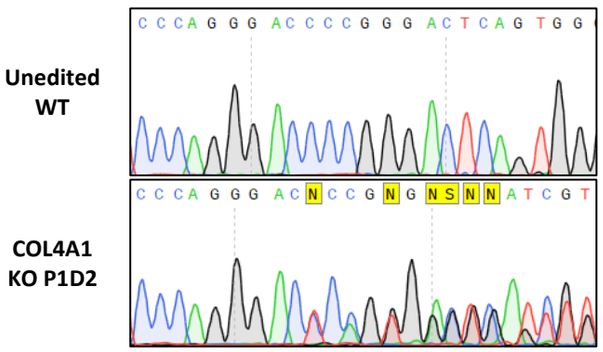

B.

	P1D2	P1E1	P1F10	P2B10	P2H5
CFD 1					
CFD 2	X				
CFD 3		X		X	
CFD 4					
CFD 5					
MIT 1		X		X	
MIT 2					
MIT 3					
MIT 4					
MIT 5			X		

Figure 3.4 Detected off-target effects in clones edited with sgRNA 15 rv. (A) Off-target CFD2 in COL4A1 KO clone P1D2. **(B)** Results of off-target sequencing in COL4A1 homozygous KO clones. Green boxes indicate a clean sequencing trace matching the WT. Red boxes with an 'X' indicate detected off-target editing.

4 clones illustrated widespread off-target activity by sgRNA 15 rv with only clone P2H5 free from off-target effect detection **(Figure 3.4 B)**.

3.1.1.2 High fidelity Cas9 to generate additional COL4A1 KO clones with decreased off-target potential

With only one clone without a BCL2L1 triplication or an off-target effect, more KO clones needed to be generated in order to work with multiple KO clones. Moreover, since the haploinsufficiency mutation in patients is heterozygous, it would be valuable to generate heterozygous KO clones that exactly mimic the patient genotype. To mitigate off-target effects, a high-fidelity R691A Cas9 variant with higher specificity (Vakulskas et al., 2018) complexed to sgRNA 15 rv was electroporated to hiPSCs. ICE analysis of the pooled cells indicated editing efficiency of 11%, lower than observed with WT Cas9 used previously. Nevertheless, 200 single cell clones were isolated and screened from this pool of edited cells **(Figure 3.5)**. Sanger sequencing identified 7 homozygous and 8 heterozygous frameshift KO clones.

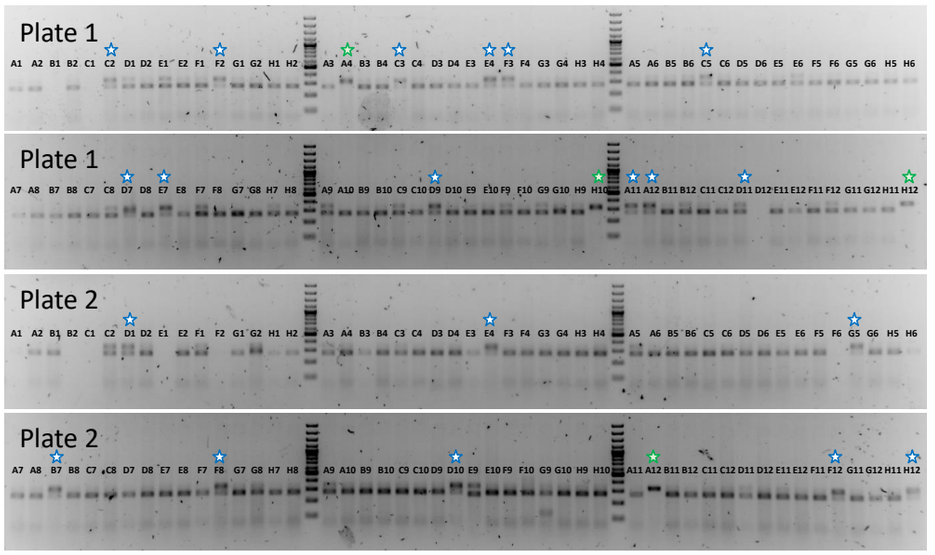

Figure 3.5. RFLP analysis of HiFi Cas9/sgRNA 15 rv edited clones. The clones designated with a star were expanded for further analysis. Green stars indicate a homozygous RFLP genotype and blue stars indicate heterozygous in the RFLP screen. (homozygous clones are undigested – 325bp, and heterozygous have 3 products – 325/263/62)

3.1.1.3 Quality controls for HiFi edited KO clones

The HiFi-edited KO clones were first analyzed for a BCL2L1 triplication **(Figure 3.6).** Again, there are two distinct populations in this assay and the five clones (P1D9, P2H12, P1H10, P1A11, and P1H12) in the lower population are determined to have normal BCL2L1 copy numbers. P1C5 was the only clone

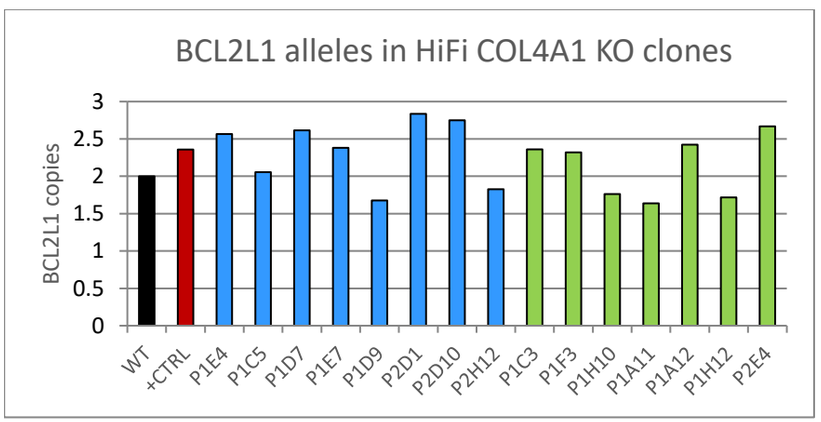

Figure 3.6. BCL2L1 assay of COL4A1 homozygous KO clones edited with HiFi Cas9. Quantification of BCL2L1 copy numbers of 7 homozygous (green) and 8 heterozygous COL4A1 KO clones (blue). The unedited WT (black) and is set to 2 BCL2L1 copies. The positive control (red) was an independently generated single cell clone that has given 3 BCL2L1 copies for this assay in previous experiments. Duplicates were performed for each sample and averaged.

not clearly in one of these populations, but sequencing freshly extracted gDNA revealed it was a mixed clone and it was discarded. Off-target sequencing at the top 10 predicted off-target regions in the HiFi edited clones did not reveal a single off-target effect in the 5 tested clones. The occurrence of OnTEs were examined next by qgPCR and SNP genotyping according to Weisheit et al. (2021) **(Figure 3.7)**. Only clone P1H12 could potentially have lost an on-target allele because it seemingly has the same Indels on both alleles. The other clones with differentially edited alleles have both alleles visible on the genotyping sequencing reaction. The qgPCR shows that there are no clones with aberrations to an on-target allele. Furthermore, SNP genotyping did not reveal any LOH events in any clone. Next, DNA

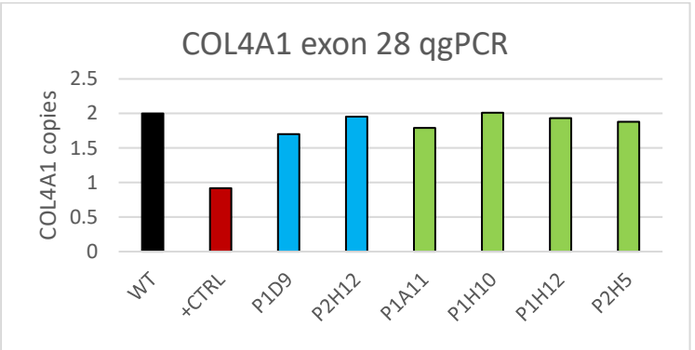

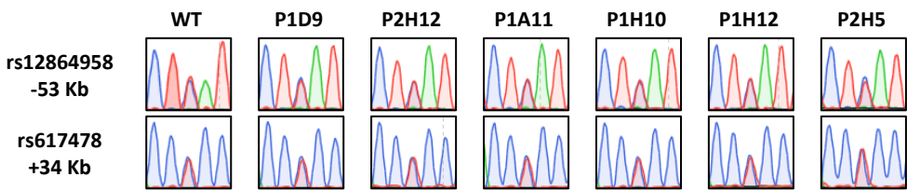

Figure 3.7 Analysis of OnTEs in COL4A1 KO clones. **(Top)** A COL4A1 exon 28 qgPCR was performed. The unedited WT clone (black) is set to 2 copies. The positive control (red) previously gave 1 exon 28 copy with this assay. Two heterozygous clones (blue) and four homozygous clones (green) were tested. Duplicates were performed for each sample and averaged. **(Bottom)** Nearby SNPs were genotyped in the unedited WT and KO clones.

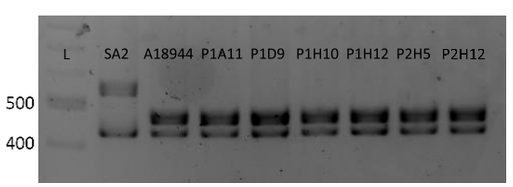

Sample ID	Chr	Start	End	Size	Value
P2H5	7	132641519	133191127	549608	3
P2H5	23	153764528	154916845	1152317	3
P1D9	7	132952188	133528090	575902	3
P1D9	12	37605611	38045401	439790	3
P2H12	7	132952188	133500995	548807	3
P2H12	12	37605611	38043740	438129	3
P1H10	7	132952188	133500995	548807	3

Figure 3.8 DNA fingerprinting and karyotyping COL4A1 KO clones. (Left) The 6 COL4A1 KO clones were compared to the parent cell line (A18944) and another WT line (SA2) with a fingerprinting PCR amplifying VNTR D1S80 **(Right)** Detected CNVs larger than 350 Kb in COL4A1 KO clones.

fingerprinting and molecular karyotyping with a SNP microarray were performed **(Figure 3.8)**. Each clone clearly shares the same band pattern as the parent cell line (A18944 WT) and not the SA2 WT line, which is also used in our laboratory. In the molecular karyotyping analysis, CNV events are only considered above a size of 600 Kb to 1 Mb, as this microarray-based assay is dependent on the analysis of a sufficient number of SNPs to be reliable. All clones (P1H12 and P1A11 were not tested) exhibit an approximately 500 Kb triplication in chromosome 7. As this CNV is also present in the unedited cell line and below the size threshold, it was not regarded as problematic. There are additional CNVs present but this does not completely diminish their potential to model COL4A1 cSVD: The triplications on chromosome 12 in clones P1D9 and P2H12 are less than 500 Kb. The 1.1 Mb triplication on chromosome 23 of clone P2H5 is larger than the size threshold and therefore likely real, but the use of both multiple KO/KO clones will ensure any observed phenotypes are driven by the COl4A1 mutation and not a triplicated region of the chromosome. The COL4A1 KO clones were examined for common pluripotency markers by immunofluorescence **(Figure 3.9)**. Each of the tested clones exhibit typical staining of Tra-160 and SSEA4 in the cytoplasm and the transcription factors Nanog and Oct4 in the nucleus.

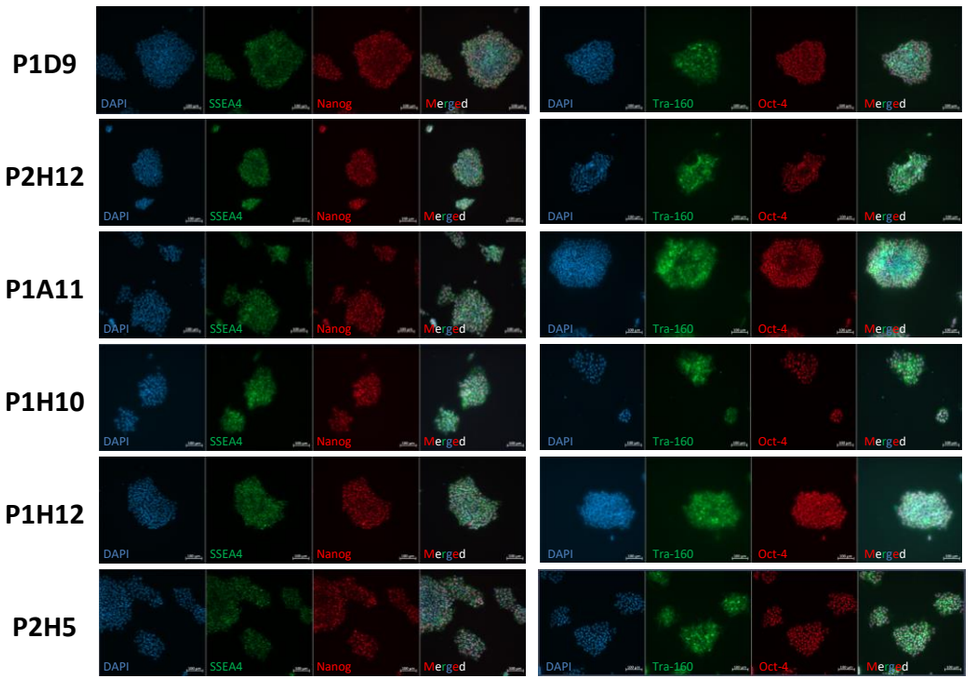

Figure 3.9 Immunofluorescence stainings for pluripotency markers in COL4A1 KO hiPSCs. The pluripotency markers SSEA4, Nanog, Tra-160, and Oct-4 are expressed in all COL4A1 KO hiPSC clones.

3.1.2 COL4A1^{G755R} genome editing in hiPSCs (ClinVar: VCV000161974.16)

The glycine mutation, COL4A1^{G755R}, exchanges a small non-polar glycine for a large polar arginine in the triple helix domain and may inhibit normal triple helix formation. In order to KI this mutation in hiPSCs, sgRNA 45 rv was designed to cut 2bp from the mutation. This sgRNA had a specificity score of 82 which was substantially higher than other sgRNAs cutting close to the mutation and is blocked for re-editing at the most PAM proximal base following successful HDR. Electroporation of an sgRNA 45 rv/HiFi Cas9 complex and a symmetric repair template resulted in less than 10% HDR that unexpectedly decreased with the addition of one of the reported HDR enhancing compounds Alt-R HDR Enhancer (Skarnes et al., 2019) or M3914 (Riesenberg et al., 2019) **(Figure 3.10)**. From these electroporations, 400 single cell clones were screened with an RFLP assay and 4 heterozygous and 1 homozygous KI clone were identified. However, Sanger sequencing revealed Indels that were also present in every clone.

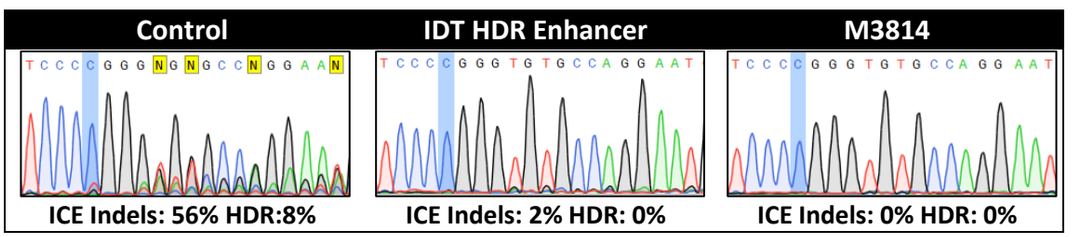

Figure 3.10. Testing HDR enhancing compounds for the COL4A1^{G755R} KI using commercial HiFi Cas9. The highlighted base would be changed from C>T in a successfully generated COL4A1^{G755R} KI clone.

3.1.2.1 Electroporation of an asymmetric repair ssODN

Given the low rates of HDR, an asymmetric repair template was designed and delivered to the cells **(Figure 3.11)**. There was a slight increase from 5% to 9% HDR with the asymmetric design. Moreover, the use of the Lonza 4D nucleofector in this electroporation increased the cutting efficiency observed

with the symmetric repair template from 56% to 88%. Single cell clone screening was again plagued with Indels that were present in 11 heterozygous and 4 homozygous KI clones that were identified from the 400 single cell clones that were screened.

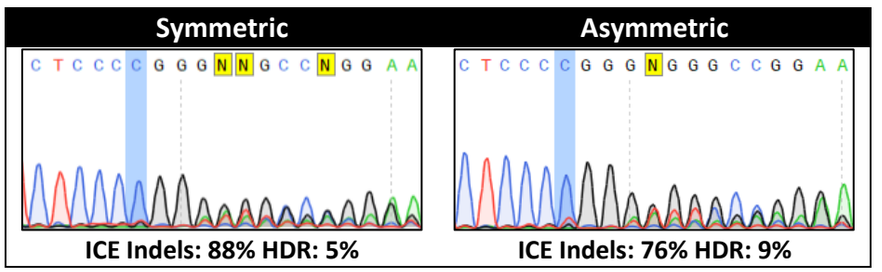

Figure 3.11 Sequencing reactions from pooled cells after Lonza electroporation with symmetric and asymmetric repair templates for COL4A1^{G755R} KI. The highlighted base would be changed from C>T in a successfully generated COL4A1^{G755R} KI clone.

3.1.2.2 COL4A1^{G755R} KI strategy with double silent mutations (DSM)

Due to the inability to efficiently generate a KI clone without additional Indels, a new editing strategy was designed that incorporates two additional silent mutations that block the sgRNA from binding after successful KI incorporation and should prevent undesired Indel generation. Electroporation with the newly designed COL4A1^{G755R} double silent mutation (DSM) repair template resulted in an astounding 65% rate of HDR **(Figure 3.12)**. Given this rate of HDR, standard RFLP clone screening was not necessary and 24 clones were immediately Sanger sequenced. Fourteen clones homozygous for the COL4A1^{G755R} (ClinVar: VCV000161974.16) and both silent mutations were identified. Importantly, no Indels were present in these clones.

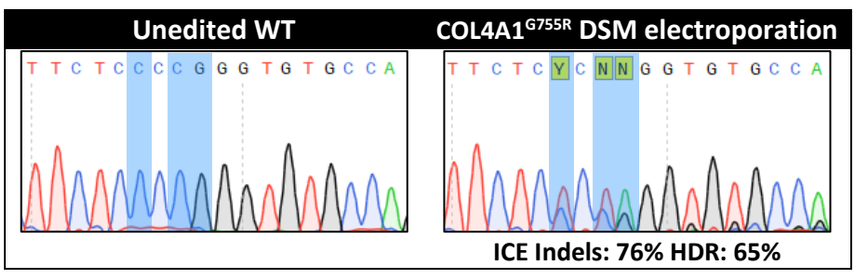

Figure 3.12 Sequence of pooled cells electroporated with the COL4A1^{G755R}DSM repair template. The highlighted bases from left to right are the locations of the R755R, G755R, and P747P mutations present on the asymmetric DSM repair template. Note that COL4A1 is a reverse transcript and the forward strand is shown here.

3.1.2.3 Quality controls of COL4A1^{G755R} DSM clones

The 14 COL4A1^{G755R} DSM KI clones were examined for a BCL2L1 triplication using the qPCR assay **(Figure 3.13)**. Only 4 of these clones had values slightly lower than 2 and were determined to have the normal two copies of BCL2L1. Next, a qgPCR was performed to test for OnTEs in the 4 clones with normal BCL2L1 copy numbers **(Figure 3.14 Left)**. The on-target allele copy number values for these clones are all less than 2 but greater than 1.5 and none of these values are clearly indicative of an OnTE. Clone C3 was selected for further QC analysis because its value was closest to 2. Nearby heterozygous SNPs were genotyped in clone C3 to test for LOH and found to remain heterozygous **(Figure 3.14 Right)**.

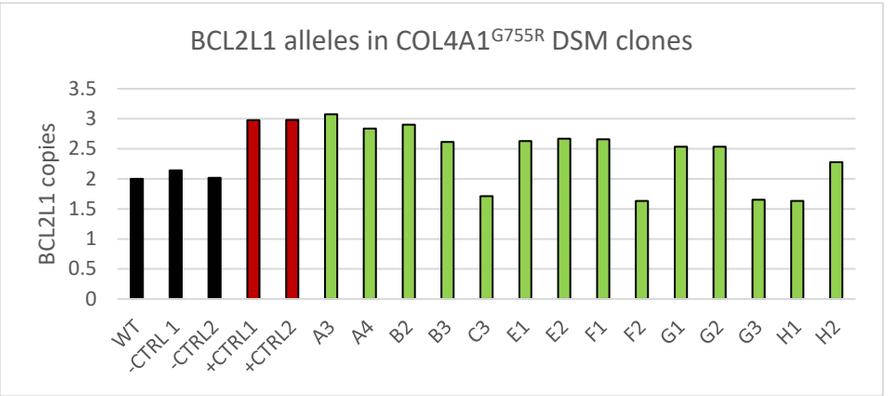

Figure 3.13 BCL2L1 assay for COL4A1^{G755R} DSM clones. The unedited WT and two karyotyped negative controls are shown in black, two positive controls for BCL2L1 triplications are shown in red, and the 14 tested clones are shown in green. Duplicates were performed for each sample and averaged.

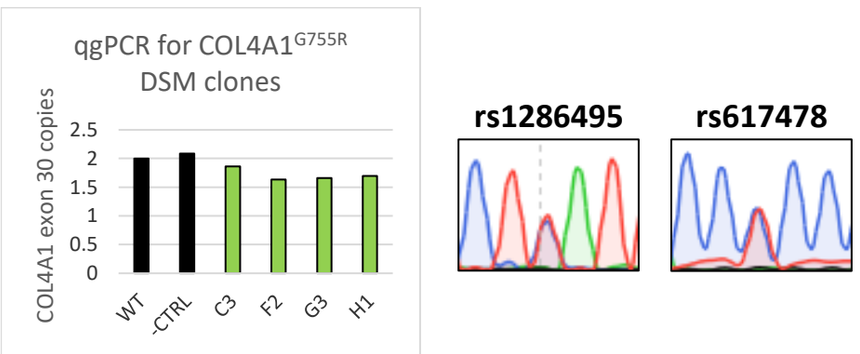

Figure 3.14 OnTE analysis for COL4A1^{G755R} DSM KI clones. (Left) qgPCR for COL4A1 exon 30. Negative controls are shown in black. Duplicates were performed for each sample and averaged. **(Right)** SNP genotyping in clone C3.

The top ten predicted off-targets for sgRNA 45 rv were identified and sequenced in clone C3 revealing no apparent off-target editing. This is unsurprising because the specificity score of sgRNA 45 rv was quite high (82) and HiFi Cas9 was used. Clone C3 was subjected to DNA fingerprinting and molecular karyotyping **(Figure 3.15)**. Clone C3 shared the same band pattern as A18944 WT, indicating that it was correctly generated from this line. Moreover, the only detected CNV event over 350 Kb in this clone is the same triplication on chromosome 7 that is present in the parental cell line.

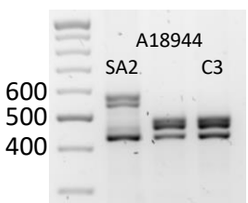

Sample ID	Chr	Start	End	Size	Value
C3	7	132952188	133490582	538394	3

Figure 3.15 Fingerprinting and karyotyping COL4A1^{G755R} clone C3. (Left) Fingerprinting PCR comparing clone C3 to the parent A18944 WT line and SA2 WT. **(Right)** Table of CNVs over 350 Kb detected in clone C3.

3.1.3 Design of COL4A1 3'-UTR (c.*35C>A) KI (ClinVar: VCV000689432.1)

There are several reported COL4A1 3'-UTR mutations causing a subtype of cSVD called PADMAL (pontine autosomal dominant microangiopathy with leukoencephalopathy) **(Figure 3.16)**. The (c.*35C>A) mutation (ClinVar: VCV000689432.1) was selected to KI to hiPSCs because a collaborating

group was working with a COL4A1 (c.*35C>A) mouse model and the miR-29 binding site is completely conserved between humans and mice.

Mutation	Reported symptoms	References
c.*31G>T	WMH, ICH	(Verdura et al., 2016)
c.*32G>A	Hereditary multi-infarct dementia, lacunas	(Siitonen et al., 2017; Zhao et al., 2019)
c.*32G>T	WMH, ICH, microbleeds, cognitive impairment	(Verdura et al., 2016)
c.*33T>A	White matter lesions, lacunas, brain atrophy, microbleeds	(Sakai et al., 2020)
c.*34G>T	Lacunas, ICH	(Qing Li et al., 2022)
c.*35C>A	WMH, lacunas	(Verdura et al., 2016)
c.*36T>A	ICH, lacunar infarcts, and microbleeds, cognitive impairment	(Mönkäre et al., 2021)

Figure 3.16 COL4A1 3'-UTR PADMAL mutations. The table displays identified mutations and symptoms exhibited by patients.

3.1.3.1 Electroporation for COL4A1 (c.*35C>A) KI

For the COL4A1 (c.*35C>A) KI editing, the closest possible sgRNA cuts 8bp from the KI. This sgRNA was electroporated with HiFi Cas9 and a symmetric repair template. The effects of Alt-R HDR Enhancer and M3814 on HDR editing outcomes were also tested at this locus. After electroporation, there was no detected HDR in any condition and only mild cutting efficiency with 18% Indels generated in the normal condition using the BTX electroporation system **(Figure 3.17).** ICE estimates 0% HDR but upon visual inspection, there does appear to be a small C>T bump that could represent HDR editing outcomes. Four hundred single cell clones were screened from these electroporations. There was in fact some HDR as 11 clones did incorporate the KI but each harbored additional Indels.

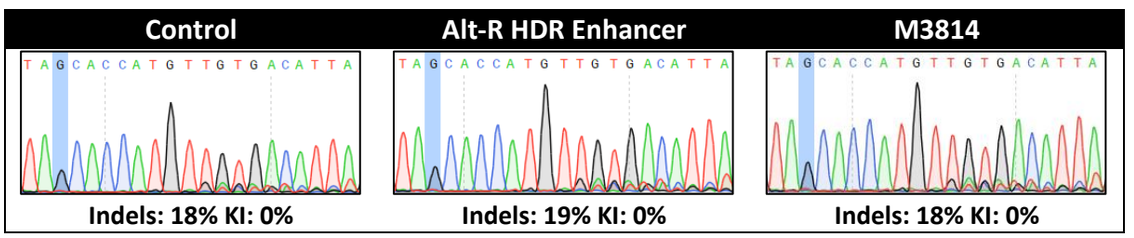

Figure 3.17 Sequences of pooled cells from electroporation for the (c.*35C>A) KI. Sequencing reactions from control, Alt-R HDR Enhancer, and M3814 conditions are shown. The highlighted base is the location of the (c.*35C>A) mutation where a G>T would represent a successful KI.

3.1.3.2 Asymmetric repair template design and electroporation for (c.*35C>A) KI

Similar to the COL4A1^{G755R} KI editing, an asymmetric repair template was designed for the (c.*35C>A) KI to attempt to increase HDR editing outcomes. Using the Lonza 4D nucleofector, electroporations delivering the symmetric and asymmetric repair templates were performed yielding slightly increased rates of Indel generation **(Figure 3.18)**. However, there is still no substantial HDR activity even with the asymmetric repair template. From these cells, 600 single cell clones were screened. There were 6

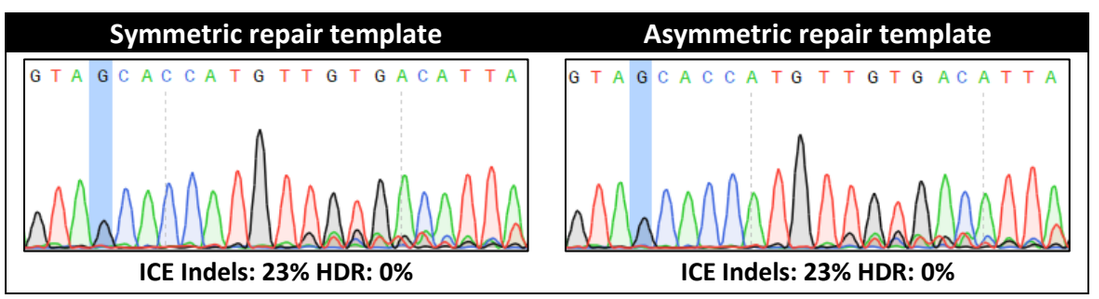

Figure 3.18 Sequences of pooled cells electroporated with symmetric or asymmetric (c.*35C>A) repair templates. Sequencing reactions from symmetric and asymmetric repair template delivered cells. The highlighted base is the location of the (c.*35C>A) mutation where a G>T would represent a successful KI.

clones with the (c.*35C>A) (ClinVar: VCV000689432.1) KI on at least one allele but again every KI clone incorporated additional Indels.

3.1.3.3 Electroporation and clone screening for the CORRECT 1st step of the (c.*35C>A) KI

To efficiently generate a (c.*35C>A) KI clone absent from unwanted Indels, a new two-step editing strategy based on CORRECT was designed (Kwart et al., 2017). Delivery of the new repair template with the (c.*35C>A) and a "GGG" 1st step blocking mutation generated 29% and 7% HDR in independent electroporations **(Figure 3.19 Top)**. From these two editing experiments, a total of 600 clones were screened with an RFLP assay **(Figure 3.19 Middle)**. Sanger sequencing confirmed 3 homozygous clones for both the (c.*35C>A) KI and "GGG" blocking mutation and 27 clones heterozygous clones for the (c.*35C>A) KI and homozygous for the blocking "GGG" **(Figure 3.19 Bottom)**.

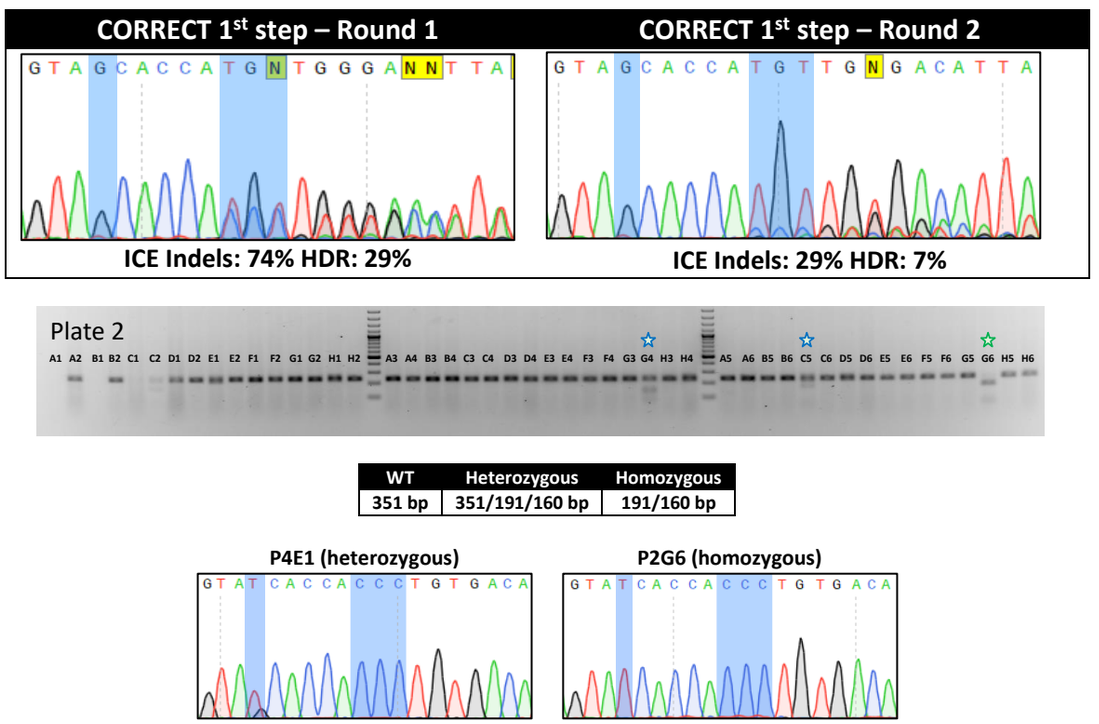

Figure 3.19 Generation of 1st step CORRECT (c.*35C>A) KI. (Top) Sequencing reactions from electroporated pooled cells. Single highlighted base is the location of the (c.*35C>A) mutation and the other 3 highlighted bases represent the designed ACA>GGG mutation. **(Middle)** Example of clones screened with the HphI RFLP assay. Green stars indicate homozygous clones and blue stars indicate heterozygous clones. **(Bottom)** Sanger sequencing of heterozygous clone P4E1 and homozygous clone P2G6 that confirm the RFLP genotype.

3.1.3.4 Quality controls for 1st step (c.*35C>A) KI clones

Before electroporating one of the 1st step clones to generate the final CORRECT (c.*35C>A) KI clone, some of the QCs assays must be performed to prevent a clone with a deleterious effect from being edited and producing only similarly damaged clones. The BCL2L1 assay was performed for all of the clones from the first **(Figure 3.20 Top)** and second editing round **(Figure 3.20 Bottom)**. Out of all 30 clones analyzed for a BCL2L1 triplication, 18 have values indicating a normal BCL2L1 copy number, and only one homozygous (c.*35C>A) KI clone (P2G6) does not clearly have a BCL2L1 triplication. Next, a qgPCR was performed to test for destruction of an OnTE allele in homozygous clone P2G6 and 3 heterozygous clones **(Figure 3.21 Left)**. Given that two alleles can be seen on the sequencing reaction

of the heterozygous clones, these served as quasi negative controls for the assay and clone P2G6 does not appear hemizygous. SNP genotyping was only performed in homozygous clone P2G6 and heterozygous clone P4E1 **(Figure 3.21 Right)**. Both SNPs tested in these clones remain heterozygous after the 1st step of editing. Clones P2G6 and P4E1 were also sequenced at the top 10 *in silico* predicted off-target regions without detection of any off-targets. Lastly, clones P2G6 and P4E1 were molecular karyotyped and the only detected CNV was the triplication in chromosome 7 also present in the unedited WT line.

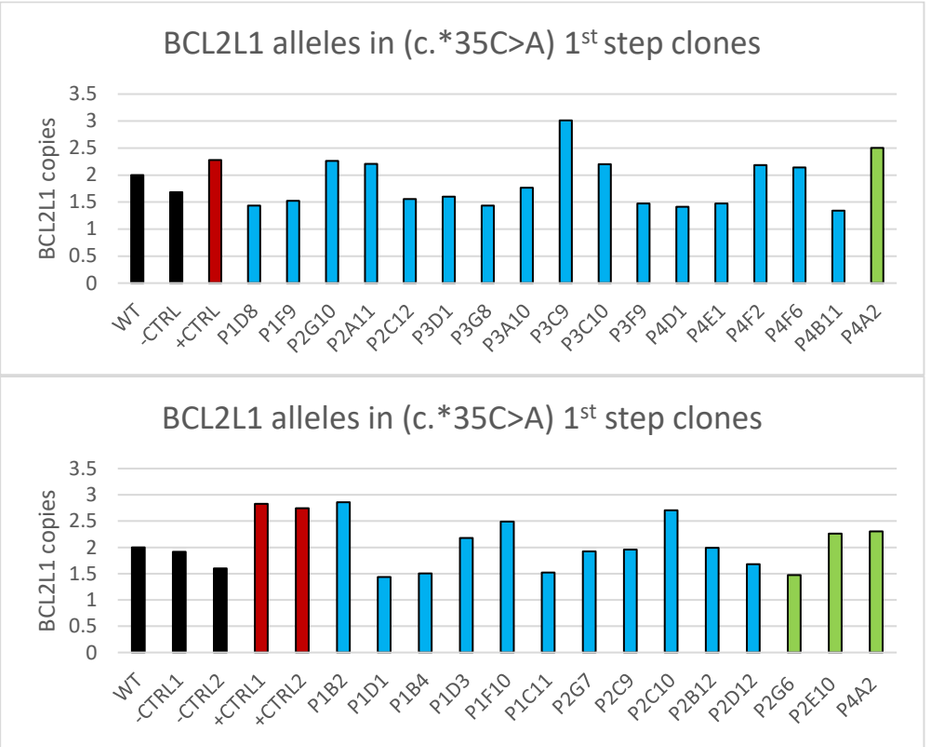

Figure 3.20 BCL2L1 assay of COL4A1 (c.*35C>A) 1st step clones. **(Top)** Quantification of 16 heterozygous (blue) and 1 homozygous clone (green) from the 1st round. **(Bottom)** Quantification of BCL2L1 copy numbers of 11 heterozygous (blue) and 2 homozygous clones (green) from the 2nd round. Homozygous clone P4A2 (round 1) was tested again. Unedited WT (black) is set to 2 alleles. Negative controls (black) are karyotyped COL4A1 KO clones. The positive controls are independently generated clones that have given 3 BCL2L1 copies for this assay in previous experiments and are shown in red. Duplicates were performed for each sample and averaged.

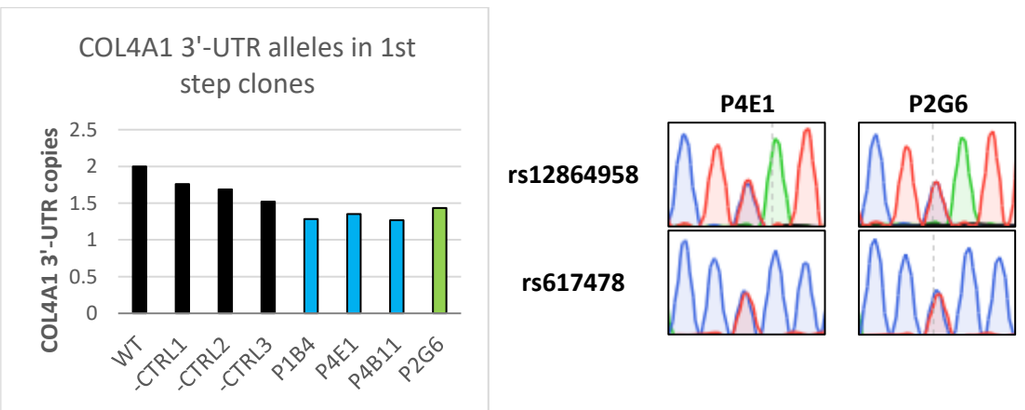

Figure 3.21. OnTE analysis of 1st step (c.*35C>A) clones. (Left) qgPCR of COL4A1 3′-UTR. Unedited WT (black) is set to 2 alleles. Negative controls (black) are clones edited with sgRNA 15 rv in COL4A1 exon 28. Three heterozygous (c.*35C>A) clones (blue) and one homozygous (c.*35C>A) clone (green) were tested. Duplicates were performed for each sample and averaged. **(Right)** SNP genotyping in heterozygous clone P4E1 and homozygous clone P2G6.

3.1.3.5 Electroporation of clone P2G6 for the CORRECT (c.*35C>A) 2nd editing step

Given that clone P2G6 passed all of the tested QC assays and is already homozygous for the (c.*35C>A) KI, it was electroporated with the 2nd step sgRNA (sgRNA 4 rv) and a repair template containing only the (c.*35C>A) KI. This resulted in a rate of 44% HDR **(Figure 3.22 Top)**. RFLP screening of 200 clones yielded 46 homozygous clones **(Figure 3.22 Middle)**. Only 24 were Sanger sequenced and 15 CORRECT (c.*35C>A) KI clones were identified with clone P1B4 shown in **Figure 3.22** (**Bottom)**.

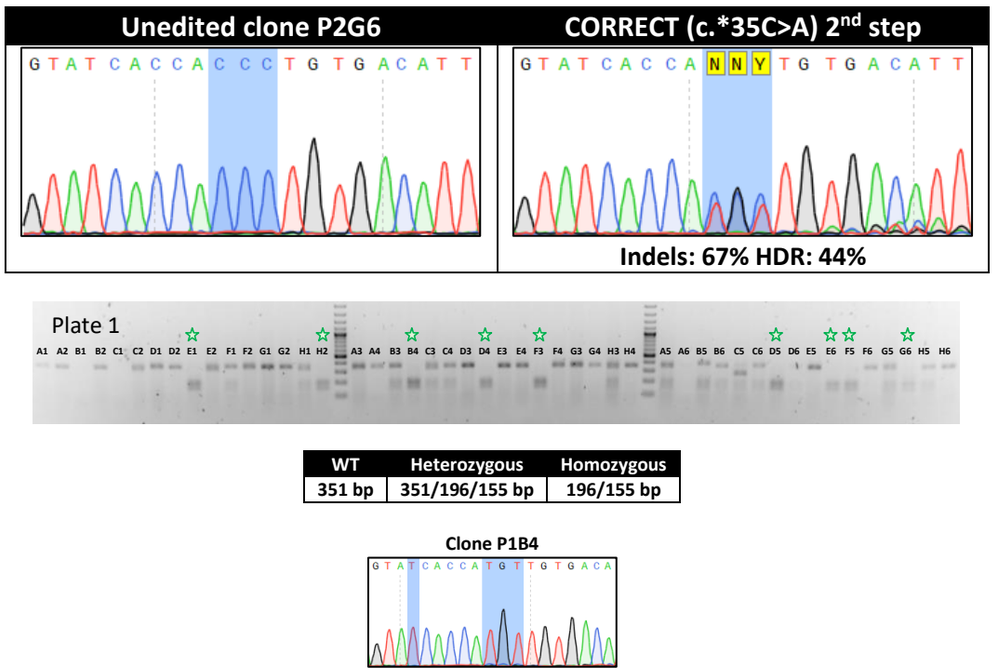

Figure 3.22 Generation of 2nd step CORRECT (c.*35C>A) KI clone. (Top) Sequencing reactions of pooled cells after electroporation. The highlighted bases in unedited clone P2G6 are the newly inserted PAM sequence. The same bases are highlighted in the pool of edited cells. **(Middle)** Example of RFLP clone screening with NlaIII**. (Bottom)** Sanger sequence to confirm homozygous genotype in clone P1B4.

3.1.3.6 Quality controls of CORRECT (c.*35C>A) KI clones

The 2nd step CORRECT (c.*35C>A) KI clones were first tested with the BCL2L1 assay **(Figure 3.23).** The positive control is unexpectedly high with over 4 copies of BCL2L1. However, none of the 15 tested clones appear to have an abnormal copy number of BCL2L1. Next, the OnTE QC assays were performed

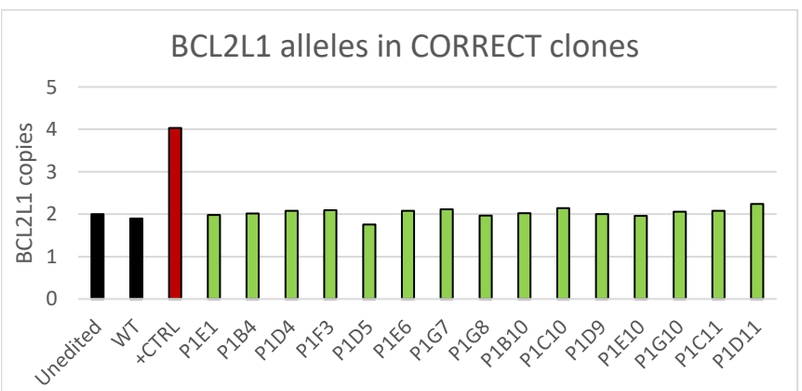

Figure 3.23 BCL2L1 assay applied to CORRECT (c.*35 C>A) clones generated from clone P2G6. Unedited clone P2G6 and WT were used as negative controls (black). The positive control is a clone previously testing to have 3 alleles in this assay (red). The tested clones (green) are all homozygous for a scarless incorporation of the (c.*35 C>A) KI. Duplicates were performed for each sample and averaged.

with the qgPCR revealing an apparent triplication in clone P1D5 but otherwise all other clones seem to have two intact on-target alleles **(Figure 3.24 Left)**. Clone P1B4 was analyzed for LOH **(Figure 3.24 Right)**. Both genotyped SNPs remain heterozygous in this clone. The top 10 predicted *in silico* off-target regions from this new sgRNA were sequenced in clone P1B4 without off-target effect detection. Lastly, CORRECT clone P1B4 was DNA fingerprinted and molecular karyotyped **(Figure 3.25)**. Fingerprinting confirmed this clone was generated from the A18944 WT line and karyotyping only revealed the chromosome triplication also present in the parent cell line.

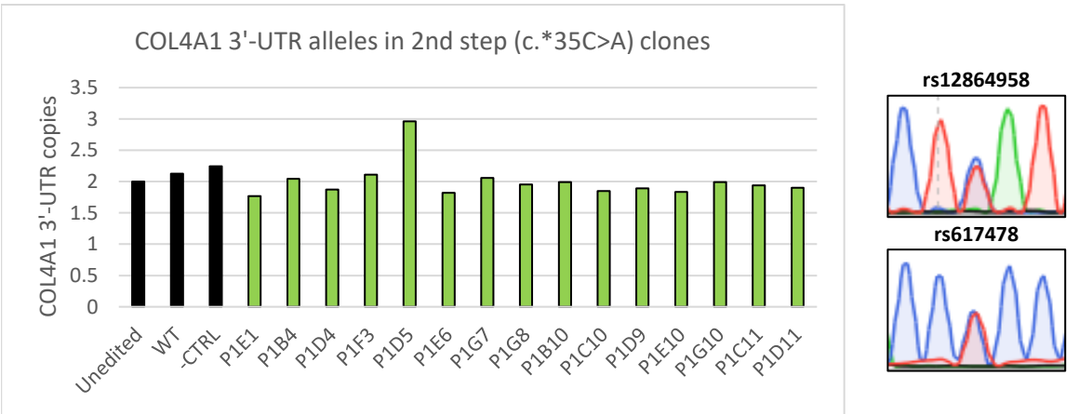

Figure 3.24 OnTE analysis of CORRECT (c.*35C>A) clones. (Left) qgPCR of COL4A1 3'UTR. Unedited clone P1G6, WT, and -CTRL are shown in black. Tested clones are displayed in green. Duplicates were performed for each sample and averaged. **(Right)** SNP genotyping of CORRECT clone P1B4.

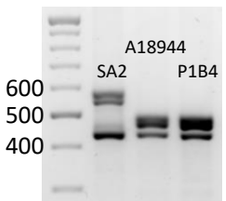

Sample ID	Chr	Start	End	Size	Value
P2G6-P1B4	7	132952188	133500995	548807	3

Figure 3.25 DNA fingerprinting and karyotyping CORRECT (c.*35C>A) KI clone P1B4. (Left) Fingerprinting PCR comparing clone P1B4 to the unedited A18944 WT and SA2 WT cell lines. **(Right)** Detected CNVs over 350 Kb.

3.2 COL4A1 KO characterization

A qPCR was performed on COL4A1 KO clones with two COL4A1 primer combinations, one amplifying before the edit (B) and the other after the edit (E), as well as one combination amplifying COL4A2. **(Figure 3.26 Left)**. The homozygous KO ECs (P1H10 and P2H5) display a drastic reduction of COL4A1 with both primer combinations compared to the WT ECs. The heterozygous KO ECs have slightly different levels of COL4A1 mRNA from each other with around 0.8 for clone P1D9 and below 0.5 for P2H12. However, after COL4A1 is normalized to COL4A2, the ratio of COL4A1/COL4A2 in the heterozygous clones is 0.63 (P1D9) and 0.52 (P2H12) **(Figure 3.26 Right)**. While COL4A2 fluctuated a bit, it always scales with the expected values of COL4A1.

Endothelial cells from COL4A1 homozygous KO clone P1H10, heterozygous KO clone P2H12, and WT cell lines were stained for the tight junction protein ZO-1, an antibody specific for COL4A2, and a non-discriminating COLIV antibody reacting with COL4A1 to 6 **(Figure 3.27)**. The COLIV staining (white) is visibly reduced in the both heterozygous and homozygous KO clones compared to the WT mirroring the measured mRNA levels. In the heterozygous KO and more strikingly in the homozygous KO there are some distinct puncta visible in the COLIV staining that co-localize with puncta in the COL4A2

staining **(Figure 3.28)**. A heterotrimer between two α1 (COL4A1) chains and one α2 (COL4A2) chain must be formed for the protein to be secreted. If the ratio of COL4A1 to COL4A2 is perturbed, there may be unpaired collagen IV alpha chains that are unable to be secreted. This ratio was previously seen to be decreased on the mRNA level **(Figure 3.26)**.

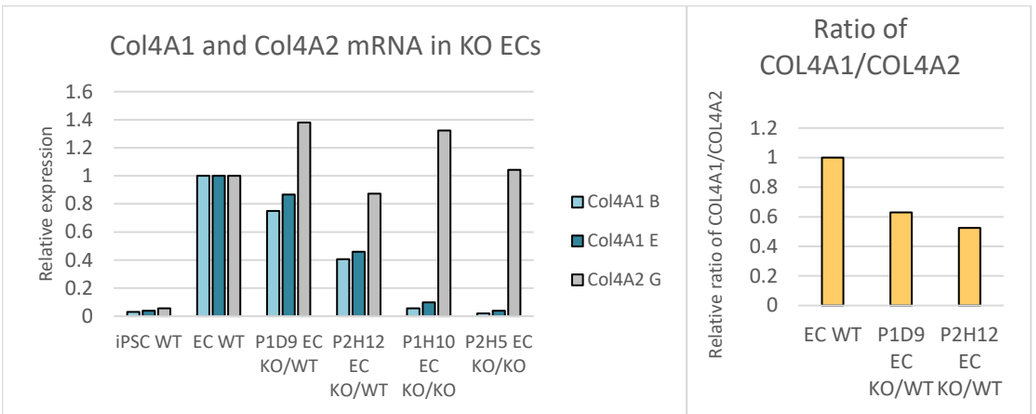

Figure 3.26 qPCR for COL4A1 and COL4A2 in COL4A1 KO clones. (Left) COL4A1 B amplifies before the frameshift (light blue) targeted by sgRNA 15 rv and COL4A1 E amplifies after it (blue). Primer combination COL4A2 G amplifies exons 34-36 of COL4A2 (grey). Values are normalized to RPL22 and EC WT is subsequently set to 1 for each primer combination. Triplicates were performed for each sample and averaged. **(Right)** The COL4A1 to COL4A2 ratio was calculated by averaging the triplicates for COL4A1 B and COL4A2 G and dividing the values by each other. EC WT was set to 1 and the clones were normalized to this value.

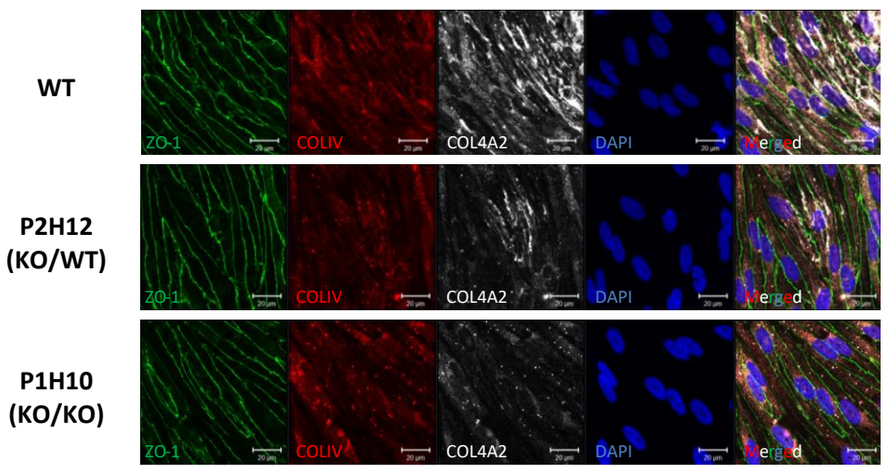

Figure 3.27 Immunofluorescence stainings of COL4A1 KO clones. ZO-1 (green) marks the cell-cell junctions. COLIV (red) reacts with all type IV collagen. COL4A2 (white) reacts specifically with the NC1 domain of COL4A2.

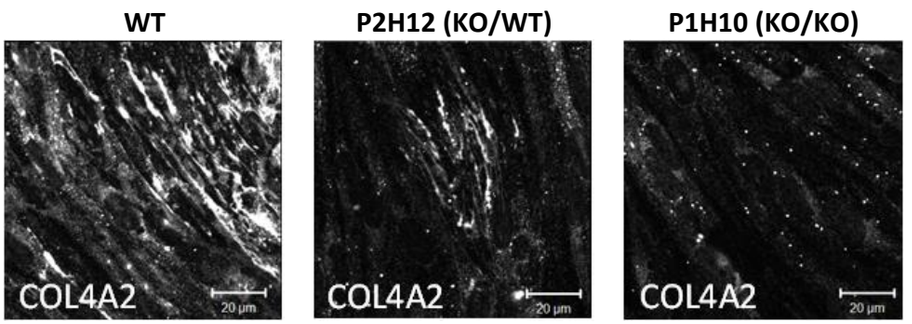

Figure 3.28 Increased zoom of COL4A2 staining in COL4A1 KOs. The puncta are clearly visible and more frequent in ECs with more null COL4A1 alleles.

3.2.1 Functional analysis of barrier formed by COL4A1 KO ECs

Given that COL4A1 is knocked out on the mRNA and protein level, an analysis of the strength of the barrier formed by these ECs was assessed by TEER measurements **(Figure 3.29)**. Unexpectedly, the TEER from COL4A1 KO ECs is consistently higher compared to WT ECs (P = 3.62E-06). In order to determine if the increase could be replicated on a different coating, the TEER was measured in the KO ECs on a fibronectin coating **(Figure 3.30)**. Seeded on fibronectin, COL4A1 KO ECs still produce a higher

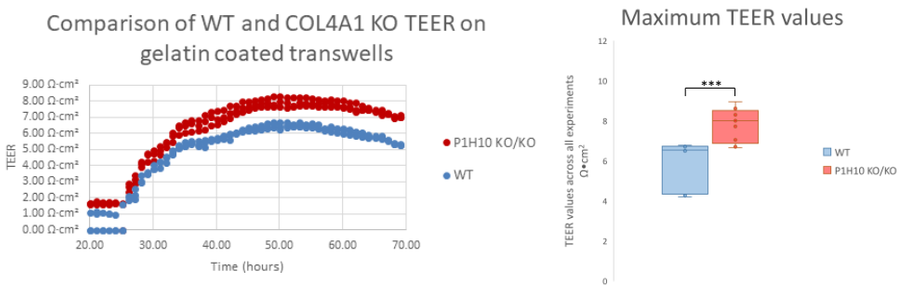

Figure 3.29 Monoculture TEER of COL4A1 KO P1H10 on a gelatin coating. (Left) Representative TEER experiment comparing WT ECs to P1H10 COL4A1 homozygous KO ECs. **(Right)** Maximum TEER values for all replicates across 3 experiments comparing P1H10 and WT ECs on a gelatin coating. A paired T-Test was performed. (P=3.62E-06).

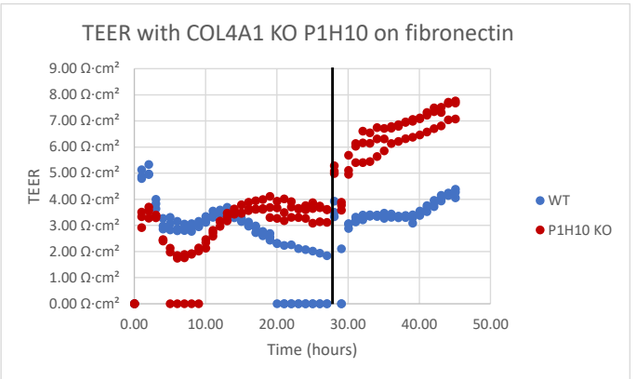

Figure 3.30 TEER measurement of ECs grown on fibronectin coated transwells. The black bar represents a full media change where VEGF supplementation was removed.

maximum TEER value compared to the WT control. There could be a compensating mechanism causing the increased TEER values observed in the COL4A1 KO ECs. One possibility is an increase of other ECM proteins that could allow these ECs to more strongly attach to the transwell surface. Moreover, collagen IV or TIMP1 binding to integrin β1 (ITGB1) have been shown to directly impact junctional proteins and EC barrier strength (Izawa et al., 2018; Osada et al., 2011; Tang et al., 2020). An upregulation of ITGB1 or TIMP1 could explain the increased barrier in the KO ECs. Various ECM proteins, ITGB1, TIMP1, and junction proteins were analyzed by qPCR in KO clone P1H10 **(Figure 3.31)**. On a gelatin coating, there are small increases in LAMC1 and HSPG2 in the KO. ITGB1 is 30% increased in the KO while TIMP1 is unchanged. VE-cadherin, CD31, and occludin are all increased in the KO potentially explaining the increased TEER measurement. On fibronectin, claudin-5, occludin, VE-cadherin, and CD31 were all increased compared to the WT and seem to reflect the higher TEER measurements in the KO.

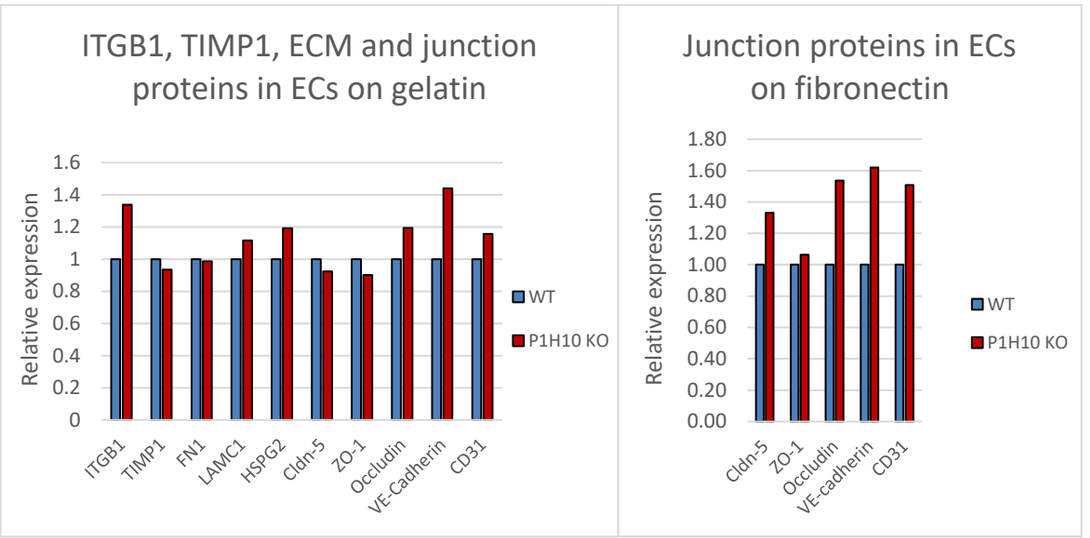

Figure 3.31 qPCR panel comparing COL4A1 KO P1H10 ECs to isogenic WT controls. (Left) ECs grown on a gelatin coating. **(Right)** ECs grown on a fibronectin coating. Triplicates were performed and averaged. All values are normalized to the EMC7 housekeeping gene and the EC WT is set to 1.

It is crucial to confirm if there is also increased in TEER in independent COL4A1 KO clones. To this effect, a TEER measurement was made using homozygous KO clones P2H5 and P1A11 that were differentiated into ECs and plated on gelatin **(Figure 3.32)**. Clone P1H10 was included in this differentiation but due to technical problems, there were no ECs generated from this clone. Unlike clone P1H10, the TEER in these clones are reduced. This may indicate that the increased TEER previously observed with clone P1H10 is an unspecific effect in the clone and not caused by COL4A1 KO.

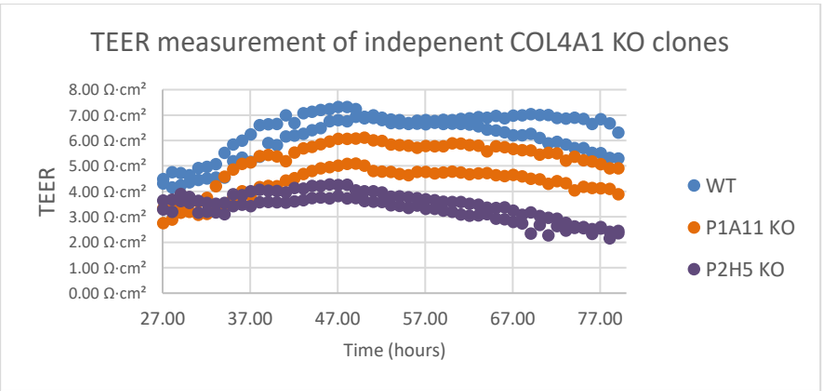

Figure 3.32 TEER measurement in ECs from WT and COL4A1 KO/KO clones P1A11 and P2H5 on gelatin coated transwells. Duplicates are shown for each cell line. Media was changed and VEGF supplementation removed at 26 hours after the start of measurement.

3.2.2 Effect of 3'-UTR (c.35*C>A) mutation on collagen IV expression

Fibroblasts from PADMAL patients with the (c.*35C>A) mutation in the 3'-UTR of COL4A1 exhibit increased expression of COL4A1 mRNA (Verdura et al., 2016). To test if this can be reproduced in NVU cells derived from hiPSCs with the (c.*35C>A) KI, endothelial cells, smooth muscle cells, and pericytes from (c.*35C>A) KI clone P1B4 were analyzed for COL4A1 and COL4A2 by qPCR. Two independent endothelial cell differentiations, 4 smooth muscle cell differentiations, and 3 pericyte differentiations were analyzed **(Figure 3.33)**. There was no obvious or significant increase of COL4A1 in the endothelial cells or smooth muscle cells and the COL4A1/COL4A2 ratios were unaltered. However, there was a

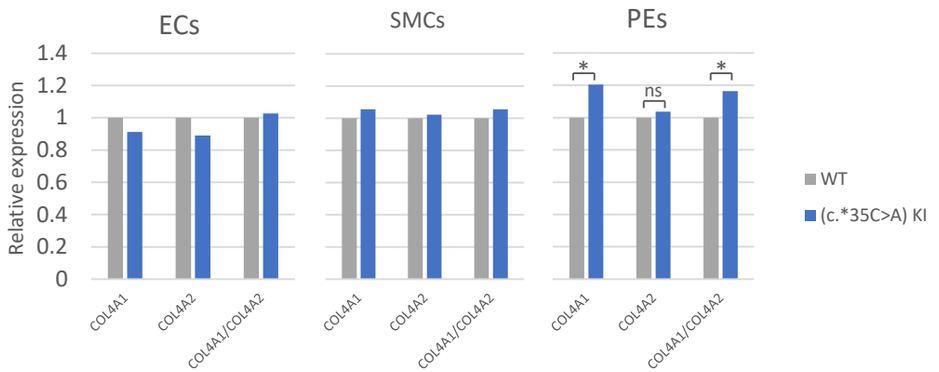

Figure 3.33 COL4A1 and COL4A2 expression of (c.*35C>A) KI in neurovascular unit cell types. COL4A1 and COL4A2 mRNA levels 21 days after the beginning of each resepective differentiation. WT cells are grey and (c.*35C>A) KI cells are blue. Paired T-tests were performed to compare WT and KI cells. COL4A1 is significantly increased in KI PEs (P=0.013) and COL4A1/COl4A2 raitio in PEs is also significantly increased (P=0.036).

significant increase of COL4A1 in pericytes (P=0.013) and an increase in the COL4A1/COL4A2 ratio (P=0.036). The COL4A2 levels in the mutant pericytes were not significantly changed. There is a trend of higher COL4A1 and COL4A2 in WT hiPSC-derived pericytes compared to other WT hiPSC-derived NVU cell types further suggesting this cell type may be considerably involved in COL4A1-related disease pathology. **(Figure 3.34)**.

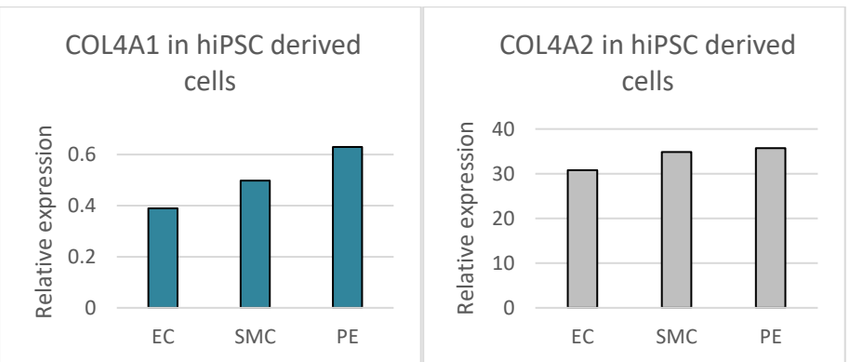

Figure 3.34 Comparison of COL4A1 and COL4A2 expression in hiPSC-derived neurovascular cell types. WT endothelial cells, smooth muscle cells, and pericytes at day *in vitro* 21 analyzed for COL4A1 and COL4A2 by qPCR. Triplicates were performed and averaged.

3.2.3 COL4A1^{G755R} KI exhibits normal COL4A1 expression

Ascorbic acid reportedly increases expression of type IV collagen in human cells (Kishimoto et al., 2013), and increased expression may promote the presence of disease relevant phenotypes in the hiPSC model. Ascorbic acid-2 phosphate was added to the media of WT, and COL4A1^{G755R} KI ECs before the cells were analyzed for COL4A1 and COL4A2. Both genotypes exhibit increased collagen IV mRNA with the addition of ascorbic acid (AA) **(Figure 3.35 Left)**.The untreated COL4A1^{G755R} KI ECs have slightly lower mRNA levels compared to the WT. However, the ratio of COL4A1 to COL4A2 is unaffected **(Figure 3.35 Right)**.

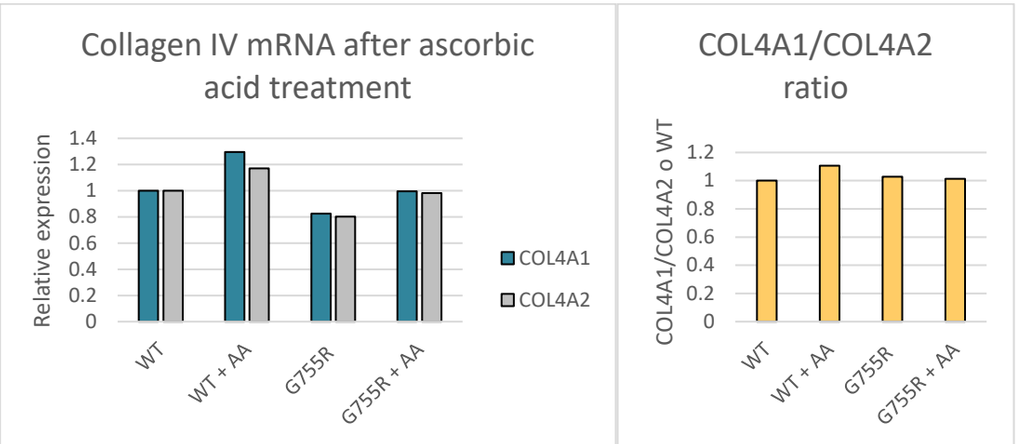

Figure 3.35 qPCR of COL4A1 and COL4A2 in WT and COL4A1^{G755R} KI ECs. (Left) COL4A1 (E) and COL4A2 (G) primer combinations were used. Triplicates were performed and averaged. All values are normalized to the EMC7 housekeeping gene and the EC WT is set to 1. **(Right)** Ratio of COL4A1 to COL4A2 in WT and COL4A1^{G755R} KI ECs. WT is set to 1 and other values are normalized to the WT.

3.2.4 Collagen IV expression pattern of COL4A1^{G755R} KI ECs in 3D cultures

The COL4A1^{G755R} KI is predicted to affect heterotrimer formation and/or structure. Given secretion of collagen IV requires α1-α1-α2 heterotrimer formation, the secretion of collagen IV in COL4A1^{G755R} KI ECs was examined in 3D cultures **(Figure 3.36)**. Different time points were analyzed by immunofluorescence, but extracellular collagen IV was not prominent in the WT cultures until Day 11. COL4A1 signal can be seen in the extracellular space in both the WT and COL4A1^{G755R} KI cultures at Day 11 indicating that the COLA4^{G755R} KI ECs are able to form α1-α1-α2 heterotrimers. However, it remains to be elucidated if the heterotrimer is formed as efficiently and secreted to the same extent as WT ECs. Nonetheless, hiPSC-ECs with a homozygous COL4A1^{G755R} mutation can form and secrete collagen IV α1-α1-α2 heterotrimers in 3D.

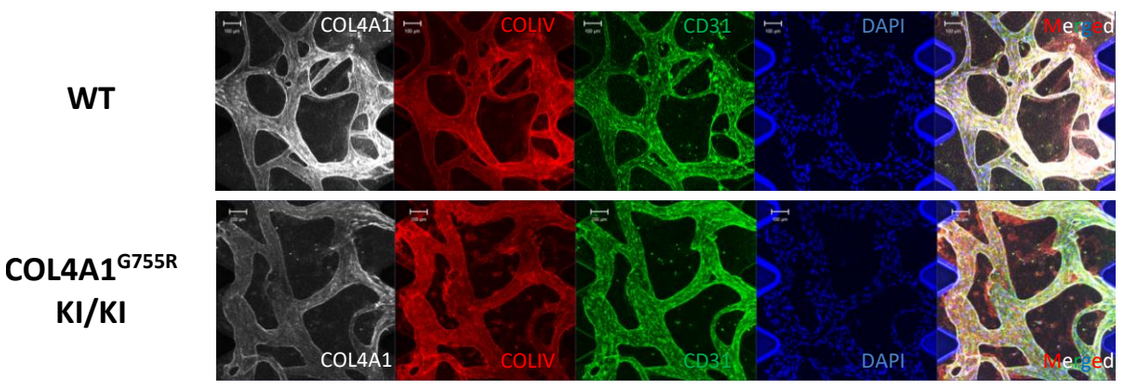

Figure 3.36 Secretion and deposition of collagen IV in WT and COL4A1^{G755R} 3D cultures. Immunofluorescence images of 3D endothelial cell cultures after 11 days. Note the collagen IV and COL4A1 staining can be observed in the extracellular space in both the WT and KI cultures.

3.2.5 Perfusion of 3D cultures

The 3D cultures generated in the microfluidic device are more physiological because the endothelial cells self-organize to form tubes reminiscent of blood vessels. However, these microfluidic cultures have static media conditions. To increase the physiological relevance of these cultures further, the ibidi pump system was adapted to perfuse media through these cultures. A proof of principle experiment was performed in which human blood was successfully perfused through the 3D cultures **(Figure 3.37**

Top). Moreover, perfusion of media for 3 days improved survival in one experiment **(Figure 3.37 Bottom)**. However, the thickness of the tubes of the perfused culture appear to be increasing with prolonged perfusion. The increase in survivability in this experiment is promising but further optimizations are needed in order to prevent the change in morphology observed after perfusion.

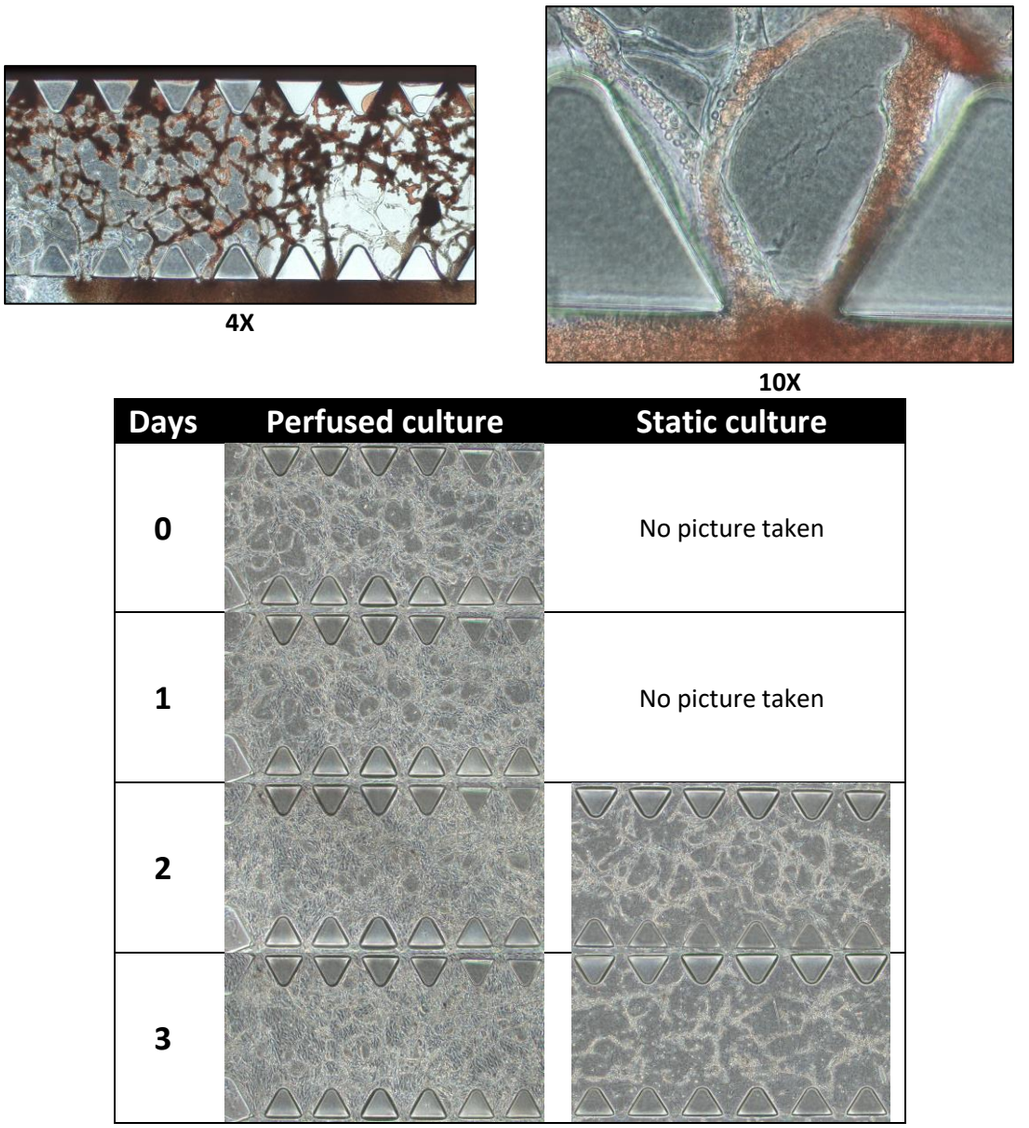

Figure 3.37 Perfusion of 3D cultures with the ibidi pump system. (Top) Perfusion of human blood in 3D endothelial cell cultures. A 4X overview at the beginning of the perfusion is shown on the left. A 10X image of the erythrocytes entering a culture is shown on the right. **(Bottom)** 4X images of a culture perfused for 3 days with normal media. (Day 1 was with 2mbar and days 2 and 3 were with 3mbar). Note that the static culture in day 2 exhibits many bright areas indicative of dying cells or cell debris and at day 3 more cell death is observed and the tubes are discontinuous. The perfused culture remains alive at day 3 but the tubes have become substantially larger.

3.3 Chapter summary

Three distinct types of cSVD-causing COL4A1 mutations were edited into human iPSCs to generate hiPSC lines with these disease mutations. The first mutation causes COL4A1 haploinsufficiency in patients by creating a frameshift in the middle of the gene. Human iPSC cell lines were generated with both a heterozygous and homozygous frameshift in exactly the same location as the patients (ClinVar:

VCV000161440.4). Next, the COL4A1^{G755R} mutation (ClinVar: VCV000161974.16) was knocked into human iPSCs by utilizing silent blocking mutations. Finally, the 3'-UTR (c.*35C>A) PADMAL mutation (ClinVar: VCV000689432.1) was scarlessly incorporated the human iPSCs via a two-step editing strategy based on CORRECT.

Following CRISPR/Cas9 editing of these cell lines, necessary quality controls were performed to verify the final cell lines used to model COL4A1 monogenic cSVD do not harbor deleterious effects from the CRISPR/Cas9 editing process. All of the cell lines were examined for a triplication of the BCL2L1 locus and aberrations of the CRISPR targeted allele via qPCR assays. The top 10 predicted off-target sites determined by the CFD and MIT algorithms from CRISPOR for each sgRNA used were sequenced in the edited clones. Nearby heterozygous SNPs rs12864959 and rs617478 were sequenced in each cell line to ensure LOH had not occurred. Pluripotency markers were only examined in the COL4A1 KO cell lines but the COL4A1^{G755R} and (c.*35C>A) KIs appeared to have normal iPSC morphology and could be differentiated into vascular cell types. A fingerprinting PCR confirmed that each cell line was generated with the A18944 WT human iPSC line. Finally, molecular karyotyping was performed in every cell line to detect large CNVs. These quality control assays are necessary to confidently attribute disease phenotypes to the COL4A1 mutations in succeeding experiments.

The COL4A1 KO reduces COL4A1 mRNA levels by approximately half in the heterozygous mutants and to nearly zero in the homozygous mutants, and immunofluorescence staining also suggests there is a gene dose dependent decrease of collagen IV in the COL4A1 KO mutants. Moreover, COL4A2 staining reveals puncta in the heterozygous KO and more prominently in the homozygous KO that could indicate unpaired collagen IV α2 chains that are unable to form heterotrimers because of an insufficiency of collagen IV α1 chains. Unexpectedly the TEER measurements were significantly increased in homozygous COL4A1 KO clone P1H10. The mRNA expression of several AJs and TJs seemed to be increased in this KO clone. However, a single TEER experiment with other independent homozygous KO clones revealed a decrease of TEER and additional TEER experiments are necessary to determine the true effect of a COL4A1 KO on TEER.

COL4A1 and COL4A2 mRNA expression was examined in hiPSC-derived neurovascular cell types carrying the (c.*35C>A) mutation. There was no significant difference of COL4A1 expression for endothelial cells or smooth muscles cells. However, pericytes had a significant upregulation of COL4A1 but not COL4A2. In the mutant pericytes, the COL4A1/COL4A2 ratio is perturbed and the disease mechanisms of PADMAL are likely linked to this ratio.

Endothelial cells derived from hiPSCs harboring the COL4A1^{G755R} mutation were embedded in a fibrin gel inside a 3D microfluidic device. These endothelial cells self-organized to form tubes and secreted collagen IV intro the extracellular space. Therefore, the COL4A1^{G755R} mutation does not completely abolish collagen IV heterotrimer formation in hiPSC-ECs.

Lastly, a pump system was adapted to the 3D microfluidic devices. While survival is prolonged with the addition of flow, the applied pressure requires further optimization because the morphology of the endothelial cell tubes drastically changed under flow.

Chapter 4 Discussion

4.1 CRISPR/Cas9 is a versatile genome editing tool

Three distinct COL4A1 mutations were generated in hiPSCs with the same CRISPR/Cas9 workflow but each with a slightly different approach. The COL4A1 KO was generated by Indel-induced frameshifts in exon 28 of COL4A1 through NHEJ. Two additional silent mutations were used to help generate the COL4A1^{G755R} KI. Lastly, a two-step editing strategy incorporating and removing blocking mutations based on CORRECT (Kwart et al., 2017) was used to achieve a scarless incorporation of the 3'-UTR (c.*35C>) mutation.

4.1.1 RNP delivery of Cas9/sgRNA complex efficiently edits hiPSCs

As described in the introduction, there are 3 main modes to deliver Cas9 machinery to a cell: DNA, mRNA, and protein (Yip, 2020). Delivery of Cas9 using a DNA plasmid is a widely accessible method already established in our lab. However, transfection of hiPSCs with foreign DNA is typically low. Moreover, plasmid expression of Cas9 results in sustained expression and increased likelihood of off-target effects (Wu et al., 2014; Yip, 2020). In order to simplify the editing procedure by foregoing a selection step and reduce the timeframe of Cas9 expression, delivery of a Cas9/sgRNA RNP complex was tested and compared to plasmid delivery of the same sgRNA and Cas9 conferring puromycin resistance for selection.

The Cas9 plasmid and sgRNA 15 rv (targeting exon 28) could achieve 61% Indel generation after 3 days of puromycin selection. Conversely, delivery of a Cas9/sgRNA 15 rv RNP complex edited 63% of the hiPSCs (without any selection). Therefore, given similar editing efficiencies in this initial test, Cas9 RNPs were subsequently used to generate the single cell KO clones and the KI clones in this thesis.

4.1.2 HDR enhancing compounds reduced Indel formation but did not increase HDR rates

The default DNA repair pathway after a DSB is NHEJ. However, HDR must be utilized in order to generate a specific KI mutation. For this reason, numerous studies have focused on developing methods and using compounds to increase the rate of HDR in genome editing experiments (Aird et al., 2018; Z. Hu et al., 2018; Riesenberg et al., 2019; Riesenberg & Maricic, 2018; Skarnes et al., 2019). In this work, HDR enhancing compounds M3814 and Alt-R HDR Enhancer were used to promote the HDR pathway. M3814 is a potent inhibitor of DNA PKcs that has been tested for cancer therapy (Riesenberg et al., 2019). DNA PKcs activity is required for the NHEJ pathway and ablation of the kinase activity should favor use of other DNA repair pathways such as HDR (Riesenberg et al., 2019). Alt-R HDR Enhancer is available from IDT with a proprietary undisclosed composition and structure, but it has been reported to increase the HDR pathway in hiPSCs (Skarnes et al., 2019).

Initial electroporations for both of the KI mutations using symmetric repair ssODNs and HDR enhancing molecules did not yield high rates of HDR or the successful isolation of a single cell KI clone. At the COL4A1^{G755R} locus with HiFi Cas9 and sgRNA 45 rv, there was 56% Indels and 8% HDR determined by ICE. Addition of M3814 and Alt-R HDR Enhancer stunted NHEJ and resulting in 0% and 2% Indels respectively. However, HDR was also reduced as ICE also estimated 0% HDR when these compounds were added. Given the absence of both NHEJ and HDR, it is possible there was an issue with the delivery

of the Cas9/sgRNA complex to the cells. The RNP complex was incubated together for the control and HDR enhancer conditions. There were 56% Indels generated in the control condition indicating the RNP complex was unaffected during incubation. However, after incubation there could have been a pipetting error, a bubble in the electroporation cuvette, or degradation of the RNP complex only affecting the electroporations with the enhancers. A lack of DSB generation in these conditions could explain the apparent absence of both HDR and NHEJ.

These compounds were also tested during generation of the (c.*35C>A) KI. Here, the compounds were added to the media for 48 hours instead of just 24 hours. This was the first test of sgRNA 57 rv and there was a moderate to low activity of 18% Indels determined by ICE. Interestingly, addition of both HDR compounds to the media did not seem to inhibit NHEJ at the DSB generated by this sgRNA as there were 18% and 19% Indels estimated with M3814 and Alt-R HDR Enhancer respectively. However, HDR was also not increased with the addition of these compounds as every condition produced a predicted rate of 0% HDR.

4.1.3 Asymmetric repair template design had a small locus dependent effect on HDR

In addition to increasing HDR through addition of small molecules or compounds, several studies outlined in **Section 1.7.5** have investigated the effect of repair template design on HDR editing outcomes finding that asymmetric designs can result in the higher rates of HDR (Liang et al., 2017; Richardson et al., 2016; Skarnes et al., 2019; Y. Wang et al., 2018). After generating a DSB, Cas9 first releases the 3' end of the strand containing the PAM. This asymmetric release prompted Richardson and colleagues to design and test asymmetric repair templates complementary to the strand released first with longer overhangs on the PAM proximal side resulting in increased rates of HDR. Subsequent studies have also tested asymmetric repair template designs and observed increased HDR but exact design principles are not agreed upon and the optimal design seems to be locus dependent. Previous experiments in our lab have utilized asymmetric repair template design, and we also have been unable to detect a definitive pattern correlating design parameters to rates of HDR. Since the effect of repair template design seems to be region dependent, it requires testing at each locus. For both the COL4A1^{G755R} and (c.*35C>A) KIs, an asymmetric repair template was designed to have 67 bp on the PAM distal side and 33 bp on the PAM proximal side. Original symmetric template design used the sequence containing the sgRNA to prevent binding of the template with the sgRNA. The new template sequence, however, was generated from the strand complementary to the sgRNA and the strand released first by Cas9. An initial test using an asymmetrically designed repair ssODN for the COL4A1^{G755R} mutation slightly increased HDR **(Figure 3.11)**. Visual inspection of the highlighted C seems to reveal a marginally higher T bump indicative of the COL4A1^{G755R} mutation when the asymmetric repair template is delivered. ICE approximation confirms this with an estimated 5% and 9% rate of HDR for the symmetric and asymmetric repair templates respectively. In this experiment, changing from the BTX electroporation system to the Lonza 4D nucleofector notably increased Indel formation from 56% to 88%. Despite increased Indels in the Lonza 4D nucleofector, the rate of HDR did not clearly increase with the symmetric repair template.

An asymmetrically designed repair template for the (c.*35C>A) KI was also tested. Here, the Lonza electroporation system again increased Indel generation, albeit to a lesser extent, from 18% to 23%. However, both repair template designs did not generate enough KI alleles to be detected by the ICE algorithm. The locus-dependent increase of HDR with an asymmetric repair template design is in line with previous experiments conducted in our lab.

4.1.4 Single cell KI clones could not be generated without Indels in the absence of blocking mutations

Generation of both the COL4A1^{G755R} and (c.*35C>A) KIs via the HDR pathway proved challenging in congruence with low reported rates of HDR in mammalian cells (G. Li et al., 2017; Paquet et al., 2016; Pickar-Oliver & Gersbach, 2019). Blocking mutations increase the efficiency of HDR editing by preventing Cas9 nuclease activity after the mutation is incorporated in the DNA (Paquet et al., 2016).

By design, the COL4A1^{G755R} mutation blocks the most proximal base relative to the PAM of sgRNA 45 rv and should prevent sgRNA 45rv from binding and re-cutting the HDR-edited allele. Nevertheless, identifying a single cell HDR clone without additional Indels was not achieved even with HDR enhancing compounds or alternative ssODN designs. After screening 800 clones, 20 single cell clones incorporated the COL4A1^{G755R} mutation on at least 1 allele but also had additional Indels indicating HDR was occurring but not preventing re-cutting.

The initial design of the (c.*35C>A) KI did not include a blocking mutation. The closest possible sgRNA (sgRNA 57 rv) cuts the DNA 8 bp away from the mutation. This region of DNA is a noncoding region making it impossible to implement a silent protein coding mutation. Initial attempts to knock-in the (c.*35C>A) mutation were plagued with exceedingly low rates of HDR. Moreover, sgRNA 57 rv only generated 23% Indels even with the Lonza 4D nucleofector. Nevertheless, 1,000 single cell clones were isolated and screened for the (c.*35C>A) KI. The HDR editing rate was non-zero as sequencing revealed 17 clones with the KI on at least one allele. Unfortunately, all of these clones also harbored Indels similar to the clones edited at the COL4A1^{G755R} locus.

4.1.5 Blocking mutations substantially increase HDR

A new editing strategy implementing two silent blocking mutations was designed for the COL4A1^{G755R} KI. With the addition of the silent mutations, one base of the PAM and the two most PAM proximal bases of the sgRNA are blocked. The protein sequence is unaltered outside of the disease causing glycine to arginine substitution. Electroporation using this new repair template with sgRNA45 rv resulted in 65% HDR editing determined by ICE. This is an unusually high rate of HDR exceeding rates of NHEJ generated by some sgRNAs in our workflow. The high rate of HDR allowed that only one plate of clones needed to be screened in this experiment and sequencing of 24 clones yielded 14 homozygous KI clones. Notably, there were no Indels generated in these 14 clones. Adding two blocking mutations increased the rate of HDR by more than 7-fold exemplifying the influence blocking mutations can have on DNA repair outcomes. Observation of increased HDR rates with blocking mutations close to the PAM is in congruence with previous reports (Okamoto et al., 2019; Paquet et al., 2016).

While blocking mutations promote efficient KI generation (Okamoto et al., 2019), it is impossible to design silent blocking mutations in non-coding regions such as the 3'-UTR of COL4A1 where the miR-29 binding site mutation is located. After single cell clones could not be generated with the (c.*35C>A) KI without additional Indels, a two-step editing scheme was designed based on CORRECT (Kwart et al., 2017). Since a single blocking mutation at the first base of the sgRNA binding site was not sufficient to easily generate a COL4A1^{G755R} KI clone, the first 3 bases that bind to the sgRNA were mutated in the first step of the (c.*35C>A) CORRECT design. The (c.*35C>A) mutation was also incorporated in this

step. This 3 base mutation ACA>GGG creates a new PAM for a new sgRNA in the 2nd step. It also ensures that when the GGG is converted back to ACA, the new PAM is destroyed and the cutting activity of the new sgRNA will be potently inhibited.

Electroporation for the 1st step of the (c.*35C>A) CORRECT editing strategy using the Lonza 4D nucleofector produced an estimated 80% Indels and 26% KI. There was a staggering increase of Indels in comparison to the previous edit without the 1st step CORRECT repair template (from 23% to 80%) with two possible explanations. The sgRNA complex could have not perfectly formed in the first experiment due to RNAase contamination or another unknown reason. We have observed in previous experiments in our lab with typically very active sgRNAs that in rare cases they seemingly lose all activity in RNP electroporations. RNAase contamination in an isolated experiment could degrade the sgRNA before it is complexed and delivered to the cells. However, in these experiments there is typically close to zero Indel generation and in the (c.*35C>A) electroporation there was 23% Indel generation making this explanation unlikely. Visual inspection of the sequencing trace from the 2nd experiment with 80% Indels suggests that many Indels are actually HDR for insertion of the "GGG" in about 30 to 40% of the sequences. However, because the peak for the (c.*35C>A) KI appears to be present in less than 10% of sequencing traces it seems that the ICE algorithm took these two events into account to estimate a rate of 26% HDR. Nonetheless, solely from visual examination from the sequencing reaction, it appears that the "GGG" was incorporated more efficiently than the (c.*35C>A) mutation confirming that mutations closer to the cut site of an sgRNA are more efficiently integrated (Paquet et al., 2016) even when the mutations are introduced on the same repair template. There were 27 heterozygous and 3 homozygous clones for the (c.*35C>A) KI identified. All of which were homozygous for the "GGG" mutation further suggesting that this mutation is more efficiently incorporated due to its proximity and sgRNA blocking potential.

The 2nd step electroporation of homozygous clone P2G6 was also very efficient with a 44% KI determined by ICE. At this locus, blocking mutations strategically placed at the most proximal 3 bases relative to the PAM or destroying the PAM itself effectively increased HDR repair outcomes and protected the KI from sgRNA re-cutting (Okamoto et al., 2019; Paquet et al., 2016).

4.1.6 HiFi Cas9 (R691A) mitigated off-target detection in the top 10 predicted *in silico* off-target regions

Unintended off-target editing can occasionally occur with the CRISPR/Cas9 system in regions almost complementary to the sgRNA. Single mismatches to the sgRNA, especially in the PAM distal region that binds to the sgRNA last, can be tolerated by Cas9 and the DNA can still be cleaved (Hsu et al., 2013). As the five homozygous COL4A1 frameshift clones were generated with WT Cas9 using sgRNA 15rv with a low specificity score of 68, the top 5 predicted *in silico* off-targets from the CFD and MIT algorithms were analyzed for off-target editing. Four of these five clones exhibited off-target editing denoted by double peaks indicating a DSB followed by error-prone NHEJ repair. Off-target regions predicted by both algorithms were affected and in two clones there were even multiple regions affected. There was only a single clone without detected off-target effects. However, given the high rate of off-targets (6 off-targets in 50 sequenced regions) it is conceivable that this clone could have an off-target effect at an unexamined region.

Additional COL4A1 KO clones were generated using a modified HiFi Cas9 (R691A) that is reported to tolerate sgRNA mismatches to a lesser extent resulting in reduced off-target effects (Vakulskas et al., 2018). Five more COL4A1 KO clones were generated by RNP delivery of HiFi Cas9 complexed with sgRNA 15 rv and sequenced at the same 10 predicted off-target regions. Astonishingly, there were no detected off-targets. This is in contrast to 12% of the sequenced regions exhibiting off-targets cutting from clones edited with WT Cas9. The low specificity of sgRNA 15 rv was useful to demonstrate the reduction of off-target activity with HiFi Cas9 and highlights the importance of selecting sgRNAs with high specificities.

The sgRNAs designed for the COL4A1^{G755R} KI as well as the 1st and 2nd step of the miR-29 CORRECT KI have specificity scores of 82, 76, and 78 respectively. Editing experiments using these sgRNAs were performed with HiFi Cas9 and the top 5 off targets from the MIT and CFD databases were always sequenced. The combination of selecting sgRNAs with higher specificities and utilizing HiFi Cas9 resulted in no further off-targets being detected.

4.1.7 Genome editing human iPSCs selects for a triplication of BCL2L1 on chromosome 20

During genome editing, iPSCs are abnormally stressed from culturing techniques such as electroporation and single cell plating. Stressful culture conditions can enrich for chromosomal alterations that adapt the cells to the harsh conditions. One of the most common changes is a partial or complete triplication of chromosome 20 that includes the BCL2L1 locus (Baker et al., 2016). BCL2L1 encodes the long, apoptotic protein Bcl-Xl that enhances human embryonic stem cell survival when overexpressed (Bai et al., 2012). Naturally, an additional copy of this gene could increase the survival of hiPSCs in stressful culture conditions.

There was a high frequency of apparent BCL2L1 triplication in single cell clones that were generated in this thesis. A qPCR using gDNA and primers amplifying BCL2L1 was used to analyze the copy numbers of this locus in edited single cell clones (Baker et al., 2016). Altogether, 56% (44 out of 79) of the single cell clones generated from the A18944 WT iPSC line seem to have a BCL2L1 triplication. Given this high rate of triplication, a mosaic triplication could have occurred at this locus before genome editing and cells with the survival-enhancing triplication may be favored during single cell clone generation. Strikingly, electroporation of karyotyped clone P2G6 and sub clone generation during the 2nd step of the (c.*35C>A) CORRECT editing did not produce any clones with a BCL2L1 triplication in the 15 tested sub clones. Even if the A18944 WT line is mosaic for trisomy, clone P2G6 would not be because it was generated from a single cell from the A18944 WT line and later karyotyped. Given that the editing procedures were performed exactly the same, the elimination of BCL2L1 triplication from edited P2G6 sub clones strongly suggests that the passage of the A18944 WT line used for editing is mosaic for a BCL2L1 triplication.

4.1.8 OnTEs were nearly absent across all editing experiments

We recently reported that CRISPR/Cas9 editing can generate OnTEs in up to 40% of hiPSC edited clones and described incidences of insertions, deletions, and complex rearrangements affecting single alleles (Weisheit et al., 2020). All of the COL4A1 mutants were analyzed for OnTEs by qgPCR as described in the nature protocols report (Weisheit et al., 2021). There were no copy number variations detected in the KO or DSM (double silent mutation) COL4A1^{G755R} clones tested by qgPCR. Although the qgPCR assay for exon 30 produced values slightly lower than 2, the values were much closer to 2 than 1.

Furthermore, the expression of COL4A1 was unaffected, further confirming the presence of two alleles. Finally, 4 clones from the 1st step and 15 from the 2nd step of the (c.*35C>A) CORRECT editing strategy were tested with a qgPCR assay. Out of all of these clones, there was only 1 clone with an abnormal copy number variation. Clone P1D5 from the 2nd step had a value of 2.96 indicating a triplication of this region. We have not previously observed an OnTE triplication but there is potentially one in this clone.

In addition to loss of an on-target allele, we reported both large and small regions of LOH after CRISPR/Cas9 editing (Weisheit et al., 2020). To test for small regions of LOH, heterozygous SNPs are identified close to the edit in the unedited WT line. These SNPs are subsequently genotyped after CRISPR/Cas9 editing to exclude LOH events at least as large as the distance between the DSB and the SNP. The SNPs rs12864958 and rs617478 were used to test for LOH in all 3 COL4A1 mutants. These SNPs range from 53 Kb and 20 Kb upstream and 34 Kb to 67 Kb downstream from the COL4A1 mutations. Genotyping these SNPs in all of the edited cell lines as well as karyotyping with a SNP microarray did not reveal any LOH events. Nonetheless, it still remains possible that LOH events smaller than the distance of these SNPs to the sgRNA cut site could have occurred and not have been detected. Ideally, SNPs would have been selected closer to the edit to potentially identify smaller regions of LOH. However, in this unedited WT line, several SNPs with a high minor allele frequency greater than 0.3 were genotyped and found to be homozygous. Seemingly, this region of the genome has very little variability in this cell line, so LOH would either only affect very few SNPs in this region with low impact on the phenotype of the edited cells, or could not occur at all if the region is completely homozygous.

4.1.9 Karyotyping via a SNP microarray confirms origin of single cell clones and suggests COL4A1 heterozygous KO lines could be derived from the same clone

All of the clones karyotyped with a SNP microarray were shown to have a potential triplication of around 500kb in the same region on chromosome 7, a triplication also observed in the parental cell line. In the two heterozygous KO clones P1D9 and P2H12, there was an additional potential triplication of 400kb identified on chromosome 12. Closer inspection of these clones reveals they have the same COL4A1 genotype (-8, WT). These clones were isolated from the same pool of edited cells suggesting that the same single cell clone was isolated twice. After electroporation, the cells are plated in one well and recover for a few days before being dissociated with Accutase and plated as single cells. An edited cell that has divided before the Accutase split would result in two single cell colonies from the original cell, and if the 400 Kb triplication on chromosome 12 occurred before cell division, it would be present in both subsequently isolated clones. Alternatively, but much more unlikely, this triplication occurred twice in isolated events in cells with the same COL4A1 genotype.

4.1.10 Pluripotency stainings performed for COL4A1 KOs reveal no evident loss of pluripotency

During the expansion of edited single cell clones from a 96-well to a 6-well plate, spontaneous differentiation is frequently observed. Differentiated cells are easily identified because they often have flatter morphology or create abnormal clumps or rings in the hiPSC colonies. Differentiated cells can be removed from the cultures by leaving EDTA on the cells for less time during splitting to keep the

flatter differentiated cells from detaching or scraping off the differentiated cells with a pipette tip under a microscope.

To confirm that expanded cell lines remain in a pluripotent state, expression of the pluripotency markers Nanog, Tra-160, SSEA4, and Oct-4 can be examined. These pluripotency markers were analyzed in the COL4A1 KO cell lines by immunofluorescence staining without detection of irregularities. Due to time constraints, the COL4A1^{G755R} and (c.*35C>A) KI clones were never examined. However, the hiPSCs from these KI clones had no apparent morphological differences compared to WT hiPSCs and exhibited little to no spontaneous differentiation. The absence of spontaneous differentiation indicates a high likelihood of pluripotent hiPSCs. Furthermore, endothelial cells and smooth muscle cells were differentiated from the COL4A1^{G755R} KI and endothelial cells, smooth muscle cells, and pericytes from the (c.*35C>A) KI with no obvious difference of differentiation efficiency compared to WT hiPSCs. This suggests that the hiPSCs maintained pluripotency during editing and that the mutations do not have a major impact on the capability of these vascular cell types to be differentiated. However, this was not systematically investigated and only mesoderm derived differentiations were performed with these cells. Further experiments demonstrating expression of pluripotent markers in the KI iPSCs and measurement of differentiation efficiency into vascular cell types would determine the impact, if any, of the COL4A1 mutations on vascular differentiation capability.

4.2 Characterization of Collagen IV expression in the COL4A1 mutants

CRISPR/Cas9 KO generation leverages the error-prone NHEJ repair pathway to induce a frameshift in a coding region that introduces a premature termination codons (PTCs) in the mRNA. This in turn initiates NMD of the mRNA creating a gene KO (Shalem et al., 2015). However, the presence of a PTC does not always dictate that NMD will occur and gene expression will be completely ablated. Alternative splicing and exon skipping have been widely reported in CRISPR/Cas9 edited cells occasionally resulting in incomplete protein KO or expression of mutant protein isoforms (Kapahnke et al., 2016; Mou et al., 2017; Tuladhar et al., 2019). NMD typically does not result from PTCs less than 50-55 nucleotides upstream of an exon-exon border because the exon junction complex (EJC), which is responsible for initiating the NMD pathway, is removed from the mRNA. If a PTC lies more than 50-55 nucleotides upstream from the exon-exon border, the EJC is less likely to be removed allowing NMD to occur (Popp & Maquat, 2016).

Mutations in the two families with a COL4A1 reduction both have a -1 frameshift that introduces a PTC 54 nucleotides from the exon 31-32 border (Lemmens et al., 2013). There was NMD of the mutant COL4A1 transcripts in both of these families. Generation of the COL4A1 KO with sgRNA15 rv targets the exact location of the (c.2085del) in family A of the study. A -1 frameshift here introduces the same PTC and should also cause NMD. Moreover, the other possible frameshift (-2) at this location introduces a PTC that is 91 nucleotides upstream from the exon 29-30 border and should similarly result in COL4A1 mRNA NMD.

If NMD occurs in frameshift alleles, assuming no compensating expression mechanism, heterozygous KO clones would be expected to have a reduction to approximately half of the levels of COL4A1 mRNA compared to the WT and the homozygous KOs would be expected to have a severe reduction. The expression of COL4A1 and COL4A2 was examined by qPCR in endothelial cells with a homozygous and heterozygous KO genotype with results exactly in line with this prediction. Homozygous KO clones

P1H10 and P2H5 both have less than 10% COL4A1 mRNA relative to the WT and the heterozygous clones P1D9 and P2H12 exhibited 80% and 50% of COL4A1 mRNA relative to the unedited WT. Moreover, normalization of COL4A1 mRNA to COL4A2 mRNA reveals that both of these heterozygous KO clones have nearly half of the ratio of COL4A1 to COL4A2.

Furthermore, collagen IV immunofluorescence staining of 2D-cultured endothelial cells from heterozygous KO clone P2H12 and homozygous KO clone P1H10 mirrors the qPCR results. There is an obvious decrease of fluoresce in the collagen IV heterozygous KO that is further reduced in the homozygous KO. It must be noted, however, that this collagen IV antibody is not specific and reacts with all 6 collagen IV α chains. Nonetheless, while not presently confirmed in this model, it is very probable that COL4A1 and COL4A2 are the predominantly expressed α chains. Brain specific endothelial cells principally express COL4A1 and COL4A2 (Xu et al., 2019), but these cells are in 2D monoculture and have not received signals from other NVU cells so they may not be entirely brain specific. Nonetheless, α1 and α2 are solely expressed during early embryonic development (Khoshnoodi et al., 2008) and hiPSC-derived cells often display a fetal cell phenotype. For example, mesenchymal stem cells (MSCs) derived from iPSCs develop a fetal transcriptomic signature and secretome regardless of the age of the donor (Spitzhorn et al., 2019). Additionally, iPSC-derived neurons are known to express primarily the fetal 0N3R tau isoform (Miguel et al., 2019). Therefore, it can be speculated that hiPSC-derived ECs predominantly express the α1 and α2 chains of collagen IV.

4.2.1 COL4A1 and COL4A2 mRNA seem to fluctuate in hiPSC-EC cultures

During angiogenesis, there is a distinction between leading tip cells that migrate towards VEGF gradients and the following stalk cells that proliferate to form a lumen and support the elongation of the vessel. Leading tip cells predominantly express VEGFR2 with low notch1 signaling and stalk cells express more VEGFR1 resulting from high notch1 (Blanco & Gerhardt, 2013). VEGFR2 is the principle mediator of VEGF produced angiogenesis and is responsible for migration, survival, proliferation, and tube formation. Contrastingly, VEGFR1 serves as a decoy receptor thereby limiting the VEGF activity in the cell (Blanco & Gerhardt, 2013). Notch signaling has long been known to be an important mediator of cell cycle arrest and contact inhibition in endothelial cells (Noseda et al., 2004). Recently, notch1 signaling was demonstrated to control the activity of GTPase rab10 that was necessary for LH3 trafficking to collagen IV containing vesicles and consequently collagen IV secretion (Gross et al., 2021). Building from this, tip cells with high VEGFR2 and VEGF signaling in combination with low notch signaling would exhibit stunted collagen IV secretion while trailing stalk cells with higher VEGFR1 expression and notch1 signaling would support secretion of collagen IV into the BM to stabilize the formed vessel.

Given the difficulty to predict the complicated interplay of signaling pathways of tip cells and stalk cells in 2D EC cultures, it is likely difficult to assess small changes of COL4A1 mRNA that may result from the (c.*35C>A) KI. After endothelial cells are plated following a split or MACS sorting, they rapidly proliferate until a confluent layer is formed. At some point, the confluent endothelial cells will undergo contact inhibition and upregulate notch signaling. Small differences in plating density could potentially impact the timing of contact inhibition in a given culture, drastically impacting gene expression especially at the mRNA level. Following MACS sorting, the CD-144 fraction is counted with a Neubauer chamber and plated. Counting cells with this method can produce errors estimated to be around 10% in either direction (Collins et al., 2010). Such variability may mask the effect of genetic COL4A1

mutations, which could potentially explain why there was no detected increase of COL4A1 in the (c.*35C>A) KI endothelial cells.

4.2.2 Silent mutations incorporated in the COL4A1^{G755R} KI do not impact COL4A1 expression

Mutations that alter the DNA sequence of a protein-coding gene but retain the same protein sequence are typically characterized as "silent" mutations. However, these mutations are not always innocuous as they can alter splicing and mRNA folding leading to changes in protein expression (Chamary & Hurst, 2009). COL4A1^{G755R} carriers have a (c.2263 G>A) mutation that changes the codon from "GGG" for glycine to "AGG" for arginine. However, in the DSM COL4A1^{G755R} hiPSCs clone the codon for arginine in this position is "AGA". Moreover, the codon for proline in position 754 was changed from "CCC" to "CCU". Even though these codons frequently appear in the COL4A1 transcript and makeup roughly one third of the codons for both of these amino acids, COL4A1 expression could still be affected by the integrated silent mutations. An initial qPCR experiment analyzing COL4A1 and COL4A2 in DSM COL4A1^{G755R} KI endothelial cells seems not to confirm this hypothesis. Although there appears to be a slight reduction in COL4A1 upon first glance, there is no effect if COL4A1 is normalized to COL4A2. Slight differences in culture conditions described in **section 4.2.2** likely explain the small observed difference prior to COL4A1 normalization.

4.2.3 COL4A1^{G755R} KI endothelial cells readily secrete collagen IV in 3D

The COL4A1^{G755R} mutation causes cSVD with ICH and white matter disease in the absence of porencephaly (Jeanne & Gould, 2017). Glycines in the triple helix domain are nudged towards the center of the heterotrimer triple helix through hydrophobic interactions and easily fit there due to their small size (Chioran et al., 2017). Heterotrimer formation is likely affected by the COL4A1^{G755R} mutation that replaces a glycine with a large polar arginine in the triple helix domain. Secretion of collagen IV only occurs with fully formed and post-translationally modified heterotrimers. Furthermore, the extent of intracellular collagen IV accumulation in mice is correlated with the position of the glycine mutations. Mutations in the triple helix domain closer to the NC1 domain result in higher intracellular accumulation (Jeanne & Gould, 2017). It is believed that missense mutations near the beginning of the formation of the triple helix, next to the NC1 domain, are more deleterious to proper folding of the helix. The COL4A1^{G755R} mutation occurs around the middle of the triple helix domain and it is unclear how this mutation affects triple helix formation and secretion. Affected patients harbor a heterozygous mutation but the hiPSCs generated have a homozygous incorporation of the COL4A1^{G755R} mutation. This implies that in patients, assuming each allele is equally expressed and localized in the ER, 25% of the heterotrimers will be unaffected, 50% have one affected α1 chain, and 25% have both affected α1 chains (Kuo et al., 2012). In the hiPSC model, the DSM COL4A1^{G755R} KI cells will express the mutation on all α1 chains further challenging heterotrimer formation.

Immunofluorescence staining of collagen IV in the 3D cultures generated by COL4A1^{G755R} KI endothelial cells illustrates substantial collagen IV in the extracellular space. Importantly, the collagen IV must have been produced by the endothelial cells because they are embedded within a fibrin gel. In 2D cultures, collagen IV in the fetal bovine serum of the media can potentially be deposited on top of the cell layer through interactions with pre-existing laminin networks produced by endothelial cells. In the 3D cultures, this would only be possible if either the collagen IV in the serum of the media diffused through the fibrin gel or penetrated the endothelial cell barrier. Given that widespread collagen IV deposition

was not observed in 2D endothelial cell cultures with COL4A1 homozygous KO clone P1H10, there is very little to no collagen IV in the serum of the media and it is extremely unlikely that it contributed to the collagen IV deposition in the 3D experiment with the COL4A1^{G755R} KI. The deposition of collagen IV in the COL4A1^{G755R} KI culture appears comparable to the WT culture 11 days after tube formation. However, this needs to be repeated and quantified before concrete comparisons can be established.

Nevertheless, if there truly is comparable collagen IV secretion in a homozygous human mutant, ER stress is not a likely contributor to cSVD from this mutation. Moreover, if BM deposition is comparable to WT cells, cSVD progression in these patients is likely also not driven by a deficiency of collagen IV heterotrimers in the BM. Therefore, the most likely causal mechanism for disease progression would be deposition of mutant heterotrimers in the BM affecting the physiology in an unknown manner. The COL4A1^{G755R} mutation does not overlap with known binding sites for integrins, laminin, fibronectin, or HSPG (Parkin et al., 2011). Nonetheless, unknown binding sites for other molecules could be affected by this mutation or collagen IV networks formed with this mutation could be inherently unstable leading to an overall instability of the NVU that could increase the risk of ICH in patients. EM (electron microscopy) studies of mutant heterotrimers could potentially elucidate if there is an altered suprastructure that may contribute to an unstable BM.

4.2.4 Unexpected TEER measurement from KO: potential compensating mechanism or clonal effect?

Endothelial cells derived from the COL4A1 KO clone P1H10 display increased TEER values relative to the control WT cells on gelatin and fibronectin coatings. Both of these ECM molecules can bind to β1 integrins on the endothelial cell surface (Barczyk et al., 2010; Davidenko et al., 2016). Cell-matrix signaling regulated by β1 integrin binding ECM molecules has been shown to be necessary for normal AJ and TJ organization and function (Izawa et al., 2018; Osada et al., 2011; H. Yamamoto et al., 2015). If the COL4A1 KO endothelial cells upregulated integrin expression in response to a COL4A1 deficiency, increased integrin binding to a given substrate could enhance AJ and TJ expression and orientation to produce a tighter barrier. Furthermore, increased integrin expression on the cell surface could recruit abnormally high amounts of laminin to the cell surface to create an overcrowded and dysregulated extracellular matrix potentially explaining the strikingly thickened basement membrane observed in fibroblasts from patients with COL4A1 haploinsufficiency (Lemmens et al., 2013). Characterization of β1 integrin expression in KO endothelial cells through qPCR, western blot, and immunofluorescence can determine if there are differences between COL4A1 KO and WT endothelial cells.

However, two additional homozygous COL4A1 KO clones were differentiated into endothelial cells and failed to reproduce the increased TEER value demonstrated by clone P1H10. Differentiations with additional untested KO clones in parallel with clone P1H10 can elucidate the true effect of a COL4A1 KO on TEER. Moreover, a permeability assay using dextran could provide an alternative measurement that serves as a proxy for barrier strength. Since COL4A1 is the main scaffolding of the BM and provides necessary structural support to the NVU, it would not be surprising if the increased TEER observed with COL4A1 KO clone P1H10 was caused by a non-specific side effect of genome editing. During CRISPR/Cas9 editing, a single cell is edited and gives rise to an entire mutant cell line. If there are any genetic or epigenetic alterations in the original cell or in the first few dividing cells, the entire cell line will be impacted. To account for genetic changes, SNP karyotyping was used to ensure that large aberrations have not occurred. Furthermore, SNP genotyping probed for smaller events of LOH near

the edit. Lastly, off-target sequencing examined the ten most likely regions for off-target editing. However, it remains a possibility that an undetected region of LOH, off-target effect, or point mutation is present in clone P1H10 that affects the TEER in an unpredictable manner. Moreover, hiPSCs can be epigenetically unstable (Rebuzzini et al., 2016; Yoshihara et al., 2017) and single-cell clones can be affected in unexpected ways. To account for this, several clones with the same mutation can be used to help identify outliers that may have a phenotype driven by a clonal affect as opposed to the edited genotype.

4.3 Strengths and limitations of the monogenic COL4A1 cSVD human iPSC model

Every model organism or system has advantages that can be exploited, as well as limiting disadvantages. The hiPSC system has the obvious advantage that human cells are being directly investigated to study a human disease. Moreover, an *in vitro* system is easily manipulable allowing complete control of cell types and genotypes and is very easily visualized. This is an advantage compared to *in vivo* models where small capillaries are difficult to visualize and cellular control of genotypes is complicated. Nevertheless, because an entire organism is not recapitulated, complicated disease progression involving organ interactions, for instance, will fail to be represented *in vitro*. Moreover, the timescale of cell cultures is drastically different compared to disease progression in human patients and phenotypes may take longer to develop than is permitted by culture survival. In addition, 3D microfluidic devices can be restrictive in terms of experimental design and availability because researchers are limited to commercially available chip designs or require specialized knowledge to design and produce custom devices. Furthermore, it remains difficult to use these devices to model small capillaries in the range of 5 µm in diameter.

4.3.1 The 3D microfluidic *in vitro* system in this work provides easy visualization and complete cellular control

Direct visualization of the small cerebral vessels affected in cSVD is impossible in patients (Chojdak-Łukasiewicz et al., 2021). Visualization of cerebral vessels in live mice has been achieved with 2-photon imaging (Hill et al., 2015), and even optogenetic control of mural cells in the brain has been established (Tong et al., 2021). In some studies, the retinal vasculature has been explanted to serve as a proxy for the cerebral vasculature for live imaging measurements (Ratelade et al., 2020). These methods, however, are technically complicated and require specialized equipment. Conversely, *in vitro* systems allow unrestricted visual access as well as genetic manipulation of the system. Specifically, the microfluidic device used for 3D gel-embedded cultures in this work is compatible with microscopy of live and fixed cultures (Campisi et al., 2018). Individual cell types can be easily labelled with fluorescent reporters or encoded with optogenetic sensors. Moreover, independent differentiations of each NVU cell type warrants complete control of mutant and WT cellular combinations in co-cultures allowing the study of cell-specific contributions to disease phenotypes. Permeability assays using a fluorescent molecule such as dextran can easily be applied to this 3D culture system to investigate barrier integrity in real time. Taken together, unhindered visualization and control of cellular composition are clear advantages of the hiPSC model.

4.3.2 Comparison of animal models to a human cellular system

Mouse models have been extensively used to elucidate features of COL4A1 related cSVD (Jeanne & Gould, 2017; Joutel & Faraci, 2014; Ratelade et al., 2020). However, one primary goal of disease research is to develop treatments for disease and often human systems are required for drug screening and clinical translation. A mere 8% of cancer-treatment drugs deemed effective in mice translated to humans with a similar effect (Mak et al., 2014), and more than 400 clinical trials to treat Alzheimer's disease developed from animal models failed to be successful (King, 2018).

This does not detract from the value of mouse and other animal models. In fact, collagen IV α1 and α2 chains share 90.6% and 83.5% identity between mice and humans respectively (Muthukumaran et al., 1989). Other animal models have been used to examine collagen IV disease mutations as well as investigate basic collagen IV biology. Glycine substitutions in COL4A1 and COL4A2 orthologues in the C. elegans hinted at intracellular accumulation as a disease mechanism before it was detected in corresponding mouse models (Gupta et al., 1997). Studies in drosophila have demonstrated the importance of collagen IV to stabilize the BM (Borchiellini et al., 1996) as well as helped elucidate important aspects of collagen IV biology including the function of TANGO1 (M. Liu et al., 2017) and involvement of Rab-10 in collagen IV transport (Lerner et al., 2013). Animal models are advantageous because they encompass the entire organism but they lack human biology on a cellular level. Conversely, human models exemplify human biological context to fill this niche. Human cellular models are beginning to strive towards recapitulating more aspects of an organism by expanding in 3 dimensions with the development of organoids and other 3D culture systems (Campisi et al., 2018; C. Liu et al., 2018; Rowe & Daley, 2019). Great strides continue to be made to this effect but currently the complex biology of an entire organism cannot be fully recapitulated *in vitro*. Taken together, collagen IV disease related research will presently benefit the most by combining available *in vivo* and *in vitro* models and exploiting the strengths of each system.

4.3.3 Advantages and drawbacks of the 3D NVU model

The 3D microfluidic setup (Campisi et al., 2018) used in this thesis more accurately depicts the human brain vascular biology compared to 2D cultures. The 3D NVU model mimics angiogenesis with self-organized endothelial cell tubes. Moreover, the use of a fibrin gel dictates that the cells secrete their own ECM as opposed to adhere to a pre-coated ECM protein on a 2D surface.

Nevertheless, the system has some drawbacks. One major disadvantage is the cost and availability of the microfluidic devices used to generate the cultures. Each microfluidic chip costs around 25€ and can be used for 3 cultures that must be created simultaneously. Given that iPSC culture is typically an expensive endeavor, the cost of these microfluidic devices could hinder a project with a limited budget. Moreover, there is a single manufacturer of these devices and a limited number of distributors. The delivery of these microfluidic devices has proven to be problematic taking in the range of half of a year to arrive. However, a recently published protocol details how to construct these microfluidic devices in house and presents a possible solution (Hajal et al., 2022). Not only would this eliminate most of the associated cost and create unlimited accessibility, but it would also confer design flexibility. Requiring specialized knowledge, assembling the microfluidic devices in-house would be difficult to set up but once established would provide substantial benefits.

Due to their small size, there is limited cellular material available for mRNA and protein analysis from experiments in these microfluidic devices. Manufacturing the device in-house would eliminate this problem as larger devices could be designed. This would likely support qPCR analysis and RNA-seq

methods as well as protein analysis by western blot. A proteomics study, however, would be inherently difficult because separation of the cellular components from the fibrin gel remains a challenge and the abundance of fibrin would dilute out the signal from other proteins in mass spectrometry analysis.

Lastly, these 3D microfluidic cultures are designed to more closely mimic *in vivo* processes. However, in our hands the cultures do not consistently survive for more than 2 weeks. These cultures are short-lived and the conditions remain constant. However, human brain development continues with a massive production of astrocytes just after birth (Robertson, 2014), myelination lasts several decades (Jakovcevski et al., 2009), and the brain vasculature responds to external neural activity by adjusting cerebral blood flow to meet nutritional and oxygen requirements (Ashby & Mack, 2021), and the vasculature must constantly adapt to a changing brain. Presently, the 3D microfluidic cultures do not fully recapitulate an adaptive cerebral vasculature. Moreover, patients will COL4A1 disease mutations do not display cSVD symptoms for the first several decades of life (Lemmens et al., 2013; Verdura et al., 2016), which makes it very challenging to model the disease in a two-week 3D culture. Collagen IV deposition was visible after 11 days in the 3D cultures but should continue to increase with a longer culturing time. Increased production and/or deposition of collagen IV should reproduce more aspects of cSVD and greatly improve this model. Extending the culturing time of the microfluidic 3D cultures by enhancing their survival would greatly improve their value in disease modeling.

4.3.4 Application of flow to the 3D NVU model

Introducing physiological flow in these cultures will likely improve the lifetime of these cultures. This would not only provide a constant supply of oxygen and nutrients to the cells, but also subject the cells to shear stress which is an important regulator of gene expression in endothelial cells. It has been established that flow-induced sheer stress causing morphological changes to ECs making them become elongated and oriented in the direction of flow (Galbraith et al., 1998). Apoptotic pathways have been shown to be inhibited in ECs by shear stress (Dimmeler et al., 1996). Moreover, nitric oxide synthase (Uematsu et al., 1995) and TJs such as occludin and ZO-1 (Chistiakov et al., 2017) are demonstrated to increase in ECs under shear stress.

An additional potential benefit of long term cultures is the replacement of the fibrin gel with cell-generated ECM. Fibrin is primarily found in blood clots and plays an essential role in wound healing (Laurens et al., 2006). When necessary, plasmins (H. Smith & Marshall, 2010) and MMPs (Hotary et al., 2002) can degrade fibrin. If long-term cultures can be established, it is conceivable that most or all of the fibrin is degraded and replaced with ECM deposited by the cultured cells, which would more closely recapitulate the BM of the human brain.

Moreover, integrins form focal adhesion complexes on the endothelial cell surface binding to laminins and collagen IV in the BM. There is evidence that these integrins can act as force sensors measuring the shear stress induced by blood flow (Chistiakov et al., 2017; Kechagia et al., 2019). In COL4A1 mutant cultures, especially the COL4A1^{G755R} where the COL4A1 structure is modified, there could be a deficit of integrin binding causing a phenotype that may only be detected with a culture subjected to flow. Taken together, the enormous impact shear stress has on the endothelial cell phenotype makes it a critical aspect to model within the 3D NVU *in vitro* model.

4.4 Outlook and future perspectives

There are several experiments that can build on what has been described in this thesis. The main part of this thesis focused on the generation of the COL4A1 mutant cell lines, and this has been successfully achieved. The path to elucidate disease-relevant phenotypes using these cell lines has been paved and begun to be traversed. In this section, the most important follow-up experiments are outlined.

4.4.1 Determination of a conclusive effect of COL4A1 mutations on TEER

Given that ECs from KO clone P1H10 consistently produced higher TEER values compared to WT ECs but two other KO clones produced lower values in a single experiment, it remains to be determined what the true effect the COL4A1 KO is on TEER and barrier properties. EC differentiations should be repeated with these two KO clones in parallel with clone P1H10 and monocultures TEER experiments should be repeated at least 3 independent times. If there are still conflicting results, the 4 homozygous KO clones that have off-target effects can also be tested under the assumption that the off-target effect will not have an impact on the barrier strength.

Once a conclusive effect of COL4A1 KO is determined, a rescue experiment could be performed in which COL4A1 is expressed in the KO ECs by delivery of COL4A1 mRNA via LNPs, for example, while the TEER is measured to determine if the loss of COL4A1 is responsible for the changed TEER value. Even simpler, to determine if intracellular or extracellular loss of COL4A1 contributes to the altered barrier, the ECs can be plated on collagen-IV coated transwells for a TEER measurement.

The TEER values generated by DSM COL4A1^{G755R} and (c.*35C>A) KI endothelial cells should be evaluated. Since the tested COL4A1 KO clones produced conflicting results, at least 3 clones should be tested for each KI. Currently, there is only 1 completely quality controlled KI clone for each mutation but there are 4 additional genotyped clones with a homozygous COL4A1^{G755R} mutation and 13 with the (c.*35C>A) mutation that can be used to corroborate a TEER experiment with the quality-controlled clone. Only if conflicting TEER results are observed do additional clones need to be subjected to further QC experiments.

Nonetheless, the (c.*35C>A) KI may not have a drastic impact on the TEER as the phenotype would be the result of slight increases of the collagen IV α1 chain that likely take longer to develop than the length of a standard TEER experiment. The COL4A1^{G755R} KI, conversely, seems to secrete mutant collagen IV that may differentially impact BM stability or impact physiological cell-matrix signaling. In agreement with previous reports, addition of ascorbic acid to the media increased COL4A1 and COL4A2 on the mRNA level in both WT and COL4A1^{G755R} KI ECs (Kishimoto et al., 2013). Supplementation with ascorbic acid could exacerbate a collagen IV related phenotype and should be tested in a TEER experiment.

A co-culture TEER experiment with the incorporation of mural cells is an important experiment after monoculture TEER is characterized for the COL4A1 mutants. Mural cells produce more collagen IV than endothelial cells (Vanlandewijck et al., 2018), and this has been confirmed in our iPSC-derived SMCs and PEs on the mRNA level. Especially for the COL4A1^{G755R} KI where secretion of mutant collagen IV could be driving the cSVD phenotype, addition of mural cells should deposit more collagen and intensify any phenotype in comparison to WT cells. Finally, addition of astrocytes to create a triculture will increase the physiological relevance. Astrocytes secrete several signaling factors that upregulate TJs in ECs (Abbott et al., 2006; Alvarez et al., 2011; Dehouck et al., 1990) that could increase TEER and tease out small differences such as those expected from the (c.*35C>A) mutation.

In addition, dextran permeability assays would provide a complementary measurement of barrier strength in the COL4A1 mutants. Given that breakdown of the BBB in cSVD and stroke can be attributed to disruption or loss of TJs (Quick et al., 2021; Y. Yang et al., 2007), it is imaginable that the COL4A1 disease causing mutations cause TJ abnormalities thereby decreasing both TEER and permeability values.

4.4.2 Complete characterization of TJs expression and organization

Mentioned above, there is a breakdown of the BBB in cSVD that is likely caused by defective TJs. To investigate this in COL4A1 monogenic cSVD, close examination of TJ expression and organization should be performed for all of the COL4A1 mutants. It is conceivable that TJ structure and/or expression is affected and could be an indicator of a possible disease mechanism. Collagen IV binds to β1 integrins on the endothelial cell surface (Barczyk et al., 2010). Moreover, collagen IV signaling through β1 integrins is necessary for normal VE-Cadherin, claudin-5, occludin, and ZO-1 expression as well as organization and is an important component for BBB maintenance and microvessel stability (Izawa et al., 2018; Osada et al., 2011; H. Yamamoto et al., 2015). Therefore, key AJ and TJ proteins should be systematically analyzed by immunofluorescence. Seeding density should be carefully controlled in order to achieve comparable densities of fixed cells and quantifications should be made of the mean fluorescence of the junction proteins normalized to DAPI. Additionally, high magnification images should be captured and junctional boundaries closely inspected to distinguish discontinuous junctions that could be present in the mutants. Finally, EM studies can help elucidate difference in TJ structure between WT and COL4A1 mutants.

4.4.3 Quantification of ER stress and intracellular accumulation of collagen IV

Collagen IV mutations have been reported to cause intracellular accumulation of the protein (Jeanne et al., 2015; Jeanne & Gould, 2017; Joutel et al., 2016; Murray et al., 2014). This has been considered a potential collagen IV disease mechanism as intracellular retention can initiate the unfolded protein response (UPR) and cause ER stress (F. Jones et al., 2016; Murray et al., 2014; D. Wang et al., 2017).

One method to examine intracellular accumulation of collagen IV in mutant cells exploits the capability of bacterial collagenase to digest the collagenous triple helix domain but not the 7S or NC1 domains thereby preserving their quaternary structure. Secreted heterotrimers form dimers through sulfilimine bonds between two NC1 domains and this never occurs intracellularly (Vanacore et al., 2009). A western blot following a collagenase digest using an NC1 domain specific antibody can discriminate between dimers and monomers (Boudko et al., 2018). Given that dimers only form outside the cell, a decrease of dimers relative to monomers would suggest that less collagen IV is being secreted. While this is an indirect method, differences between NC1 monomers and dimers can be attributed to the COL4A1 mutations and a reduction of extracellular dimers may correlate with increased ER stress. Consequently, ER stress should be investigated in parallel to further support and strengthen the results from this experiment.

ER stress can be directly analyzed by qPCR and WB in 2D endothelial cell and mural cell cultures. Commonly used ER stress markers include ATF6, eIF2α, CHOP, and BiP as well as the UPR markers Dnajb1 and PDAI3 (Abdullahi et al., 2017). Moreover, tunicamycin can be used as a positive control to induce ER stress within the *in vitro* hiPSC model (Abdullahi et al., 2017). Most likely, the highest levels of ER stress and intracellular accumulation will be observed in the homozygous COL4A1 KO because

the α2 chain is still expressed on the mRNA level, it cannot form heterotrimers, and in endothelial cells it seems to be localized intracellularly in distinct punctate **(Figure 3.28)**. As mentioned previously, these punctate can be quantified and a correlation between their number and ER stress should be closely examined.

4.4.4 RNA-seq and proteomics study of COL4A1 mutants

COL4A1 mRNA expression in the mouse brain is highest in pericytes followed by SMCs and ECs (Vanlandewijck et al., 2018). Preliminary data from the hiPSC-derived cells in this thesis mirrors the same trend. COL4A1 mRNA expression was highest in WT hiPSC-derived pericytes compared to SMCs and ECs. Moreover, a significant increase of COL4A1 was only observed in pericytes derived from the (c.*35C>A) KI. Therefore, an RNA-seq and proteomics study of (c.*35C>A) KI pericytes as well as COL4A1^{G755R} KI and COL4A1 heterozygous and homozygous KO pericytes would be particularly interesting. The high expression of collagen IV in pericytes combined with a monogenic cSVD COL4A1 mutation is very likely to generate transcriptomic and proteomic changes related to a disease phenotype. Bulk RNA sequencing and proteomics of 2D COL4A1 mutant pericytes would yield several differentially expressed genes that could be further investigated and connected to cSVD. Moreover, an RNA-seq and proteomics study could be used to confirm results from other experiments such as an ER stress pathway analysis. Finally, if there are interesting results from TEER experiments, TJ analysis, or even β1 integrin expression, an RNA-seq and proteomics study on the affected mutant ECs could be used to further investigate the affected pathway.

4.4.5 Characterize the COL4A1 mutants in 3D microfluidic cultures

Preliminary experiments demonstrated that the COL4A1^{G755R} mutation does not completely abolish the secretion of collagen IV in 3D cultures. The extent of collagen IV deposition by COL4A1^{G755R} KI endothelial cells should be quantified and compared to the WT. The same experiment and quantification should be performed for the (c.*35C>A) KI and both COL4A1 KO genotypes to get a better understanding about the extent of collagen IV secretion by these mutants in 3D. Moreover, it will be interesting to examine if the same collagen IV α2 punctate observed in 2D are also present in 3D cultures.

Given that collagen IV is the main stabilizing molecule of the BM (Reed et al., 2019), COL4A1 mutants may not establish a complete collagen IV network to sufficiently stabilize vessels predisposing patients to ICH. Dextran permeability assays of 3D cultures that have had sufficient time to generate an ECM may elucidate small differences caused by these COL4A1 mutations. However, COL4A1 and COL4A2 null mice do not display impaired basement membrane formation (Pöschl et al., 2004) and COL4A1$^{\Delta ex41}$mutant mice do not exhibit cerebral hemorrhaging when a surgical birth is performed suggesting that the vasculature is properly formed but fragile without the stability conferred by normal collagen IV in the BM (Gould et al., 2006). Seemingly, even the most drastic COL4A1 mutations do not impact the vasculature directly but rather destabilize it and predispose it to damage from previously benign stressors. Static 3D cultures do not impose much stress on the endothelial cell tubes. Exposing the cultures to external stress may be imperative to effectively elucidate differences caused by the COL4A1 mutants and using a pump system to introduce flow could achieve this. Different levels of pressure can be applied to the cultures while dextran is perfused. Using the ibidi pump, the pressure

can be increased stepwise until the cultures rupture. This could elucidate small differences of vessel stability between cultures of different genotypes.

4.5 Conclusion

There are several mutations identified in COL4A1 associated with cSVD. The majority of mutations are glycine substitutions in the triple helix domain but other mutations such as frameshifts and 3'-UTR mutations have also been reported and linked to cSVD. However, the specific disease mechanisms remain unknown. COL4A1 mouse models have yielded numerous insights furthering our understanding of monogenic COL4A1 cSVD. However, complementary human models have been underutilized in COL4A1 cSVD research.

In this work, hiPSC and CRISPR/Cas9 technology were exploited to provide the tools to investigate the contribution of three distinct familial COL4A1 cSVD causing mutations within a human system. A frameshift KO (ClinVar: VCV000161440.4), triple helix domain glycine substitution COL4A1^{G755R} (ClinVar: VCV000161974.16), and 3'-UTR (C.*35C>A) PADMAL mutation (ClinVar: VCV000689432.1) were independently edited into the genome of separate hiPSC lines using the versatile CRISPR/Cas9 system. These generated hiPSC lines were rigorously quality controlled.

Finally, the collagen IV expression was characterized in these lines. The frameshift KO was found to have intracellular α2 puncta in differentiated endothelial cells. In 3D cultures, the COL4A1^{G755R} KI does not completely inhibit the secretion of collagen IV by endothelial cells. Pericytes express more collagen IV than smooth muscle cells and endothelial cells on an mRNA level and exhibit increased COL4A1 expression in the (c.*35C>A) mutant. At this preliminary stage, there are no definitive links between the mutations and cSVD but the tools to elucidate them have been developed. The experiments outlined in **section 4.4** may uncover mechanisms that link these mutations to cSVD.

5. References

Abbott, N. J., Rönnbäck, L., & Hansson, E. (2006). Astrocyte-endothelial interactions at the blood-brain barrier. *Nature Reviews Neuroscience*, 7(1), 41-53. https://doi.org/10.1038/nrn1824

Abdullahi, A., Stanojcic, M., Parousis, A., Patsouris, D., & Jeschke, M. G. (2017). Modeling Acute ER stress in vivo and in vitro. *Shock*, *47*(4), 506–513. https://doi.org/10.1097/SHK.0000000000000759

Aird, E. J., Lovendahl, K. N., st. Martin, A., Harris, R. S., & Gordon, W. R. (2018). Increasing Cas9-mediated homology-directed repair efficiency through covalent tethering of DNA repair template. *Communications Biology*, *1*(1), 54. https://doi.org/10.1038/s42003-018-0054-2

Allen, F., Crepaldi, L., Alsinet, C., Strong, A. J., Kleshchevnikov, V., de Angeli, P., Páleníková, P., Khodak, A., Kiselev, V., Kosicki, M., Bassett, A. R., Harding, H., Galanty, Y., Muñoz-Martínez, F., Metzakopian, E., Jackson, S. P., & Parts, L. (2019). Predicting the mutations generated by repair of Cas9-induced double-strand breaks. *Nature Biotechnology*, *37*(1), 64–72. https://doi.org/10.1038/nbt.4317

Alvarez, J. I., Dodelet-Devillers, A., Kebir, H., Ifergan, I., Fabre, P. J., Terouz, S., Sabbagh, M., Wosik, K., Bourbonnière, L., Bernard, M., van Horssen, J., de Vries, H. E., Charron, F., & Prat, A. (2011). The hedgehog pathway promotes blood-brain barrier integrity and CNS immune quiescence. *Science*, *334*(6063), 1727–1731. https://doi.org/10.1126/science.1206936

Ando, Y., Okada, H., Takemura, G., Suzuki, K., Takada, C., Tomita, H., Zaikokuji, R., Hotta, Y., Miyazaki, N., Yano, H., Muraki, I., Kuroda, A., Fukuda, H., Kawasaki, Y., Okamoto, H., Kawaguchi, T., Watanabe, T., Doi, T., Yoshida, T., … Ogura, S. (2018). Brain-Specific Ultrastructure of Capillary Endothelial Glycocalyx and Its Possible Contribution for Blood Brain Barrier. *Scientific Reports*, *8*(1), 17523. https://doi.org/10.1038/s41598-018-35976-2

Andrae, J., Gallini, R., & Betsholtz, C. (2008). Role of platelet-derived growth factors in physiology and medicine. *Genes and Development*, 22(10), 1276–1312). https://doi.org/10.1101/gad.1653708

Andreone, B. J., Chow, B. W., Tata, A., Lacoste, B., Ben-Zvi, A., Bullock, K., Deik, A. A., Ginty, D. D., Clish, C. B., & Gu, C. (2017). Blood-Brain Barrier Permeability Is Regulated by Lipid Transport-Dependent Suppression of Caveolae-Mediated Transcytosis. *Neuron*, *94*(3), 581–594. https://doi.org/10.1016/j.neuron.2017.03.043

Annes, J. P., Munger, J. S., & Rifkin, D. B. (2003). Making sense of latent TGFβ activation. In *Journal of Cell Science*, 116(2), 217–224. https://doi.org/10.1242/jcs.00229

Armulik, A., Genové, G., & Betsholtz, C. (2011). Pericytes: Developmental, Physiological, and Pathological Perspectives, Problems, and Promises. *Developmental Cell*, 21(2), 193–215. https://doi.org/10.1016/j.devcel.2011.07.001

Ashby, J. W., & Mack, J. J. (2021). Endothelial Control of Cerebral Blood Flow. *American Journal of Pathology*, 191(11), 1906–1919. https://doi.org/10.1016/j.ajpath.2021.02.023

Aumailley, M., Bruckner-Tuderman, L., Carter, W. G., Deutzmann, R., Edgar, D., Ekblom, P., Engel, J., Engvall, E., Hohenester, E., Jones, J. C. R., Kleinman, H. K., Marinkovich, M. P., Martin, G. R., Mayer, U., Meneguzzi, G., Miner, J. H., Miyazaki, K., Patarroyo, M., Paulsson, M., … Yurchenco, P. D. (2005). A simplified laminin nomenclature. *Matrix Biology*, 24(5), 323–332. https://doi.org/10.1016/j.matbio.2005.05.006

Ayloo, S., & Gu, C. (2019). Transcytosis at the blood–brain barrier. *Current Opinion in Neurobiology*, 57, 32–38. https://doi.org/10.1016/j.conb.2018.12.014

Ayloo, S., Lazo, C. G., Sun, S., Zhang, W., Cui, B., & Gu, C. (2022). Pericyte-to-endothelial cell signaling via vitronectin-integrin regulates blood-CNS barrier. *Neuron*, *110*(10), 1641–1655. https://doi.org/10.1016/j.neuron.2022.02.017

Bader, B. L., Smyth, N., Nedbal, S., Miosge, N., Baranowsky, A., Mokkapati, S., Murshed, M., & Nischt, R. (2005). Compound Genetic Ablation of Nidogen 1 and 2 Causes Basement Membrane Defects and Perinatal Lethality in Mice. *Molecular and Cellular Biology*, *25*(15), 6846–6856. https://doi.org/10.1128/mcb.25.15.6846-6856.2005

Baeten, K. M., & Akassoglou, K. (2011). Extracellular matrix and matrix receptors in blood-brain barrier formation and stroke. *Developmental Neurobiology*, *71*(11), 1018–1039. https://doi.org/10.1002/dneu.20954

Bai, H., Chen, K., Gao, Y. X., Arzigian, M., Xie, Y. L., Malcosky, C., Yang, Y. G., Wu, W. S., & Wang, Z. Z. (2012). Bcl-xL enhances single-cell survival and expansion of human embryonic stem cells without affecting self-renewal. *Stem Cell Research*, *8*(1), 26–37. https://doi.org/10.1016/j.scr.2011.08.002

Baker, D., Hirst, A. J., Gokhale, P. J., Juarez, M. A., Williams, S., Wheeler, M., Bean, K., Allison, T. F., Moore, H. D., Andrews, P. W., & Barbaric, I. (2016). Detecting Genetic Mosaicism in Cultures of Human Pluripotent Stem Cells. *Stem Cell Reports*, *7*(5), 998–1012. https://doi.org/10.1016/j.stemcr.2016.10.003

Ban, H., Nishishita, N., Fusaki, N., Tabata, T., Saeki, K., Shikamura, M., Takada, N., Inoue, M., Hasegawa, M., Kawamata, S., & Nishikawa, S. I. (2011). Efficient generation of transgene-free human induced pluripotent stem cells (iPSCs) by temperature-sensitive Sendai virus vectors. *Proceedings of the National Academy of Sciences of the United States of America*, *108*(34), 14234–14239. https://doi.org/10.1073/pnas.1103509108

Barber, A. J., & Lieth, E. (1997). Agrin accumulates in the brain microvascular basal lamina during development of the blood-brain barrier. *Developmental Dynamics*, *208*(1), 62–74. https://doi.org/10.1002/(sici)1097-0177(199701)208:1<62::aid-aja6>3.0.co;2-%23

Barczyk, M., Carracedo, S., & Gullberg, D. (2010). Integrins. *Cell and Tissue Research*, *339*, 269–280. https://doi.org/DOI 10.1007/s00441-009-0834-6

Barrangou, R. (2014). Cas9 targeting and the CRISPR revolution. *Science*, 344(6185), 707–708. https://doi.org/10.1126/science.1252964

Barrangou, R., Fremaux, C., Deveau, H., Richards, M., Boyaval, P., Moineau, S., Romero, D. A., & Horvath, P. (2007). CRISPR provides acquired resistance against viruses in prokaryotes. *Science*, *315*(5819), 1709–1712. https://doi.org/10.1126/science.1138140

Behrens, D. T., Villone, D., Koch, M., Brunner, G., Sorokin, L., Robenek, H., Bruckner-Tuderman, L., Bruckner, P., & Hansen, U. (2012). The epidermal basement membrane is a composite of separate laminin- or collagen IV-containing networks connected by aggregated perlecan, but not by nidogens. *Journal of Biological Chemistry*, *287*(22), 18700–18709. https://doi.org/10.1074/jbc.M111.336073

Bell, R. D., Winkler, E. A., Singh, I., Sagare, A. P., Deane, R., Wu, Z., Holtzman, D. M., Betsholtz, C., Armulik, A., Sallstrom, J., Berk, B. C., & Zlokovic, B. v. (2012). Apolipoprotein e controls cerebrovascular integrity via cyclophilin A. *Nature*, *485*(7399), 512–516. https://doi.org/10.1038/nature11087

Benavente, O. R., Coffey, C. S., Conwit, R., Hart, R. G., McLure, L. A., Pearce, L. A., Pergola, P. E., Szychowski, J. M., & The SPS3 Study Group. (2013). Blood-pressure targets in patients with recent lacunar stroke: The SPS3 randomised trial. *The Lancet*, *382*(9891), 507–515. https://doi.org/10.1016/S0140-6736(13)60852-1

Benson, K., Cramer, S., & Galla, H. J. (2013). Impedance-based cell monitoring: Barrier properties and beyond. *Fluids and Barriers of the CNS*, 10(1), 5. https://doi.org/10.1186/2045-8118-10-5

Ben-Zvi, A., Lacoste, B., Kur, E., Andreone, B. J., Mayshar, Y., Yan, H., & Gu, C. (2014). Mfsd2a is critical for the formation and function of the blood-brain barrier. *Nature*, *509*(7501), 507–511. https://doi.org/10.1038/nature13324

Bergmann, S., Lawler, S. E., Qu, Y., Fadzen, C. M., Wolfe, J. M., Regan, M. S., Pentelute, B. L., Agar, N. Y. R., & Cho, C. F. (2018). Blood–brain-barrier organoids for investigating the permeability of CNS therapeutics. *Nature Protocols*, *13*(12), 2827–2843. https://doi.org/10.1038/s41596-018-0066-x

Bernas, M. J., Cardoso, F. L., Daley, S. K., Weinand, M. E., Campos, A. R., Ferreira, A. J. G., Hoying, J. B., Witte, M. H., Brites, D., Persidsky, Y., Ramirez, S. H., & Brito, M. A. (2010). Establishment of primary cultures of human brain microvascular endothelial cells to provide an in vitro cellular model of the blood-brain barrier. *Nature Protocols*, *5*(7), 1265–1272. https://doi.org/10.1038/nprot.2010.76

Bhalerao, A., Sivandzade, F., Archie, S. R., Chowdhury, E. A., Noorani, B., & Cucullo, L. (2020). In vitro modeling of the neurovascular unit: Advances in the field. *Fluids and Barriers of the CNS*, 17, 22. https://doi.org/10.1186/s12987-020-00183-7

Bhave, G., Cummings, C. F., Vanacore, R. M., Kumagai-Cresse, C., Ero-Tolliver, I. A., Rafi, M., Kang, J. S., Pedchenko, V., Fessler, L. I., Fessler, J. H., & Hudson, B. G. (2012). Peroxidasin forms sulfilimine chemical bonds using hypohalous acids in tissue genesis. *Nature Chemical Biology*, *8*(9), 784–790. https://doi.org/10.1038/nchembio.1038

Blanchette, M., & Daneman, R. (2015). Formation and maintenance of the BBB. *Mechanisms of Development*, *138*, 8–16. https://doi.org/10.1016/j.mod.2015.07.007

Blanco, R., & Gerhardt, H. (2013). VEGF and Notch in tip and stalk cell selection. *Cold Spring Harbor Perspectives in Medicine*, *3*(1), a006569. https://doi.org/10.1101/cshperspect.a006569

Bonnans, C., Chou, J., & Werb, Z. (2014). Remodelling the extracellular matrix in development and disease. *Nature Reviews Molecular Cell Biology*, 15(12), 786–801. https://doi.org/10.1038/nrm3904

Borchiellini, C., Coulon, J., & le Parco, Y. (1996). The function of type IV collagen during Drosophila muscle development. *Mechanisms of Development*, *58*(1–2), 179–191. https://doi.org/10.1016/S0925-4773(96)00574-6

Boudko, S. P., Danylevych, N., Hudson, B. G., & Pedchenko, V. K. (2018). Basement membrane collagen IV: Isolation of functional domains. *Methods in Cell Biology*, 143, 171–185. https://doi.org/10.1016/bs.mcb.2017.08.010

Boutaud, A., Borza, D.-B., Bondar, O., Gunwar, S., Netzer, K.-O., Singh, N., Ninomiya, Y., Sado, Y., Noelken, M. E., & Hudson, B. G. (2000). Type IV Collagen of the Glomerular Basement Membrane. *Journal of Biological Chemistry*, *275*(39), 30716–30724. https://doi.org/10.1074/jbc.m004569200

Brinkman, E. K., Chen, T., Amendola, M., & van Steensel, B. (2014). Easy quantitative assessment of genome editing by sequence trace decomposition. *Nucleic Acids Research*, *42*(22), e168. https://doi.org/10.1093/nar/gku936

Brouns, S. J. J., Jore, M. M., Lundgren, M., Westra, E. R., Slijkhuis, R. J. H., Snijders, A. P. L., Dickman, M. J., Makarova, K. S., Koonin, E. v., & van der Oost, J. (2008). Small CRISPR RNAs guide antiviral defense in prokaryotes. *Science*, *321*(5891), 960–964. https://doi.org/10.1126/science.1159689

Brown, K. L., Cummings, C. F., Vanacore, R. M., & Hudson, B. G. (2017). Building collagen IV smart scaffolds on the outside of cells. *Protein Science*, 26(11), 2151–2161. https://doi.org/10.1002/pro.3283

Brunner, J., Ragupathy, S., & Borchard, G. (2021). Target specific tight junction modulators. *Advanced Drug Delivery Reviews*, 171, 266–288. https://doi.org/10.1016/j.addr.2021.02.008

Bugiani, M., Kevelam, S. H., Bakels, H. S., Waisfisz, Q., Ceuterick-De Groote, C., Niessen, H. W. M., Abbink, T. E. M., Lesnik Oberstein, S. A. M. J., & van der Knaap, M. S. (2016). Cathepsin A-related arteriopathy with strokes and leukoencephalopathy (CARASAL). *Neurology*, *87*(17), 1777–1786. https://doi.org/10.1212/WNL.0000000000003251

Burek, M., Salvador, E., & Förster, C. Y. (2012). Generation of an immortalized murine brain microvascular endothelial cell line as an in vitro blood brain barrier model. *Journal of Visualized Experiments*, *66*, e4022. https://doi.org/10.3791/4022

Campbell, H. K., Maiers, J. L., & DeMali, K. A. (2017). Interplay between tight junctions & adherens junctions. *Experimental Cell Research*, 358(1), 29-44. https://doi.org/10.1016/j.yexcr.2017.03.061

Campisi, M., Shin, Y., Osaki, T., Hajal, C., Chiono, V., & Kamm, R. D. (2018). 3D self-organized microvascular model of the human blood-brain barrier with endothelial cells, pericytes and astrocytes. *Biomaterials*, *180*, 117–129. https://doi.org/10.1016/j.biomaterials.2018.07.014

Chamary, J. v., & Hurst, L. D. (2009). The Price of Silent Mutations. *Scientific American*, *300*(6), 46–53. https://doi.org/10.1038/scientificamerican0609-46

Chauhan, G., Arnold, C. R., Chu, A. Y., Fornage, M., Reyahi, A., Bis, J. C., Havulinna, A. S., Sargurupremraj, M., Smith, A. V., Adams, H. H. H., Choi, S. H., Pulit, S. L., Trompet, S., Garcia, M. E., Manichaikul, A., Teumer, A., Gustafsson, S., Bartz, T. M., Bellenguez, C., … Debette, S. (2016). Identification of additional risk loci for stroke and small vessel disease: a meta-analysis of genome-wide association studies. *The Lancet Neurology*, *15*(7), 695–707. https://doi.org/10.1016/S1474-4422(16)00102-2

Chen, Z., Migeon, T., Verpont, M. C., Zaidan, M., Sado, Y., Kerjaschki, D., Ronco, P., & Plaisier, E. (2016). HANAC syndrome Col4a1 mutation causes neonate glomerular hyperpermeability and adult glomerulocystic kidney disease. *Journal of the American Society of Nephrology*, *27*(4), 1041–1054. https://doi.org/10.1681/ASN.2014121217

Cheung, C., Bernardo, A. S., Pedersen, R. A., & Sinha, S. (2014). Directed differentiation of embryonic origin-specific vascular smooth muscle subtypes from human pluripotent stem cells. *Nature Protocols*, *9*(4), 929–938. https://doi.org/10.1038/nprot.2014.059

Cheung, C., Bernardo, A. S., Trotter, M. W. B., Pedersen, R. A., & Sinha, S. (2012). Generation of human vascular smooth muscle subtypes provides insight into embryological origin-dependent disease susceptibility. *Nature Biotechnology*, *30*(2), 165–173. https://doi.org/10.1038/nbt.2107

Chioran, A., Duncan, S., Catalano, A., Brown, T. J., & Ringuette, M. J. (2017). Collagen IV trafficking: The inside-out and beyond story. *Developmental Biology*, 431(2), 124–133. https://doi.org/10.1016/j.ydbio.2017.09.037

Chistiakov, D. A., Orekhov, A. N., & Bobryshev, Y. v. (2017). Effects of shear stress on endothelial cells: go with the flow. *Acta Physiologica*, 219(2), 382–402. https://doi.org/10.1111/apha.12725

Cho, C. F., Wolfe, J. M., Fadzen, C. M., Calligaris, D., Hornburg, K., Chiocca, E. A., Agar, N. Y. R., Pentelute, B. L., & Lawler, S. E. (2017). Blood-brain-barrier spheroids as an in vitro screening platform for brain-penetrating agents. *Nature Communications*, *8*, 15623. https://doi.org/10.1038/ncomms15623

Choi, J. C. (2015). Genetics of Cerebral Small Vessel Disease. *Journal of Stroke*, *17*(1), 7–16.

Chojdak-Łukasiewicz, J., Dziadkowiak, E., Zimny, A., & Paradowski, B. (2021). Cerebral small vessel disease: A review. *Advances in clinical and experimental medicine : official organ Wroclaw Medical University*, 30(2), 349–356. https://doi.org/10.17219/acem/131216

Christian, M., Cermak, T., Doyle, E. L., Schmidt, C., Zhang, F., Hummel, A., Bogdanove, A. J., & Voytas, D. F. (2010). Targeting DNA double-strand breaks with TAL effector nucleases. *Genetics*, *186*(2), 757–761. https://doi.org/10.1534/genetics.110.120717

Coisne, C., Dehouck, L., Faveeuw, C., Delplace, Y., Miller, F., Landry, C., Morissette, C., Fenart, L., Cecchelli, R., Tremblay, P., & Dehouck, B. (2005). Mouse syngenic in vitro blood-brain barrier model: A new tool to examine inflammatory events in cerebral endothelium. *Laboratory Investigation*, *85*(6), 734–746. https://doi.org/10.1038/labinvest.3700281

Collins, C. E., Young, N. A., Flaherty, D. K., Airey, D. C., & Kaas, J. H. (2010). A rapid and reliable method of counting neurons and other cells in brain tissue: A comparison of flow cytometry and manual counting methods. *Frontiers in Neuroanatomy*, *4*, 5. https://doi.org/10.3389/neuro.05.005.2010

Conant, D., Hsiau, T., Rossi, N., Oki, J., Maures, T., Waite, K., Yang, J., Joshi, S., Kelso, R., Holden, K., Enzmann, B. L., & Stoner, R. (2022). Inference of CRISPR Edits from Sanger Trace Data. *CRISPR Journal*, *5*(1), 123–130. https://doi.org/10.1089/crispr.2021.0113

Cucullo, L., Couraud, P. O., Weksler, B., Romero, I. A., Hossain, M., Rapp, E., & Janigro, D. (2008). Immortalized human brain endothelial cells and flow-based vascular modeling: A marriage of convenience for rational neurovascular studies. *Journal of Cerebral Blood Flow and Metabolism*, *28*(2), 312–328. https://doi.org/10.1038/sj.jcbfm.9600525

Cummings, C. F., Pedchenko, V., Brown, K. L., Colon, S., Rafi, M., Jones-Paris, C., Pokydeshava, E., Liu, M., Pastor-Pareja, J. C., Stothers, C., Ero-Tolliver, I. A., Scott McCall, A., Vanacore, R., Bhave, G., Santoro, S., Blackwell, T. S., Zent, R., Pozzi, A., & Hudson, B. G. (2016). Extracellular chloride signals collagen IV network assembly during basement membrane formation. *Journal of Cell Biology*, *213*(4), 479–494. https://doi.org/10.1083/jcb.201510065

Curley, S. M., & Cady, N. C. (2018). Biologically-derived nanomaterials for targeted therapeutic delivery to the brain. *Science progress*, 101(3), 273–292. https://doi.org/10.3184/003685018X15306123582346

Daneman, R., & Prat, A. (2015). The blood–brain barrier. *Cold Spring Harbor Perspectives in Biology*, *7*(1). https://doi.org/10.1101/cshperspect.a020412

Dar, A., Domev, H., Ben-Yosef, O., Tzukerman, M., Zeevi-Levin, N., Novak, A., Germanguz, I., Amit, M., & Itskovitz-Eldor, J. (2012). Multipotent vasculogenic pericytes from human pluripotent stem cells promote recovery of murine ischemic limb. *Circulation*, *125*(1), 87–99. https://doi.org/10.1161/CIRCULATIONAHA.111.048264

Davidenko, N., Schuster, C. F., Bax, D. v., Farndale, R. W., Hamaia, S., Best, S. M., & Cameron, R. E. (2016). Evaluation of cell binding to collagen and gelatin: a study of the effect of 2D and 3D architecture and surface chemistry. *Journal of Materials Science: Materials in Medicine*, *27*(10), 148. https://doi.org/10.1007/s10856-016-5763-9

Davis, A. J., Chen, B. P. C., & Chen, D. J. (2014). DNA-PK: A dynamic enzyme in a versatile DSB repair pathway. *DNA Repair*, *17*, 21–29. https://doi.org/10.1016/j.dnarep.2014.02.020

Davis, J. M., Boswell, B. A., & Bachinger, H. P. (1989). Thermal stability and folding of type IV procollagen and effect of peptidyl-prolyl cis-trans-isomerase on the folding of the triple helix. *Journal of Biological Chemistry*, *264*(15), 8956–8962. https://doi.org/10.1016/s0021-9258(18)81887-7

Dehouck, M. -P, Méresse, S., Delorme, P., Fruchart, J. -C, & Cecchelli, R. (1990). An Easier, Reproducible, and Mass-Production Method to Study the Blood–Brain Barrier In Vitro. *Journal of Neurochemistry*, *54*(5), 1798–1801. https://doi.org/10.1111/j.1471-4159.1990.tb01236.x

Delsing, L., Dönnes, P., Sánchez, J., Clausen, M., Voulgaris, D., Falk, A., Herland, A., Brolén, G., Zetterberg, H., Hicks, R., & Synnergren, J. (2018). Barrier Properties and Transcriptome Expression in Human iPSC-Derived Models of the Blood–Brain Barrier. *Stem Cells*, *36*(12), 1816–1827. https://doi.org/10.1002/stem.2908

Delsing, L., Herland, A., Falk, A., Hicks, R., Synnergren, J., & Zetterberg, H. (2020). Models of the blood-brain barrier using iPSC-derived cells. *Molecular and Cellular Neuroscience*, 107, 103533. https://doi.org/10.1016/j.mcn.2020.103533

Deltcheva, E., Chylinski, K., Sharma, C. M., Gonzales, K., Chao, Y., Pirzada, Z. A., Eckert, M. R., Vogel, J., & Charpentier, E. (2011). CRISPR RNA maturation by trans-encoded small RNA and host factor RNase III. *Nature*, *471*(7340), 602–607. https://doi.org/10.1038/nature09886

de Silva, T. M., & Miller, A. A. (2016). Cerebral small vessel disease: Targeting oxidative stress as a novel therapeutic strategy? *Frontiers in Pharmacology*, 7, 61. https://doi.org/10.3389/fphar.2016.00061

DeStefano, J. G., Xu, Z. S., Williams, A. J., Yimam, N., & Searson, P. C. (2017). Effect of shear stress on iPSC-derived human brain microvascular endothelial cells (dhBMECs). *Fluids and Barriers of the CNS*, *14*(1), 20. https://doi.org/10.1186/s12987-017-0068-z

di Donato, I., Bianchi, S., de Stefano, N., Dichgans, M., Dotti, M. T., Duering, M., Jouvent, E., Korczyn, A. D., Lesnik-Oberstein, S. A. J., Malandrini, A., Markus, H. S., Pantoni, L., Penco, S., Rufa, A., Sinanović, O., Stojanov, D., & Federico, A. (2017). Cerebral Autosomal Dominant Arteriopathy with Subcortical Infarcts and Leukoencephalopathy (CADASIL) as a model of small vessel disease: Update on clinical, diagnostic, and management aspects. *BMC Medicine*, 15, 41. https://doi.org/10.1186/s12916-017-0778-8

Dimmeler, S., Haendeler, J., Rippmann, V., Nehls, M., & Zeiher, A. M. (1996). Shear stress inhibits apoptosis of human endothelial cells. *FEBS Letters*, *399*(1–2), 71–74. https://doi.org/10.1016/S0014-5793(96)01289-6

Dohgu, S., Takata, F., Yamauchi, A., Nakagawa, S., Egawa, T., Naito, M., Tsuruo, T., Sawada, Y., Niwa, M., & Kataoka, Y. (2005). Brain pericytes contribute to the induction and up-regulation of blood-brain barrier functions through transforming growth factor-β production. *Brain Research*, *1038*(2), 208–215. https://doi.org/10.1016/j.brainres.2005.01.027

Dong, L., Chen, Y., Lewis, M., Hsieh, J. C., Reing, J., Chaillet, J. R., Howell, C. Y., Melhem, M., Inoue, S., Kuszak, J. R., DeGeest, K., & Chung, A. E. (2002). Neurologic defects and selective disruption of basement membranes in mice lacking entactin-1/nidogen-1. *Laboratory Investigation*, *82*(12), 1617–1630. https://doi.org/10.1097/01.LAB.0000042240.52093.0F

Doudna, J. A., & Charpentier, E. (2014). The new frontier of genome engineering with CRISPR-Cas9. *Science*, 346(6213), 1258096. https://doi.org/10.1126/science.1258096

Drummond, G. R., Selemidis, S., Griendling, K. K., & Sobey, C. G. (2011). Combating oxidative stress in vascular disease: NADPH oxidases as therapeutic targets. *Nature Reviews Drug Discovery*, 10(6), 453–471. https://doi.org/10.1038/nrd3403

Duncan, K. G., Fessler, L. I., Bachinger, H. P., & Fessler, J. H. (1983). Procollagen IV. Association to tetramers. *Journal of Biological Chemistry*, *258*(9), 5869–5877. https://doi.org/10.1016/s0021-9258(20)81976-0

Dunn, P. J., Harvey, N. R., Maksemous, N., Smith, R. A., Sutherland, H. G., Haupt, L. M., & Griffiths, L. R. (2022). Investigation of Mitochondrial Related Variants in a Cerebral Small Vessel Disease Cohort. *Molecular Neurobiology*, 59(9) 5366–5378. https://doi.org/10.1007/s12035-022-0291

Edwards, D. N., & Bix, G. J. (2019). Roles of blood-brain barrier integrins and extracellular matrix in stroke. *American Journal of Physiology - Cell Physiology*, *316*(2), C252–C263. https://doi.org/10.1152/ajpcell.00151.2018

Ehrlich, P. (1906). The relations existing between chemical constitution, distribution and pharmacological action. *Collected Studies on Immunity New York: John Wiley & Sons*.

Eigenmann, D. E., Xue, G., Kim, K. S., Moses, A. v., Hamburger, M., & Oufir, M. (2013). Comparative study of four immortalized human brain capillary endothelial cell lines, hCMEC/D3, hBMEC, TY10, and BB19, and optimization of culture conditions, for an in vitro blood-brain barrier model for drug permeability studies. *Fluids and Barriers of the CNS*, *10*, 33. https://doi.org/10.1186/2045-8118-10-33

Engler, A. J., Sweeney, H. L., Discher, D. E., & Schwarzbauer, J. E. (2007). Extracellular matrix elasticity directs stem cell differentiation. *Journal of Musculoskeletal & Neuronal Interactions*, *7*(4), 335.

Erdmann, R. S., & Wennemers, H. (2010). Functionalizable collagen model peptides. *Journal of the American Chemical Society*, *132*(40), 13957–13959. https://doi.org/10.1021/ja103392t

Etchevers, H. C., Vincent, C., le Douarin, N. M., & Couly, G. F. (2001). The cephalic neural crest provides pericytes and smooth muscle cells to all blood vessels of the face and forebrain. *Development*, *128*(7), 1059–1068. https://doi.org/10.1242/dev.128.7.1059

Faal, T., Phan, D. T. T., Davtyan, H., Scarfone, V. M., Varady, E., Blurton-Jones, M., Hughes, C. C. W., & Inlay, M. A. (2019). Induction of Mesoderm and Neural Crest-Derived Pericytes from Human

Pluripotent Stem Cells to Study Blood-Brain Barrier Interactions. *Stem Cell Reports*, *12*(3), 451–460. https://doi.org/10.1016/j.stemcr.2019.01.005

Farach-Carson, M. C., & Carson, D. D. (2007). Perlecan - A multifunctional extracellular proteoglycan scaffold. *Glycobiology*, 17(9), 897–905. https://doi.org/10.1093/glycob/cwm043

Farach-Carson, M. C., Warren, C. R., Harrington, D. A., & Carson, D. D. (2014). Border patrol: Insights into the unique role of perlecan/heparan sulfate proteoglycan 2 at cell and tissue borders. *Matrix Biology*, *34*, 64–79. https://doi.org/10.1016/j.matbio.2013.08.004

Fidler, A. L., Darris, C. E., Chetyrkin, S. v, Pedchenko, V. K., Boudko, S. P., Brown, K. L., Gray Jerome, W., Hudson, J. K., Rokas, A., & Hudson, B. G. (2017). Collagen IV and basement membrane at the evolutionary dawn of metazoan tissues. *ELife*, *6*(e24176). https://doi.org/10.7554/elife.24176

Fidler, A. L., Vanacore, R. M., Chetyrkin, S. v., Pedchenko, V. K., Bhave, G., Yin, V. P., Stothers, C. L., Rose, K. L., McDonald, W. H., Clark, T. A., Borza, D. B., Steele, R. E., Ivy, M. T., Aspirnauts, T., Hudson, J. K., & Hudson, B. G. (2014). A unique covalent bond in basement membrane is a primordial innovation for tissue evolution. *Proceedings of the National Academy of Sciences of the United States of America*, *111*(1), 331–336. https://doi.org/10.1073/pnas.1318499111

French, C., Waskiewicz, A., & Lehmann, O. (2014). Mutation of FOXC1 and PITX2 induces cerebral small-vessel disease. *Journal of Clinical Investigation*, *124*(11), 4877–4881. https://doi.org/10.1172/JCI75109

Furuse, M. (2010). Molecular basis of the core structure of tight junctions. *Cold Spring Harbor perspectives in biology*, 2(1), a002907. https://doi.org/10.1101/cshperspect.a002907

Furuse, M., Hirase, T., Itoh, M., Nagafuchi, A., Yonemura, S., Tsukita, S., & Tsukita, S. (1993). Occludin: A novel integral membrane protein localizing at tight junctions. *Journal of Cell Biology*, *123*(6 II), 1777–1788. https://doi.org/10.1083/jcb.123.6.1777

Galbraith, G. G., Skalak, R., & Chien, S. (1998). Shear stress induces spatial reorganization of the endothelial cell cytoskeleton. *Cell Motility and the Cytoskeleton*, *40*(4), 317–330. https://doi.org/10.1002/(SICI)1097-0169(1998)40:4<317::AID-CM1>3.0.CO;2-8

Gasiunas, G., Barrangou, R., Horvath, P., & Siksnys, V. (2012). Cas9-crRNA ribonucleoprotein complex mediates specific DNA cleavage for adaptive immunity in bacteria. *Proceedings of the National Academy of Sciences of the United States of America*, *109*(39), E2579–E2586. https://doi.org/10.1073/pnas.1208507109

Gastfriend, B. D., Nishihara, H., Canfield, S. G., Foreman, K. L., Engelhardt, B., Palecek, S. P., & Shusta, E. v. (2021). Wnt signaling mediates acquisition of blood-brain barrier properties in naive endothelium derived from human pluripotent stem cells. *ELife*, *10*(e70992). https://doi.org/10.7554/eLife.70992

Gatseva, A., Sin, Y. Y., Brezzo, G., & van Agtmael, T. (2019). Basement membrane collagens and disease mechanisms. *Essays in Biochemistry*, 63(3), 297–312. https://doi.org/10.1042/EBC20180071

Gautam, J., Zhang, X., & Yao, Y. (2016). The role of pericytic laminin in blood brain barrier integrity maintenance. *Scientific Reports*, *6*, 36450. https://doi.org/10.1038/srep36450

Giau, V. van, Bagyinszky, E., Youn, Y. C., An, S. S. A., & Kim, S. Y. (2019). Genetic factors of cerebral small vessel disease and their potential clinical outcome. *International Journal of Molecular Sciences*, 20(17), 4298. https://doi.org/10.3390/ijms20174298

Gilbert, L. A., Larson Matthew H, Leonardo, M., Zairan, L., Brar Gloria A, Torres Sandra E, Noam, S. G., Onn, B., Whitehead Evan H, & Doudna Jennifer A. (2013). CRISPR-mediated modular RNA-guided regulation of transcription in eukaryotes. *Cell*, *154*(2), 442–451. https://doi.org/10.1016/j.cell.2013.06.044.

González, F., Boué, S., & Belmonte, J. C. I. (2011). Methods for making induced pluripotent stem cells: Reprogramming à la carte. *Nature Reviews Genetics*, 12(4), 231–242. https://doi.org/10.1038/nrg2937

Gould, D. B., Marchant, J. K., Savinova, O. v., Smith, R. S., & John, S. W. M. (2007). Col4a1 mutation causes endoplasmic reticulum stress and genetically modifiable ocular dysgenesis. *Human Molecular Genetics*, *16*(7), 798–807. https://doi.org/10.1093/hmg/ddm024

Gould, D. B., Phalan, F. C., Breedveld, G. J., van Mil, S. E., Smith, R. S., Schimenti, J. C., Aguglia, U., van der Knaap, M. S., Heutink, P., & John, S. W. M. (2005). Mutations in Col4a1 cause perinatal cerebral hemorrhage and porencephaly. *Science*, *308*(5725), 1167–1171. https://doi.org/10.1126/science.1109418

Gould, D. B., Phalan, F. C., van Mil, S. E., Sundberg, J. P., Vahedi, K., Massin, P., Bousser, M. G., Heutink, P., Miner, J. H., Tournier-Lasserve, E., & John, S. W. M. (2006). Role of COL4A1 in Small-Vessel Disease and Hemorrhagic Stroke. *New England Journal of Medicine*, *354*(14), 1489–1496. https://doi.org/10.1056/nejmoa053727

Grant, R. I., Hartmann, D. A., Underly, R. G., Berthiaume, A. A., Bhat, N. R., & Shih, A. Y. (2019). Organizational hierarchy and structural diversity of microvascular pericytes in adult mouse cortex. *Journal of Cerebral Blood Flow and Metabolism*, *39*(3), 411–425. https://doi.org/10.1177/0271678X17732229

Greco, G. E., Matsumoto, Y., Brooks, R. C., Lu, Z., Lieber, M. R., & Tomkinson, A. E. (2016). SCR7 is neither a selective nor a potent inhibitor of human DNA ligase IV. *DNA Repair*, *43*, 18–23. https://doi.org/10.1016/j.dnarep.2016.04.004

Grimpe, B., Probst, J. C., & Hager, G. (1999). Suppression of nidogen-1 translation by antisense targeting affects the adhesive properties of cultured astrocytes. *GLIA*, *28*(2), 138–149. https://doi.org/10.1002/(SICI)1098-1136(199911)28:2<138::AID-GLIA5>3.0.CO;2-8

Gross, S. J., Webb, A. M., Peterlin, A. D., Durrant, J. R., Judson, R. J., Raza, Q., Kitajewski, J. K., & Kushner, E. J. (2021). Notch regulates vascular collagen IV basement membrane through modulation of lysyl hydroxylase 3 trafficking. *Angiogenesis*, *24*, 789–805. https://doi.org/10.1007/s10456-021-09791-9

Guiraud, S., Migeon, T., Ferry, A., Chen, Z., Ouchelouche, S., Verpont, M. C., Sado, Y., Allamand, V., Ronco, P., & Plaisier, E. (2017). HANAC Col4a1 Mutation in Mice Leads to Skeletal Muscle Alterations due to a Primary Vascular Defect. *American Journal of Pathology*, *187*(3), 505–516. https://doi.org/10.1016/j.ajpath.2016.10.020

Gupta, M. C., Graham, P. L., & Kramer, J. M. (1997). Characterization of α1(IV) collagen mutations in Caenorhabditis elegans and the effects of α1 and α2(IV) mutations on type IV collagen distribution. *Journal of Cell Biology*, *137*(5), 1185–1196. https://doi.org/10.1083/jcb.137.5.1185

Haeren, R. H. L., Rijkers, K., Schijns, O. E. M. G., Dings, J., Hoogland, G., van Zandvoort, M. A. M. J., Vink, H., & van Overbeeke, J. J. (2018). In vivo assessment of the human cerebral microcirculation and its glycocalyx: A technical report. *Journal of Neuroscience Methods*, *303*, 114–125. https://doi.org/10.1016/j.jneumeth.2018.03.009

Hainsworth, A. H., & Markus, H. S. (2008). Do in vivo experimental models reflect human cerebral small vessel disease? A systematic review. *Journal of Cerebral Blood Flow and Metabolism*, 28(12), 1877–1891. https://doi.org/10.1038/jcbfm.2008.91

Hajal, C., Offeddu, G. S., Shin, Y., Zhang, S., Morozova, O., Hickman, D., Knutson, C. G., & Kamm, R. D. (2022). Engineered human blood–brain barrier microfluidic model for vascular permeability analyses. *Nature Protocols*, 17(1), 95–128. https://doi.org/10.1038/s41596-021-00635-w

Halilagic, A., Ribes, V., Ghyselinck, N. B., Zile, M. H., Dollé, P., & Studer, M. (2007). Retinoids control anterior and dorsal properties in the developing forebrain. *Developmental Biology*, *303*(1), 362–375. https://doi.org/10.1016/j.ydbio.2006.11.021

Hall, C. N., Reynell, C., Gesslein, B., Hamilton, N. B., Mishra, A., Sutherland, B. A., Oâ Farrell, F. M., Buchan, A. M., Lauritzen, M., & Attwell, D. (2014). Capillary pericytes regulate cerebral blood flow in health and disease. *Nature*, *508*, 55–60. https://doi.org/10.1038/nature13165

Hamilton, N. B., Attwell, D., & Hall, C. N. (2010). Pericyte-mediated regulation of capillary diameter: a component of neurovascular coupling in health and disease. *Frontiers in Neuroenergetics*, *2*, 5. https://doi.org/10.3389/fnene.2010.00005

Hara, K., Shiga, A., Fukutake, T., Nozaki, H., Miyashita, A., Yokoseki, A., Kawata, H., Koyama, A., Arima, K., Takahashi, T., Ikeda, M., Shiota, H., Tamura, M., Shimoe, Y., Hirayama, M., Arisato, T., Yanagawa, S., Tanaka, A., Nakano, I., … Onodera, O. (2009). Association of HTRA1 Mutations and Familial Ischemic Cerebral Small-Vessel Disease. *New England Journal of Medicine*, *360*(17), 1729–1739. https://doi.org/10.1056/nejmoa0801560

Haridhasapavalan, K. K., Raina, K., Dey, C., Adhikari, P., & Thummer, R. P. (2020). An Insight into Reprogramming Barriers to iPSC Generation. *Stem Cell Reviews and Reports*, 16(1), 56–81. https://doi.org/10.1007/s12015-019-09931-1

Hatoum-Aslan, A., Maniv, I., & Marraffini, L. A. (2011). Mature clustered, regularly interspaced, short palindromic repeats RNA (crRNA) length is measured by a ruler mechanism anchored at the precursor processing site. *Proceedings of the National Academy of Sciences of the United States of America*, *108*(52), 21218–21222. https://doi.org/10.1073/pnas.1112832108

Heigwer, F., Kerr, G., & Boutros, M. (2014). E-CRISP: Fast CRISPR target site identification. *Nature Methods*, 11(2), 122–123. https://doi.org/10.1038/nmeth.2812

Helms, H. C., Abbott, N. J., Burek, M., Cecchelli, R., Couraud, P. O., Deli, M. A., Förster, C., Galla, H. J., Romero, I. A., Shusta, E. v., Stebbins, M. J., Vandenhaute, E., Weksler, B., & Brodin, B. (2015). In vitro models of the blood-brain barrier: An overview of commonly used brain endothelial cell culture models and guidelines for their use. *Journal of Cerebral Blood Flow and Metabolism*, 36(5), 862–890. https://doi.org/10.1177/0271678X16630991

Henderson, C. E., Phillips, H. S., Pollock, R. A., Davies, A. M., Lemeulle, C., Armanini, M., Simpson, L. C., Moffet, B., Vandlen, R. A., Koliatsos, V. E., & Rosenthal, A. (1994). GDNF: A potent survival factor for motoneurons present in peripheral nerve and muscle. *Science*, *266*(5187), 1062–1064. https://doi.org/10.1126/science.7973664

Heo, J. H., Lucero, J., Abumiya, T., Koziol, J. A., Copeland, B. R., & del Zoppo, G. J. (1999). Matrix metalloproteinases increase very early during experimental focal cerebral ischemia. *Journal of Cerebral Blood Flow and Metabolism*, *19*(6), 624–633. https://doi.org/10.1097/00004647-199906000-00005

Heye, A. K., Thrippleton, M. J., Chappell, F. M., Valdés Hernández, M. D. C., Armitage, P. A., Makin, S. D., Muñoz Maniega, S., Sakka, E., Flatman, P. W., Dennis, M. S., & Wardlaw, J. M. (2016). Blood pressure and sodium: Association with MRI markers in cerebral small vessel disease. *Journal of Cerebral Blood Flow and Metabolism*, *36*(1), 264–274. https://doi.org/10.1038/jcbfm.2015.64

Higashi, T., & Miller, A. L. (2017). Tricellular junctions: How to build junctions at the TRICkiest points of epithelial cells. *Molecular Biology of the Cell*, 28(15), 2023–2034. https://doi.org/10.1091/mbc.E16-10-0697

Hill, R. A., Tong, L., Yuan, P., Murikinati, S., Gupta, S., & Grutzendler, J. (2015). Regional Blood Flow in the Normal and Ischemic Brain Is Controlled by Arteriolar Smooth Muscle Cell Contractility and Not by Capillary Pericytes. *Neuron*, *87*(1), 95–110. https://doi.org/10.1016/j.neuron.2015.06.001

Hockemeyer, D., & Jaenisch, R. (2016). Induced pluripotent stem cells meet genome editing. *Cell Stem Cell*, 18(5), 573–586. https://doi.org/10.1016/j.stem.2016.04.013

Hohenester, E., & Yurchenco, P. D. (2013). Laminins in basement membrane assembly. In *Cell Adhesion and Migration*, 7(1), 56–63. https://doi.org/10.4161/cam.21831

Hollmann, E. K., Bailey, A. K., Potharazu, A. v., Neely, M. D., Bowman, A. B., & Lippmann, E. S. (2017). Accelerated differentiation of human induced pluripotent stem cells to blood-brain barrier endothelial cells. *Fluids and Barriers of the CNS*, *14*(1), 9. https://doi.org/10.1186/s12987-017-0059-0

Holster, T., Pakkanen, O., Soininen, R., Sormunen, R., Nokelainen, M., Kivirikko, K. I., & Myllyharju, J. (2007). Loss of assembly of the main basement membrane collagen, type IV, but not fibril-forming collagens and embryonic death in collagen prolyl 4-hydroxylase i null mice. *Journal of Biological Chemistry*, *282*(4), 2512–2519. https://doi.org/10.1074/jbc.M606608200

Hotary, K. B., Yana, I., Sabeh, F., Li, X. Y., Holmbeck, K., Birkedal-Hansen, H., Allen, E. D., Hiraoka, N., & Weiss, S. J. (2002). Matrix metalloproteinases (MMPs) regulate fibrin-invasive activity via MT1-MMP-dependent and -independent processes. *Journal of Experimental Medicine*, *195*(3), 295–308. https://doi.org/10.1084/jem.20010815

Hsu, P. D., Lander, E. S., & Zhang, F. (2014). Development and applications of CRISPR-Cas9 for genome engineering. *Cell*, 157(6), 1262–1278. https://doi.org/10.1016/j.cell.2014.05.010

Hsu, P. D., Scott, D. A., Weinstein, J. A., Ran, F. A., Konermann, S., Agarwala, V., Li, Y., Fine, E. J., Wu, X., Shalem, O., Cradick, T. J., Marraffini, L. A., Bao, G., & Zhang, F. (2013). DNA targeting specificity of RNA-guided Cas9 nucleases. *Nature Biotechnology*, *31*(9), 827–832. https://doi.org/10.1038/nbt.2647

Hudson, B. G., Reeders, S. T., & Tryggvason, K. (1993). Type IV collagen: Structure, gene organization, and role in human diseases. Molecular basis of goodpasture and alport syndromes and diffuse leiomyomatosis. *Journal of Biological Chemistry*, 238(35), 26033–26036. https://doi.org/10.1016/s0021-9258(19)74270-7

Hu, J. H., Miller, S. M., Geurts, M. H., Tang, W., Chen, L., Sun, N., Zeina, C. M., Gao, X., Rees, H. A., Lin, Z., & Liu, D. R. (2018). Evolved Cas9 variants with broad PAM compatibility and high DNA specificity. *Nature*, *556*(7699), 57–63. https://doi.org/10.1038/nature26155

Hu, Z., Shi, Z., Guo, X., Jiang, B., Wang, G., Luo, D., Chen, Y., & Zhu, Y. S. (2018). Ligase IV inhibitor SCR7 enhances gene editing directed by CRISPR-Cas9 and ssODN in human cancer cells. *Cell and Bioscience*, *8*(1). https://doi.org/10.1186/s13578-018-0200-z

Huneau, C., Houot, M., Joutel, A., Béranger, B., Giroux, C., Benali, H., & Chabriat, H. (2018). Altered dynamics of neurovascular coupling in CADASIL. *Annals of Clinical and Translational Neurology*, *5*(7), 788–802. https://doi.org/10.1002/acn3.574

Iadecola, C. (2017). The Neurovascular Unit Coming of Age: A Journey through Neurovascular Coupling in Health and Disease. *Neuron*, 96(1), 17–42. https://doi.org/10.1016/j.neuron.2017.07.030

Iba, T., & Levy, J. H. (2019). Derangement of the endothelial glycocalyx in sepsis. *Journal of Thrombosis and Haemostasis*, 17(2), 283–294. https://doi.org/10.1111/jth.14371

Igarashi, Y., Utsumi, H., Chiba, H., Yamada-Sasamori, Y., Tobioka, H., Kamimura, Y., Furuuchi, K., Kokai, Y., Nakagawa, T., Mori, M., & Sawada, N. (1999). Glial cell line-derived neurotrophic factor induces barrier function of endothelial cells forming the blood-brain barrier. *Biochemical and Biophysical Research Communications*, *261*(1), 108–112. https://doi.org/10.1006/bbrc.1999.0992

Iliff, J. J., Wang, M., Liao, Y., Plogg, B. A., Peng, W., Gundersen, G. A., Benveniste, H., Vates, G. E., Deane, R., Goldman, S. A., Nagelhus, E. A., & Nedergaard, M. (2012). A paravascular pathway facilitates CSF flow through the brain parenchyma and the clearance of interstitial solutes, including amyloid β. *Science Translational Medicine*, *4*(147), 147ra111. https://doi.org/10.1126/scitranslmed.3003748

Ishikawa, Y., Ito, S., Nagata, K., Sakai, L. Y., & Bächinger, H. P. (2016). Intracellular mechanisms of molecular recognition and sorting for transport of large extracellular matrix molecules. *Proceedings of the National Academy of Sciences of the United States of America*, *113*(41), E6036-6044. https://doi.org/10.1073/pnas.1609571113

Izawa, Y., Gu, Y. H., Osada, T., Kanazawa, M., Hawkins, B. T., Koziol, J. A., Papayannopoulou, T., Spatz, M., & del Zoppo, G. J. (2018). β1-integrin–matrix interactions modulate cerebral microvessel endothelial cell tight junction expression and permeability. *Journal of Cerebral Blood Flow and Metabolism*, *38*(4), 641–658. https://doi.org/10.1177/0271678X17722108

Jackson, R. J., Meltzer, J. C., Nguyen, H., Commins, C., Bennett, R. E., Hudry, E., & Hyman, B. T. (2021). APOE4 derived from astrocytes leads to blood–brain barrier impairment. *Brain*, *145*(10), 3582–3593. https://doi.org/10.1093/brain/awab478

Jakovcevski, I., Filipovic, R., Mo, Z., Rakic, S., & Zecevic, N. (2009). Oligodendrocyte development and the onset of myelination in the human fetal brain. *Frontiers in Neuroanatomy*, 3, 5. https://doi.org/10.3389/neuro.05.005.2009

Jamieson, J. J., Linville, R. M., Ding, Y. Y., Gerecht, S., & Searson, P. C. (2019). Role of iPSC-derived pericytes on barrier function of iPSC-derived brain microvascular endothelial cells in 2D and 3D. *Fluids and Barriers of the CNS*, *16*(1), 15. https://doi.org/10.1186/s12987-019-0136-7

Janmey, P. A., Wells, R. G., Assoian, R. K., & McCulloch, C. A. (2013). From tissue mechanics to transcription factors. *Differentiation*, *86*(3), 112–120. https://doi.org/10.1016/j.diff.2013.07.004

Jansen, R., van Embden, J. D. A., Gaastra, W., & Schouls, L. M. (2002). Identification of genes that are associated with DNA repeats in prokaryotes. *Molecular Microbiology*, *43*(6), 1565–1575. https://doi.org/10.1046/j.1365-2958.2002.02839.x

Jayadev, R., & Sherwood, D. R. (2017). Basement membranes. *Current Biology*, *27*(6), R207–R211. https://doi.org/10.1016/j.cub.2017.02.006.

Jeanne, M., & Gould, D. B. (2017). Genotype-phenotype correlations in pathology caused by collagen type IV alpha 1 and 2 mutations. *Matrix Biology*, 57-58, 29–44. Elsevier B.V. https://doi.org/10.1016/j.matbio.2016.10.003

Jeanne, M., Jorgensen, J., & Gould, D. B. (2015). Molecular and genetic analyses of collagen type IV mutant mouse models of spontaneous intracerebral hemorrhage identify mechanisms for stroke prevention. *Circulation*, *131*(18), 1555–1565. https://doi.org/10.1161/CIRCULATIONAHA.114.013395

Jeske, R., Albo, J., Marzano, M., Bejoy, J., & Li, Y. (2020). Engineering Brain-Specific Pericytes from Human Pluripotent Stem Cells. *Tissue Engineering - Part B: Reviews*, 26(4), 367–382. https://doi.org/10.1089/ten.teb.2020.0091

Jinek, M., Chylinski, K., Fonfara, I., Hauer, M., Doudna, J. A., & Charpentier, E. (2012). A programmable dual-RNA-guided DNA endonuclease in adaptive bacterial immunity. *Science*, *337*(6096), 816–821. https://doi.org/10.1126/science.1225829

Jones, A. R., & Shusta, E. v. (2007). Blood-brain barrier transport of therapeutics via receptor-mediation. *Pharmaceutical Research*, 24(9), 1759–1771. https://doi.org/10.1007/s11095-007-9379-0

Jones, F. E., Bailey, M. A., Murray, L. S., Lu, Y., McNeilly, S., Schlo̅tzer-Schrehardt, U., Lennon, R., Sado, Y., Brownstein, D. G., Mullins, J. J., Kadler, K. E., & van Agtmael, T. (2016). ER stress and basement membrane defects combine to cause glomerular and tubular renal disease resulting from Col4a1 mutations in mice. *DMM Disease Models and Mechanisms*, *9*(2), 165–176. https://doi.org/10.1242/dmm.021741

Joutel, A., & Faraci, F. M. (2014). Cerebral small vessel disease: Insights and opportunities from mouse models of collagen IV-related small vessel disease and cerebral autosomal dominant arteriopathy with subcortical infarcts and leukoencephalopathy. *Stroke*, *45*(4), 1215–1221. https://doi.org/10.1161/STROKEAHA.113.002878

Joutel, A., Haddad, I., Ratelade, J., & Nelson, M. T. (2016). Perturbations of the cerebrovascular matrisome: A convergent mechanism in small vessel disease of the brain? *Journal of Cerebral Blood Flow and Metabolism*, 36(1), 143–157. https://doi.org/10.1038/jcbfm.2015.62

Jucker, M., Tian, M., Norton, D. D., Sherman, C., & Kusiak, J. W. (1996). Laminin α2 is a component of brain capillary basement membrane: Reduced expression in dystrophic dy mice. *Neuroscience*, *71*(4), 1153–1161. https://doi.org/10.1016/0306-4522(95)00496-3

Kadry, H., Noorani, B., & Cucullo, L. (2020). A blood–brain barrier overview on structure, function, impairment, and biomarkers of integrity. *Fluids and Barriers of the CNS*, 17(1), 69. https://doi.org/10.1186/s12987-020-00230-3

Kamp, J. A., Moursel, L. G., Haan, J., Terwindt, G. M., Lesnik Oberstein, S. A. M. J., van Duinen, S. G., & van Roon-Mom, W. M. C. (2014). Amyloid β in hereditary cerebral hemorrhage with amyloidosis-Dutch type. *Reviews in the Neurosciences*, *25*(5), 641–651. https://doi.org/10.1515/revneuro-2014-0008

Kang, M., & Yao, Y. (2020). Basement Membrane Changes in Ischemic Stroke. *Stroke*, 51, 1344–1352. https://doi.org/10.1161/STROKEAHA.120.028928

Kapahnke, M., Banning, A., & Tikkanen, R. (2016). Random splicing of several exons caused by a single base change in the target exon of CRISPR/cas9 mediated gene knockout. *Cells*, *5*(4). https://doi.org/10.3390/cells5040045

Kaya, M., & Ahishali, B. (2021). Basic physiology of the blood-brain barrier in health and disease: a brief overview. *Tissue Barriers*, 9(1), 1840913. https://doi.org/10.1080/21688370.2020.1840913

Kechagia, J. Z., Ivaska, J., & Roca-Cusachs, P. (2019). Integrins as biomechanical sensors of the microenvironment. *Nature Reviews Molecular Cell Biology*, 20(8), 457–473. https://doi.org/10.1038/s41580-019-0134-2

Khalilgharibi, N., & Mao, Y. (2021). To form and function: On the role of basement membrane mechanics in tissue development, homeostasis and disease. *Open Biology*, 11, 200360. https://doi.org/10.1098/rsob.200360

Khoshnoodi, J., Pedchenko, V., & Hudson, B. G. (2008). Mammalian collagen IV. *Microscopy Research and Technique*, 71(5), 357–370. https://doi.org/10.1002/jemt.20564

Kim, S.-H., Turnbull, J., & Guimond, S. (2011). Extracellular matrix and cell signalling: The dynamic cooperation of integrin, proteoglycan and growth factor receptor. *Journal of Endocrinology*, 209(2), 139–151. https://doi.org/10.1530/JOE-10-0377

Kim, Y.-G., Cha, J., & Chandrasegaran, S. (1996). Hybrid restriction enzymes: Zinc finger fusions to Fok I cleavage domain. *Proceedings of the National Academy of Sciences of the United States of America*, *93*(3), 1156–1160. https://doi.org/10.1073/pnas.93.3.1156

King, A. (2018). The search for better animal models of Alzheimer's disease. *Nature* 559(7715), S13–S15). https://doi.org/10.1038/d41586-018-05722-9

Kishimoto, Y., Saito, N., Kurita, K., Shimokado, K., Maruyama, N., & Ishigami, A. (2013). Ascorbic acid enhances the expression of type 1 and type 4 collagen and SVCT2 in cultured human skin fibroblasts. *Biochemical and Biophysical Research Communications*, *430*(2), 579–584. https://doi.org/10.1016/j.bbrc.2012.11.110

Kleinstiver, B. P., Prew, M. S., Tsai, S. Q., Topkar, V. v., Nguyen, N. T., Zheng, Z., Gonzales, A. P. W., Li, Z., Peterson, R. T., Yeh, J. R. J., Aryee, M. J., & Joung, J. K. (2015). Engineered CRISPR-Cas9 nucleases with altered PAM specificities. *Nature*, *523*(7561), 481–485. https://doi.org/10.1038/nature14592

Koide, T., Takahara, Y., Asada, S., & Nagata, K. (2002). Xaa-Arg-Gly triplets in the collagen triple helix are dominant binding sites for the molecular chaperone HSP47. *Journal of Biological Chemistry*, *277*(8), 6178–6182. https://doi.org/10.1074/jbc.M106497200

Komor, A. C., Kim, Y. B., Packer, M. S., Zuris, J. A., & Liu, D. R. (2016). Programmable editing of a target base in genomic DNA without double-stranded DNA cleavage. *Nature*, *533*, 420–424. https://doi.org/10.1038/nature17946

Korn, J., Christ, B., & Kurz, H. (2002). Neuroectodermal origin of brain pericytes and vascular smooth muscle cells. *Journal of Comparative Neurology*, *442*(1), 78–88. https://doi.org/10.1002/cne.1423

Krencik, R., Weick, J. P., Liu, Y., Zhang, Z. J., & Zhang, S. C. (2011). Specification of transplantable astroglial subtypes from human pluripotent stem cells. *Nature Biotechnology*, *29*(6), 528–534. https://doi.org/10.1038/nbt.1877

Kröger, S., & Schröder, J. E. (2002). Agrin in the developing CNS: New roles for a synapse organizer. *News in Physiological Sciences*, 17(5), 207–212. https://doi.org/10.1152/nips.01390.2002

Kumar, A., D'Souza, S. S., Moskvin, O. v., Toh, H., Wang, B., Zhang, J., Swanson, S., Guo, L. W., Thomson, J. A., & Slukvin, I. I. (2017). Specification and Diversification of Pericytes and Smooth Muscle Cells from Mesenchymoangioblasts. *Cell Reports*, *19*(9), 1902–1916. https://doi.org/10.1016/j.celrep.2017.05.019

Kuo, D. S., Labelle-Dumais, C., & Gould, D. B. (2012). Col4a1 and col4a2 mutations and disease: Insights into pathogenic mechanisms and potential therapeutic targets. *Human Molecular Genetics*, *21*(R1), R97–R110. https://doi.org/10.1093/hmg/dds346

Kusuma, S., Shen, Y. I., Hanjaya-Putra, D., Mali, P., Cheng, L., & Gerecht, S. (2013). Self-organized vascular networks from human pluripotent stem cells in a synthetic matrix. *Proceedings of the National Academy of Sciences of the United States of America*, *110*(31), 12601–12606. https://doi.org/10.1073/pnas.1306562110

Kwart, D., Paquet, D., Teo, S., & Tessier-Lavigne, M. (2017). Precise and efficient scarless genome editing in stem cells using CORRECT. *Nature Protocols*, *12*(2), 329–354. https://doi.org/10.1038/nprot.2016.171

Laurens, N., Koolwijk, P., & de Maat, M. P. (2006). Fibrin structure and wound healing. *Journal of thrombosis and haemostasis : JTH*, 4(5), pp. 932–939. https://doi.org/10.1111/j.1538-7836.2006.01861.x

LeBleu, V. S., MacDonald, B., & Kalluri, R. (2007). Structure and function of basement membranes. *Experimental Biology and Medicine*, 232(9), 1121–1129. https://doi.org/10.3181/0703-MR-72

Lee, S. W., Kim, W. J., Choi, Y. K., Song, H. S., Son, M. J., Gelman, I. H., Kim, Y. J., & Kim, K. W. (2003). SSeCKS regulates angiogenesis and tight junction formation in blood-brain barrier. *Nature Medicine*, *9*(7), 900–906. https://doi.org/10.1038/nm889

Lemmens, R., Maugeri, A., Niessen, H. W. M., Goris, A., Tousseyn, T., Demaerel, P., Corveleyn, A., Robberecht, W., Knaap, V. der, Thijs, V. N., & Zwijnenburg, P. J. G. (2013). Novel COL4A1 mutations cause cerebral small vessel disease by haploinsufficiency. *Human Molecular Genetics*, *22*(2), 391–397. https://doi.org/10.1093/hmg/dds436

Lerner, D. W., McCoy, D., Isabella, A. J., Mahowald, A. P., Gerlach, G. F., Chaudhry, T. A., & Horne-Badovinac, S. (2013). A Rab10-Dependent Mechanism for Polarized Basement Membrane Secretion during Organ Morphogenesis. *Developmental Cell*, *24*(2), 159–168. https://doi.org/10.1016/j.devcel.2012.12.005

Lewandowski, M. (1900). Zur Lehre von der Cerebrospinalflüssigkeit. *Z. Klein Forsch*, *40*, 480–494.

Li, F., Lan, Y., Wang, Y., Wang, J., Yang, G., Meng, F., Han, H., Meng, A., Wang, Y., & Yang, X. (2011). Endothelial Smad4 Maintains Cerebrovascular Integrity by Activating N-Cadherin through Cooperation with Notch. *Developmental Cell*, *20*(3), 291–302. https://doi.org/10.1016/j.devcel.2011.01.011

Li, G., Zhang, X., Zhong, C., Mo, J., Quan, R., Yang, J., Liu, D., Li, Z., Yang, H., & Wu, Z. (2017). Small molecules enhance CRISPR/Cas9-mediated homology-directed genome editing in primary cells. *Scientific Reports*, *7*, 8943. https://doi.org/10.1038/s41598-017-09306-x

Li, Q., Wang, C., Li, W., Zhang, Z., Wang, S., Wupuer, A., Hu, X., Wumaier, K., Zhu, Y., Li, H., & Yu, W. (2022). A Novel Mutation in COL4A1 Gene in a Chinese Family with Pontine Autosomal Dominant Microangiopathy and Leukoencephalopathy. *Translational Stroke Research*, *13*(2), 238–244. https://doi.org/10.1007/s12975-021-00926-0

Li, Q., Yang, Y., Reis, C., Tao, T., Li, W., Li, X., & Zhang, J. H. (2018). Cerebral Small Vessel Disease. *Cell Transplantation*, 27(12), 1711–1722. SAGE Publications Ltd. https://doi.org/10.1177/0963689718795148

Li, X., Tao, Y., Bradley, R., Du, Z., Tao, Y., Kong, L., Dong, Y., Jones, J., Yan, Y., Harder, C. R. K., Friedman, L. M., Bilal, M., Hoffmann, B., & Zhang, S. C. (2018). Fast Generation of Functional Subtype Astrocytes from Human Pluripotent Stem Cells. *Stem Cell Reports*, *11*(4), 998–1008. https://doi.org/10.1016/j.stemcr.2018.08.019

Li, Y., Balasubramanian, U., Cohen, D., Zhang, P. W., Mosmiller, E., Sattler, R., Maragakis, N. J., & Rothstein, J. D. (2015). A comprehensive library of familial human amyotrophic lateral sclerosis induced pluripotent stem cells. *PLoS ONE*, *10*(3), e0118266. https://doi.org/10.1371/journal.pone.0118266

Lian, X., Bao, X., Al-Ahmad, A., Liu, J., Wu, Y., Dong, W., Dunn, K. K., Shusta, E. v., & Palecek, S. P. (2014). Efficient differentiation of human pluripotent stem cells to endothelial progenitors via small-molecule activation of WNT signaling. *Stem Cell Reports*, *3*(5), 804–816. https://doi.org/10.1016/j.stemcr.2014.09.005

Liang, X., Potter, J., Kumar, S., Ravinder, N., & Chesnut, J. D. (2017). Enhanced CRISPR/Cas9-mediated precise genome editing by improved design and delivery of gRNA, Cas9 nuclease, and donor DNA. *Journal of Biotechnology*, *241*, 136–146. https://doi.org/10.1016/j.jbiotec.2016.11.011

Lin, L. F. H., Doherty, D. H., Lile, J. D., Bektesh, S., & Collins, F. (1993). GDNF: A glial cell line - Derived neurotrophic factor for midbrain dopaminergic neurons. *Science*, *260*(5111), 1130–1132. https://doi.org/10.1126/science.8493557

Lindblom, P., Gerhardt, H., Liebner, S., Abramsson, A., Enge, M., Hellström, M., Bäckström, G., Fredriksson, S., Landegren, U., Nyström, H. C., Bergström, G., Dejana, E., Östman, A., Lindahl, P., & Betsholtz, C. (2003). Endothelial PDGF-B retention is required for proper investment of pericytes in the microvessel wall. *Genes and Development*, *17*(15), 1835–1840. https://doi.org/10.1101/gad.266803

Linville, R. M., DeStefano, J. G., Sklar, M. B., Xu, Z., Farrell, A. M., Bogorad, M. I., Chu, C., Walczak, P., Cheng, L., Mahairaki, V., Whartenby, K. A., Calabresi, P. A., & Searson, P. C. (2019). Human iPSC-derived blood-brain barrier microvessels: validation of barrier function and endothelial cell behavior. *Biomaterials*, *190–191*, 24–37. https://doi.org/10.1016/j.biomaterials.2018.10.023

Lippmann, E. S., Al-Ahmad, A., Azarin, S. M., Palecek, S. P., & Shusta, E. v. (2014). A retinoic acid-enhanced, multicellular human blood-brain barrier model derived from stem cell sources. *Scientific Reports*, *4*, 4160. https://doi.org/10.1038/srep04160

Lippmann, E. S., Azarin, S. M., Kay, J. E., Nessler, R. A., Wilson, H. K., Al-Ahmad, A., Palecek, S. P., & Shusta, E. v. (2012). Derivation of blood-brain barrier endothelial cells from human pluripotent stem cells. *Nature Biotechnology*, *30*(8), 783–791. https://doi.org/10.1038/nbt.2247

Liskay, R. M., Letsou, A., & Stachelek, J. L. (1987). Homology requirement for efficient gene conversion between duplicated chromosomal sequences in mammalian cells. *Genetics*, *115*(1), 161–167. https://doi.org/10.1093/genetics/115.1.161

Liu, C., Oikonomopoulos, A., Sayed, N., & Wu, J. C. (2018). Modeling human diseases with induced pluripotent stem cells: From 2D to 3D and beyond. *Development (Cambridge)*, *145*(5), dev156166. https://doi.org/10.1242/dev.156166

Liu, M., Feng, Z., Ke, H., Liu, Y., Sun, T., Dai, J., Cui, W., & Pastor-Pareja, J. C. (2017). Tango1 spatially organizes ER exit sites to control ER export. *Journal of Cell Biology*, *216*(4), 1035–1049. https://doi.org/10.1083/jcb.201611088

Lu, P., Takai, K., Weaver, V. M., & Werb, Z. (2011). Extracellular Matrix degradation and remodeling in development and disease. *Cold Spring Harbor Perspectives in Biology*, *3*(12), a005058. https://doi.org/10.1101/cshperspect.a005058

Lu, T. M., Houghton, S., Magdeldin, T., Barcia Durán, J. G., Minotti, A. P., Snead, A., Sproul, A., Nguyen, D. H. T., Xiang, J., Fine, H. A., Rosenwaks, Z., Studer, L., Rafii, S., Agalliu, D., Redmond, D., & Lis, R. (2021). Pluripotent stem cell-derived epithelium misidentified as brain microvascular endothelium requires ETS factors to acquire vascular fate. *Proceedings of the National Academy of Sciences of the United States of America*, *118*(8), e2016950118. https://doi.org/10.1073/pnas.2016950118

Mahley, R. W., Weisgraber, K. H., & Huang, Y. (2009). Apolipoprotein E: Structure determines function, from atherosclerosis to Alzheimer's disease to AIDS. *Journal of Lipid Research*, 50(April Supplement, S183–S188. https://doi.org/10.1194/jlr.R800069-JLR200

Makarova, K. S., Grishin, N. v., Shabalina, S. A., Wolf, Y. I., & Koonin, E. v. (2006). A putative RNA-interference-based immune system in prokaryotes: Computational analysis of the predicted enzymatic machinery, functional analogies with eukaryotic RNAi, and hypothetical mechanisms of action. *Biology Direct*, 1, 7. https://doi.org/10.1186/1745-6150-1-7

Mak, I. W. Y., Evaniew, N., & Ghert, M. (2014). Lost in translation: Animal models and clinical trials in cancer treatment. *American Journal of Translational Research*, 6(2), 114–118.

Mammoto, A., Connor, K. M., Mammoto, T., Yung, C. W., Huh, D., Aderman, C. M., Mostoslavsky, G., Smith, L. E. H., & Ingber, D. E. (2009). A mechanosensitive transcriptional mechanism that controls angiogenesis. *Nature*, *457*(7233), 1103–1108. https://doi.org/10.1038/nature07765

Mann, G. E., Yudilevich, D. L., & Sobrevia, L. (2003). Regulation of amino acid and glucose transporters in endothelial and smooth muscle cells. *Physiological Reviews*, 83(1), 183–252. https://doi.org/10.1152/physrev.00022.2002

Mao, M., Alavi, M. v., Labelle-Dumais, C., & Gould, D. B. (2015). Type IV Collagens and Basement Membrane Diseases: Cell Biology and Pathogenic Mechanisms. *Current Topics in Membranes*, 61–116. https://doi.org/10.1016/bs.ctm.2015.09.002

Marini, S., Anderson, C. D., & Rosand, J. (2020). Genetics of Cerebral Small Vessel Disease. *Stroke,* 51(1), 12–20. https://doi.org/10.1161/STROKEAHA.119.024151

McVey, M., Khodaverdian, V. Y., Meyer, D., Cerqueira, P. G., & Heyer, W. D. (2016). Eukaryotic DNA Polymerases in Homologous Recombination. *Annual Review of Genetics*, 50, 393–421. https://doi.org/10.1146/annurev-genet-120215-035243

Menezes, M. J., McClenahan, F. K., Leiton, C. v., Aranmolate, A., Shan, X., & Colognato, H. (2014). The extracellular matrix protein laminin α2 regulates the maturation and function of the blood–brain barrier. *Journal of Neuroscience*, *34*(46), 15260–15280. https://doi.org/10.1523/JNEUROSCI.3678-13.2014

Meuwissen, M., Halley, D., Smit, L., Lequin, M., Cobben, J., de Coo, R., van Harssel, J., Sallevelt, S., Woldringh, G., van der Knaap, M., de Vries, L., & Mancini, G. (2015). The expanding phenotype of COL4A1 and COL4A2 mutations: clinical data on 13 newly identified families and a review of the literature. *Genetics in Medicine*, *17*(11), 843–853. https://doi.org/10.1038/gim.2014.210

Miguel, L., Rovelet-Lecrux, A., Feyeux, M., Frebourg, T., Nassoy, P., Campion, D., & Lecourtois, M. (2019). Detection of all adult Tau isoforms in a 3D culture model of iPSC-derived neurons. *Stem Cell Research*, *40*, 101541. https://doi.org/10.1016/j.scr.2019.101541

Miranti, C. K., & Brugge, J. S. (2002). Sensing the environment: A historical perspective on integrin signal transduction. *Nature Cell Biology*, *4*(4), E83–E90. https://doi.org/10.1038/ncb0402-e83

Mishra, A., Reynolds, J. P., Chen, Y., Gourine, A. v., Rusakov, D. A., & Attwell, D. (2016). Astrocytes mediate neurovascular signaling to capillary pericytes but not to arterioles. *Nature Neuroscience*, *19*(12), 1619–1627. https://doi.org/10.1038/nn.4428

Mizuno, T., Mizuta, I., Watanabe-Hosomi, A., Mukai, M., & Koizumi, T. (2020). Clinical and Genetic Aspects of CADASIL. *Frontiers in Aging Neuroscience*, 12, 91. https://doi.org/10.3389/fnagi.2020.00091

Mojica, F. J. M., Díez-Villaseñor, C., García-Martínez, J., & Soria, E. (2005). Intervening sequences of regularly spaced prokaryotic repeats derive from foreign genetic elements. *Journal of Molecular Evolution*, *60*(2), 174–182. https://doi.org/10.1007/s00239-004-0046-3

Mojica, F. J. M., Díez-Villaseñor, C., Soria, E., & Juez, G. (2000). Biological significance of a family of regularly spaced repeats in the genomes of Archaea, Bacteria and mitochondria. *Molecular Microbiology*, 361), 244–246. https://doi.org/10.1046/j.1365-2958.2000.01838.x

Mojica, F. J. M., & Rodriguez-Valera, F. (2016). The discovery of CRISPR in archaea and bacteria. *FEBS Journal*, 283, 3162–3169. https://doi.org/10.1111/febs.13766

Mönkäre, S., Kuuluvainen, L., Kun-Rodrigues, C., Carmona, S., Schleutker, J., Bras, J., Pöyhönen, M., Guerreiro, R., & Myllykangas, L. (2021). Whole-exome sequencing of Finnish patients with vascular cognitive impairment. *European Journal of Human Genetics*, *29*(4), 663–671. https://doi.org/10.1038/s41431-020-00775-9

Mönkäre, S., Kuuluvainen, L., Schleutker, J., Bras, J., Roine, S., Pöyhönen, M., Guerreiro, R., & Myllykangas, L. (2022). Genetic analysis reveals novel variants for vascular cognitive impairment. *Acta Neurologica Scandinavica*, *146*(1), 42–50. https://doi.org/10.1111/ane.13613

Montgomery, N. T., Zientek, K. D., Pokidysheva, E. N., & Bächinger, H. P. (2018). Post-translational modification of type IV collagen with 3-hydroxyproline affects its interactions with glycoprotein

VI and nidogens 1 and 2. *Journal of Biological Chemistry*, *293*(16), 5987–5999. https://doi.org/10.1074/jbc.RA117.000406

Moore, C. J., & Winder, S. J. (2010). Dystroglycan versatility in cell adhesion: A tale of multiple motifs. *Cell Communication and Signaling*, 8, 3. https://doi.org/10.1186/1478-811X-8-3

Moro, L., Venturino, M., Bozzo, C., Silengo, L., Altruda, F., Beguinot, L., Tarone, G., & Defilippi, P. (1998). Integrins induce activation of EGF receptor: Role in MAP kinase induction and adhesion-dependent cell survival. *EMBO Journal*, *17*(22), 6622–6623. https://doi.org/10.1093/emboj/17.22.6622

Moser, M., Nieswandt, B., Ussar, S., Pozgajova, M., & Fässler, R. (2008). Kindlin-3 is essential for integrin activation and platelet aggregation. *Nature Medicine*, *14*(3), 325–330. https://doi.org/10.1038/nm1722

Mou, H., Smith, J. L., Peng, L., Yin, H., Moore, J., Zhang, X. O., Song, C. Q., Sheel, A., Wu, Q., Ozata, D. M., Li, Y., Anderson, D. G., Emerson, C. P., Sontheimer, E. J., Moore, M. J., Weng, Z., & Xue, W. (2017). CRISPR/Cas9-mediated genome editing induces exon skipping by alternative splicing or exon deletion. *Genome Biology*, *18*(1), 108. https://doi.org/10.1186/s13059-017-1237-8

Muiño, E., Gallego-Fabrega, C., Cullell, N., Carrera, C., Torres, N., Krupinski, J., Roquer, J., Montaner, J., & Fernández-Cadenas, I. (2017). Systematic review of cysteine-sparing NOTCH3 missense mutations in patients with clinical suspicion of CADASIL. *International Journal of Molecular Sciences*, 18(9), 1964. https://doi.org/10.3390/ijms18091964

Müller, K., Courtois, G., Ursini, M. V., & Schwaninger, M. (2017). New Insight into the Pathogenesis of Cerebral Small-Vessel Diseases. *Stroke*, *48*(2), 520–527. https://doi.org/10.1161/STROKEAHA.116.012888

Murray, L. S., Lu, Y., Taggart, A., van Regemorter, N. v., Vilain, C., Abramowicz, M., Kadler, K. E., & van Agtmael, T. (2014). Chemical chaperone treatment reduces intracellular accumulation of mutant collagen IV and ameliorates the cellular phenotype of a COL4A2 mutation that causes haemorrhagic stroke. *Human Molecular Genetics*, *23*(2), 283–292. https://doi.org/10.1093/hmg/ddt418

Muthukumaran, G., Blumberg, B., & Kurkinen, M. (1989). The complete primary structure for the α1-chain of mouse collagen IV. Differential evolution of collagen IV domains. *Journal of Biological Chemistry*, *264*(11), 6310–6317. https://doi.org/10.1016/S0021-9258(18)83349-X

Myllyharju, J. (2005). Intracellular post-translational modifications of collagens. *Topics in Current Chemistry*, *247*, 115–147. https://doi.org/10.1007/b103821

Naik, P., & Cucullo, L. (2012). In vitro blood-brain barrier models: Current and perspective technologies. *Journal of Pharmaceutical Sciences*, 101(4), 1337–1354. https://doi.org/10.1002/jps.23022

Nakagawa, S., Deli, M. A., Kawaguchi, H., Shimizudani, T., Shimono, T., Kittel, Á., Tanaka, K., & Niwa, M. (2009). A new blood-brain barrier model using primary rat brain endothelial cells, pericytes and astrocytes. *Neurochemistry International*, *54*(3–4), 253–263. https://doi.org/10.1016/j.neuint.2008.12.002

Nam, K. H., Haitjema, C., Liu, X., Ding, F., Wang, H., Delisa, M. P., & Ke, A. (2012). Cas5d protein processes Pre-crRNA and assembles into a cascade-like interference complex in subtype I-C/Dvulg crispr-cas system. *Structure*, *20*(9), 1574–1584. https://doi.org/10.1016/j.str.2012.06.016

Neal, E. H., Marinelli, N. A., Shi, Y., McClatchey, P. M., Balotin, K. M., Gullett, D. R., Hagerla, K. A., Bowman, A. B., Ess, K. C., Wikswo, J. P., & Lippmann, E. S. (2019). A Simplified, Fully Defined Differentiation Scheme for Producing Blood-Brain Barrier Endothelial Cells from Human iPSCs. *Stem Cell Reports*, *12*(6), 1380–1388. https://doi.org/10.1016/j.stemcr.2019.05.008

Neuhaus, W., Bogner, E., Wirth, M., Trzeciak, J., Lachmann, B., Gabor, F., & Noe, C. R. (2006). A novel tool to characterize paracellular transport: The APTS-dextran ladder. *Pharmaceutical Research*, *23*(7), 1491–1501. https://doi.org/10.1007/s11095-006-0256-z

Neumaier, F., Zlatopolskiy, B. D., & Neumaier, B. (2021). Drug Penetration into the Central Nervous System: Pharmacokinetic Concepts and In Vitro Model Systems. *Pharmaceutics*, *13*(10), 1542. MDPI AG. Retrieved from http://dx.doi.org/10.3390/pharmaceutics13101542

Nitta, T., Hata, M., Gotoh, S., Seo, Y., Sasaki, H., Hashimoto, N., Furuse, M., & Tsukita, S. (2003). Size-selective loosening of the blood-brain barrier in claudin-5-deficient mice. *Journal of Cell Biology*, *161*(3), 653–660. https://doi.org/10.1083/jcb.200302070

Noseda, M., Chang, L., McLean, G., Grim, J. E., Clurman, B. E., Smith, L. L., & Karsan, A. (2004). Notch Activation Induces Endothelial Cell Cycle Arrest and Participates in Contact Inhibition: Role of p21 Cip1 Repression. *Molecular and Cellular Biology*, *24*(20), 8813–8822. https://doi.org/10.1128/mcb.24.20.8813-8822.2004

Oecal, S., Socher, E., Uthoff, M., Ernst, C., Zaucke, F., Sticht, H., Baumann, U., & Gebauer, J. M. (2016). The pH-dependent client release from the collagen-specific chaperone HSP47 is triggered by a tandem histidine pair. *Journal of Biological Chemistry*, *291*(24), 12612–12626. https://doi.org/10.1074/jbc.M115.706069

Okamoto, S., Amaishi, Y., Maki, I., Enoki, T., & Mineno, J. (2019). Highly efficient genome editing for single-base substitutions using optimized ssODNs with Cas9-RNPs. *Scientific Reports*, *9*(1), 4811. https://doi.org/10.1038/s41598-019-41121-4

Omidi, Y., Campbell, L., Barar, J., Connell, D., Akhtar, S., & Gumbleton, M. (2003). Evaluation of the immortalised mouse brain capillary endothelial cell line, b.End3, as an in vitro blood-brain barrier model for drug uptake and transport studies. *Brain Research*, *990*(1–2), 95–112. https://doi.org/10.1016/S0006-8993(03)03443-7

Orlova, V. v., van den Hil, F. E., Petrus-Reurer, S., Drabsch, Y., ten Dijke, P., & Mummery, C. L. (2014). Generation, expansion and functional analysis of endothelial cells and pericytes derived from human pluripotent stem cells. *Nature Protocols*, *9*(6), 1514–1531. https://doi.org/10.1038/nprot.2014.102

Osada, T., Gu, Y. H., Kanazawa, M., Tsubota, Y., Hawkins, B. T., Spatz, M., Milner, R., & del Zoppo, G. J. (2011). Interendothelial claudin-5 expression depends on cerebral endothelial cell-matrix adhesion by B 1-integrins. *Journal of Cerebral Blood Flow and Metabolism*, *31*(10), 1972–1985. https://doi.org/10.1038/jcbfm.2011.99

Pacitti, D., Privolizzi, R., & Bax, B. E. (2019). Organs to cells and cells to organoids: The evolution of In vitro central nervous system modelling. *Frontiers in Cellular Neuroscience*, 13, 129. https://doi.org/10.3389/fncel.2019.00129

Papakonstantinou, E., Bacopoulou, F., Brouzas, D., Megalooikonomou, V., D'Elia, D., Bongcam-Rudloff, E., & Vlachakis, D. (2019). NOTCH3 and CADASIL syndrome: a genetic and structural overview. *EMBnet.Journal*, *24*, e921. https://doi.org/10.14806/ej.24.0.921

Paques, F., & Duchateau, P. (2007). Meganucleases and DNA Double-Strand Break-Induced Recombination: Perspectives for Gene Therapy. *Current Gene Therapy*, *7*(1), 49–66. https://doi.org/10.2174/156652307779940216

Paquet, D., Kwart, D., Chen, A., Sproul, A., Jacob, S., Teo, S., Olsen, K. M., Gregg, A., Noggle, S., & Tessier-Lavigne, M. (2016). Efficient introduction of specific homozygous and heterozygous mutations using CRISPR/Cas9. *Nature*, *533*(7601), 125–129. https://doi.org/10.1038/nature17664

Parkin, J. des, San Antonio, J. D., Pedchenko, V., Hudson, B., Jensen, S. T., & Savige, J. (2011). Mapping structural landmarks, ligand binding sites, and missense mutations to the collagen IV heterotrimers predicts major functional domains, novel interactions, and variation in phenotypes in inherited diseases affecting basement membranes. *Human Mutation*, 32(2), 127–143. https://doi.org/10.1002/humu.21401

Park, T. E., Mustafaoglu, N., Herland, A., Hasselkus, R., Mannix, R., FitzGerald, E. A., Prantil-Baun, R., Watters, A., Henry, O., Benz, M., Sanchez, H., McCrea, H. J., Goumnerova, L. C., Song, H. W., Palecek, S. P., Shusta, E., & Ingber, D. E. (2019). Hypoxia-enhanced Blood-Brain Barrier Chip recapitulates human barrier function and shuttling of drugs and antibodies. *Nature Communications*, *10*(1), 2621. https://doi.org/10.1038/s41467-019-10588-0

Paschaki, M., Lin, S. C., Wong, R. L. Y., Finnell, R. H., Dollé, P., & Niederreither, K. (2012). Retinoic acid-dependent signaling pathways and lineage events in the developing mouse spinal cord. *PLoS ONE*, *7*(3), e32447. https://doi.org/10.1371/journal.pone.0032447

Pasi, M., & Cordonnier, C. (2020). Clinical Relevance of Cerebral Small Vessel Diseases. *Stroke*, 51(1), 47–53. https://doi.org/10.1161/STROKEAHA.119.024148

Patsch, C., Challet-Meylan, L., Thoma, E. C., Urich, E., Heckel, T., O'Sullivan, J. F., Grainger, S. J., Kapp, F. G., Sun, L., Christensen, K., Xia, Y., Florido, M. H. C., He, W., Pan, W., Prummer, M., Warren, C. R., Jakob-Roetne, R., Certa, U., Jagasia, R., … Cowan, C. A. (2015). Generation of vascular endothelial and smooth muscle cells from human pluripotent stem cells. *Nature Cell Biology*, *17*(8), 994–1003. https://doi.org/10.1038/ncb3205

Pen, A. E., & Jensen, U. B. (2017). Current status of treating neurodegenerative disease with induced pluripotent stem cells. *Acta Neurologica Scandinavica*, 135(1), 57–72. https://doi.org/10.1111/ane.12545

Perriot, S., Mathias, A., Perriard, G., Canales, M., Jonkmans, N., Merienne, N., Meunier, C., el Kassar, L., Perrier, A. L., Laplaud, D. A., Schluep, M., Déglon, N., & du Pasquier, R. (2018). Human Induced Pluripotent Stem Cell-Derived Astrocytes Are Differentially Activated by Multiple Sclerosis-Associated Cytokines. *Stem Cell Reports*, *11*(5), 1199–1210. https://doi.org/10.1016/j.stemcr.2018.09.015

Pickar-Oliver, A., & Gersbach, C. A. (2019). The next generation of CRISPR–Cas technologies and applications. *Nature Reviews Molecular Cell Biology*, 20(8), 490–507. https://doi.org/10.1038/s41580-019-0131-5

Plaisier, E., Chen, Z., Gekeler, F., Benhassine, S., Dahan, K., Marro, B., Alamowitch, S., Paques, M., & Ronco, P. (2010). Novel COL4A1 mutations associated with HANAC syndrome: A role for the triple helical CB3[IV] domain. *American Journal of Medical Genetics, Part A*, *152 A*(10), 2550–2555. https://doi.org/10.1002/ajmg.a.33659

Plaisier, E., Gribouval, O., Alamowitch, S., Mougenot, B., Prost, C., Verpont, M. C., Marro, B., Desmettre, T., Cohen, S. Y., Roullet, E., Dracon, M., Fardeau, M., van Agtmael, T., Kerjaschki, D., Antignac, C., & Ronco, P. (2007). COL4A1 Mutations and Hereditary Angiopathy, Nephropathy, Aneurysms, and Muscle Cramps. *New England Journal of Medicine*, *357*(26), 2657–2695. https://doi.org/10.1056/nejmoa071906

Pokidysheva, E., Boudko, S., Vranka, J., Zientek, K., Maddox, K., Moser, M., Fässler, R., Ware, J., & Bächinger, H. P. (2014). Biological role of prolyl 3-hydroxylation in type IV collagen. *Proceedings of the National Academy of Sciences of the United States of America*, *111*(1), 161–166. https://doi.org/10.1073/pnas.1307597111

Popel, A. S., & Johnson, P. C. (2005). Microcirculation and hemorheology. *Annual Review of Fluid Mechanics*, 37, 43–69. https://doi.org/10.1146/annurev.fluid.37.042604.133933

Popp, M. W., & Maquat, L. E. (2016). Leveraging rules of nonsense-mediated mRNA decay for genome engineering and personalized medicine. *Cell*, 165(6), 1319–1322. https://doi.org/10.1016/j.cell.2016.05.053

Pöschl, E., Schlötzer-Schrehardt, U., Brachvogel, B., Saito, K., Ninomiya, Y., & Mayer, U. (2004). Collagen IV is essential for basement membrane stability but dispensable for initiation of its assembly during early development. *Development*, *131*(7), 1619–1628. https://doi.org/10.1242/dev.01037

Praça, C., Rosa, S. C., Sevin, E., Cecchelli, R., Dehouck, M. P., & Ferreira, L. S. (2019). Derivation of Brain Capillary-like Endothelial Cells from Human Pluripotent Stem Cell-Derived Endothelial Progenitor Cells. *Stem Cell Reports*, *13*(4), 599–611. https://doi.org/10.1016/j.stemcr.2019.08.002

Profaci, C. P., Munji, R. N., Pulido, R. S., & Daneman, R. (2020). The blood–brain barrier in health and disease: Important unanswered questions. *Journal of Experimental Medicine*, 217(4), e20190062. https://doi.org/10.1084/jem.20190062

Prudhomme, J. G., Sherman, I. W., Land, K. M., Moses, A. v., Stenglein, S., & Nelson, J. A. (1996). Studies of plasmodium falciparum cytoadherence using immortalized human brain capillary endothelial cells. *International Journal for Parasitology*, *26*(6), 647–655. https://doi.org/10.1016/0020-7519(96)00027-6

Qian, T., Maguire, S. E., Canfield, S. G., Bao, X., Olson, W. R., Shusta, E. v., & Palecek, S. P. (2017). Directed differentiation of human pluripotent stem cells to blood-brain barrier endothelial cells. *Science Advances*, *3*(11), e1701679. https://doi.org/10.1126/sciadv.1701679

Qosa, H., Miller, D. S., Pasinelli, P., & Trotti, D. (2015). Regulation of ABC efflux transporters at blood-brain barrier in health and neurological disorders. *Brain Research*, 1628, 298–316. https://doi.org/10.1016/j.brainres.2015.07.005

Quick, S., Moss, J., Rajani, R. M., & Williams, A. (2021). A Vessel for Change: Endothelial Dysfunction in Cerebral Small Vessel Disease. *Trends in Neurosciences389*, 44(4), 289–305. https://doi.org/10.1016/j.tins.2020.11.003

Ragg, H. (2007). The role of serpins in the surveillance of the secretory pathway. *Cellular and Molecular Life Sciences*, 64(21), 2763–2770. https://doi.org/10.1007/s00018-007-7157-0

Ran, F. A., Hsu, P. D., Wright, J., Agarwala, V., Scott, D. A., & Zhang, F. (2013). Genome engineering using the CRISPR-Cas9 system. *Nature Protocols*, *8*(11), 2281–2308. https://doi.org/10.1038/nprot.2013.143

Rannikmäe, K., Henshall, D. E., Thrippleton, S., Ginj Kong, Q., Chong, M., Grami, N., Kuan, I., Wilkinson, T., Wilson, B., Wilson, K., Paré, G., & Sudlow, C. (2020). Beyond the Brain: Systematic Review of Extracerebral Phenotypes Associated with Monogenic Cerebral Small Vessel Disease. *Stroke*, *51*, 3007–3017. https://doi.org/10.1161/STROKEAHA.120.029517

Raote, I., Bellido, M. O., Pirozzi, M., Zhang, C., Melville, D., Parashuraman, S., Zimmermann, T., & Malhotra, V. (2017). TAN GO1 assembles into rings around COP II coats at ER exit sites. *Journal of Cell Biology*, *216*(4), 901–909. https://doi.org/10.1083/jcb.201608080

Ratelade, J., Klug, N. R., Lombardi, D., Angelim, M. K. S. C., Dabertrand, F., Dabertrand, F., Domenga-Denier, V., Salman, R. A. S., Smith, C., Gerbeau, J. F., Nelson, M. T., Nelson, M. T., Joutel, A., Joutel, A., & Joutel, A. (2020). Reducing Hypermuscularization of the Transitional Segment between Arterioles and Capillaries Protects against Spontaneous Intracerebral Hemorrhage. *Circulation*, *141*, 2078–2094. https://doi.org/10.1161/CIRCULATIONAHA.119.040963

Ratelade, J., Mezouar, N., Domenga-Denier, V., Rochey, A., Plaisier, E., & Joutel, A. (2018). Severity of arterial defects in the retina correlates with the burden of intracerebral haemorrhage in COL4A1-related stroke. *Journal of Pathology*, *244*(4), 408–420. https://doi.org/10.1002/path.5023

Rauch, S. M., Huen, K., Miller, M. C., Chaudry, H., Lau, M., Sanes, J. R., Johanson, C. E., Stopa, E. G., & Burgess, R. W. (2011). Changes in brain β-amyloid deposition and aquaporin 4 levels in response to altered agrin expression in mice. *Journal of Neuropathology and Experimental Neurology*, *70*(12), 1124–1137. https://doi.org/10.1097/NEN.0b013e31823b0b12

Rautavuoma, K., Takaluoma, K., Sormunen, R., Myllyharju, J., Kivirikko, K. I., & Soininen, R. (2004). Premature aggregation of type IV collagen and early lethality in lysyl hydroxylase 3 null mice. *Proceedings of the National Academy of Sciences of the United States of America*, *101*(39), 14120–14125. https://doi.org/10.1073/pnas.0404966101

Rebuzzini, P., Zuccotti, M., Redi, C. A., & Garagna, S. (2016). Achilles' heel of pluripotent stem cells: genetic, genomic and epigenetic variations during prolonged culture. *Cellular and Molecular Life Sciences*, 73(13), 2453–2466. https://doi.org/10.1007/s00018-016-2171-8

Reed, M. J., Damodarasamy, M., & Banks, W. A. (2019). The extracellular matrix of the blood–brain barrier: structural and functional roles in health, aging, and Alzheimer's disease. *Tissue Barriers*, 7(4), e1651157. https://doi.org/10.1080/21688370.2019.1651157

Reitsma, S., Slaaf, D. W., Vink, H., van Zandvoort, M. A. M. J., & Oude Egbrink, M. G. A. (2007). The endothelial glycocalyx: Composition, functions, and visualization. *Pflugers Archiv European Journal of Physiology*, 454(3), 345–359. https://doi.org/10.1007/s00424-007-0212-8

Rensma, S. P., van Sloten, T. T., Launer, L. J., & Stehouwer, C. D. A. (2018). Cerebral small vessel disease and risk of incident stroke, dementia and depression, and all-cause mortality: A systematic review and meta-analysis. *Neuroscience and Biobehavioral Reviews*, 90, 164–173. https://doi.org/10.1016/j.neubiorev.2018.04.003

Reyahi, A., Nik, A. M., Ghiami, M., Gritli-Linde, A., Pontén, F., Johansson, B. R., & Carlsson, P. (2015). Foxf2 Is Required for Brain Pericyte Differentiation and Development and Maintenance of the Blood-Brain Barrier. *Developmental Cell*, *34*(1), 19–32. https://doi.org/10.1016/j.devcel.2015.05.008

Riazuddin, S., Ahmed, Z. M., Fanning, A. S., Lagziel, A., Kitajiri, S. I., Ramzan, K., Khan, S. N., Chattaraj, P., Friedman, P. L., Anderson, J. M., Belyantseva, I. A., Forge, A., Riazuddin, S., & Friedman, T. B. (2006). Tricellulin is a tight-junction protein necessary for hearing. *American Journal of Human Genetics*, *79*(6), 1040–1051. https://doi.org/10.1086/510022

Rice, G. I., Rodero, M. P., & Crow, Y. J. (2015). Human Disease Phenotypes Associated With Mutations in TREX1. *Journal of Clinical Immunology*, 35(3), 235–243. https://doi.org/10.1007/s10875-015-0147-3

Richardson, C. D., Ray, G. J., DeWitt, M. A., Curie, G. L., & Corn, J. E. (2016). Enhancing homology-directed genome editing by catalytically active and inactive CRISPR-Cas9 using asymmetric donor DNA. *Nature Biotechnology*, *34*(3), 339–344. https://doi.org/10.1038/nbt.3481

Ries, C. (2014). Cytokine functions of TIMP-1. *Cellular and Molecular Life Sciences*, 71(4), 659–672. https://doi.org/10.1007/s00018-013-1457-3

Riesenberg, S., Chintalapati, M., Macak, D., Kanis, P., Maricic, T., & Pääbo, S. (2019). Simultaneous precise editing of multiple genes in human cells. *Nucleic Acids Research*, *47*(19), e116. https://doi.org/10.1093/NAR/GKZ669

Riesenberg, S., & Maricic, T. (2018). Targeting repair pathways with small molecules increases precise genome editing in pluripotent stem cells. *Nature Communications*, *9*(1), 2164. https://doi.org/10.1038/s41467-018-04609-7

Riordan, S. M., Heruth, D. P., Zhang, L. Q., & Ye, S. Q. (2015). Application of CRISPR/Cas9 for biomedical discoveries. *Cell and Bioscience*, 5(1), 33. https://doi.org/10.1186/s13578-015-0027-9

Robertson, J. M. (2014). Astrocytes and the evolution of the human brain. *Medical Hypotheses*, *82*(2), 236–239. https://doi.org/10.1016/j.mehy.2013.12.004

Rosa, S., Praça, C., Pitrez, P. R., Gouveia, P. J., Aranguren, X. L., Ricotti, L., & Ferreira, L. S. (2019). Functional characterization of iPSC-derived arterial- and venous-like endothelial cells. *Scientific Reports*, *9*(1), 3826. https://doi.org/10.1038/s41598-019-40417-9

Rosenberg, R. N., & Pascual, J. M. (2020). Rosenberg's Molecular and Genetic Basis of Neurological and Psychiatric Disease. In *Rosenberg's Molecular and Genetic Basis of Neurological and Psychiatric Disease: Volume 2* (5th ed.). https://doi.org/10.1016/B978-0-12-813866-3.00043-6

Rost, N. S., Cloonan, L., Kanakis, A. S., Fitzpatrick, K. M., Azzariti, D. R., Clarke, V., Lourenco, C. M., Germain, D. P., Politei, J. M., Homola, G. A., Sommer, C., Üçeyler, N., & Sims, K. B. (2016). Determinants of white matter hyperintensity burden in patients with Fabry disease. *Neurology*, *86*(20), 1880–1886. https://doi.org/10.1212/WNL.0000000000002673

Rouet, P., Smih, F., & Jasin, M. (1994). Introduction of double-strand breaks into the genome of mouse cells by expression of a rare-cutting endonuclease. *Molecular and Cellular Biology*, *14*(12), 8096–8106. https://doi.org/10.1128/mcb.14.12.8096

Rowe, R. G., & Daley, G. Q. (2019). Induced pluripotent stem cells in disease modelling and drug discovery. *Nature Reviews Genetics*, 20(7), 377–388. https://doi.org/10.1038/s41576-019-0100-z

Rutten, J. W., van Eijsden, B. J., Duering, M., Jouvent, E., Opherk, C., Pantoni, L., Federico, A., Dichgans, M., Markus, H. S., Chabriat, H., & Lesnik Oberstein, S. A. J. (2019). The effect of NOTCH3 pathogenic variant position on CADASIL disease severity: NOTCH3 EGFr 1–6 pathogenic variant are associated with a more severe phenotype and lower survival compared with EGFr 7–34 pathogenic variant. *Genetics in Medicine*, *21*(3), 676–682. https://doi.org/10.1038/s41436-018-0088-3

Sado, Y., Kagawa, M., Naito, I., Ueki, Y., Seki, T., Momota, R., Oohashi, T., & Ninomiya, Y. (1998). Organization and expression of basement membrane collagen IV genes and their roles in human disorders. *Journal of Biochemistry*, 123(5), 767–776. https://doi.org/10.1093/oxfordjournals.jbchem.a022003

Saito, M., & Marumo, K. (2010). Collagen cross-links as a determinant of bone quality: A possible explanation for bone fragility in aging, osteoporosis, and diabetes mellitus. *Osteoporosis International*, 21(2), 195–214. https://doi.org/10.1007/s00198-009-1066-z

Sakai, N., Uemura, M., Kato, T., Nozaki, H., Koyama, A., Ando, S., Kamei, H., Kato, M., & Onodera, O. (2020). Hemorrhagic cerebral small vessel disease caused by a novel mutation in 3′ UTR of collagen type IV alpha 1. *Neurology: Genetics*, *6*(1), e383. https://doi.org/10.1212/NXG.0000000000000383

Sano, Y., Shimizu, F., Abe, M., Maeda, T., Kashiwamura, Y., Ohtsuki, S., Terasaki, T., Obinata, M., Kajiwara, K., Fujii, M., Suzuki, M., & Kanda, T. (2010). Establishment of a new conditionally immortalized human brain microvascular endothelial cell line retaining an in vivo blood-brain barrier function. *Journal of Cellular Physiology*, *225*(2), 519–528. https://doi.org/10.1002/jcp.22232

Santiago, Y., Chan, E., Liu, P. Q., Orlando, S., Zhang, L., Urnov, F. D., Holmes, M. C., Guschin, D., Waite, A., Miller, J. C., Rebar, E. J., Gregory, P. D., Klug, A., & Collingwood, T. N. (2008). Targeted gene knockout in mammalian cells by using engineered zinc-finger nucleases. *Proceedings of the National Academy of Sciences of the United States of America*, *105*(15), 5809–5814. https://doi.org/10.1073/pnas.0800940105

Saskin, A., Sillon, G., Palfreeman, N., & Buhas, D. (2018). COL4A1/2 CNVs and cerebral small vessel disease: Narrowing in on the critical chromosomal region. *Neurology*, *90*(22), 1026–1028. https://doi.org/10.1212/WNL.0000000000005601

Schindelin, J., Arganda-Carreras, I., Frise, E., Kaynig, V., Longair, M., Pietzsch, T., Preibisch, S., Rueden, C., Saalfeld, S., Schmid, B., Tinevez, J. Y., White, D. J., Hartenstein, V., Eliceiri, K., Tomancak, P., & Cardona, A. (2012). Fiji: An open-source platform for biological-image analysis. *Nature Methods*, 9(7), 676–682. https://doi.org/10.1038/nmeth.2019

Schymeinsky, J., Nedbal, S., Miosge, N., Pöschl, E., Rao, C., Beier, D. R., Skarnes, W. C., Timpl, R., & Bader, B. L. (2002). Gene Structure and Functional Analysis of the Mouse Nidogen-2 Gene: Nidogen-2 Is Not Essential for Basement Membrane Formation in Mice. *Molecular and Cellular Biology*, *22*(19), 6820–6830. https://doi.org/10.1128/mcb.22.19.6820-6830.2002

Shah, S. A., Erdmann, S., Mojica, F. J. M., & Garrett, R. A. (2013). Protospacer recognition motifs. *RNA Biology*, *10*(5), 891–899. https://doi.org/10.4161/rna.23764

Shalem, O., Sanjana, N. E., & Zhang, F. (2015). High-throughput functional genomics using CRISPR-Cas9. *Nature Reviews Genetics*, 16(5), 299–311. https://doi.org/10.1038/nrg3899

Shen, M. W., Arbab, M., Hsu, J. Y., Worstell, D., Culbertson, S. J., Krabbe, O., Cassa, C. A., Liu, D. R., Gifford, D. K., & Sherwood, R. I. (2018). Predictable and precise template-free CRISPR editing of pathogenic variants. *Nature*, *563*(7733), 646–651. https://doi.org/10.1038/s41586-018-0686-x

Shi, Y., & Wardlaw, J. M. (2016). Update on cerebral small vessel disease: A dynamic whole-brain disease. *Stroke and Vascular Neurology*, 1(3), e000035. https://doi.org/10.1136/svn-2016-000035

Sieczkiewicz, G. J., & Herman, I. M. (2003). TGF-β1 signaling controls retinal pericyte contractile protein expression. *Microvascular Research*, *66*(3), 190–196. https://doi.org/10.1016/S0026-2862(03)00055-4

Siegenthaler, J. A., Sohet, F., & Daneman, R. (2013). "Sealing off the CNS": Cellular and molecular regulation of blood-brain barriergenesis. In *Current Opinion in Neurobiology*, 23(6), 1057–1064. https://doi.org/10.1016/j.conb.2013.06.006

Siitonen, M., Börjesson-Hanson, A., Pöyhönen, M., Ora, A., Pasanen, P., Bras, J., Kern, S., Kern, J., Andersen, O., Stanescu, H., Kleta, R., Baumann, M., Kalaria, R., Kalimo, H., Singleton, A., Hardy, J., Viitanen, M., Myllykangas, L., & Guerreiro, R. (2017). Multi-infarct dementia of Swedish type is caused by a 3'UTR mutation of COL4A1. *Brain*, 140(5), e29. https://doi.org/10.1093/brain/awx062

Simkin, D., Papakis, V., Bustos, B. I., Ambrosi, C. M., Ryan, S. J., Baru, V., Williams, L. A., Dempsey, G. T., McManus, O. B., Landers, J. E., Lubbe, S. J., George, A. L., & Kiskinis, E. (2022). Homozygous might be hemizygous: CRISPR/Cas9 editing in iPSCs results in detrimental on-target defects that escape standard quality controls. *Stem Cell Reports*, *17*(4), 993–1008. https://doi.org/10.1016/j.stemcr.2022.02.008

Sims, K., Politei, J., Banikazemi, M., & Lee, P. (2009). Stroke in fabry disease frequently occurs before diagnosis and in the absence of other clinical events: Natural history data from the fabry registry. *Stroke*, *40*(3), 788–794. https://doi.org/10.1161/STROKEAHA.108.526293

Singh, R., Kuscu, C., Quinlan, A., Qi, Y., & Adli, M. (2015). Cas9-chromatin binding information enables more accurate CRISPR off-target prediction. *Nucleic Acids Research*, *43*(18), e118. https://doi.org/10.1093/nar/gkv575

Sipilä, L., Ruotsalainen, H., Sormunen, R., Baker, N. L., Lamande, S. R., Vapola, M., Wang, C., Sado, Y., Aszodi, A., & Myllyla, R. (2007). Secretion and assembly of type IV and VI collagens depend on glycosylation of hydroxylysines. *Journal of Biological Chemistry*, *282*(46), 33381–33388. https://doi.org/10.1074/jbc.M704198200

Sivandzade, F., & Cucullo, L. (2018). In-vitro blood–brain barrier modeling: A review of modern and fast-advancing technologies. *Journal of Cerebral Blood Flow and Metabolism*, 38(10), 1667–1681. https://doi.org/10.1177/0271678X18788769

Sixt, M., Engelhardt, B., Pausch, F., Hallmann, R., Wendler, O., & Sorokin, L. M. (2001). Endothelial cell laminin isoforms, laminins 8 and 10, play decisive roles in T cell recruitment across the blood-brain barrier in experimental autoimmune encephalomyelitis. *Journal of Cell Biology*, *153*(5), 933–945. https://doi.org/10.1083/jcb.153.5.933

Skarnes, W. C., Pellegrino, E., & McDonough, J. A. (2019). Improving homology-directed repair efficiency in human stem cells. *Methods*, *164–165*, 18–28. https://doi.org/10.1016/j.ymeth.2019.06.016

Smith, E. E., Saposnik, G., Biessels, G. J., Doubal, F. N., Fornage, M., Gorelick, P. B., Greenberg, S. M., Higashida, R. T., Kasner, S. E., & Seshadri, S. (2017). Prevention of Stroke in Patients with Silent Cerebrovascular Disease. *Stroke*, *48*(2), e44. https://doi.org/10.1161/STR.0000000000000116

Smith, H. W., & Marshall, C. J. (2010). Regulation of cell signalling by uPAR. *Nature Reviews Molecular Cell Biology*, 11(1), 23–26. https://doi.org/10.1038/nrm2821

Smyth, L. C. D., Rustenhoven, J., Scotter, E. L., Schweder, P., Faull, R. L. M., Park, T. I. H., & Dragunow, M. (2018). Markers for human brain pericytes and smooth muscle cells. *Journal of Chemical Neuroanatomy*, *92*, 48–60. https://doi.org/10.1016/j.jchemneu.2018.06.001

Spagnolo, L., Rivera-Calzada, A., Pearl, L. H., & Llorca, O. (2006). Three-Dimensional Structure of the Human DNA-PKcs/Ku70/Ku80 Complex Assembled on DNA and Its Implications for DNA DSB Repair. *Molecular Cell*, *22*(4), 511–519. https://doi.org/10.1016/j.molcel.2006.04.013

Spitzhorn, L. S., Megges, M., Wruck, W., Rahman, M. S., Otte, J., Degistirici, Ö., Meisel, R., Sorg, R. V., Oreffo, R. O. C., & Adjaye, J. (2019). Human iPSC-derived MSCs (iMSCs) from aged individuals acquire a rejuvenation signature. *Stem Cell Research and Therapy*, *10*(1), 100. https://doi.org/10.1186/s13287-019-1209-x

Srinivasan, B., Kolli, A. R., Esch, M. B., Abaci, H. E., Shuler, M. L., & Hickman, J. J. (2015). TEER Measurement Techniques for In Vitro Barrier Model Systems. *Journal of Laboratory Automation*, 20(2), 107–126. https://doi.org/10.1177/2211068214561025

Stam, A. H., Kothari, P. H., Shaikh, A., Gschwendter, A., Jen, J. C., Hodgkinson, S., Hardy, T. A., Hayes, M., Kempster, P. A., Kotschet, K. E., Bajema, I. M., van Duinen, S. G., Maat-Schieman, M. L. C., de Jong, P. T. V. M., de Smet, M. D., de Wolff-Rouendaal, D., Dijkman, G., Pelzer, N., Kolar, G. R., … Ferrari, M. D. (2016). Retinal vasculopathy with cerebral leukoencephalopathy and systemic manifestations. *Brain a Journal of Neurology*, *139*(11), 2909–2922. https://doi.org/10.1093/aww253

Stamatovic, S. M., Johnson, A. M., Keep, R. F., & Andjelkovic, A. v. (2016). Junctional proteins of the blood-brain barrier: New insights into function and dysfunction. *Tissue Barriers*, 4(1), e1154641. https://doi.org/10.1080/21688370.2016.1154641

Stanness, C. A., Guatteo, E., & Janigro, D. (1996). A dynamic model of the blood-brain barrier "in vitro." *NeuroToxicology*, *17*(2), 481–496.

Stawikowski, M. J., Aukszi, B., Stawikowska, R., Cudic, M., & Fields, G. B. (2014). Glycosylation modulates melanoma cell α2β1 and α3β1 integrin interactions with type IV collagen. *Journal of Biological Chemistry*, *289*(31), 21591–21604. https://doi.org/10.1074/jbc.M114.572073

Stebbins, M. J., Gastfriend, B. D., Canfield, S. G., Lee, M. S., Richards, D., Faubion, M. G., Li, W. J., Daneman, R., Palecek, S. P., & Shusta, E. v. (2019). Human pluripotent stem cell–derived brain pericyte–like cells induce blood-brain barrier properties. *Science Advances*, *5*(3), eaau7375. https://doi.org/10.1126/sciadv.aau7375

Steiner, E., Enzmann, G. U., Lyck, R., Lin, S., Rüegg, M. A., Kröger, S., & Engelhardt, B. (2014). The heparan sulfate proteoglycan agrin contributes to barrier properties of mouse brain endothelial cells by stabilizing adherens junctions. *Cell and Tissue Research*, *358*(2), 465–479. https://doi.org/10.1007/s00441-014-1969-7

Stephenson, M., Reich, D. H., & Boheler, K. R. (2020). Induced pluripotent stem cell-derived vascular smooth muscle cells. *Vascular Biology*, *2*(1), R1–R15. https://doi.org/10.1530/vb-19-0028

Sterneckert, J. L., Reinhardt, P., & Schöler, H. R. (2014). Investigating human disease using stem cell models. *Nature Reviews Genetics*, 15(9), 625–639. https://doi.org/10.1038/nrg3764

Stins, M. F., Badger, J., & Sik Kim, K. (2001). Bacterial invasion and transcytosis in transfected human brain microvascular endothelial cells. *Microbial Pathogenesis*, *30*(1), 19–28. https://doi.org/10.1006/mpat.2000.0406

Stratman, A. N., Malotte, K. M., Mahan, R. D., Davis, M. J., & Davis, G. E. (2009). Pericyte recruitment during vasculogenic tube assembly stimulates endothelial basement membrane matrix formation. *Blood*, *114*(24), 5091–5101. https://doi.org/10.1182/blood-2009-05-222364

Sundberg, C., & Rubin, K. (1996). Stimulation of β1 integrins on fibroblasts induces PDGF independent tyrosine phosphorylation of PDGF β-receptors. *Journal of Cell Biology*, *132*(4), 741–752. https://doi.org/10.1083/jcb.132.4.741

Sweeney, M. D., Ayyadurai, S., & Zlokovic, B. v. (2016). Pericytes of the neurovascular unit: Key functions and signaling pathways. *Nature Neuroscience*, 19(6), 771–783. https://doi.org/10.1038/nn.4288

Sweeney, M. D., Zhao, Z., Montagne, A., Nelson, A. R., & Zlokovic, B. v. (2019). Blood-brain barrier: From physiology to disease and back. *Physiological Reviews*, 99(1), 21–78. https://doi.org/10.1152/physrev.00050.2017

Tabata, H. (2015). Diverse subtypes of astrocytes and their development during corticogenesis. *Frontiers in Neuroscience*, 9, 114. https://doi.org/10.3389/fnins.2015.00114

Takahashi, K., Tanabe, K., Ohnuki, M., Narita, M., Ichisaka, T., Tomoda, K., & Yamanaka, S. (2007). Induction of Pluripotent Stem Cells from Adult Human Fibroblasts by Defined Factors. *Cell*, *131*(5), 861–872. https://doi.org/10.1016/j.cell.2007.11.019

Takahashi, K., & Yamanaka, S. (2006). Induction of Pluripotent Stem Cells from Mouse Embryonic and Adult Fibroblast Cultures by Defined Factors. *Cell*, *126*(4), 663–676. https://doi.org/10.1016/j.cell.2006.07.024

Tang, J., Kang, Y., Huang, L., Wu, L., & Peng, Y. (2020). TIMP1 preserves the blood–brain barrier through interacting with CD63/integrin β1 complex and regulating downstream FAK/RhoA signaling. *Acta Pharmaceutica Sinica B*, *10*(6), 987–1003. https://doi.org/10.1016/j.apsb.2020.02.015

Tan, R., Traylor, M., Rutten-Jacobs, L., & Markus, H. (2017). New insights into mechanisms of small vessel disease stroke from genetics. *Clinical Science*, *131*(7), 515–531. https://doi.org/10.1042/CS20160825

Tapia, N., & Schöler, H. R. (2016). Molecular Obstacles to Clinical Translation of iPSCs. *Cell Stem Cell*, 19(3), 298–309. https://doi.org/10.1016/j.stem.2016.06.017

TCW, J., Wang, M., Pimenova, A. A., Bowles, K. R., Hartley, B. J., Lacin, E., Machlovi, S. I., Abdelaal, R., Karch, C. M., Phatnani, H., Slesinger, P. A., Zhang, B., Goate, A. M., & Brennand, K. J. (2017). An Efficient Platform for Astrocyte Differentiation from Human Induced Pluripotent Stem Cells. *Stem Cell Reports*, *9*(2), 600–614. https://doi.org/10.1016/j.stemcr.2017.06.018

Tham, D. K. L., Joshi, B., & Moukhles, H. (2016). Aquaporin-4 cell-surface expression and turnover are regulated by dystroglycan, dynamin, and the extracellular matrix in astrocytes. *PLoS ONE*, *11*(10), e0165439. https://doi.org/10.1371/journal.pone.0165439

Thomsen, L. B., Burkhart, A., & Moos, T. (2015). A triple culture model of the blood-brain barrier using porcine brain endothelial cells, astrocytes and pericytes. *PLoS ONE*, *10*(8), e0134765. https://doi.org/10.1371/journal.pone.0134765

Thomsen, M. S., Routhe, L. J., & Moos, T. (2017). The vascular basement membrane in the healthy and pathological brain. *Journal of Cerebral Blood Flow and Metabolism*, 37(10), 3300–3317. https://doi.org/10.1177/0271678X17722436

Thrippleton, M. J., Backes, W. H., Sourbron, S., Ingrisch, M., van Osch, M. J. P., Dichgans, M., Fazekas, F., Ropele, S., Frayne, R., van Oostenbrugge, R. J., Smith, E. E., & Wardlaw, J. M. (2019). Quantifying blood-brain barrier leakage in small vessel disease: Review and consensus recommendations. *Alzheimer's and Dementia*,15(6) 850–858. https://doi.org/10.1016/j.jalz.2019.01.013

Tong, L., Hill, R. A., Damisah, E. C., Murray, K. N., Yuan, P., Bordey, A., & Grutzendler, J. (2021). Imaging and optogenetic modulation of vascular mural cells in the live brain. *Nature Protocols*, *16*(1), 472–496. https://doi.org/10.1038/s41596-020-00425-w

Topakian, R., Barrick, T. R., Howe, F. A., & Markus, H. S. (2010). Blood-brain barrier permeability is increased in normal-appearing white matter in patients with lacunar stroke and leucoaraiosis. *Journal of Neurology, Neurosurgery and Psychiatry*, *81*(2), 192–197. https://doi.org/10.1136/jnnp.2009.172072

Trouillet, A., Lorach, H., Dubus, E., el Mathari, B., Ivkovic, I., Dégardin, J., Simonutti, M., Paques, M., Guillonneau, X., Sennlaub, F., Sahel, J. A., Ronco, P., Plaisier, E., & Picaud, S. (2017). Col4a1 mutation generates vascular abnormalities correlated with neuronal damage in a mouse model of HANAC syndrome. *Neurobiology of Disease*, *100*, 52–61. https://doi.org/10.1016/j.nbd.2016.12.014

Tuladhar, R., Yeu, Y., Tyler Piazza, J., Tan, Z., Rene Clemenceau, J., Wu, X., Barrett, Q., Herbert, J., Mathews, D. H., Kim, J., Hyun Hwang, T., & Lum, L. (2019). CRISPR-Cas9-based mutagenesis frequently provokes on-target mRNA misregulation. *Nature Communications*, *10*(1), 4056. https://doi.org/10.1038/s41467-019-12028-5

Uematsu, M., Ohara, Y., Navas, J. P., Nishida, K., Murphy, T. J., Alexander, R. W., Nerem, R. M., & Harrison, D. G. (1995). Regulation of endothelial cell nitric oxide synthase mRNA expression by shear stress. *American Journal of Physiology - Cell Physiology*, *269*(6 Pt 1), c1371–c1378. https://doi.org/10.1152/ajpcell.1995.269.6.c1371

Umeda, K., Ikenouchi, J., Katahira-Tayama, S., Furuse, K., Sasaki, H., Nakayama, M., Matsui, T., Tsukita, S., Furuse, M., & Tsukita, S. (2006). ZO-1 and ZO-2 Independently Determine Where Claudins Are Polymerized in Tight-Junction Strand Formation. *Cell*, *126*(4), 741–754. https://doi.org/10.1016/j.cell.2006.06.043

Urich, E., Patsch, C., Aigner, S., Graf, M., Iacone, R., & Freskgård, P. O. (2013). Multicellular self-assembled spheroidal model of the blood brain barrier. *Scientific Reports*, *3*, 1500. https://doi.org/10.1038/srep01500

Urnov, F. D., Miller, J. C., Lee, Y. L., Beausejour, C. M., Rock, J. M., Augustus, S., Jamieson, A. C., Porteus, M. H., Gregory, P. D., & Holmes, M. C. (2005). Highly efficient endogenous human gene correction using designed zinc-finger nucleases. *Nature*, *435*(7042), 646–651. https://doi.org/10.1038/nature03556

Vakulskas, C. A., Dever, D. P., Rettig, G. R., Turk, R., Jacobi, A. M., Collingwood, M. A., Bode, N. M., McNeill, M. S., Yan, S., Camarena, J., Lee, C. M., Park, S. H., Wiebking, V., Bak, R. O., Gomez-Ospina, N., Pavel-Dinu, M., Sun, W., Bao, G., Porteus, M. H., & Behlke, M. A. (2018). A high-fidelity Cas9 mutant delivered as a ribonucleoprotein complex enables efficient gene editing in human hematopoietic stem and progenitor cells. *Nature Medicine*, *24*(8), 1216–1224. https://doi.org/10.1038/s41591-018-0137-0

Valtavaara, M., Szpirer, C., Szpirer, J., & Myllylä, R. (1998). Primary structure, tissue distribution, and chromosomal localization of a novel isoform of lysyl hydroxylase (lysyl hydroxylase 3). *Journal of Biological Chemistry*, *273*(21), 12881–12886. https://doi.org/10.1074/jbc.273.21.12881

Vanacore, R., Ham, A. J. L., Voehler, M., Sanders, C. R., Conrads, T. P., Veenstra, T. D., Sharpless, B., Dawson, P. E., & Hudson, B. G. (2009). A Sulfilimine Bond Identified in Collagen IV. *Science*, *325*(5945), 1230–1234. https://doi.org/10.1126/science.1176811

Vandenhaute, E., Dehouck, L., Boucau, M.-C., Sevin, E., Uzbekov, R., Tardivel, M., Gosselet, F., Fenart, L., Cecchelli, R., & Dehouck, M.-P. (2011). Modelling the Neurovascular Unit and the Blood-Brain Barrier with the Unique Function of Pericytes. *Current Neurovascular Research*, *8*(4), 258–269. https://doi.org/10.2174/156720211798121016

van Geest, R. J., Klaassen, I., Vogels, I. M. C., van Noorden, C. J. F., & Schlingemann, R. O. (2010). Differential TGF-β signaling in retinal vascular cells: A role in diabetic retinopathy? *Investigative Ophthalmology and Visual Science*, *51*(4), 1857–1865. https://doi.org/10.1167/iovs.09-4181

Vanlandewijck, M., He, L., Mäe, M. A., Andrae, J., Ando, K., del Gaudio, F., Nahar, K., Lebouvier, T., Laviña, B., Gouveia, L., Sun, Y., Raschperger, E., Räsänen, M., Zarb, Y., Mochizuki, N., Keller, A., Lendahl, U., & Betsholtz, C. (2018). A molecular atlas of cell types and zonation in the brain vasculature. *Nature*, *554*(7693), 475–480. https://doi.org/10.1038/nature25739

Vatine, G. D., Barrile, R., Workman, M. J., Sances, S., Barriga, B. K., Rahnama, M., Barthakur, S., Kasendra, M., Lucchesi, C., Kerns, J., Wen, N., Spivia, W. R., Chen, Z., van Eyk, J., & Svendsen, C. N. (2019). Human iPSC-Derived Blood-Brain Barrier Chips Enable Disease Modeling and Personalized Medicine Applications. *Cell Stem Cell*, *24*(6), 995–1005. https://doi.org/10.1016/j.stem.2019.05.011

Verdura, E., Hervé, D., Bergametti, F., Jacquet, C., Morvan, T., Prieto-Morin, C., Mackowiak, A., Manchon, E., Hosseini, H., Cordonnier, C., Girard-Buttaz, I., Rosenstingl, S., Hagel, C., Kuhlenbaümer, G., Leca-Radu, E., Goux, D., Fleming, L., van Agtmael, T., Chabriat, H., … Tournier-Lasserve, E. (2016). Disruption of a miR-29 binding site leading to COL4A1 upregulation causes pontine autosomal dominant microangiopathy with leukoencephalopathy. *Annals of Neurology*, *80*(5), 741–753. https://doi.org/10.1002/ana.24782

Veres, A., Gosis, B. S., Ding, Q., Collins, R., Ragavendran, A., Brand, H., Erdin, S., Talkowski, M. E., & Musunuru, K. (2014). Low incidence of Off-target mutations in individual CRISPR-Cas9 and TALEN targeted human stem cell clones detected by whole-genome sequencing. *Cell Stem Cell*, *15*(1), 27–30. https://doi.org/10.1016/j.stem.2014.04.020

Verma, P., & Greenberg, R. A. (2016). Noncanonical views of homology-directed DNA repair. *Genes and Development*, 30(10), 1138–1154. https://doi.org/10.1101/gad.280545.116

Vigh, J. P., Kincses, A., Ozgür, B., Walter, F. R., Santa-Maria, A. R., Valkai, S., Vastag, M., Neuhaus, W., Brodin, B., Dér, A., & Deli, M. A. (2021). Transendothelial electrical resistance measurement across the blood–brain barrier: A critical review of methods. *Micromachines*, 12(6), 685. https://doi.org/10.3390/mi12060685

Villaseñor, R., Lampe, J., Schwaninger, M., & Collin, L. (2019). Intracellular transport and regulation of transcytosis across the blood–brain barrier. *Cellular and Molecular Life Sciences*, 76(6), 1081–1092. https://doi.org/10.1007/s00018-018-2982-x

Viswanathan, A., & Greenberg, S. M. (2011). Cerebral amyloid angiopathy in the elderly. *Annals of Neurology*, *70*(6), 871–880. https://doi.org/10.1002/ana.22516

Voulgaris, D., Nikolakopoulou, P., & Herland, A. (2022). Generation of Human iPSC-Derived Astrocytes with a mature star-shaped phenotype for CNS modeling. *Stem Cell Reviews and Reports*, *18*(7), 2494–2512. https://doi.org/https://doi.org/10.1007/s12015-022-1037

Wallez, Y., & Huber, P. (2008). Endothelial adherens and tight junctions in vascular homeostasis, inflammation and angiogenesis. *Biochimica et Biophysica Acta - Biomembranes*, 1778(3), 794–809. https://doi.org/10.1016/j.bbamem.2007.09.003

Walshe, T. E., Saint-Geniez, M., Maharaj, A. S. R., Sekiyama, E., Maldonado, A. E., & D'Amore, P. A. (2009). TGF-β is required for vascular barrier function, endothelial survival and homeostasis of the adult microvasculature. *PLoS ONE*, *4*(4), e5149. https://doi.org/10.1371/journal.pone.0005149

Wang, D., Mohammad, M., Wang, Y., Tan, R., Murray, L. S., Ricardo, S., Dagher, H., van Agtmael, T., & Savige, J. (2017). The Chemical Chaperone, PBA, Reduces ER Stress and Autophagy and Increases Collagen IV α5 Expression in Cultured Fibroblasts From Men With X-Linked Alport Syndrome and Missense Mutations. *Kidney International Reports*, *4*(3), 739–748. https://doi.org/10.1016/j.ekir.2017.03.004

Wang, J. F., Zhang, X. F., & Groopman, J. E. (2001). Stimulation of β1 Integrin Induces Tyrosine Phosphorylation of Vascular Endothelial Growth Factor Receptor-3 and Modulates Cell Migration. *Journal of Biological Chemistry*, *276*(45), 41950–41957. https://doi.org/10.1074/jbc.M101370200

Wang, J., & Milner, R. (2006). Fibronectin promotes brain capillary endothelial cell survival and proliferation through α5β1 and αvβ3 integrins via MAP kinase signalling. *Journal of Neurochemistry*, *96*(1), 148–159. https://doi.org/10.1037/0022-0663.98.1.148

Wang, Y., Liu, K. I., Sutrisnoh, N. A. B., Srinivasan, H., Zhang, J., Li, J., Zhang, F., Lalith, C. R. J., Xing, H., Shanmugam, R., Foo, J. N., Yeo, H. T., Ooi, K. H., Bleckwehl, T., Par, Y. Y. R., Lee, S. M., Ismail, N. N. B., Sanwari, N. A. B., Lee, S. T. V., … Tan, M. H. (2018). Systematic evaluation of CRISPR-Cas systems reveals design principles for genome editing in human cells. *Genome Biology*, *19*(1), 62. https://doi.org/10.1186/s13059-018-1445-x

Wardlaw, J. M. (2010). Blood-brain barrier and cerebral small vessel disease. *Journal of the Neurological Sciences*, *299*(1–2), 66–71. https://doi.org/10.1016/j.jns.2010.08.042

Wardlaw, J. M., Farrall, A., Armitage, P. A., Carpenter, T., Chappell, F., Doubal, F., Chowdhury, D., Cvoro, V., & Dennis, M. S. (2008). Changes in background blood-brain barrier integrity between lacunar and cortical ischemic stroke subtypes. *Stroke*, *39*(4), 1327–1332. https://doi.org/10.1161/STROKEAHA.107.500124

Wardlaw, J. M., Smith, C., & Dichgans, M. (2019). Small vessel disease: mechanisms and clinical implications. *The Lancet Neurology*, 18(7), 684–696. https://doi.org/10.1016/S1474-4422(19)30079-1

Wardlaw, J. M., Smith, E. E., Biessels, G. J., Cordonnier, C., Fazekas, F., Frayne, R., Lindley, R. I., O'Brien, J. T., Barkhof, F., Benavente, O. R., Black, S. E., Brayne, C., Breteler, M., Chabriat, H., DeCarli, C., de Leeuw, F. E., Doubal, F., Duering, M., Fox, N. C., … Dichgans, M. (2013). Neuroimaging standards for research into small vessel disease and its contribution to ageing and neurodegeneration. *The Lancet Neurology*, 12(8), 822–838. https://doi.org/10.1016/S1474-4422(13)70124-8

Weisheit, I., Kroeger, J. A., Malik, R., Klimmt, J., Crusius, D., Dannert, A., Dichgans, M., & Paquet, D. (2020). Detection of Deleterious On-Target Effects after HDR-Mediated CRISPR Editing. *Cell Reports*, *31*(8), 107689. https://doi.org/10.1016/j.celrep.2020.107689

Weisheit, I., Kroeger, J. A., Malik, R., Wefers, B., Lichtner, P., Wurst, W., Dichgans, M., & Paquet, D. (2021). Simple and reliable detection of CRISPR-induced on-target effects by qgPCR and SNP genotyping. *Nature Protocols*, *16*(3), 1714–1739. https://doi.org/10.1038/s41596-020-00481-2

Weksler, B., Romero, I. A., & Couraud, P. O. (2013). The hCMEC/D3 cell line as a model of the human blood brain barrier. *Fluids and Barriers of the CNS*, 10, 16. https://doi.org/10.1186/2045-8118-10-16

Whitelock, J. M., Melrose, J., & Iozzo, R. v. (2008). Diverse cell signaling events modulated by Perlecan. *Biochemistry*, 47(43), 11174–11183. https://doi.org/10.1021/bi8013938

Whittaker, E., Thrippleton, S., Chong, L., Collins, V., Ferguson, A., Henshall, D., Lancastle, E., Wilkinson, T., Wilson, B., Wilson, K., Sudlow, C., Wardlaw, J., & Rannikmäe, K. (2022). Systemic review of cerebral phenotypes associated with monogenic small vessel disease. *Systemic Review of Cerebral Phenotypes Associated with Monogenic Small Vessel Disease*, *11*(12), e025629. https://doi.org/10.1161/JAHA.121.025629

Widmera, C., Gebauerb, J. M., Brunsteinb, E., Rosenbaumc, S., Zauckec, F., Drogemüllerd, C., Leebd, T., & Baumannb, U. (2012). Molecular basis for the action of the collagen-specific chaperone Hsp47/SERPINH1 and its structure-specific client recognition. *Proceedings of the National Academy of Sciences of the United States of America*, *109*(33), 13243–13247. https://doi.org/10.1073/pnas.1208072109

Williams, I. M., & Wu, J. C. (2019). Generation of Endothelial Cells From Human Pluripotent Stem Cells. *Arteriosclerosis, Thrombosis, and Vascular Biology*, *39*(7), 1317–1329. https://doi.org/10.1161/atvbaha.119.312265

Wilson, D. G., Phamluong, K., Li, L., Sun, M., Cao, T. C., Liu, P. S., Modrusan, Z., Sandoval, W. N., Rangell, L., Carano, R. A. D., Peterson, A. S., & Solloway, M. J. (2011). Global defects in collagen secretion in a Mia3/TANGO1 knockout mouse. *Journal of Cell Biology*, *193*(5), 935–951. https://doi.org/10.1083/jcb.201007162

Wilson, R., Lees, J. F., & Bulleid, N. J. (1998). Protein disulfide isomerase acts as a molecular chaperone during the assembly of procollagen. *Journal of Biological Chemistry*, *273*(16), 9637–9643. https://doi.org/10.1074/jbc.273.16.9637

Winkler, E. A., Bell, R. D., & Zlokovic, B. v. (2011). Central nervous system pericytes in health and disease. *Nature Neuroscience*, 14(11), 1398–1405. https://doi.org/10.1038/nn.2946

Wolff, A., Antfolk, M., Brodin, B., & Tenje, M. (2015). In Vitro Blood-Brain Barrier Models - An Overview of Established Models and New Microfluidic Approaches. *Journal of Pharmaceutical Sciences*, 104(9), 2727–2746. https://doi.org/10.1002/jps.24329

Workman, M. J., & Svendsen, C. N. (2020). Recent advances in human iPSC-derived models of the blood-brain barrier. *Fluids and Barriers of the CNS*, 17(1), 30. https://doi.org/10.1186/s12987-020-00191-7

Wu, X., Kriz, A. J., & Sharp, P. A. (2014). Target specificity of the CRISPR-Cas9 system. *Quantitative Biology*, 2(2), 59–70. https://doi.org/10.1007/s40484-014-0030-x

Xiao, J., Sun, X., Madhan, B., Brodsky, B., & Baum, J. (2015). NMR studies demonstrate a unique AAB composition and chain register for a heterotrimeric type IV collagen model peptide containing a natural interruption site. *Journal of Biological Chemistry*, *290*(40), 24201–24209. https://doi.org/10.1074/jbc.M115.654871

Xue, C., & Greene, E. C. (2021). DNA Repair Pathway Choices in CRISPR-Cas9-Mediated Genome Editing. *Trends in Genetics*, 37(7), 639–656. https://doi.org/10.1016/j.tig.2021.02.008

Xu, L., Nirwane, A., & Yao, Y. (2019). Basement membrane and blood-brain barrier. *Stroke and Vascular Neurology*, 4(2), e000198. https://doi.org/10.1136/svn-2018-000198

Yamamoto, H., Ehling, M., Kato, K., Kanai, K., van Lessen, M., Frye, M., Zeuschner, D., Nakayama, M., Vestweber, D., & Adams, R. H. (2015). Integrin β1 controls VE-cadherin localization and blood vessel stability. *Nature Communications*, *6*, 6429. https://doi.org/10.1038/ncomms7429

Yamamoto, Y., Kojima, K., Taura, D., Sone, M., Washida, K., Egawa, N., Kondo, T., Minakawa, E. N., Tsukita, K., Enami, T., Tomimoto, H., Mizuno, T., Kalaria, R. N., Inagaki, N., Takahashi, R., Harada-Shiba, M., Ihara, M., & Inoue, H. (2020). Human iPS cell-derived mural cells as an in vitro model of hereditary cerebral small vessel disease. *Molecular Brain*, *13*, 38. https://doi.org/10.1186/s13041-020-00573-w

Yan, Y., Shin, S., Jha, B. S., Liu, Q., Sheng, J., Li, F., Zhan, M., Davis, J., Bharti, K., Zeng, X., Rao, M., Malik, N., & Vemuri, M. C. (2013). Efficient and Rapid Derivation of Primitive Neural Stem Cells and Generation of Brain Subtype Neurons From Human Pluripotent Stem Cells. *Stem Cells Translational Medicine*, *2*(11), 862–870. https://doi.org/10.5966/sctm.2013-0080

Yang, A. C., Vest, R. T., Kern, F., Lee, D. P., Agam, M., Maat, C. A., Losada, P. M., Chen, M. B., Schaum, N., Khoury, N., Toland, A., Calcuttawala, K., Shin, H., Pálovics, R., Shin, A., Wang, E. Y., Luo, J., Gate, D., Schulz-Schaeffer, W. J., … Wyss-Coray, T. (2022). A human brain vascular atlas reveals diverse mediators of Alzheimer's risk. *Nature*, *603*(7903), 885–892. https://doi.org/10.1038/s41586-021-04369-3

Yang, Y., Estrada, E. Y., Thompson, J. F., Liu, W., & Rosenberg, G. A. (2007). Matrix metalloproteinase-mediated disruption of tight junction proteins in cerebral vessels is reversed by synthetic matrix metalloproteinase inhibitor in focal ischemia in rat. *Journal of Cerebral Blood Flow and Metabolism*, *27*(4), 697–709. https://doi.org/10.1038/sj.jcbfm.9600375

Yao, Y. (2017). Laminin: loss-of-function studies. *Cellular and Molecular Life Sciences*, 74(6), 1095–1115. https://doi.org/10.1007/s00018-016-2381-0

Yao, Y. (2019). Basement membrane and stroke. *Journal of Cerebral Blood Flow & Metabolism*, *39*(1), 3–19. https://doi.org/10.1177/0271678X18801467

Yao, Y., Chen, Z. L., Norris, E. H., & Strickland, S. (2014). Astrocytic laminin regulates pericyte differentiation and maintains blood brain barrier integrity. *Nature Communications*, *5*, 3413. https://doi.org/10.1038/ncomms4413

Yeh, C. D., Richardson, C. D., & Corn, J. E. (2019). Advances in genome editing through control of DNA repair pathways. *Nature Cell Biology*, 21(12), 1468–1478. https://doi.org/10.1038/s41556-019-0425-z

Ye, M., Sanchez, H. M., Hultz, M., Yang, Z., Bogorad, M., Wong, A. D., & Searson, P. C. (2014). Brain microvascular endothelial cells resist elongation due to curvature and shear stress. *Scientific Reports*, *4*, 4681. https://doi.org/10.1038/srep04681

Yeo, N. C., Chavez, A., Lance-Byrne, A., Chan, Y., Menn, D., Milanova, D., Kuo, C. C., Guo, X., Sharma, S., Tung, A., Cecchi, R. J., Tuttle, M., Pradhan, S., Lim, E. T., Davidsohn, N., Ebrahimkhani, M. R., Collins, J. J., Lewis, N. E., Kiani, S., & Church, G. M. (2018). An enhanced CRISPR repressor for targeted mammalian gene regulation. *Nature Methods*, *15*(8), 611–616. https://doi.org/10.1038/s41592-018-0048-5

Yip, B. H. (2020). Recent advances in CRISPR/Cas9 delivery strategies. *Biomolecules*, 10(6), 839. https://doi.org/10.3390/biom10060839

Yoshihara, M., Hayashizaki, Y., & Murakawa, Y. (2017). Genomic Instability of iPSCs: Challenges Towards Their Clinical Applications. *Stem Cell Reviews and Reports*, 13(1), 7–16. https://doi.org/10.1007/s12015-016-9680-6

Yu, S. M., Li, Y., & Kim, D. (2011). Collagen mimetic peptides: Progress towards functional applications. *Soft Matter*, 7(18), 7927–7938. https://doi.org/10.1039/c1sm05329a

Yuan, W., Lv, Y., Zeng, M., & Fu, B. M. (2009). Non-invasive measurement of solute permeability in cerebral microvessels of the rat. *Microvascular Research*, *77*(2), 166–173. https://doi.org/10.1016/j.mvr.2008.08.004

Yurchenco, P. D. (2011). Basement membranes: Cell scaffoldings and signaling platforms. *Cold Spring Harbor Perspectives in Biology*, *3*(2), a004911. https://doi.org/10.1101/cshperspect.a004911

Yurchenco, P. D., & Ruben, G. C. (1987). Basement membrane structure in situ: Evidence for lateral associations in the type IV collagen network. *Journal of Cell Biology*, *105*(6 Pt. 1), 2559–2568. https://doi.org/10.1083/jcb.105.6.2559

Zaccaria, M. L., di Tommaso, F., Brancaccio, A., Paggi, P., & Petrucci, T. C. (2001). Dystroglycan distribution in adult mouse brain: A light and electron microscopy study. *Neuroscience*, *104*(2), 311–324. https://doi.org/10.1016/S0306-4522(01)00092-6

Zhang, X. H., Tee, L. Y., Wang, X. G., Huang, Q. S., & Yang, S. H. (2015). Off-target effects in CRISPR/Cas9-mediated genome engineering. *Molecular Therapy - Nucleic Acids*, 4(11), e264. https://doi.org/10.1038/mtna.2015.37

Zhao, F., Zhong, L., & Luo, Y. (2021). Endothelial glycocalyx as an important factor in composition of blood-brain barrier. *CNS Neuroscience and Therapeutics*, *27*(1), 26–35. https://doi.org/10.1111/cns.13560

Zhao, Y.-Y., Duan, R. N., Ji, L., Liu, Q. J., & Yan, C. Z. (2019). Cervical Spinal Involvement in a Chinese Pedigree with Pontine Autosomal Dominant Microangiopathy and Leukoencephalopathy Caused by a 3' Untranslated Region Mutation of COL4A1 Gene. *Stroke*, *50*(9), 2307–2313. https://doi.org/10.1161/STROKEAHA.119.024875

Zhao, Z., Sagare, A. P., Ma, Q., Halliday, M. R., Kong, P., Kisler, K., Winkler, E. A., Ramanathan, A., Kanekiyo, T., Bu, G., Owens, N. C., Rege, S. v., Si, G., Ahuja, A., Zhu, D., Miller, C. A., Schneider, J. A., Maeda, M., Maeda, T., … Zlokovic, B. v. (2015). Central role for PICALM in amyloid-β blood-brain barrier transcytosis and clearance. *Nature Neuroscience*, *18*(7), 978–987. https://doi.org/10.1038/nn.4025

Zhou, Q., Yang, D., Ombrello, A. K., Zavialov, A. v., Toro, C., Zavialov, A. v., Stone, D. L., Chae, J. J., Rosenzweig, S. D., Bishop, K., Barron, K. S., Kuehn, H. S., Hoffmann, P., Negro, A., Tsai, W. L., Cowen, E. W., Pei, W., Milner, J. D., Silvin, C., … Aksentijevich, I. (2014). Early-Onset Stroke and Vasculopathy Associated with Mutations in ADA2. *New England Journal of Medicine*, *370*(10), 911–920. https://doi.org/10.1056/nejmoa1307361

Zhu, J., Li, X., Yin, J., Hu, Y., Gu, Y., & Pan, S. (2018). Glycocalyx degradation leads to blood–brain barrier dysfunction and brain edema after asphyxia cardiac arrest in rats. *Journal of Cerebral Blood Flow and Metabolism*, *38*(11), 1979–1992. https://doi.org/10.1177/0271678X17726062

Zlokovic, B. v. (2008). The Blood-Brain Barrier in Health and Chronic Neurodegenerative Disorders. *Neuron*, 57(2), 178–201. https://doi.org/10.1016/j.neuron.2008.01.003

6. Acknowledgements

Firstly, I would like to thank Dominik because without him this entire dissertation and project would not be possible. My original plan was to seek out a PhD program in the US when I had completed my masters with the GSN. It was actually by luck after a game of rock, paper, and scissors with a classmate that I had the opportunity to participate in the GSN course for a week in his lab where I was inspired by the research being done. This eventually led to an opportunity to pursue a PhD project in Dominik's lab. For me, this was the perfect scenario because I knew how great Dominik already was as a mentor, the research was cutting-edge, and the colleagues were lovely. I am so grateful that everything worked out this way and I was able to begin my PhD journey with Dominik in October 2019. Naturally, there were both good and bad times during the PhD, but no matter what Dominik was always there for me as a mentor. I cannot thank Dominik enough for helping me grow and progress as a scientist and as a professional. Over the last few years, I have become an expert in genome editing and hiPSCs that would not have been remotely possible without Dominik's help and support.

I would also like to give a giant acknowledgement to all of my colleagues in the PaquetLab. The working environment was overwhelmingly pleasant and everyone without exceptions was helpful whenever I needed something. Every moment with my colleagues was enjoyable. In the stressful and competitive environment of academia this can be a rare occurrence and I was truly blessed with amazing colleagues. I would also like to thank all of you for all of the memories outside of the lab like thanksgiving and Christmas dinners as well as outings to the Isar and such. These times relieved the stress that comes along with a PhD and I will cherish these unforgettable moments forever.

I would very much like to thank my family for their support from across the pond during my PhD. We were only able to see each other once or twice a year but each one of these times was special to me and allowed me to reset and start fresh once I went back to my PhD. In the meantime, all of the video calls helped me get through tough times and also good times. To my mom and dad, somehow you were able to raise me and that in and of its self is a great achievement more so than this dissertation and I hope that I was able to make you proud with what I have accomplished. It is all possible because you have supported me through thick and thin from my NCSSM mishaps, my uncertain beginning at Wingate, and through my progression as an international masters and PhD student. To Stina and Peter, I am so grateful to have siblings like you. Whether you guys know it or not, you have helped me keep my head straight through crazy times and even though we are all very different I could not ask for a better brother and sister. To Gran and Grandpa (Kroeger) you have supported me tremendously and even as I write this you are asking me how my progress on the dissertation is going. I am so grateful to have that kind of support. To Grandma and Grandpa (Galioto), I am also thankful for the love and support you have sent my way. I was pleasantly surprised that you guys appeared on the video before my rugby final and yes I do remember who you are! To everyone else in my family, I would like to thank you from afar for supporting me from afar. I really have the best family and cannot wait to see everyone this Christmas.

The entire GSN team has been very helpful and supportive since the beginning. Even at the start when I had issues with my master's Zeugnis, Stephanie was there with me at the Studentenkanzlei in the city center to help me. I am very grateful to have been a part of an extraordinary graduate school.

Last but certainly not least, I would like to thank my amazing girlfriend Klaudja. Words cannot describe what she means to me. At this point, we have only known each other for less than a year but you have impacted my life in such a positive way and continue to challenge me to become better. Of course you have supported me while writing the dissertation but your love and support extends far beyond that. This is a turning point in my life and I could not have a better woman by my side during this time.

7. Curriculum Vitae

Education

10/2019 – Present	**LMU Munich**. Neuroscience PhD expected from the Graduate School of Systemic Neurosciences March 2023.
10/2017 – 09/2019	**LMU Munich**. Neuroscience MSc from the Graduate School of Systemic Neurosciences.
08/2012 – 05/2017	**Wingate University**. BSc in mathematics and chemistry with minors in physics and philosophy
08/2011 – 06/2012	**North Carolina School of Science and Math.** Boarding school specializing in science and math for highly gifted students.

Professional Experience

01/2019 – Present

Institute for Stroke and Dementia Research, LMU Munich, Prof. Dr. Paquet

- CRISPR/Cas9 genome editing in human induced pluripotent stem cells (hiPSCs) in multiple genes, characterizing CRISPR/Cas9 side effects, differentiation of neural and vascular cell types from hiPSCs, and generation of 3D vascular cultures with perfusion. (Masters and PhD projects)

04/2018 – 12/2018

Division of Neurobiology, LMU Munich, PD Dr. Kopp-Scheinpflug

- Immunofluorescence labelling and confocal microscopy and *Ex vivo* electrophysiology of mouse auditory brainstem

03/2018 – 04/2018

Department of Chemistry, Wingate University, Dr. Wilson

- Solid phase peptide synthesis using d-amino acid derivatives

05/2016 – 07/2016

Department of Physics and Astronomy, University of South Carolina, Dr. Altschul

- Placed constraints on theoretical Lorentz-Violating Dispersion Relations

08/2015 – 10/2016

Department of Chemistry, Wingate University, Dr. Kroeger

- Quantitative gas chromatography-mass spectrometry to determine caffeine and oxalic acid content in tea

06/2011 – 07/2011

Department of Kinesiology, University of North Carolina at Charlotte, Dr. Huet

- Optimization of sex determination assay of neonatal mice using PCR

06/2010 – 07/2010

Department of Physics & Optical Science, University of North Carolina at Charlotte, Dr. Jofre

- Calculated the temperature of shrinking hydrosomes trapped by a laser

8. List of publications

Weisheit, I., **Kroeger, J. A.**, Malik, R., Klimmt, J., Crusius, D., Dannert, A., Dichgans, M., & Paquet, D. (2020). Detection of deleterious on-target effects after HDR-mediated CRISPR editing. ***Cell Reports***, *31*(8), 107689. https://doi.org/10.1016/j.celrep.2020.107689

Weisheit, I., **Kroeger, J. A**., Malik, R., Wefers, B., Lichtner, P., Wurst, W., Dichgans, M., & Paquet, D. (2021). Simple and reliable detection of CRISPR-induced on-target effects by QGPCR and SNP genotyping. ***Nature Protocols***, *16*(3), 1714–1739. https://doi.org/10.1038/s41596-020-00481-2

9. Eidesstattliche Erklärung/Affidavit

Joseph Kroeger

Hiermit versichere ich an Eides statt, dass ich die vorliegende Dissertation “Generation and Characterization of COL4A1 Small Vessel Disease Mutations in a Human iPSC Model” selbstständig angefertigt habe, mich außer der angegebenen keiner weiteren Hilfsmittel bedient und alle Erkenntnisse, die aus dem Schrifttum ganz oder annähernd übernommen sind, als solche kenntlich gemacht und nach ihrer Herkunft unter Bezeichnung der Fundstelle einzeln nachgewiesen habe.

I hereby confirm that the dissertation “Generation and Characterization of COL4A1 Small Vessel Disease Mutations in a Human iPSC Model” is the result of my own work and that I have only used sources or materials listed and specified in the dissertation.

München/Munich Joseph Kroeger

06.12.2022 _____

10. Declaration of author contributions

Chapter 3.1: Genome editing via plasmid delivery in HEK293 and hiPSCs was optimized by Isabel Weisheit (IW), Julien Klimmt (JK), and Dennis Crusius (DC). The optimization of RNP delivery of CRISRP/Cas9 was performed by IW and Joseph Anthony Kroeger (JAK). All genome editing experiments were performed and analyzed by JAK. The OnTE qgPCR and LOH assays were designed by Dominik Paquet (DP) and IW and optimized by IW and JAK. The molecular karyotyping assays were performed at Life&Brain GmbH, or at the HelmholtzZentrum München with analysis by DP, DC and JAK. 2D stainings were optimized by JK (also chapter 3.2). All quality control assays were performed and analyzed by JAK.

Chapter 3.2: The endothelial cell and smooth muscle cell differentiations were established by IW in collaboration with Tom Webb, University of Leicester, UK. They were further characterized by IW and Judit González-Gallego (JG). The pericyte differentiation is based on the published protocol by Orlova et al., 2014 and was established in the lab by IW. It was further characterized by IW and JG. The qPCR assay was optimized by Carolina Cardoso Gonçalves and JAK. Primers for qPCR were designed and tested by JAK and JG or used as published. The qPCR experiments were performed and analyzed by JAK. 2D stainings were performed by JAK and imaged by JG and JAK. 3D culture stainings were optimized by JG, and 3D culture staining experiments were performed and analyzed by JAK. The TEER assay was established and optimized by JAK. All TEER experiments were performed and analyzed by JAK. The 3D cultures were based on Campisi et al., 2018 and established, optimized, and characterized by JG. The 3D culture experiments were performed by JAK. The perfusion of the 3D cultures was optimized by JAK and the perfusion experiments were performed by JAK.